Design Report

BNL AGS E821

A New Precision Measurement of the Muon $(g-2)$ Value at the level of 0.35 ppm

Boston University, Brookhaven National Laboratory, Cornell University, Fairfield University, University of Heidelberg, University of Illinois, Max Planck Institute für Med. Forschung - Heidelberg, University of Minnesota, Scuola Normale Superiore, University of Tokyo, KEK, Riken, Yale University

3^{rd} Edition

Second (Revised) Printing - September 1995

Collaboration Members

D.H. Brown, R.M. Carey, W. Earle, E.S. Hazen, F. Krienen, M. Messier, J.P. Miller, J. Ouyang, V.A. Monitch, B.L. Roberts,† L.R. Sulak, G. Varner, W.A. Worstell - **Boston University**

J. Benante, H.N. Brown, G. Bunce,§ J. Cullen, G.T. Danby, C. Gardner, J. Geller, H. Hseuh, J.W. Jackson, L. Jia, R. Larsen, Y.Y. Lee, R.E. Meier, W. Meng, W.M. Morse,‡ C. Pai, C. Pappas, I. Polk, S. Rankowitz, J. Sandberg, Y. Semertzidis, R. Shutt, L. Snydstrup, A. Soukas, A. Stillman, T. Tallerico, F. Toldo, K. Woodle - **Brookhaven National Laboratory**

T. Kinoshita, Y. Orlov - **Cornell University**

D. Winn - **Fairfield University**

J. Gerhaeuser, A. Grossmann, K. Jungmann, G. zu Putlitz, P. von Walter - **University of Heidelberg**

B. Bunker, P.T. Debevec, W. Deninger, D.W. Hertzog, T. Jones, S. Sedykh, D. Urner - **University of Illinois**

M.A. Green - **LBL/BNL**

U. Haeberlen -**Max Planck Institiute für Med. Forschung, Heidelberg**

P. Cushman, S. Giron, J. Kindem, D. Maxam, D. Miller, C. Timmermans, D. Zimmerman - **University of Minnesota**

L.M. Barkov, D.N. Grigorev, B.I. Khazin, E.A. Kuraev, Yu.M. Shatunov, E. Solodov - **Institute of Nuclear Physics, Novosibirsk**

K. Nagamine - **University of Tokyo**

K. Endo, H. Hirabayashi, S. Ichii, S. Kurokawa, Y. Mizumachi, T. Sato, A. Yamamoto - **KEK**

K. Ishida - **Riken**

M. Deng, S.K. Dhawan, A.A. Disco, F.J.M. Farley, X. Fei, V.W. Hughes†, D. Kawall, M. Grosse-Perdekamp, R. Prigl, S.I. Redin, - **Yale University**

†Co-Spokesmen

‡Resident Spokesman

§Project Manager

Preface (Overview, Progress, and Milestones)

The for the muon *(g-2)* experiment, E821 at the Brookhaven AGS, was first proposed to the Brookhaven program committee in September 1985. It was defended for a second time in October 1986, and "first stage approval" was granted on 17 November 1986. A revised proposal was submitted in October 1987. Final approval was granted on 3 March 1988. Originally there was a four-year construction schedule, which began in FY89. This schedule was subsequently changed to a five-year one, which has stretched further. The first beam is now scheduled for early 1996.

This document is the third and last edition of the Design Report for E821. Its predecessors have, by necessity, been a statement of intentions as much as a source of details about the experiment, since at the time of their preparation many of the details were still being worked out.

The situation is much different now. With beam just over a year away, the superconducting coils wound and installed in their cryostats, the storage ring magnet almost completed, this document is much more mature than its predecessors, and only a few details remain to be resolved.

Muon injection now plays a central role in achieving the precision advertised in the experiment's name. A working decision to go with a magnetic kicker has been taken, and the necessary R&D is well along.

The beamline, superconducting inflector, storage ring magnet, shimming of the magnet, field monitoring and control, are all well along in development or construction. The electron detectors are in production and their electronics are in the final prototype stage. The data acquisition system and the slow control system are being designed, and the host computer is already installed in the $(g-2)$ building. The beam dynamics calculations, which were scarcely existent when the previous editions were written, have matured, and have even been carried out independently at several institutions.

A rather detailed management structure has developed, and it is described in detail in Chapter 24. Coordination between the various tasks is crucial to the success of the project, and this is now being overseen seen by a number of coordinators who are listed in Chapter 24.

A number of important R&D tests have been carried out over the past few years, and the results have been reported in *Muon (g-2) Technical Notes*. These notes, which document the R&D program, include the refrigerator acceptance test, shimming studies with the test magnet, detector studies with test beam, and quadrupole and kicker studies, among other topics, may be obtained from the *(g-2)* Secretary, Mrs. Joan Depken, BNL. Only the title and a brief description is given below in the footnotes. [1-23] Additional details are given in the appropriate chapters.

1. #190 *Acceptance test of the g-2 refrigerator*, Authors: R. Meier, A. Esper, and L. Jia, 29 November 1993, Refrigerator test with dummy load.
2. #187 *The performance of the WFD in the summer '93 Testbeam run*, Author: Rob Carey, Date: 9 March 1994, The WFD is the wave form digitizer that will be used to read the electron calorimeters. Results are compared with ADCs and 2.5 ns interleaved reads with two WFDs is tried with the AGS test beam.

3. #178 *High frequency attenuation in 50 ohm cables,* Authors: B. Lee Roberts and Christopher Roof, Date: November 1993,.
4. #177 *July 1993 g-2 test beam results for the calorimeter, FSD, and SSD,* Authors: T.D. Jones, G. Garino, D.W. Hertzog, R. Carey, J. Miller, J. Ouyang, L. Roberts, W. Worstell, K. Arrington, D. Kefford, J. Kennedy, R. Pisani, C. Sanzeni, D.R. Winn, P. Cushman, Date: November 1993, Studies of the electron calorimeter, front and side scintillation detectors with the AGS test beam.
5. #169 *Minutes of the Quadrupole Meeting of August 18, 1993,* Author: Yannis K. Semertzidis, Date: August 28, 1993, Final dimensions, test results, pressure requirements, DC high voltage and resonant frequency of trapped electrons gives electric field to 0.5possibility of pumping between AGS cycles.
6. #168 *Test setup for measuring the magnetic field due to kicker eddy currents,* Authors: Yannis K. Semertzidis, Francis J.M. Farley, Richard Larsen, William M. Morse, Joe Yelk, Date: August 27, 1993, Development of a test setup to measure varying magnetic fields, such as the remnant field from the muon kicker. A 6 mG measurement was made in the test..
7. #161 *Results of the tests of the Heidelberg NMR system at Los Alamos,* Authors: R. Prigl, K. Jungmann, G. zu Putlitz, P. v. Walter, U. Haeberlen, X. Fei, V. W. Hughes, M. Janousch, W. Liu, W. Schwarz, Date: June 1993.
8. #156 *Results of Boston University g-2 Electron Calorimeter June 1992 Beam Test,* Authors: D.H. Brown, R.M. Carey, M.B. Chertok, S. Doulas, C.S. Lin, J.P. Miller, B.L. Roberts, W.A. Worstell, X.F. Zhang, G.T. Zwart, R. Pisani, K. Segall, D. Wall, D.R. Winn, Date: April 18, 1993.
9. #144 *Development of distribution ion pumps (DIPs) for g-2 beam vacuum system,* Author: H.C. Hseuh, Date: March 1993, Tests of proposed DIPs in a test magnet.
10. #139 *Results on the Position Sensitive Detector–Summary of the last 2 years,* Authors: P. Cushman and S. Hou, Date: January 19, 1993, Tests with a source and test beam of the proposed fiber hodoscope.
11. #134 *Progress on the electrostatic kicker,* Author: Zhifeng Liu, Date: December 1992, Tests of insulators for the proposed electrostatic muon kicker.
12. #129 *Progress on the NMR Magnetic Field Measurement System,* Authors: U. Haeberlen, K. Jungmann, R. Prigl, G. zu Putlitz, P. v. Walter, Date: September 1992, Includes studies of NMR in a Heidelberg test magnet.
13. #113 *Tests of Prototype Electrostatic Quadrupoles,* Authors: S. Doulas, F. Krienen, R. Larsen, W. Morse, J. Yelk, T. Zwart, Date: April 1992, Misc: tests on hyperbolic quads.
14. #89 *Response of Photomultiplier Tube to Radiation,* Authors: G. Brown and W. Morse, Date: September 1991, Misc: remarks on tests using a source and tests by AGS E871.
15. #87 *Survey of the Magnetic Field Fluctuations and Perturbations for Muon g-2 Experiment,* Authors: X. Fei, K. Woodle, and S. Dhawan, Date: July, 1991, Fluxgate magnetometers were used to measure magnetic field fluctuations in the g-2 building. A 1 mG field due to AGS cycling was observed.

16. #85 *Energy Resolution, Leakage and Light Yield Studies of the g-2 prototype Scintillating Fiber Calorimeter,* Authors: Detector Group, Boston, Fairfield and Yale Universities, Date: August 1991, Misc: First Results of the May-June 1991 AGS A3 beamline tests.
17. #75 *Pulser for Test of Electrostatic Quadrupoles,* Authors: G. Brown, F. Krienen, R. C. Larsen, W. M. Morse, J. Yelk, Date: April 1991.
18. #61 *Prototype of g-2 digitron,* Authors: William M. Morse, Joseph Yelk, Date: October 1990.
19. #47 *Comments on 1989 flash test,* Author: W. M. Morse, Date: May 1990.
20. #45 *Results of the wire chamber flash test,* Author: W. M. Morse, Date: April 1990, Misc: includes comments on effects of phototubes viewing charged particles.
21. #44 *Status of shimming studies with the BNL test magnet,* Author: K. Woodle, Date: 23 April 1990.
22. #39 *g-2 Building Floor Stability,* Authors: A. Pendzick, F. Karl, J. Mills, J. Sullivan, Date: May 23, 1989.
23. #37 *Results of Flash Tests at BNL, May 17-18 1989,* Authors: P. Cushman, S. Dhawan, B. Kerosky, M. May, J. Miller, B.L. Roberts, D. Winn, K. Woodle, W. Worstell, Date: 6 Feb. 1990.

This document represents a substantial amount of work on the part of the collaboration members. Credit for its success must be spread widely over the membership. John Cumings "cut and pasted" hundreds of figures and several chapters for the final draft and the final version of the third edition. Without his help and good cheer, this edition would have been even later in reaching the collaboration. Mrs. Joan Depkin has been essential both in the preparation of chapters by BNL AGS staff as well as in the reproduction, collating and distribution of past editions of this report. She also continues to be the librarian and distributor for the *(g-2)* technical notes, and her help in this final edition as well as in the earlier ones is gratefully acknowledged. Ms. Pat Fleming at Yale played a major role in putting the previous two editions together, and her contributions both there and to this edition are gratefully acknowledged.

This document was typeset using TEXsis and I am grateful to Frank Paige for help in some of its subtleties.

A draft of the third edition was prepared in time for the DOE review of the experiment in May 1994. It has taken some months to finish the revisions to the manuscript, and the editor appreciates all the help and cooperation he has received from his colleagues in producing this document. In the interest of making this report available in a finite time, the editor has been forced to resist making further editorial and clarifying changes to the chapters submitted by the various teams.

BLR - Boston, March 1995

WBS Correlation with Chapters

The Work Breakdown Structure, while a useful accounting tool, does not correspond chapter by chapter to the presentation in this document. In order to help the interested reader find the sections relevant to a given WBS category, the following key is included.

1.1 Storage Ring Magnet
- 1.1.2 Magnet Yoke and Base - Chapter 8.
- 1.1.3 Coil and Cryostat - Chapter 8.
- 1.1.4 Assembly of Ring - Chapter 8.
- 1.1.5 Refrigerator - Chapter 9.

1.2 Beam Monitoring and Dynamics
- 1.2.2 Injection Into the Ring - Chapters 5, 6 and 15.
- 1.2.3 Particle Orbits/Phase Space - Chapter 5.
- 1.2.4 Primary Beam Monitoring - Chapter 6.
- 1.2.5 Secondary Beam Monitoring - Chapter 6.
- 1.2.6 Pion/Muon Beam in the Ring - Chapter 5, 15.

1.3 Magnetic Field Shims - Chapter 14.

1.4 Ring Vacuum and Quadrupoles
- 1.4.2 Ring Vacuum Chamber - Chapter 13.
- 1.4.3 Quadrupole Electrodes - Chapter 11.
- 1.4.4 Beam Vacuum System - Chapter 6.
- 1.4.5 Pulse Equipment - Chapter 11.
- 1.4.6 Tests - Chapter 13.
- 1.4.7 Inflector Cryostat - Chapters 9, 10.
- 1.4.8 Inflector Power Supply - Chapter 10.
- 1.4.9 Inflector Coil - Chapter 10.

1.5 Detectors - Chapter 16.

1.6 AGS Beam + Experimental Hall - Chapters 6, 7.

1.7 Field Measurement and Control - Chapter 14

1.8 Muon Kicker - Chapter 12

1.9 DAQ and Control
- 1.9.2 Host Computer - Chapter 17.
- 1.9.3 VME-Based DAQ - Chapters 16, 17.
- 1.9.4 Slow Control - Chapter 18.
- 1.9.5 DAQ Integration - Chapter 17, 18.

Chapter 1.
Introduction

Revised February 1994

This report describes the design and construction of a unique, high precision superconducting storage ring for 3 GeV/c muons, along with the beamline, detectors, and data acquisition system which are to be used in a new precision measurement of the muon $(g-2)$ value at the Brookhaven National Laboratory.

The goal of AGS E821 is a precision measurement of the muon $(g-2)$ value, or equivalently the anomalous magnetic dipole moment $a_\mu = \frac{1}{2}(g-2)$, to 0.35 ppm which would be an improvement by a factor of 20 compared to the present experimental accuracy of 7.3 ppm from the last CERN experiment. [1,2] The ultrahigh precision aimed for in the BNL experiment presents unusual challenges in physics and in technology.

1.1. General Motivation and Scope

A measurement of a_μ with a precision of 0.35 ppm will provide one of the most sensitive and crucial tests of the standard theory. With the planned and expected improvement by a factor of 3 to 4 in the experimental determination of the hadronic contribution $a_\mu(had)$ to a_μ, the theoretical value of a_μ will be known with a precision of about 0.3 ppm. Hence a comparison of theory and experiment will provide the following:

- A very high precision test of the theoretical value of a_μ which is based on the standard theory and has its dominant contribution from virtual quantum electrodynamic processes. The standard theory incorporates the viewpoint that the muon is a heavy point-like lepton and the precision of the comparison will correspond to processes with four-momentum transfer $Q^2 = 10^3 (GeV/c)^2$.
- A measurement for the first time, with an accuracy of 23%, of the weak interaction contributions to a_μ which arise from single loop diagrams with virtual W and Z bosons. This measurement will provide a crucial test of the renormalizability of the unified electroweak theory.

In addition, the following results will be obtained:

- Comparison of a_μ^- and a_μ^+ as a test of CPT invariance.

- Measurement of the lifetimes of μ^+ and μ^- in the laboratory frame of reference as a test of special relativity and of CPT invariance.
- An improvement on the limit on the electric dipole moment of the muon as a test of T invariance.

Beyond the standard model the muon $(g-2)$ value provides a sensitive and general test for:

- Compositeness or substructure of leptons and gauge bosons.
- Extensions of the standard model with additional particle groups such as gauge bosons or supersymmetric particles.

The physics involved in muon $(g-2)$ is discussed in Chapter 2. A brief summary of the AGS experiment including its parameters and various features is given in Chapter 3.

1.2. Overview of the AGS Experiment

The principle of the experiment is based on the spin motion of polarized muons in a storage ring and is the same as that of the third CERN measurement of a_μ. [1] In a magnetic field B in a storage ring the spin precesses with an angular frequency ω_s which is greater than the orbital cyclotron angular frequency ω_c by ω_a, the $(g-2)$ precession frequency:

$$\omega_a = \omega_s - \omega_c = \frac{e}{mc} a_\mu B. \tag{1.2.1}$$

This equation applies for all values of the momentum. For a special value of the relativistic variable γ, an electric field does not contribute to the spin precession, and the vertical focussing in the storage ring can be provided by electric quadrupoles, with no effect on the spin precession of a central momentum muon. This "magic momentum" is p_μ is 3.09 GeV/c or equivalently the "magic γ" is $\gamma = 29.3$. The use of electrostatic quadrupoles for vertical focussing permits the magnetic field to be as pure a dipole field as it is possible to make.

An accurate determination of a_μ requires an accurate measurement of $\mathbf{B}$ and of ω_a together with knowledge of the constant $\frac{e}{mc}$. Our experiment aims at a determination of a_μ to 0.35 ppm, a factor of 20 improvement over the latest CERN measurement.

Longitudinally polarized muons of 3 GeV/c are stored in the ring, either by pion injection into the storage ring which is followed by $\pi \rightarrow \mu$ decay which provides the kick to place muons onto stable stored orbits, or by direct muon injection together with a fast

kicker. The storage efficiency for muons stored per incident pion is $\sim$ 26 *ppm*, whereas with direct muon injection it is 7%. The physics of muon storage is discussed in Chapter 4.

Electrons from muon decay are detected with calorimeters and their times of arrival are accurately measured. Because of the parity violating correlation between muon spin direction and electron emission direction, the $(g-2)$ frequency ω_a appears as a modulation of the muon decay electron spectrum. The magnetic field $\mathbf{B}$ will be measured by proton NMR. We plan to measure ω_a to about 0.3 ppm, limited principally by statistics, and $\mathbf{B}$ to about 0.1 ppm.

The principal equipment to be built is the superferric storage ring with $\mathbf{B} = 1.45$ T and a diameter of 14.22 m. Since we must know $\mathbf{B}$ averaged over the muon storage volume with cross sectional diameter 9 cm to 0.1 ppm, the requirements on the field homogeneity and stability are unusually stringent. Our design of the storage ring including the requirement of high precision is discussed in Chapters 8 and 14.

A new beam line is under construction. The beam starts with a fast kicker for proton ejection at H10 in the AGS, followed by a and a new secondary production target station. The secondary beamline will provide either π or μ beams at 3 GeV/c for injection into the storage ring. The storage ring and the $(g-2)$ experiment will be located in the old $80''$ bubble chamber building. The beamline, the inflector and the electric quadrupoles are discussed in Chapters 6, 10 and 11 respectively. The muon kicker is covered in Chapter 12, and the vacuum system is discussed in Chapter 13.

The electron detectors, which are to be located on the inside of the ring, must handle high rates and provide precise time interval measurements with systematic effects less than 20 ps. The detectors and electronics are discussed in Chapter 16, the data acquisition and on-line system are discussed in Chapter 17. Slow control is covered in Chapter 18, and off-line and simulation is covered in Chapter 19.

Although the principle of our AGS experiment is the same as that of the third CERN experiment, [1] we aim to achieve a 20 fold greater precision. This increased precision will be possible principally due to a proton beam intensity with the AGS Booster some 100 times that at CERN where the dominant error was statistical. The principal systematic error of about 1.5 ppm at CERN was due to limited knowledge of the magnetic field. Our experiment is designed to improve our knowledge of the field to 0.1 ppm. Great care must be paid to maintaining all the systematic errors at the level of 0.1 ppm or less. These questions of errors are discussed in Chapter 5.

Table 1.3.1: DOE Construction Cost Estimate (2/94)

WBS	Item	$E\&C(K\$)$	To go($K\$$)	Total($K\$$)
1.1	Storage Ring Magnet	4459	772	5231
1.2	Beam Monitoring	0	0	0
1.3	Magnetic Shims	276	135	411
1.4	Vacuum Chamber/Quad	243	703	946
1.5	Detectors	0	444	444
1.6	Beam/Exp. Hall	1803	1656	3459
1.7	Field Measurement	0	60	60
1.8	Muon Kicker	0	790	790
1.9	DAQ & Control	0	175	175
1.13	Direct Labor	3532	180	3712
Total	E821	10313	4915	15228

1.3. Budget and Schedule Summary

A detailed analysis of the costs and schedules has been carried out. The total construction cost of the AGS Muon $(g-2)$ experiment to DOE is estimated to be \$15 M. A breakdown of the costs by major components is given in Table 1.3.1. We note that the costs shown in the above table are U.S. D.O.E. costs only.

The construction funding is distributed among four sources: U.S. Department of Energy (DOE), U.S. National Science Foundation (NSF), Japan (US-Japan Program in High Energy Physics [KEK, University of Tokyo]) and Germany (University of Heidelberg). The present six-year construction schedule covers the period FY89-FY95, with the muon kicker being built in FY96 in parallel with the first data collection run using pion injection. Details of personnel and management are given in Chapter 24, budget and schedule are discussed in Chapter 25.

1.4. References

1. J. Bailey et al., Nucl. Phys. B150, 1 (1979).

2. F. J. M. Farley and E. Picasso, *Quantum Electrodynamics* ed. by T. Kinoshita (World Scientific, Singapore, 1990), p.479.

Chapter 2.
The Physics Background and Motivation

Revised February 1995

2.1. Introduction

In this chapter we review the motivation for the experiment, as well as giving a brief history of the three measurements which have been carried out at CERN. [1-3] Before discussing the theoretical interest in the muon $(g-2)$ value or anomalous magnetic moment $a_\mu = \frac{1}{2}(g-2)$, we review spin motion in a magnetic field, and also discuss the electron g value.

2.1.1. The Muon

The muon is an extremely interesting lepton whose relatively long lifetime of 2.2 μs ($c\tau = 658.65m$) makes it possible to perform precision measurements. Although its mass of 105.658387 (34) MeV is 207 times the electron's, to the accuracy of current experiments the muon appears to be a pointlike lepton. Because its mass is so much heavier than the electron's there are measurable contributions to its anomalous moment from μ, τ, π (hadrons), and $W^\pm$ and Z^0, since as compared to the electron, the relative contribution of heavier objects to the anomalous moment [4] scales as $(m_\mu/m_e)^2 = 4 \times 10^4$.

The final CERN experiment [3] clearly established the presence of hadronic radiative corrections to the muon g value. One of the principal goals of the current experiment is to reach a sensitivity adequate to establish the presence of weak radiative corrections from single loop W and Z^0 graphs. The experimental goal of ± 0.35 *ppm* precision, which represents a factor of 20 improvement over CERN, is set by the predicted 1.3 *ppm* contribution to the muon anomaly from weak radiative corrections. This measurement will provide a clean test of the renormalization prescription of the unified electroweak theory.

The muon anomaly has provided a stringent test for new theories of particle physics, since any new field or particle which couples to the muon must contribute to a_μ. The magnitude of the effect is a quantitative question of the strength of the particle's coupling to the muon and its mass.

In order to achieve a deeper and less arbitrary theory for particle physics than the present Standard Model, many speculative theories have been proposed which include new particles such as additional gauge bosons, supersymmetric particles and excited leptons. Others include substructure for leptons, gauge bosons, or quarks. All of these modifications of the Standard Model would change a_μ(theor), often by an amount which would be detected by a measurement of a_μ(expt) to an accuracy of 0.35 *ppm*. The muon anomalous g-value can be regarded as a standard against which any speculative new theory can be tested; such precision tests are complementary to direct searches for new particles with the highest energy accelerators.

Historically, the Lamb shift and the electron and muon $(g-2)$ values have played a key role in the discovery and establishment of modern quantum electrodynamics. [5] Precision measurements of hyperfine structure intervals and the Zeeman effect in hydrogen, muonium and positronium have provided important tests of QED bound state theory as well as values for the magnetic moments of fundamental particles. High energy experiments can explore the physics of the W, Z^0, and other particles by direct production and are certainly the definitive way to identify new particles and new physics which are energetically accessible.

On the other hand, it is difficult in these high energy experiments to study the properties of more massive particles which cannot be produced by the accelerators. In principle, the existence of heavier particles can be detected through their effects via virtual radiative processes on the behavior of lighter observed particles. Precise and sensitive experiments such as the muon $(g-2)$ measurement will give us an important insight into the domain of physics which is not now accessible to high-energy experiments. In this sense low-energy, high-precision experiments play a role complementary to those at high energy colliders.

A high precision measurement of a fundamental quantity such as the muon $(g-2)$ value, for which a precise value can be calculated from basic theory, provides an important calibration point for modern particle theory. Not only is this valuable for the insight it provides about the very high energy regime beyond present accelerators, but also it may reveal new and deeper aspects of physics within the accessible energy regime, as was so dramatically illustrated for quantum electrodynamics by the Lamb shift in hydrogen and the anomalous g-value of the electron.

2.1.2. Spin Precession in a Magnetic Field

Charged particles which possess an angular momentum $\vec{L}$, have an associated magnetic dipole moment which is given by

$$\vec{\mu}_\ell = g_\ell \frac{e}{2mc} \vec{L}$$

where the gyromagnetic ratio for an orbital angular momentum $g_\ell = 1$. The energy associated with a dipole in a magnetic field is

$$H = -\vec{\mu} \cdot \vec{B}$$

and the torque it experiences is given by

$$\vec{\tau} = \vec{\mu} \times \vec{B}$$

The latter equation leads to a (nonrelativistic) Larmor precession with frequency

$$\omega_\ell = \frac{g_\ell}{\hbar} \left(\frac{e\hbar}{2mc} \right) B$$

For spin angular momentum

$$\vec{\mu}_s = g_s \frac{e}{2mc} \vec{S}$$

where $g_s = 2$. The formulation of the Dirac equation, and its prediction that the gyromagnetic ratio of a spin 1/2 particle is exactly 2 (in the absence of a Pauli term) was a major step in the development of the theory of subatomic physics.

The nonrelativistic Larmor precession frequency for a positively charged particle is given by

$$\omega_s = \frac{g_s}{\hbar} \left(\frac{e\hbar}{2mc} \right) B = \left[1 + \frac{g_s - 2}{2} \right] \frac{e}{mc} B. \tag{2.1.1}$$

where the second term in brackets is the anomalous moment,

$$a = \frac{g_s - 2}{2} \tag{2.1.2}$$

and the (total) magnetic moment is given by

$$\mu = \left[\frac{q}{e} + a \right] \frac{e\hbar}{2mc} \tag{2.1.3}$$

which is the number quoted in the Particle Data Tables. [6] The first term in the square bracket is the Dirac moment (which is $+1$, 0 or -1 depending on the charge q), and the quantity a is the anomalous (Pauli) moment. We will drop the subscript s on g in the discussion below. Note that in the Particle Data Tables, three different magnetons are

used: the Bohr magneton ($\mu_B = \frac{e\hbar}{2m_e c}$), the muon magneton ($\mu_\mu = \frac{e\hbar}{2m_\mu c}$) and the nuclear magneton ($\mu_N = \frac{e\hbar}{2m_p c}$).

Both relativistically (and nonrelativistically), one finds that a charged spin 1/2 particle moving in a magnetic field will precess relative to the momentum vector with a frequency ω_a which is given by the difference between the orbital cyclotron frequency ω_c and the spin precession frequency ω_s,

$$\omega_a = \omega_s - \omega_c \tag{2.1.4}$$

where the orbital cyclotron frequency is

$$\omega_c = \frac{eB}{mc\gamma} \tag{2.1.5}$$

and the spin precession frequency is

$$\omega_s = \frac{geB}{2mc} + (1-\gamma)\frac{eB}{mc\gamma}, \tag{2.1.6}$$

with the Larmor and Thomas precession terms explicitly separated.

Thus ω_a is given by

$$\omega_a = \frac{e}{mc} a_\mu B \tag{2.1.7}$$

and is directly proportion to the anomalous moment and independent of the muon momentum. For the muon, the spin vector leads the momentum vector by this amount.

In a region in which both magnetic and electric fields are present, the relativistic formula for the precession is given by [7]

$$\vec{\omega}_a = \frac{d\Theta_R}{dt} = \frac{e}{mc}\left[a_\mu \vec{B} - \left(a_\mu - \frac{1}{\gamma^2-1}\right)\vec{\beta}\times\vec{E}\right] \tag{2.1.8}$$

where $\Theta_R = (\vec{s},\vec{\beta})$ is the angle between the muon spin direction in its rest frame and the muon velocity direction in the laboratory frame. The other quantities refer to the laboratory frame.

Eq. (2.1.8) shows the key to the most recent CERN muon $(g-2)$ experiment, [3] as well as AGS E821. At the "magic γ" where

$$\left(a_\mu - \frac{1}{\gamma^2-1}\right) = 0 \tag{2.1.9}$$

the electric field does not contribute to the precession. One can thus achieve (weak) vertical focusing with electrostatic quadrupoles, and build the storage ring magnet to have a uniform dipole magnetic field. This condition is satisfied if $\gamma = 29.3$ and $p_\mu = 3.094$ GeV/c. The AGS is well suited to deliver a copious flux of pions or muons at this momentum.

2.2. The Three CERN Measurements of the Muon $(g-2)$ Value

In this section we review briefly the CERN experiments on the muon anomalous magnetic moment. In the period from about 1959 to 1977, measurements were made of $(g-2)$ for the muon in a series of three experiments at CERN. [1,2,3]. These experiments measured the $(g-2)$ precession frequency ω_a which is the difference between the spin precession frequency ω_s and the cyclotron frequency ω_c in a magnetic field B, see Eq. (2.1.4), Eq. (2.1.5), Eq. (2.1.6), and Eq. (2.1.7).

In these experiments the direction of the muon spin is determined through the parity-violating angular asymmetry in the decay $\mu \to e\nu_e\nu_\mu$ and the momentum direction was determined from knowledge of the muon trajectory in the magnetic field. The first experiment [1] utilized low-energy muons with momenta $p_\mu \approx 90$ MeV/c in a magnetic field $\mathbf{B} = 1.6\ T$, where inhomogeneities in $\mathbf{B}$ provided focusing and drifting for the muon orbits. This experiment gave $a_\mu = (1\ 162 \pm 5) \times 10^{-6}$ (4300 *ppm*). In an experiment which uses low-energy muons, such as this first CERN experiment, the observation time is of the order of the muon lifetime, $\tau_\mu = 2.2 \times 10^{-6} s$, which limits the number of precession cycles available for observation.

In the second CERN experiment, [2] polarized muons with momenta p_μ of 1.3 GeV/c ($\gamma = 12$) were produced by the decay of pions which were in turn produced by a primary proton beam hitting a production target inside the storage ring. Muon decay electrons were detected by several detectors placed in a shielded position 180^0 around the ring from the production target. The $(g-2)$ precession was measured in a storage ring with $\mathbf{B} = 1.7\ T$, with weak-focusing provided by the inhomogeneous magnetic field. Since the laboratory mean lifetime was dilated to $\gamma\tau_\mu = 26 \times 10^{-6} s$, twelve times more precession cycles were observable, compared with the first experiment. This experiment gave $a_\mu = (116\ 616 \pm 31) \times 10^{-8}$ (270 *ppm*). Further improvement would have been limited by the magnetic field gradient required for focusing, and the corresponding uncertainty in the mean field applicable to the muon population (see Eq. (2.1.7)).

The third CERN experiment [3] also measured the $(g-2)$ precession frequency of high energy muons in a storage ring, but its design was based upon the observation about the classical spin motion in a magnetic and electric field given by Eq. (2.1.8). The three experiments are summarized in Table 2.2.1.

With the "magic γ" the electric part of the bracketed factor given in Eq. (2.1.8) is zero,(see Eq. (2.1.9)) ($\gamma = 29.3,\ p_\mu = 3.094$ GeV/c), and the $(g-2)$ precession frequency is determined by $\mathbf{B}$ alone and is independent of $\mathbf{E}$. This observation allows for a separated function muon storage ring in which a homogeneous magnetic dipole field $\mathbf{B}$ determines

Table 2.2.1: The CERN Experiments

The First Experiment [1]

Method: $(g-2)$ precession in a bending magnet, $\mathbf{B} = 1.6$ T, with trajectories and focussing determined by field inhomogeneities. Performed at the Synchrocyclotron, $p_\mu = 90 MeV/c$
$a_\mu = (1\ 162 \pm 5) \times 10^{-6}$ $(4300 ppm)$

The Second Experiment [2]

Method: $(g-2)$ precession in a muon storage ring $\mathbf{B} = 1.7$ T, with weak focusing provided by higher multipoles in $\mathbf{B}$. Performed at the Proton Synchrotron, $p_\mu = 1.3 Gev/c$, $\gamma = 12$
$a_\mu = (116\ 616 \pm 31) \times 10^{-8}$ $(270 ppm)$

The Third Experiment [3]

Method: $(g-2)$ precession in a muon storage ring $\mathbf{B} = 1.5$ T, with weak focusing provided by electrostatic quadrupoles. Performed at the Proton Synchrotron, $p_\mu = 3.1 Gev/c)$, $\gamma = 29.3$
$a_\mu = (1\ 165\ 924 \pm 8.5) \times 10^{-9}$ $(7.3 ppm)$

---

the $(g-2)$ precession frequency, and an electric quadrupole field provides vertical weak-focusing for the muons. This elimination of the magnetic field gradient in the third CERN experiment permitted a significant improvement in accuracy, since the average magnetic field which enters into Eq. (2.1.7) breaks down into an integration over the storage volume of each multipole of the field times the corresponding moment of the muon distribution, and little information existed on the muon distribution in the CERN experiments. Furthermore, the additional time dilation of the muon lifetime to from $26\mu s$ to $64\mu s$ at $\gamma = 29.3$ gave an additional improvement in accuracy.

The muon storage ring, magnet cross section, quadrupole electrodes, and a data sample from the third CERN experiment are shown in Fig. 2.2.1. The precession frequency ω_a (see Eq. (2.1.7)) of the spin relative to the momentum vector was measured by observing the decay electrons emerging on the inside of the ring. As the angular distribution in the decay rotated with the muon spin, the counting rate for the high energy electrons (emitted in the forward direction) was modulated at the frequency ω_a. The magnetic field

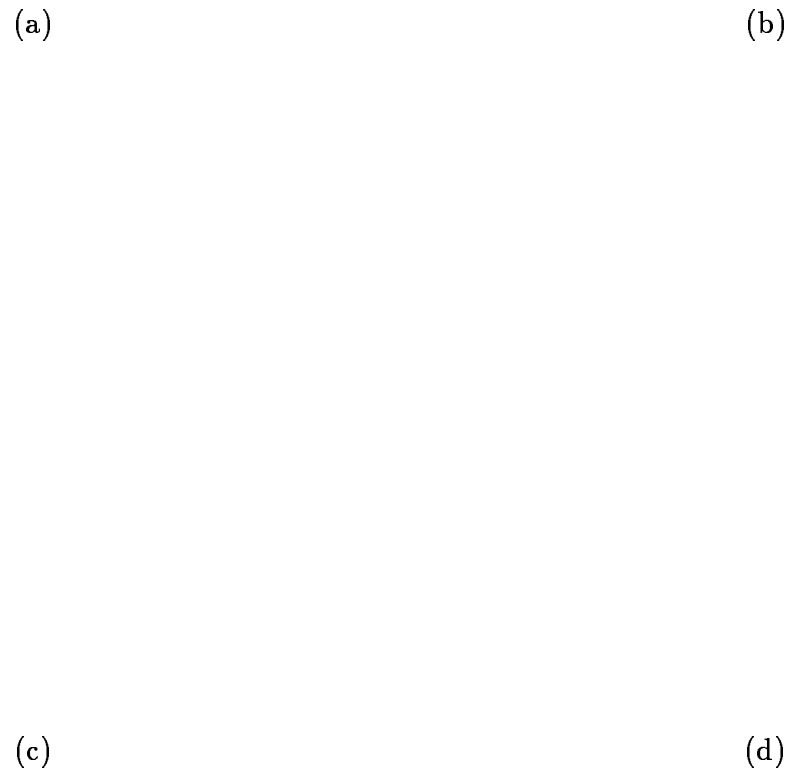

Figure 2.2.1: The Third CERN Experiment - (a) shows a plan view of the storage ring, which was composed of forty separate magnets excited by a single set of coils. Each of the sectors was stabilized separately. All dimensions are in mm. (b) A cross section of the magnet. (c) The electrostatic quadrupoles and vacuum chamber. (d) Muon decay electrons as a function of time. The $(g-2)$ oscillations are clearly visible superimposed on the muon lifetime curve.

was homogeneous to 20 *ppm* over the muon storage area which had a cross section 12 cm (horizontal) x 8 cm (vertical), and the effective mean magnetic field averaged over the muon orbits was known to 1.5 *ppm*. The electric quadrupole field was pulsed with an electrode voltage of + 24 kV on the top and bottom electrodes and -4 kV on the side electrodes for μ^+ storage.

The $(g-2)$ precession frequency ω_a is deduced from the decay electron counting data which, with no losses except from muon decay, is of the form

$$N = N_0 e^{(-t/\gamma\tau)}\{1 - A\cos(\omega_a t \ + \ \phi)\} \tag{2.2.1}$$

in which $\gamma\tau$ = laboratory muon lifetime. The asymmetry parameter A is the product of the stored muon polarization and the asymmetry in $\mu - e$ decay, which is a function of electron energy, and of the angular and energy spread of the electrons that are accepted by the detection system. Data showing the modulation of the decay electron counting rate at the frequency ω_a are given in Fig. 2.2.1(d).

In addition to values of ω_a and $\mathbf{B}$, determination of a_μ from Eq. (2.1.7) requires a value of the constant (e/mc). Since the magnetic field is measured by a proton resonance frequency ω_p (corrected for molecular and bulk diamagnetic shielding), the constant needed is

$$\lambda = \frac{\mu_\mu}{\mu_p}, \tag{2.2.2}$$

and a_μ is then given by

$$a_\mu = \frac{R}{(\lambda - R)}, \tag{2.2.3}$$

where $R = \omega_a/\omega_p$.

The errors quoted for the measurement of a_μ in the CERN experiment [3] are listed in Table 2.2.2. The overall one-standard-deviation error was 7.3 *ppm*, which was dominated by the statistical counting error of 7.0 *ppm* in the determination of ω_a. The overall systematic error was 2 *ppm*, which was due almost entirely to uncertainty in the mean magnetic field $\mathbf{B}$ in the storage ring, which involved an average over space, time, and muon distribution. Additional smaller systematic errors are associated with the deviation of the muon orbits from the ideal reference orbit.

The statistical error in ω_a determined from Eq. (2.2.1) is

$$\frac{\delta\omega_a}{\omega_a} = \frac{\sqrt{2}}{\omega_a A\gamma\tau N_e^{\frac{1}{2}}}, \tag{2.2.4}$$

where N_e is the total number of decay electrons recorded. For a given number of decays the accuracy is improved by increasing the number of $(g-2)$ precession cycles per lifetime,

Table 2.2.2: Errors in CERN3 Experiment [3] The small systematic errors marked * were insignificant compared to the dominant errors, and thus were not studied extensively.

Source of Error	**Error (ppm)**	**Comments**
Statistics	7.0	
Magnetic Field	1.5	Includes absolute calibration of NMR probes (~ 0.8) and average over space, time and muon distribution
Electric Field Correction	0.3	1.7 *ppm* correction
Pitch Correction	0.12	0.6 *ppm* correction
Particle Losses*	< 1.0	
Timing Errors*	< 0.5	
Total	**7.3**	

$\omega_a \gamma\tau$, (hence the advantage of highly relativistic muons with dilated lifetime $\gamma\tau$) and by maintaining a large asymmetry parameter A. In the CERN experiment the total number of electron counts N_e was 1.34×10^8, and A varied from 0.17 for the lowest energy band to 0.38 for the highest. The overall statistical error in ω_a was 7.0 *ppm*.

The principal systematic error was the uncertainty in the knowledge of **B**. Since the magnetic field of the ring was not perfectly uniform, ω_p had to be a weighted average over the muons which contribute to the counting data. It also had to be averaged correctly over any drifts in the magnetic field between the proton NMR surveys and the muon runs. In the CERN experiment the field was automatically stabilized at 40 points in the ring (just outside the vacuum tank) and monitored during the runs by 37 plunging probes which could be driven radially into the vacuum chamber in the median plane. However, the main surveys of 250,000 points in the field were made between runs with the vacuum chamber removed. The removal of the chamber required that the magnet be switched on-and-off between the field surveys and the muon runs. Nevertheless, reproducibility to $\pm$ 1 *ppm*

in the average field was achieved over periods of months. Drifts in magnetic field shape due to temperature effects meant that the field in the storage region varied even though 40 points just outside the storage region were stabilized. This was measured by the 37 plunging probes, and corrections applied. Including uncertainties in the distribution of muons inside the aperture, an overall uncertainty of 1.5 *ppm* was assigned to the mean value **B** of the magnetic field.

All other systematic uncertainties were below the level of 1 *ppm*, including those associated with particle losses, timing and changes in electronic gains, as well as with corrections for muon energy spread (electric field correction) and betatron oscillations (pitch correction).

It should be noted that the ratio of the muon and proton magnetic moments, μ_μ/μ_p, is needed as an auxiliary constant to deduce a_μ from the measured precession frequency ω_a and the field B measured in terms of a proton resonance frequency ω_p (Eq. (2.2.2) and (2.2.3)). The quantity μ_μ/μ_p was known to 0.3 *ppm* from measurement of the muonium Zeeman effect and from a μSR experiment. The best current value of λ utilizes in addition the accurately measured value of the hyperfine structure interval $\Delta\nu$ of muonium [8] and is accurate to 0.15 *ppm*. A still more precise value for λ may be obtained from more precise measurements of $\Delta\nu$ and the Zeeman effect of muonium in progress at LAMPF. [9] In addition, the muonium $1S \rightarrow 2S$ laser experiments at the Rutherford Laboratory [10] which will determine the muon mass, and thus λ is competitive with the LAMPF experiment.

The fine structure constant α which is required to obtain a_μ(theor) was known at the time of the CERN experiment [3] with adequate precision for the computation of a_μ(theor) at the time, and α is much better known now.

2.3. $(g-2)$ for the electron

The simplest Feynman diagram for the interaction of a lepton with an external field is shown in Fig. 2.3.1 1 and represents $g = 2$.

An anomalous moment can result from radiative corrections to Fig. 2.3.1 (see Fig. 2.3.2) and from internal structure if it is present. The proton anomalous moment of $+1.79\mu_N$ is a reflection of the its quark structure. For leptons, even in the absence of internal structure, radiative corrections are significant. The lowest order radiative correction to Fig. 2.3.1 is shown in Fig. 2.3.2.

Figure 2.3.1: The interaction of a spin 1/2 particle with an external magnetic field. (The $\times$ represents the static magnetic field of the storage ring and not a nucleus as it is sometimes used.)

Figure 2.3.2: The lowest order QED correction to $(g-2)$

The discovery of the anomalous moment for the electron was made in 1947 by Kusch and Foley, [11] who determined that

$$g_s = 2\,(1.00119 \pm 0.00005)\,,$$

consistent with a first-order correction of $\frac{\alpha}{2\pi}$ calculated by Schwinger. [12]

Since this seminal work, the anomalous magnetic moment of the electron, a_e, has been measured with ever-increasing precision. To the level of current measurements, QED diagrams alone suffice to determine its theoretical value, which can be written [13] as an expansion in powers of α:

$$a_e^{theory} = C_1 \left(\frac{\alpha}{\pi}\right) + C_2 \left(\frac{\alpha}{\pi}\right)^2 + C_3 \left(\frac{\alpha}{\pi}\right)^3 + C_4 \left(\frac{\alpha}{\pi}\right)^4 + ... + \delta a \qquad (2.3.1)$$

where[†] $C_1 = 0.5$, $C_2 = -0.328\ 478\ 965\ ...$, $C_3 = 1.176\ 20(14)$, $C_4 = -1.569(60)$ and $\delta a = 4.46 \times 10^{-12}$. The correction δa comes from contributions of virtual muons, hadrons, $W^{\pm}$ and Z^0. The theoretical prediction is [13]

$$a_e^{theory} = 1\ 159\ 652\ 140\ \ (28) \times 10^{-12} \tag{2.3.2}$$

where the value for the fine structure constant

$$\alpha_{QH}^{-1} = 137.035\ 997\ 9\ \ (32)$$

is taken from measurements of the quantum Hall effect.

The values of $a_{e^{\pm}}$ from the Penning trap experiments are [14]

$$a_{e^-} = 1\ 159\ 652\ 188.4\,(4.3) \times 10^{-12} \tag{2.3.3a}$$

and

$$a_{e^+} = 1\ 159\ 652\ 187.9\,(4.3) \times 10^{-12}. \tag{2.3.3b}$$

There is a 2σ agreement with QED at the level of 10^{-12} and, to the extent that the particle and anti-particle properties are the same, CPT invariance is verified at the 2×10^{-12} level. One should note that the contribution to the electron's anomaly from particles heavier than the electron is the same size as the current experimental uncertainty.

2.4. $(g-2)$ for the muon

The muon anomalous magnetic moment can be calculated in the same fashion as that of the electron. However, because the mass of the muon is much greater than that of the electron, diagrams with quark loops, or to a lesser extent, weak bosons, contribute measurably to the final result. The relative contribution of heavier particles to the muon's anomalous moment [4] goes as $\sim (m_\mu/m_e)^2$ which makes the contribution of such particles on the measured muon anomaly much larger ($\sim\ 4 \times 10^4$) than for the electron. The theoretical value for a_μ can be expressed [15]

$$a_\mu^{theory} = a_\mu^{QED} + a_\mu^{hadronic} + a_\mu^{weak} \tag{2.4.1}$$

and each of these contributions is discussed in detail below.

[†] The values of the higher order coefficients, both for the electron and the muon are constantly being refined, so these values represent a snapshot of this progress

2.4.1. The QED Contribution to a_μ

The QED contribution to the muon $(g-2)$ is again given by an expansion in α/π as for the electron anomaly Eq. (2.3.1). However, now virtual electrons, muons and tauons contribute in the lepton loops, so the coefficients are different. The coefficient $C_1 = 0.5$ is the same single photon Schwinger term shown in Fig. 2.3.2.

The expansion is given by

$$a_\mu^{QED} = C_1' \left(\frac{\alpha}{\pi}\right) + C_2' \left(\frac{\alpha}{\pi}\right)^2 + C_3' \left(\frac{\alpha}{\pi}\right)^3 + C_4' \left(\frac{\alpha}{\pi}\right)^4$$

where $C_1' = 0.5$, $C_2' = 0.765\ 857\ 39$, $C_3' = 24.045\ 11$, $C_4' = 126.12$ and $C_5' = 930$. The total QED term to eighth order is [15,16]

$$a_\mu^{QED} = 1\ 165\ 847\ 008\ (18)\ (28) \times 10^{-12} \tag{2.4.2}$$

The first uncertainty is from the calculation, the second from uncertainties in α (which was taken from the quantum Hall effect. The uncertainty in the QED contribution is negligible, compared with the proposed experimental accuracy.

2.4.2. Hadronic Contributions to a_μ

(a) (b) (c) (d)

Figure 2.4.1: Lowest order hadronic vacuum polarization diagrams

Loops where virtual hadrons are emitted and then reabsorbed contribute to the value of a_μ at a measurable level (60 parts per million), which was confirmed in the most recent CERN experiment. [3] The lowest order hadronic diagrams are shown in Fig. 2.4.1, the first order being shown in Fig. 2.4.1(a).

Figure 2.4.2: The hadronic light on light scattering. The contribution of this diagram cannot be obtained from the dispersion relation.

The contribution from these hadronic loops cannot currently be calculated reliably in QCD. However, the dominant contribution (shown in Fig. 2.4.1a) can be related, through dispersion theory, to the experimentally measured cross-section for e^+e^- annihilation into hadrons. The higher order diagrams shown in Fig. 2.4.1 can also be related to the quantity $R(s)$, defined by the expression

$$R\left(s\right) = \frac{\sigma_{tot}\left(e^+e^- \rightarrow \ hadrons\right)}{\sigma_{tot}\left(e^+e^- \rightarrow \mu^+\mu^-\right)}. \tag{2.4.3}$$

The single hadron loop contribution to $(g-2)$ is given by

$$a_\mu^{hadronic} = \left(\frac{\alpha m_\mu}{3\pi}\right)^2 \int_{4m_\pi^2}^{\infty} \frac{ds}{s^2} K\left(s\right) R\left(s\right) \tag{2.4.4}$$

where

$$K\left(s\right) = \frac{3s}{m_\mu^2}\left[x^2\left(1-\frac{x^2}{2}\right) + \left(1+x\right)^2\left(1+\frac{1}{x^2}\right)\left[ln\left(1+x\right) - x + \frac{x^2}{2}\right] + \frac{1+x}{1-x}x^2 lnx\right]$$

and

$$x = \frac{1-\beta}{1+\beta}, \qquad \beta = \sqrt{1-\frac{4m_\mu^2}{s}}$$

The integral is dominated by the kinematic regions around low-lying $\pi\pi$ resonances such as the ρ. There have been several evaluations of the hadronic contribution to a_μ, which are discussed below. To set the scale, we note that the contributions from the virtual hadron loops in Fig. 2.4.1 and Fig. 2.4.2 as evaluated by Kinoshita et al. [17] is

$$a_\mu^{had} = 7027\left(175\right) \times 10^{-11} \tag{2.4.5}$$

which corresponds to 60.6 ± 1.5 *ppm* of a_μ. The uncertainty is dominated by the knowledge of $R(s)$ (see Eq. (2.4.4)).

The dominant error arises from the accuracy with which R is known from experiment, principally in the range up to $\sqrt{s} = 1$ GeV but also in the higher energy range up to the J/ψ at $\sqrt{s} = 3.1$ GeV.

The hadronic light on light contribution shown in Fig. 2.4.2 cannot be calculated from the dispersion relation, nor can it be calculated using QCD because of the low energies involved. A paper which discussed both a simple quark model calculation and a vector dominance model calculation was published by Kinoshita et al. [17] The value of the hadronic light-on-light contribution to $a_\mu^{hadronic}$ was $49(5) \times 10^{-11}$, which should be compared with the value of a_μ^{had} given in Eq. (2.4.5).

More recently there have been active discussions about the evaluation of this light by light scattering contribution, [18-20] and additional work is in progress to improve its evaluation using chiral pertubation theory. [21] This diagram represents the fundamental theoretical limitation to the value of $a_\mu^{hadronic}$ within the standard model.

In addition to the evaluation by Kinoshita [15,17] there have been several other evaluations of $a_\mu^{hadronic}$ in the literature, [22-26] as well as a recent evaluation by Worstell et al. [27] usingthe latest data and the methods of Kinoshita et al. [17], with the ρ meson contribution taken from the VEPP-2M data [22] published after Ref. 17), and with the 1992 Particle Data Group values for masses, widths and electron pair widths for the vector mesons. The Kinoshita et al, [17] values for nonresonant contributions have been used, although more recent data have reduced these errors as well, and they are in the process of including the new data in our evaluation of $a_\mu^{hadronic}$. The result obtained from this analysis is

$$a_\mu^{hadronic} \;=\; 6\ 797\ \ (88) \times 10^{-11} \tag{2.4.6}$$

. which has an uncertainty of half that of the earlier evaluation [17] given in Eq. (2.4.5).

These evaluations of $a_\mu^{hadronic}$ are listed in Table 2.4.1. We emphasize that each of these evaluations comes from a slightly different data set for R, see Eq. (2.4.3), and a slightly different form of the dispersion relation, see Eq. (2.4.4), as discussed below.

From the integral expression for $a_\mu^{hadronic}$ above, we can factor out the energy dependence of the integrand to get the differential contribution to the muon anomaly per unit of R as a function of s:

$$\left(\frac{1}{a_\mu R\,(s)}\right) \frac{da_\mu^{hadronic}}{ds} = \frac{1}{a_\mu} \left(\frac{\alpha m_\mu}{3\pi}\right)^2 \frac{K\,(s)}{s^2} \tag{2.4.7}$$

This quantity is plotted in units of ppm/GeV^2 in Fig. 2.4.3. Since R is everywhere of order unity, this shows the relative contribution of hadronic vacuum polarization from

Table 2.4.1: Different Evaluations of first order $a_\mu^{hadronic}$. Higher Order Diagrams are estimated to be [17] $a_\mu^{hadronic}(higher\ order) = -41(7) \times 10^{-11}$ $(0.06\ ppm)$.

$a_\mu^{hadronic} \times 10^{11}$	Error in *ppm*	Reference
7068 (59) (164)	(± 1.5 *ppm*)	Kinoshita et al. [15,17]
6840 (110)	(± 0.9 *ppm*)	Barkov et al. [22]
7100 (105) (49)	(± 0.9 *ppm*)	Casas et al. [23]
7245 (66) (259)	(± 2.3 *ppm*)	Burkhardt et al. [24]
7048 (115)	(± 0.9 *ppm*)	Martinovič et al. [25]
6986 (42) (16)	(± 0.4 *ppm*)	Dubničková et al. [26]

Figure 2.4.3: Kinematic suppression factor $\frac{K(s)}{s^2}$ in units of *ppm* per GeV^2.

Table 2.4.2: Different evaluations of contributions to $a_\mu^{hadronic}$ in *ppm*, with errors.

ρ	$\omega + \phi$	J/Ψ + Υ	Nonresonant	**Total** (*ppm*)	Reference
43.43 ± 1.30	7.45 ± 0.47	0.63 ± 0.09	9.10 ± 0.55	60.61 ± 1.49	Kinoshita et al. [17,15]
42.00 ± 0.48				58.67 ± 0.94	Barkov et al. [22]
44.32 ± 0.37	7.83 ± 0.81	0.54 ± 0.04	8.21 ± 0.21	60.90 ± 0.92	Casas et al. [23]
43.61 ± 1.32	7.14 ± 0.43	0.66 ± 0.13	10.73 ± 1.82	62.14 ± 2.29	Burkhardt et al. [24]
43.79 ± 0.53	8.75 ± 0.36†	0.64 ± 0.05	9.94 ± 0.75	63.12 ± 1.03	Martinovič et al. [25]
42.39 ± 0.18	7.48 ± 0.24†	0.71 ± 0.02	9.35 ± 0.21	59.93 ± 0.37	Dubničková et al. [26]
42.00 ± 0.48	6.98 ± 0.14	0.78 ± 0.05	8.86 ± 0.50	58.62 ± 0.71	Worstell et al. [27]

†Includes the nonresonant 2 kaon contribution in the ω, ϕ energy range.

different energy ranges to the muon anomaly. Different evaluations of $a_\mu^{hadronic}$ correspond to different evaluations of R, either from different experimental data, different models, or different treatments of experimental errors.

Because different authors have broken down the hadronic vacuum polarization contributions into different energy ranges and among different categories of e^+e^- hadroproduction channels, a comparison between their analyses is not trivial. We have therefore organized hadronic contributions as tabulated by different authors into four broad categories for comparison: ρ, $\omega + \phi$, $J/\psi + \Upsilon$ (+ excitations), and non-resonant (continuum) hadroproduction. The contributions and errors associated with each contribution by each author are given in Table 2.4.2

The low energy behaviour of the physical cross section ratio, $R(s)$ is dominated mostly by the two pion spectrum which contains the ρ meson resonance with the small effect of interference with the ω meson resonance near its peak. The two pion production cross section, $\sigma_{\pi\pi}$ is calculated in terms of the electromagnetic pion form factor, $|F_\pi|$:

$$\sigma_{\pi\pi} = \frac{\pi\alpha^2}{3s}\beta_\pi{}^2 \, |F_\pi|^2 \, .$$

A model which fits the energy dependence of $|F_\pi|$ is given by the Gounaris-Sakurai formula which is a finite- and energy dependent-width correction to the usual Breit-Wigner form for

Figure 2.4.4: Experimental values of $|F_\pi|^2$ which come principally from the OLYA and CMD detectors at BINP, Novosibirsk. The solid curve corresponds to the Gounaris-Sakurai formula taking into account the $\rho - \omega$ interference. The dotted line is a parameterization with ω, ρ, $\rho'(1250)$, and $\rho''(1600)$ mesons.

a resonance. The high energy tail of the two pion spectrum is complicated by contributions from particular vector meson orbital excitations. The simplest method for inclusion of interference effects of the ρ, ω and further orbital excitations is to write the total $|F_\pi|$ as a sum of resonances:

$$|F_\pi| = |F_\rho| + a\,|F_\omega| + b\,\left|F_{\rho'}\right| + c\,\left|F_{\rho''}\right| + \ldots \tag{2.4.8}$$

Figure 2.4.5: The most recent reproduction of all existing data on the electromagnetic pion form factor by means of the unitary and analytic VMD model.

where $a, b, c, ...$ are complex numbers whose amplitudes and phases characterize the interference effects, and the additional form factors are of the Breit-Wigner form. Approximating the form factor by such a sum is one example of the vector meson dominance (VMD) approach. Competing models to fit experimental data exploit more sophisticated expressions for the resonance shapes and different combinations of the form factors before squaring to get the cross section. Several such fits to the most recent experimental data for $|F_\pi|$ are presented in Fig. 2.4.4.

A new model of the pion and kaon form factors has been presented recently in Ref. 25 and Ref. 26. The vector meson dominance (VMD) form for the resonance shape is used and the unitary and analytic structure of the form factor is exploited. Interference effects between the ρ, ω, $\rho(1450)$, $\rho(1700)$, and $\rho(2150)$ are included as in Eq. (2.4.8). Significantly, this model allows for a simultaneous fit to data for timelike (colliding beam) and spacelike (fixed target) values of the square momentum transfer and is presented in

Fig. 2.4.5. In this analysis, as in all others except Ref. 24, the systematic errors from the different experiments are combined in quadrature to obtain the total error of 0.37 *ppm* for the hadronic contribution to a_μ. This result is compared with others in Table 2.4.1.

The next largest contribution to hadronic vacuum polarization, and also one of the next most significant sources of the error, is the three pion spectrum which includes the ω and ϕ meson resonances, and the kaon pair spectra (K^+K^- and K_LK_S). As the ω and ϕ mesons are much narrower resonances than the ρ ($\Gamma_\rho = 151$ MeV while $\Gamma_\omega = 8.43$ MeV $\Gamma_\phi = 4.43$ MeV) the resonance shapes are taken as strictly Breit-Wigner. The interference between them leads to an observable dip in the cross section just before the ϕ meson resonance. Integration over the Breit-Wigner line shapes for the ω and ϕ mesons does not differ appreciably from a narrow width approximation for the narrow vector meson contribution to a_μ:

$$a_\mu^V = \frac{{m_\mu}^2}{3{m_V}^2} K\left({m_V}^2\right)\Gamma^V_{e+e-}.$$

This approximation is used for handling the charm and bottom quark meson states as well and results for 1992 Particle Data Group values are presented in Table 2.4.2.

The non-resonant continuum background is handled differently by the different authors. The main difference is the choice of energy cutoff above which they use asymptotically free perturbative QCD and in the parameterization for the data for $R(s)$ below this cutoff. A particular (simple) parameterization for $R(s)$ used by Ref. 24 is presented in Fig. 2.4.6. This evaluation is the most pessimistic about systematic errors in experimental knowledge of R at center-of-mass energies above 1.4 GeV, often using a single experimental source and adding the systematic errors from different hadronic channels linearly. The resulting overall error assessment by these authors is therefore much more pessimistic than results from the other, more detailed, evaluations cited.

In order to utilize the more accurate value of a_μ expected from the BNL experiment, it is clearly of the greatest importance that more precise measurements of R be made. An improvement by a factor of about 4 in our knowledge of R in the most important $\sqrt{s}$ range is needed. The most accurate measurements of R below $\sqrt{s} = 1.4\ GeV$ have been made at the Budker Institute of Nuclear Physics (BINP) in Novosibirsk, Russia [22] with the VEPP-2M e^+e^- collider and the detectors OLYA and CMD. These data are shown in Fig. 2.4.4 where the square of the pion form factor F_π^2 is plotted vs $\sqrt{s}$; $[F_\pi^2 \sim R]$.

VEPP-2M has a useful energy range $E_{cm} = \sqrt{s}$ from 0.36 to 1.4 GeV. The luminosity of VEPP-2M has been upgraded by the addition a wiggler, and a luminosity of $5 \times 10^{30}\ cm^{-2}s^{-1}$ was demonstrated at the ϕ resonance energy during the 1993 run.

Moreover, a new detector Cryogenic Magnetic Detector-2 (CMD2) has been built [28] which employs a superconducting magnet and was designed to achieve accuracies of 0.5%

Figure 2.4.6: Parameterization of R including resonances up to $\sqrt{s} = 10$ GeV.

in the measurement of R. CMD2 has been carefully designed to minimize systematic errors associated with luminosity measurements, particle identification, energy measurement and detection efficiency. Fig. 2.4.7 indicates the principal features of the new detector, which now includes a drift chamber, a Z-chamber, a muon range system and CsI barrel calorimeter. The BGO end cap calorimeter crystals were installed during the 1993 shutdown which completed the detector construction.

The initial runs were made in 1992 both on the ρ ($25\ nb^{-1}$) and on the ϕ ($178\ nb^{-1}$) for initial debugging and off-line reconstruction development. The total integrated luminosity was about $200nb^{-1}$. Further data were collected in 1993 on the ϕ ($1.5\ pb^{-1}$) for the study of rare decays. These data were used for the first simultaneous measurements of the four main decay channels of the ϕ in a single experiment. The accuracy obtained was comparable with the world average, and the results are being prepared for publication.

Figure 2.4.7: The new CMD2 Detector at the Budker Institute for Nuclear Physics, Novosibirsk, Russia. CMD2 started taking data at VEPP-2M in 1992 with integrated luminosities of 25 nb^{-1} at the ρ and 178 nb^{-1} at the ϕ. In 1993 an additional integrated luminosity of 1.5 pb^{-1} was obtained on the ϕ.

The VEPP-2M dedicated run for the muon $(g-2)$ energy scan, going down in energy from the ϕ with steps of $\Delta E_{cm} = 10MeV$, was started at the end of 1993 and should be completed at 0.36 GeV in the summer of 1995. About 1000 $e^+e^- \rightarrow \pi^+\pi^-$ events will be recorded at each energy point. A finer scan of perhaps 1 MeV steps is intended for the region around the ω meson in order to study the three pion contribution to $(g-2)$ and also $\rho - \omega$ interference in both the two and three pion channels. At each point the beam energy is being calibrated by the resonance depolarization method to eliminate cross section uncertainty on the resonance slopes. Special procedures will be performed to keep the trigger efficiency well understood and the detector elements' stability under control during runs.

The 1993-1994 run will give statistically sufficient data to have 0.3% accuracy in the determination of $a_\mu(had)$ and will also be used for extensive systematic errors studies. The results should be available in one to two years.

At Frascati a new ϕ factory is under construction and at this laboratory it would be possible to make accurate measurements of R in the $\sqrt{s}$ range ≤ 1 GeV [29].In addition, the Beijing Electron-Positron Collider (BEPC) is entering the planning stages for conducting

measurements of $R(s)$ in the energy range above VEPP-2M and below the J/ψ: 1.4 - 3.1 GeV [30], although the luminosity will limit the lowest energy to somewhere in the 2 GeV region.

2.4.3. Weak Contribution to a_μ

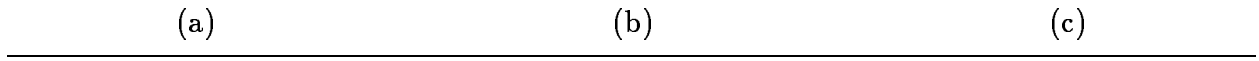

Figure 2.4.8: Single loop weak contributions to the muon $(g-2)$ value.

The weak interaction contribution based on the standard electroweak theory is a weak radiative correction to an electromagnetic interaction and arises in lowest order from the single loop diagrams in Fig. 2.4.8 which involve ν_μ, Z^0 and H particle exchange and where two vertices are weak interaction vertices. The contributions are given by [31,4]

$$\Delta a_\mu\left(W\right) = \left(\frac{G_F m_\mu^2}{8\pi^2\sqrt{2}}\right)\left(\frac{10}{3}\right) = +3.89\times 10^{-9} \tag{2.4.9a}$$

$$\Delta a_\mu\left(Z\right) = \left(\frac{G_F m_\mu^2}{8\pi^2\sqrt{2}}\right)\left(\frac{1}{3}\right)\left[\left(3-4\cos^2\theta_W\right)^2 - 5\right] = -1.94\times 10^{-9} \tag{2.4.9b}$$

$$\Delta a_\mu\left(H\right) = \left(\frac{G_F m_\mu^2}{4\pi^2\sqrt{2}}\right)\int_0^1 \frac{y^2\left(2-y\right)dy}{y^2+\left(1-y\right)\left(m_H/m_\mu\right)^2} \tag{2.4.9c}$$

$$= \left(\frac{G_F m_\mu^2}{4\pi^2\sqrt{2}}\right)\left(\frac{m_\mu}{m_H}\right)^2 ln\left[\left(\frac{m_H}{m_\mu}\right)^2\right] \tag{2.4.9d}$$

$$\leq 0.01\times 10^{-9} \text{ if } M_H \gg m_\mu \tag{2.4.9e}$$

where we take $\sin^2\theta_W = 0.233 \pm 0.002$ for the weak mixing angle.

The diagrams with the W and Z bosons contribute appreciably as given in Eq. (2.4.9). For Higgs masses much greater than 300 MeV (and standard couplings) the contribution of

H to the muon anomaly is negligible. Since LEP searches [32] establish that $m_H > 58\ GeV$, the contribution from the diagram with H is indeed negligible.

The second order weak diagrams have been calculated by Kukhto et al. [33]

The total weak contribution is[‡]

$$a_\mu\,(weak) = (1.53 \pm 0.2) \times 10^{-9} \tag{2.4.10}$$

which represents $1.31 \pm 0.04\ ppm$ of $a_\mu(theor)$.

Comparison of theory and experiment on $a_\mu(weak)$ will constitute a new and sensitive test of the unified electroweak theory with its prescription for renormalizability. Just as virtual electromagnetic radiative corrections were critical to the development of modern renormalized quantum electrodynamics, virtual radiative corrections involving both the weak and electromagnetic interactions are most important to the renormalized unified electroweak theory. The first test of radiative corrections in the electroweak theory involved the electromagnetic radiative correction to neutron beta decay and hence involved quarks and a semi-leptonic process. [34]

The radiative correction included in the fundamental relation between m_W and m_Z is central to this topic, [35] where

$$m_W^2 = \frac{\pi\alpha}{\sqrt{2}G_F\left(1 - \frac{m_W^2}{m_Z^2}\right)(1 - \Delta r)} \tag{2.4.11}$$

and m_W and m_Z are the physical masses of the W and Z bosons and G_F is the Fermi constant. The radiative correction parameter Δr arises from finite electroweak radiative corrections. The one loop radiative correction from vacuum polarization associated with the many fermions in the standard model amounts to $\Delta r \simeq +0.07$ and represents the running of α from 0 momentum to momentum m_Z. However, in addition there is an important contribution to Δr from the top quark mass m_t and a smaller one from the Higgs mass m_H. Until m_t and m_H are measured, a clean test of radiative corrections in the electroweak theory cannot be obtained from Eq. (2.4.11).

It has been pointed out to us [36] that the electroweak renormalizabliltyhas been tested in a comparison of high energy and atomic parity violation data. These tests have the complication of hadrons in the nuclei. This topic has been reviewed recently in the article by Langacker. [37]

Additional discussion on renormalization tests of the standard model is the review by Hollik. [38]

[‡] There is some question as to the correctness of the second order weak correction. [33] It is being re-evaluated by Krause and Czarnecki at Karlsruhe. The error quoted above is that estimated by Kinoshita, rather than the 0.05 quoted in [33].

2.4.4. Current Theoretical and Experimental Values of a_μ

The total theoretical value of a_μ is

$$a_\mu^{theory} = 116\ 591\ 881\ \ (176) \times 10^{-11} \tag{2.4.12}$$

where the we take the value of the uncertainty from the published value of Kinoshita et al. [17] rather than the hadronic contribution from our analysis presented in Table 2.4.2, which employed the method of Kinoshita et al. [17] We note that the uncertainty on the hadronic term (Eq. (2.4.6)), as evaluated with the new data is roughly half the the contribution of the weak term(Eq. (2.4.10)). As is clear from the discussion in section 2.4.2, the hadronic radiative corrections are receiving substantial attention. Since these corrections are important for the interpretation of some of the LEP and SLD precision results, [39] as well as the $(g-2)$ experiment, there is considerable interest in the wider community in having the uncertainty on the magnitude of these low energy corrections resolved.

The current experimental values of the muon anomaly are

$$a_{\mu^-}^{exp} = 1\ 165\ 937\,(12) \times 10^{-9} \tag{2.4.13a}$$

and

$$a_{\mu^+}^{exp} = 1\ 165\ 911\,(11) \times 10^{-9} \tag{2.4.13b}$$

(a combined accuracy of 7.3 *ppm*), in good agreement with the calculated value. The goal of the new experiment (E821) is a measurement of $(g-2)$ to the level of 0.35 *ppm*, a factor of twenty improvement over the CERN precision. This sensitivity is $\sim 23\%$ of the magnitude of the expected electroweak contribution to $(g-2)$ from single loop diagrams involving the intermediate vector bosons $W^\pm$, Z^0. A measurement at the proposed accuracy would thus provide an essential test of the renormalization of the unified electroweak theory.

2.5. New Physics Potential of E821

In the previous sections the standard model contributions to the muon $(g-2)$ value were discussed. If there are new particles which couple to the muon, they too will contribute to the anomalous moment.

A deviation from the $(g-2)$ value predicted by the standard model would be a signal for new physics. Among the possibilities would be: lepton substructure, new particles such as supersymmetric partners, additional gauge bosons, W substructure, etc. A deviation from the standard model prediction would contain two pieces of information, a magnitude and a sign. For example, supersymmetry would produce a measured value smaller than the standard model value. [15] This point is disputed in a recent paper [40] where it is claimed thatthe previous supersymmetric calculations need to be redone, and that either-sign deviation from the standard model can be accommodated by their (flipped $SU(5)$ model) supersymmetric calculation.

Relative to other probes of these same new physics possibilities, the muon g value is most sensitive to muon and W boson substructure. This topic is discussed in the literature by a number of authors, [41-45] with the paper by Méry et al. [45] having the most comprehensive.

The review by Kinoshita and Marciano [15] summarizes a range of possible new physics contributions to the muon anomalous moment, which are listed in Table 2.5.1. Limits on various parameters which will come from E821, LEP II and the LHC are given. Except where noted, these values come from the review by Kinoshita and Marciano [15].

More recently Arzt, Einhorn and Wudka [46] have developed a systematic approach, using the language of effective Lagrangians, to discuss how new physics can contribute to the muon $(g-2)$ value. They separate the discussion of new high-energy effects into two cases: those which decouple from low-energy physics, and those which do not. If Λ is the (large) energy scale at which the new physics manifests itself, in the decoupling case at energies $E << \Lambda$ observable corrections are suppressed by powers of $1/\Lambda$, whereas in the nondecoupling case, "the corrections to standard model processes are given by a chiral expansion in powers of p/Λ, where p is a typical momentum for the process at hand." [46] They conclude that in the decoupling case under some conditions the E821 sensitivity limit is $\Lambda \leq 50 TeV$, but there would be no new sensitivity to effects of an anomalous triple gauge boson vertex. On the other hand, in the nondecoupling case, E821 may be sensitive to effects from an anomalous triple gauge boson vertex, and could set interesting limits if no deviation is observed.

We emphasize that a precision measurement of $(g-2)$ is complementary to other high energy measurements. In some cases, such as composite W bosons, the limit which will

Table 2.5.1: Sensitivity to new physics of the new muon $(g-2)$ experiment

New Physics	E821 Sensitivity	Comments
μ substructure[a]	$\Lambda \geq 5\ TeV$	LHC domain
μ Form factors[b] $(1-k^2/\Lambda^2)$	$(W^{\pm})\ \Lambda > 450GeV$ $(Z^0)\ \Lambda > 64GeV$ $(\gamma)\ \Lambda > 180GeV$	$\Lambda_{LEP\ I} > 300GeV$
excited muon[c]	$m_{\mu^*} \geq 6.3\ GeV$	Already Excluded
excited muon[d]	$m_{\mu^*} \geq 400\ GeV$	LEPII comparable
$W^{\pm}$ substructure[e]	$\Lambda \geq 400\ GeV$	LEPII $\sim 100-200\ GeV$
$\frac{(g_W-2)}{2} \neq 0$[f]	≥ 0.02	LEPII$\sim$ 0.05, LHC$\sim$ 0.2
Light Higgs	$\leq$ 300MeV	$O(10^{-3}g)$ coupling
Heavy Higgs	$\leq\ 500GeV$	$O(g)$ coupling
Supersymmetry[g]	$\leq 130\ GeV$	FNAL $\bar{p}p$ collider
$W_R^{\pm}$	$\leq 250\ GeV$	FNAL $\bar{p}p$ collider
$Z^{'}(E6)$	$\leq 100\ GeV$	FNAL $\bar{p}p$ collider

[a] For substructure $\Delta a_\mu \sim m_\mu^2/\Lambda^2$

[b] See Ref. 45

[c] Chiral Invariant Interaction

[d] Traditional $\mu \cdot \mathbf{B}$ interaction (non-chiral)

[e] Goes to 0 if $M_W \to 0$ to get proper coupling to conserved current.

[f] The LEPII sensitivity is taken from the report of a 1992 Delphi working group on LEP200.

[g] Signature for SUSY in 100-200 GeV region is a value of a_μ below the SM value, although some authors take exception to this statement [40]

be placed by the new $(g-2)$ experiment is considerably better that that which will come

from LEP II or the LHC. [15] Even before the measurement of $R(s)$ is completed (see Eq. (2.4.3)) there is a window of opportunity for new physics in going from the 7.5 *ppm* measurement at CERN to better than a 1 *ppm* measurement at Brookhaven. To exploit fully the additional factor of two to three in precision available at the AGS, we will need an improved value for the hadronic contribution to $(g-2)$.

One should remember that nuclear β decay told us about the existence of the $W^{\pm}$ boson long before its direct observation. The neutral current events observed in neutrino scattering at CERN told us about the Z^0. The ingredient which was needed to make their existence convincing was the development of the renormalizeable Weinberg-Salam-Glashow theory. Once WSG was firmly in place, the discovery of the $W^{\pm}$ and Z^0 were just as expected as the discovery of the antiproton was many years before.

With the standard model now firmly in place, there is common agreement on which signatures would indicate physics beyond the standard model. The muon $(g-2)$ experiment, along with the program of rare kaon decay experiments at Brookhaven, will provide some of the most sensitive probes of new physics in the TeV mass range during the pre-LHC era.

2.6. References

1. G. Charpak, F.J.M. Farley, R.L. Garwin, T. Muller, J.C. Sens and A. Zichichi, Nuovo Cim. 37, 1241(1965).
2. J. Bailey, W. Bartl,B. von Bochmann, R.C.A. Brown, F.J.M. Farley, M. Giesch, H. Jöstlein, S. van der Meer, E. Picasso and R.W. Williams, Nuovo Cim. 9A, 369 (1972).
3. J. Bailey, K. Borer, F. Combley, H. Drumm, C. Eck, F.J.M. Farley, J.H. Field, W. Flegel, P.M. Hattersley, F. Krienen, F. Lange, G. Lebée, E. McMillan, G. Petrucci, E.Picasso, O. Runolfsson, W. von Rüden, R.W. Williams and S. Wojcicki, Nucl. Phys. B150, 1 (1979).
4. J. Calmet, S. Narison, M. Perrottet and E. De Rafael, Rev. Mod. Phys. 49, 21 (1977).
5. T. Kinoshita and D.R. Yennie in *Quantum Electrodynamics*, (Directions in High Energy Physics Vol. 7) T. Kinoshita ed., World Scientific, 1990, p.1.
6. Particle Data Group, Phys. Lett. B239 (1990).
7. V. Bargmann, L. Michel and V.L. Telegdi, Phys. Rev. Lett. 2, 435(1959) are generally given credit for this formula. As noted by J.D. Jackson in *Classical Electrodynamics*, (John Wiley & Sons, New York, 1975), p. 556, Thomas published an

equivalent equation in 1927. Other discussions of the muon spin motion are given in F.J.M. Farley, *Cargese Lectures in Physics*, (1968) Vol. 2, p. 55, Gordon and Breach; J. Bailey and E. Picasso, in Nucl. Phys. 12, 43 (1970); The observation of the special feature of muon spin motion for $\gamma = 29.3$ (the "magic" γ) was first made in [3].

8. F. Mariam et al., Phys. Rev. Lett. 49, 993 (1982); see also V.W. Hughes and G. zu Putlitz in *Quantum Electrodynamics* ed. by T. Kinoshita (World Scientific, Singapore, 1990), p. 822. There is some criticism of the accuracy of this determination of λ which is made by Eides, Karshenboim et al. (the St. Petersburg group).
9. LAMPF Experiment 1054: *Higher Precision Measurements of μ_μ/μ_p and Muonium $\Delta\nu$*, in progress.
10. K. Jungmann spokesman.
11. P. Kusch and H.M. Foley, Phys. Rev. 72, 250 (1948).
12. J. Schwinger, Phys. Rev. 73, 416 (1948), 75, 898 (1949).
13. T. Kinoshita in *Quantum Electrodynamics*, (Directions in High Energy Physics Vol. 7) T. Kinoshita ed., World Scientific, 1990, p.218, and private communication.
14. R.S. Van Dyck et al., Phys. Rev. Lett. 59, 26 (1987) and in *Quantum Electrodynamics*, (Directions in High Energy Physics Vol. 7) T. Kinoshita ed., World Scientific, 1990, p.322.
15. T. Kinoshita and W.J. Marciano in *Quantum Electrodynamics*, (Directions in High Energy Physics Vol. 7) T. Kinoshita ed., World Scientific, 1990, p. 420.
16. T. Kinoshita, Invited Talk in honor of P. Kusch, APS Spring Meeting, 1994.
17. T. Kinoshita, B. Nižić and Y. Okamoto, Phys. Rev. D31, 2108 (1985).
18. *$DA\phi NE$ Physics Handbook, Vol. II,* ed. L.Maiani, G. Pancheri and N. Paver, (1992) p301.
19. T. Kinoshita, *Current status of the hadronic light-by-light contribution to the muon g-2, Muon (g-2) Note # 163,*July 1993.
20. M. Einhorn, Phys. Rev. D49, 1668 (1994).
21. T. Kinoshita, A. Sanda and M. Hayakawa in progress.
22. L. M. Barkov, et al., Nucl. Phys. B256, 365 (1985).
23. J.A. Casas, C. López and F.J. Ynduráin, Phys. Rev. D32, 736 (1985).
24. H. Burkhardt, F. Jegerlehner, G. Penso and C. Verzegnassi, Z. Phys. C 43, 497 (1989) and F. Jegerlehner private communication 1991.
25. Ľubomír Martinovič and Stanislav Dubnička, Phys. Rev. D42, 884 (1990).
26. A.Z. Dubničková, S. Dubnička, P. Stríženec, Dubna preprint E2-92-281, (1992).

27. W.A. Worstell and D.H. Brown, *Comparison of New Evaluations of the Hadronic Contribution to the Muon (g-2) Value Muon (g-2) Note No. 220* in preparation, 1994.

28. V. M. Aulchenko, et al., Nucl. Inst. Meth., A252, 299 (1986) and Novosibirsk Preprint INP 85-118 CMD-2 Detector for VEPP-2M.

29. M. Greco, Il Nuovo Cimento 100A, 597 (1988); P. Franzini, *Proceedings, Electroweak Interactions and Unified Theories* Les Arcs, (1989) p. 159.

30. X. Fei, private communication.

31. W.A. Bardeen, R. Gastmans and B Lautrup, Nucl. Phys. B46, 319 (1972); R. Jackiw and S. Weinberg, Phys. Rev. D5, 157 (1972); I. Bars and M. Yoshimura, Phys. Rev. D6, 374 (1972).

32. D. Decamp, et al., Phys. Lett. 246B, 306 (1990).

33. T.V. Kukhto, E.A. Kuraev, A. Schiller and Z.K. Silagadze, Nucl. Phys. B 371, 567 (1992). We note that Marciano has told us that this calculation is probably incomplete and is being redone as indicated in the footnote.

34. A. Sirlin, *50 Years of Weak Interactions*, ed. by D. Cline and G. Riedasch, (HEP Group, Univ. of Wisconsin, Madison, Wisconsin, 1984), p. 93.

35. W. J. Marciano, *Ann. Rev. Nucl. Part. Sci.* 41, 469 (1991).

36. C. Wieman and E. Hinds, private communication.

37. P. Langacker, M. Luo and A. Mann, Rev. Mod. Phys. 41, 87 (1992).

38. W. Hollik, Lepton and Photon Interactions, XVI International Symposium, Ithaca, NY 1993, AIP Conf. Proc. 302, 352 (1994).

39. M.L. Swartz, Lepton and Photon Interactions, XVI International Symposium, Ithaca, NY 1993, AIP Conf. Proc. 302, 381 (1994), edited by P. Drell, D. Rubin.

40. Jorge L. Lopez, D.V. Nanopoulos and Xu Wang, Phys. Rev. D49, 366 (1994).

41. J.C. Wallet, Phys. Rev. D 32, 813 (1985).

42. Mahiko Suzuki, Phys. Lett. 153B, 289 (1985).

43. A. Grau and J.A. Grifols, Phys. Lett. 154B, 283 (1985).

44. A.I. Studenikin and I.M. Ternov, Phys. Lett. 234B, 367 1990.

45. P. Méry, S.E. Moubarik, M. Perrottet, F.M Renard, Z. Phys. C46, 229 (1990). We note that the Marseille preprint of this work, CPT-89/P.2226 is referenced in the Kinoshita-Marciano review..

46. C. Arzt, M.B. Einhorn and J. Wudka, Phys. Rev. D49, 1370 (1994).

Chapter 3.
The AGS Experiment

Revised March 1994

3.1. Principle of Experiment

The goal of the new AGS experiment is a measurement of a_μ to 0.35 *ppm*, a factor of 20 improvement over the CERN experiment which achieved 7.2 *ppm*. After considering various approaches we chose for the new AGS experiment a method similar to that used at CERN [1] but allowing for either pion or muon injection into the storage ring.

The principle of the AGS muon $(g-2)$ experiment is the same as that of the latest CERN experiment. The general arrangement is shown in Fig. 3.1.1. The ring consists of a monolithic "C" magnet, 7.112 m in radius, and the field is excited by four superconducting coils.

As for all the $(g-2)$ experiments on the electron and the muon, the difference frequency between the spin precession frequency and the orbital cyclotron frequency of the particle is measured in a homogeneous magnetic field and hence a_μ is determined. The basic equations for the spin precession frequency, the cyclotron frequency and the $(g-2)$ frequency, which were given in Chapter 2, are repeated here for convenience:

$$\omega_s = \frac{eB}{mc\gamma} + \frac{e}{mc}aB \tag{3.1.1}$$

$$\omega_c = \frac{eB}{mc\gamma} \tag{3.1.2}$$

$$\omega_a = \omega_s - \omega_c = \frac{e}{mc}aB \tag{3.1.3}$$

Polarized muons will be stored in a muon storage ring with vertical focusing provided by an electric quadrupole field. When both electric and magnetic fields are present, the equation for ω_a becomes

$$\vec{\omega}_a = \frac{e}{mc}\left[\vec{B} - \left(a - \frac{1}{\gamma^2-1}\right)\vec{\beta}\times\vec{E}\right] \tag{3.1.4}$$

When $\gamma = 29.3$ (the "magic" γ) or $p_\mu = 3.094\ GeV/c$, the coefficient of $\vec{\beta}\times\vec{E}$ vanishes and Eq. (3.1.4) reduces to Eq. (3.1.3). Hence at the magic γ, ω_a depends only on **B** and is independent of **E**.

Figure 3.1.1: A plan view of the AGS muon $(g-2)$ experiment

Decay electrons from muons stored in the ring are observed as a function of time, after π or μ injection into the ring, by electron calorimeters distributed around the inside of the ring. Since the angular distribution of the decay electrons is asymmetric with respect to the muon spin direction, the observed time distribution $N(t)$ will include a frequency component at the muon $(g-2)$ frequency ω_a. Assuming no other source of muon losses except decay,

$$N(t) = N_0 e^{-t/\gamma\tau} \left[1 - A\cos\left(\omega_a t + \phi\right)\right], \tag{3.1.5}$$

in which N_0 is a normalization constant; $\gamma\tau$ is the muon laboratory lifetime, τ = muon mean life in its rest frame and $\gamma \approx 29$, A = the muon decay asymmetry parameter, which depends on the energy and angular spread of the electrons accepted by the detector times the average polarization.

The statistical accuracy with which ω_a can be determined from the observed electron distribution is given by:

$$\frac{\Delta\omega_a}{\omega_a} = \frac{\sqrt{2}}{\omega_a A \gamma\tau N_e^{1/2}} \tag{3.1.6}$$

in which N_e is the total number of electrons observed.

Polarized muons can be injected onto stored orbits in the storage ring either by pion injection or by muon injection into the storage ring. In pion injection, a pion beam, slightly higher in momentum than the magic momentum, is injected into the ring. As the pions cross the storage region some will decay producing muons which match the acceptance of the ring and are stored. This is obviously a very inefficient but cheap mode of providing a kick to put the muons on orbit.

In muon injection, a polarized muon beam at the magic momentum is injected into the storage ring. A fast kicker is placed a quarter of a betatron wavelength around the ring from where the beam is inflected. Since the transit time around the ring is 150 ns, the kicker pulse must turn off rather rapidly, and the transient magnetic effects from this pulse must be very small and well understood.

Both options are being pursued. The experiment will begin in 1996 with pion injection into the ring, while the fast kicker is constructed. In 1997 the kicker will be in place for running.

The location of the storage ring and the design of the beam line is designed to allow either option, since there is a 72m straight decay section.

Pion injection was used in the CERN experiment. This injection technique produces an intense background of particles at injection time which must not be permitted to paralyze or to degrade the subsequent time measurement by the electron detectors. Muon injection requires a fast kicker, which may cause transient magnetic fields, but background for the

electron detectors at injection will be greatly reduced and the stored muon intensity will be over an order of magnitude greater. The fast kicker is discussed in Chapter 12.

3.2. Features and Parameters of AGS Experiment

Improvement in the $(g-2)$ measurement at BNL as compared to the CERN result will be due principally to improved statistics obtainable with the much higher proton beam intensity at the AGS ($\sim$200 times), compared to what was available at CERN.

Substantial effort has gone into designing the storage ring magnet to have as uniform a magnetic field as possible. Unlike the CERN ring, which consisted of 40 separate magnets excited by a common coil, any gaps between adjacent yoke and pole pieces in our magnet are measured in thousands of an inch. In addition we will measure the mean field $\mathbf{B}$ around the storage region to 0.1 *ppm*, a factor of 10 better than was done in the CERN experiment and thus reduce their principal systematic error to the 0.1 *ppm* level.

The precision in measurement of the time interval t in Eq. (3.1.5) must be free of systematic shifts greater than 20 ps in order to keep this contribution to the error in ω_a small compared to the statistical error. Other small systematic errors must also be kept at or below the 0.1 *ppm* level. A full discussion of errors follows in Chapter 4.

The superferric storage ring is to be homogeneous over the storage region to 1 *ppm* and the effective magnetic field averaged around the ring will be known to 0.1 *ppm*. In order to achieve a highly stable magnetic field we have chosen an iron magnet with superconducting coils, so that the field is determined primarily by the configuration of the iron. The pole piece steel is extremely high quality, low carbon magnet steel, and the field in the storage ring will be decoupled from any inhomogeneities in the yoke using the standard device of an air gap between the back side of the pole piece and the yoke.

The field value is chosen to be 1.45 T in order to stay just below saturation. The use of superconducting coils should be advantageous for stability because the coil temperature is well stabilized and coil and iron temperatures can be well isolated. Also, because of the long time constant of the coil, ripple effects from the power supply should not be troublesome.

Several techniques will be used to shim the magnetic field to the 1 *ppm* homogeneity needed for the experiment. Iron shims will be placed on the yoke to compensate for any holes, etc. which have been machined. Steel wedges, each covering a few *cm* in azimuth, with a wedge angle chosen to cancel the quadrupole component inherent in a "C" magnet, will be placed in the air gap between the yoke and the pole pieces. These can me moved

radially over a few cm to tune the dipole field by a small amount, to compensate for variations in the μ of the pole piece iron. Rose shims on the pole faces will be optimized to eliminate the sextupole moment of the field, and pole face current windings will be used to eliminate higher multipoles.

For field measurement and control, we will make extensive NMR measurements and use feedback control. NMR measurements will use fixed probes, an NMR trolley capable of moving about the ring inside the vacuum chamber, plunging probes, and absolute calibration probes.

Decay electrons will be detected with Pb-scintillating fiber electron calorimeters. The special requirements of the detectors will be the ability to handle high instantaneous rates including a large initial background and to measure time intervals with ~ 20 ps (accuracy averaged over the entire data sample).

Table 3.2.1 gives general features of the new AGS experiment, and Table 3.2.2 gives the specific parameters of the AGS experiment.

The projected counting rates and errors are discussed in the next chapter. The CERN experiment was dominated by the statistical error of 7.0 ppm, and the largest systematic error was an uncertainty of 1.5 ppm in $\mathbf{B}$. With the increased proton intensity available at the AGS, the projected statistical error on ω_a is 0.3 ppm. The improved storage ring magnet and NMR system should reduce the systematic error in $\mathbf{B}$ to about 0.1 ppm, which will be the dominant systematic error in the experiment. The total systematic error is expected to be 0.12 ppm.

In addition to the primary objective of measuring a_μ very precisely, our experiment will compare a_{μ^+} and a_{μ^-} as a test for CPT invariance, will measure the lifetimes of energetic μ^+ and μ^- in the storage ring, and will search for an electric dipole moment of the muon, as was done at CERN, [1] but all with much improved precision.

The lifetime measurement is really two tests in one. A comparison of $\tau(\mu^+)$ and $\tau(\mu^-)$ is a further test of CPT, and a precision value for $\tau(\mu^+)$ provides a check of the Einstein time dilatation factor. The determination of the lifetime is, in principle, a straightforward fit to the $(g-2)$ oscillation envelope (see Eq. (3.1.5)). In the CERN experiment the statistical error dominated, but systematic errors due to time-dependent muon losses and detector gain changes were also important. The precision achieved, both for the lifetime in flight and for the lifetime at rest (assuming special relativity), was 0.5×10^{-3} for μ^- and 10^{-3} for μ^+, respectively. The ratio $\frac{\tau(\mu^+)-\tau(\mu^-)}{\tau(\mu^+)} = (0.8 \pm 1.0) \times 10^{-3}$ was obtained in agreement with the result expected on the basis of CPT invariance, but the measured value $\tau(\mu^+) = 2.1948(10)$ μs is more than two standard deviations below the presently accepted value [2] for $\tau(\mu^+) = 2.19703(4)$ μs. The AGS experiment should achieve a much higher statistical accuracy and the comparison of $\tau(\mu^+)$ and $\tau(\mu^-)$ may reach an overall precision

Table 3.2.1: An Overview of the AGS Experiment

General Approach:

Muon Storage Ring with uniform $\vec{B}$
$Magic\ \gamma = 29.3$
$B = 1.45T$ with electrostatic quadrupoles for vertical focusing
Pion or Muon Injection

Improvements to CERN Experiment:

1. **Primary proton beam intensity with booster** $\times 200$

2. **Superconducting Inflector**

3. **Storage ring magnet: Field Homogeneity and Control - Homogeneity to** $\sim$**1** *ppm*, (CERN = 10 - 15 *ppm*) We employ the following to reach this goal:
   a. Superconducting Coils
   b. Larger Magnet Gap
   c. Azimuthal Symmetry in Iron Construction
   d. Four forms of Shimming (Active and Passive)
   e. NMR Feedback and Control

4. **Magnetic Field Measurement (NMR) Accuracy to** $\sim$**0.1** *ppm* To be achieved by:
   a. NMR Trolley Which Moves Inside the Vacuum Chamber
   b. Fixed Probes (360) Outside The Vacuum Chamber
   c. Plunging Probes (10) to Cross Calibrate with Trolley

5. **Detector System Increased Acceptance, Higher Data Rate and Time Measurement Capability**
   To be achieved by:
   a. Scalloped Vacuum Vessel to Minimize Pre-Showering
   b. Segmentation and Pulse Shape to Reject Double Events
   c. Segmented Detectors and/or a Position Sensitive Device in Front
   d. Improved High Rate Capabilities in the Detectors and Electronics

6. **Stored Muon Distribution**
   To be monitored by:
   a. Following Injection with Scintillating Fiber Monitors
   b. At Early Times by De-bunching Measurements
   c. At Early and Middle Times by Pick-up Electrodes
   d. Throughout the Storage Time by Wire Chambers

Table 3.2.2: Muon $(g-2)$ Ring Parameters

Parameter	**Value**	**Comments**
$(g-2)$ Frequency	$f_a \sim 0.23 \times 10^6/s$	$\omega_a = 2\pi f_a$ $\tau_a = 1/f_a = 4.37\mu s$
Muon Lifetime	$\gamma\tau \ = \ 64.4\ \mu s$	
Muon kinematics	$p_\mu \ = \ 3.0944\ Gev/c$ $\gamma_\mu \ = \ 29.3$	
Cyclotron Period	$\tau_{cyc} \ = \ 149\ ns$	
Central Radius	$\rho \ = \ 7112\ mm$	$(280'')$
Magnetic Field	$B \ = \ 1.4513\ T$	
Storage Aperture	9.0 cm diameter circle	
Stored μ/fill $(3.5 \times 10^{12} P.O.T.)$	1,630 17,360	π^+ injection μ^+ injection
Initial Rate One Detector	$\sim 3.7 \times 10^6$ $\sim 0.3 \times 10^6$	μ^+ injection π^+ injection
In one lifetime:	432 revolutions around ring 14.7 $(g-2)$ periods	

of 10^{-4}, which would be about a factor of 10 better than any other direct comparison of the lifetimes of free μ^+ and μ^-. [3] The test of special relativity is best done with μ^+ rather than μ^- because its lifetime at rest is much better known. A precision of 10^{-4} in determining $\tau(\mu^+)$ may be achieved from the data of the AGS muon $(g-2)$ experiment together with the time dilatation factor γ.

The existence of a muon electric dipole moment (EDM) D_μ would effectively tilt the plane of precession by an angle

$$\delta = \frac{\eta\beta}{2a} \qquad \text{where} \qquad D_\mu = \frac{\eta}{2}\frac{e\hbar}{2mc}.$$

This produces a phase difference $\Delta\phi$ in the $(g-2)$ oscillation observed at varying heights above and below the median plane. In addition, the frequency ω_a is increased to $\omega = \omega_a(1+\delta^2)^{1/2}$. It is therefore important to determine whether there is a vertical component to the precession in order to separate out the effect of an EDM from the determination of ω_a.

In the CERN experiment [1,4] scintillation counters in coincidence with the electron calorimeter, counted the number of decay electrons above and below the median plane, to search for an average $\Delta\phi$ shift. The value $D_\mu = (3.7 \pm 3.4) \times 10^{-19}\ e-cm$ was measured which is consistent with a zero value for the muon EDM. The statistical error was dominant, but in addition, an important systematic error arose from the misalignment (by about 1mm) of the split between the up and down counters with respect to the median plane of the muon orbits.

We hope for an order of magnitude improvement in the AGS experiment. The systematic errors are serious, but they should be manageable enough to permit an order of magnitude improvement on the EDM limit. [5]

In the present detector design each station will have a segmented scintillator in front of each calorimeter which will provide five vertical bins. It is planned to have at least one calorimeter station equipped with a position sensitive detector which has finer resolution.

In addition, at one point in the ring there will be a wire chamber system which will track the decay electrons, and will provide much more information on the electron distribution than it is possible to obtain with a single position measurement. By tracking the decay electron back to the point where it is tangent to the ring, one can infer the muon distribution, and its lowest moments.

It is interesting to note that the CERN $(g-2)$ storage ring magnet has had a varied and successful but unanticipated history after its use to measure muon $(g-2)$. First at CERN it was converted into a strong focusing ring and used to do the initial cooling experiment (ICE) both on stochastic cooling [6] and electron cooling, [7] which was an essential step in the development of the CERN $\bar{p}p$ collider [8] and thence in the discovery of the W and Z^0 bosons. [9] The ICE storage ring with the help of stochastic cooling was also used to measure the antiproton lifetime and set a lower limit of 32 h. [10] At present this famous ring magnet is at the Gustaf Werner Institute of Uppsala University in Sweden and is an integral part of the CELSIUS nuclear physics facility. [11] In view of this impressive history of the CERN $(g-2)$ storage ring, it is convincing to believe that other exciting experiments and uses will be found for the Brookhaven precise muon $(g-2)$ storage ring after completion of the Brookhaven $(g-2)$ experiment.

3.3. References

1. J. Bailey, et al., Nucl. Phys. B150, 1 (1979)..
2. G.P. Yost, et al., Phys. Lett. B204, 1 (1988).
3. S.L. Meyer, et al., Phys. Rev. 132, 2693 (1963).
4. J. Bailey, et al., J. Phys. G4, 345 (1978).
5. J. Miller, R. Carey and E. Hawk, $(g-2)$ note in preparation, 1994.
6. G. Carron, et al., Phys. Lett., 77B, 353 (1978); G. Carron, et al., IEEE, NS 26, 3456 (1979).
7. M. Bell, et al., Phys. Lett., 87B, 275 (1979).
8. J. Gareyte, *11th International Conference on High-Energy Accelerators*, ed. by W.S. Newman, (Birkhäuser Verlag, Basel, 1980), p. 79.
9. G. Arnison, et al., Phys. Lett. 126B, 398 (1983); P. Bagnaia, et al., em Phys. Lett. 129, 130 (1983).
10. M. Bregman, et al., Phys. Lett. 78B, 174 (1978).
11. H. Calen, et al., in *Cooler Rings and Their Applications*, ed. T. Katayama and A. Noda, (World Scientific, Singapore, 1991), p.166.

Chapter 4.
Statistical and Systematic Errors and Running Time

Revised November 1994

4.1. Introduction

We now address the most important sources of errors, statistical and systematic, in the proposed measurement of $(g-2)$.

The number of muons stored following pion or muon injection into the storage ring is a central issue in the ability to achieve a proposed statistical error. In order to carry out a calculation of this number, the beam must be modelled from the production target, through the beam line and injector and finally to a stored muon population. This has now been done, and the results were reported in a recent $(g-2)$ note [1]. The proton andpion/muon beam are discussed in Chapter 6 of this report, and the physics of muon storage is discussed in Chapter 5.

In addition to the statistical errors, the systematic errors, both for the conventional counting technique used in the third CERN experiment, [2] hereafter referred to as the T method, and the new Q method (proposed by Morse [3])are discussed below.

4.2. Statistical Errors

4.2.1. Primary and Secondary Beam Fluxes

With the Booster Accelerator, each AGS cycle can deliver up to 6×10^{13} protons in the twelve RF bunches. The cycle repetition period is around 2 s. This means a maximum intensity of 5×10^{12} protons per bunch. In the $(g-2)$ experiment we take one proton bunch at a time. Since we must assume that the machine will not reliably deliver the maximum flux, we have taken the conservative figure of 3.5×10^{12} $P.O.T.$ (Protons on Target) per fill for use in the rate calculations. The secondary beam is described in Chapter 6. The secondary beam flux calculations were carried out assuming an AGS energy of 28.5 GeV. For several years, the AGS has operated at 24 GeV to save power. [4] In going from 28.5 to 24 the π^+ flux drops by 5.4%, thus running times need to be scaled up by this factor.†

For pion injection the π^+ flux at the inflector exit is

$$N_{\pi+} = 1.79 \times 10^7 \ / \ 10^{12} P.O.T.$$

and for muon injection, the μ^+ flux at the inflector exit

$$N_{\mu+} = 7.08 \times 10^4 \ / \ 10^{12} P.O.T.$$

The total pion and muon fluxes at the inflector exit (assuming 3.5×10^{12} $P.O.T.$) would then be:

$$\text{Total } \pi^+ \text{ flux } = 6.27 \times 10^7 \qquad \text{and} \qquad \text{Total } \mu^+ \text{ flux } = 2.48 \times 10^5$$

4.2.2. The Number of Stored and Lost Muons

In the 1992 Design Report, the efficiency for an injected pion to result in a stored muon is quoted to be 134 *ppm*. This does not agree with current estimates.

It is felt that with the inflector-storage-ring geometry of the $(g-2)$ ring, the upper limit on the storage efficiency should be about 50 *ppm* for pion injection, and with scraping, it could be as low as 20 *ppm*.

Recently Mane [5] obtained a capture efficiency of 26 *ppm* after scraping, which had long term losses of 2×10^{-5} per lifetime, which is well within the level needed. These results need further study, but we feel confident enough to use them for the current estimates.

The storage efficiency of 26 *ppm* for pion injection gives

$$\mu^+ \text{ Stored per } \pi^+ \text{ Fill } = 1630$$

† In the periods of dedicated running, it may be to our advantage to run at an even lower AGS energy, to optimize protons per hour per power dollar. This would have the added benefit of lowering the singles rates in the detectors just after injection

For muon injection, the upper limit on storage efficiency is about 10%, and Mane's [5] calculation for muon injection gave an injection efficiency of 7% after scraping, with long term losses of 4×10^{-6} per lifetime. This storage efficiency gives

$$\mu^+ \text{ Stored per Fill } = 17,360$$

4.2.3. Counting Rates After Injection

Following injection, the rate of decay electrons striking the calorimeters is rather high. The instantaneous rate, assuming there is some time interval (τ_w) in μs one waits after injection for the tubes, etc. to stabilize, is given by

$$Rate = (N_\mu) \times e^{-\frac{\tau_w}{64.4}} \times \left(\frac{1}{24 \text{ Detectors}}\right) \times \left(\frac{1}{64.4 \times 10^{-6} s}\right) \times \epsilon_d$$

where $\epsilon_d = 0.45$ is the fraction of decay electrons which strike the calorimeters and 64.4 μs is the dilated muon lifetime.

After 20 μs the instantaneous calorimeter rate due to decay electrons at each of the 24 stations is 348×10^3 $/s$ for pion injection and 3.7×10^6 $/s$ for muon injection.

We should note that there is a strong sentiment for going to 8 bunches rather than 12 in the AGS.[‡] Should this happen, we would get 3/2 the flux per bunch, and the singles rate following muon injection will be 5.6 MHz. If the instantaneous counting rate is too high, we can decrease the aperture inside the storage ring, which is in some ways good, since some of the systematic errors decrease with a decrease in the aperture.

[‡] This change was made during the 1994 running period to accommodate the increased intensity in the AGS. We have been assured that it is possible to go back to 12 bunches with some loss in intensity. Since we do not need the full booster intensity of 5×10^{12} protons per bunch, we do not anticipate problems in changing back to 12 bunches.

4.2.4. Running Time Estimates - Full AGS Beam

The fractional statistical error is given by

$$\delta\varepsilon = \frac{\delta\omega_a}{\omega_a} = \frac{\sqrt{2}}{2\pi f_a \tau_\mu N^{\frac{1}{2}} A} \tag{4.2.1}$$

where $f_a = 0.229\ MHz$ is the spin precession frequency, $\tau_a = 64.4\ \mu s$ is the dilated muon lifetime, and the asymmetry $A = 0.4$ for the 15 percent of the stored muons which contribute counts for a 1.85 GeV threshold on the decay electron energy.

It follows that the number of stored muons needed for a given fractional error $\delta\varepsilon$ is given by

$$N_\mu = \frac{2}{0.15\left(2\pi f_a \tau_\mu A\right)^2 \left(\delta\varepsilon\right)^2} \tag{4.2.2}$$

Table 4.2.1: The number of stored muons needed for different statistical errors.

	Muons Needed for 7 *ppm* Error	Muons Needed for 1 *ppm* Error	Muons Needed for 0.7 *ppm* Error	Muons Needed for 0.3 *ppm* Error	Muons Needed for 0.2 *ppm* Error
N_μ	2×10^8	9.7×10^9	1.98×10^{10}	1.08×10^{11}	2.43×10^{11}

Table 4.2.2: Running time needed to reach various statistical errors for pion and muon injection. These estimates assumed that the full AGS beam was available (see text) and that the AGS would operate with a 2 second cycle time.

Particle Injected	Running Time for 7 *ppm* Error (Hrs.)	Running Time for 1 *ppm* Error (Hrs.)	Running Time for 0.7 *ppm* Error (Hrs.)	Running Time for 0.3 *ppm* Error (Hrs.)	Running Time for 0.2 *ppm* Error (Hrs.)
π^+	5.70	277	565	3072	6,923
μ^+	0.53	25.8	52.8	288	649

The number of muons needed to reach a given statistical accuracy for a range of errors, are given in Table 4.2.1. The running times needed to accumulate these errors are given in Table 4.2.2

The running time was calculated assuming the number of stored muons listed in Table 4.2.1. The AGS-Booster cycle time was assumed to be 1.8 s, and it takes an additional 0.2 s to extract the twelve bunches, for a total of 2 s per AGS cycle. In the running time calculations it was assumed that all 12 (or 8) proton bunches were taken.

It is obvious that a very large amount of beam time is required with pion injection beyond the 1 *ppm* level. On the other hand, muon injection lives up to its promise of 0.35 *ppm* in just over 200 hours.

4.2.5. Statistical Errors Achievable with Parasite and Real π Injection Runs

We will tune up the injection process, detectors, electronics, etc., in a parasite mode with a single bunch from each AGS cycle. To obtain an order of magnitude feeling for the precision one might reach after some dedicated data collection with these running conditions, after the experiment is tuned up, we give two scenarios: a) One month of pion parasite running, assuming one bunch (out of 12) per AGS cycle, and b) Two weeks of dedicated pion injection running with all 12 proton bunches.

To calculate the running time in a parasite mode, where we take one or two bunches, and then the beam is stretched and extracted, one must assume a 3 s cycle time.

a). Assuming 120 hours of data collection per week, 4.3 weeks in the month, proton flux per bunch as above, 3 second AGS cycle time, 26 *ppm* injection efficiency, we find 1.01×10^9 muons stored, which, from Eq. (4.2.2) implies a statistical error of ± 3.1 *ppm*. If we get the two, or three bunches per AGS cycle, as has been stated by the Associate Director, then divide the error by $\sqrt{2}$ or $\sqrt{3}$ to get the appropriate improved error.

b). In a dedicated run of two weeks, where we assume 140 hours of data collection per week, 2 second AGS cycle time, we find a statistical error of ± 0.99 *ppm*.

For muon injection, we just scale these errors by $\sqrt{10.65}$ which is the difference in the number of stored muons per fill from pion and muon injection. One obtains a statistical error of ± 0.95 *ppm* after a month's parasite run with muon injection (one bunch per cycle), and and ± 0.3 *ppm* for a two week dedicated muon run, which is consistent with Table 4.2.2.

4.2.6. Comparison with Earlier Estimates

While the muon injection rate is close to that found in earlier calculations, the pion rate is considerably lower. The phase space of the beam exiting the inflector imposes a limit on the injection efficiency to about 60 *ppm*. It now appears that the 134 *ppm* estimate in the first edition of the Design Report (Chapter X) was optimistic. We should note that in the running time estimates given in Table III.4 of the second edition of the design report, 100 *ppm* was used as the pion injection efficiency. Even correcting for the various factors, there seems to be a disagreement between this calculation and the second edition design report Table III.4.

We note that the earlier calculation of the injection efficiency was done well before the final beamline and inflector designs were available, and the injection efficiency depends critically on the phase space of the beam as it exits the inflector, as well as the radial position of the inflector. To accommodate the superconducting inflector, the inflector exit was moved outward radially, which would also affect the storage efficiency. Furthermore, in the early estimates, a tracking calculation was not carried out, as has now been done.

4.3. Systematic Errors

A number of possible sources of systematic errors on the measurement of f_a must be considered.

1. Errors in knowing the mean field B for the subset of stored muons which contribute to the measurement of f_a.
2. Corrections for the effect of the radial part of the electric field, from the focusing electric quadrupoles, on the spin motions for muons with momenta larger or smaller than the magic momentum.
3. The pitch correction to spin motion for muons oscillating in the vertical direction (the vertical component of betatron oscillations of the stored muons).
4. The change of mean radius as a function of time due to differential decay. Muons with above average momenta have above average storage radii and above average lifetimes. The average radius and momentum of the stored muon population will therefore slowly increase with time.
5. The effect of muon particle losses. The average polarization of the stored muons can depend slightly on their storage trajectories in the ring. If losses were larger, say, for particles stored at large average radii, then the average phase of the stored muons could change with time.

6. The effect of a non-zero electric dipole moment on the spin motion.
7. Timing errors due to imperfections in the electronics: these include rate-dependence of timing and gains in the PMTs and electronics.

4.3.1. The Most General Case: Electric and Magnetic Dipole Moments

The most general formula for the muon spin precession, assuming that the muon has both a magnetic and electric dipole moment and moves in the presence of both electric and magnetic fields, is given by

$$\omega_{\rm a} = -\frac{e}{2mc}\left[(g-2)\,\mathbf{B} - \frac{(g-2)\,\gamma}{\gamma+1}(\beta\cdot\mathbf{B})\,\beta + \eta\beta\times\mathbf{B} + \beta\times\mathbf{E}\left(\frac{2}{\beta^2}-g\right)\right] \qquad (4.3.1)$$

where $\omega_{\rm a} = \omega_{\rm s} - \omega_{\rm c}$ as before and $\omega_{\rm s}$ is the total rate of spin precession, $\omega_{\rm c}$ is the cyclotron frequency, g is the usual muon g factor, the anomaly being $a = (g-2)/2$, and η is a parameter proportional to the electric dipole moment,

$$D_\mu = \left(\frac{\eta}{2}\right)\left(\frac{e\hbar}{2mc}\right).$$

We have ignored a couple of very small terms, such as a term proportional to $\beta\cdot\mathbf{E}$.

The last term in Eq. (4.3.1), the contribution to the spin precession due to the focusing quadrupole electric field, is zero at the magic gamma, e.g. when the muon momentum is such that $\beta^2 g = 2$ ($\gamma = 29.3$="magic gamma" or $p_\mu = 3.1\ GeV$, the "magic momentum"). We therefore have chosen the average gamma for stored muons to be magic.

The range of stored muon momenta $\frac{\Delta p}{p} \approx \pm 0.005$. The muons with gamma below 29.3 have a smaller than average storage radius, where the radial **E**-field is negative, while the muons with gamma above 29.3 have a larger than average storage radius, where the radial **E**-field is positive. Therefore, the change in ω_a due to the last term in Eq. (4.3.1) has the same sign for muons both above and below the magic gamma. This leads to the need for a correction discussed below in the **E**-field correction subsection.

4.3.2. The Effect of a Hypothetical Electric Dipole Moment

On theoretical grounds there is reason to believe that the electric dipole moment (EDM) of the muon is extremely small, and therefore is not likely to affect $\omega_{\rm a}$. With a non-zero EDM, by far the largest effect on ω_a comes from the third term in Eq. (4.3.1), which causes the spin precession vector to tip outward radially by the angle $\delta = tan^{-1}(\eta\beta/2a)$ and causes the magnitude of ω_a to increase by the factor $\sqrt{1+(\frac{\eta\beta}{2a})^2} = \sqrt{1+\delta^2}$. The tipping of the direction of $\omega_{\rm a}$ leads to an average vertical component in the decay electron momenta which oscillates at frequency f_a. This produces a corresponding oscillation in the average vertical detection position of electrons, which we plan to measure using vertically segmented counters (either the FSDs or PSDs, see Chapter 16).

Experimentally, CERN III [2] established the best experimental limit, $D_\mu = (3.7 \pm 3.4) \times 10^{-19} e - cm$, or $\delta = 3.8 \times 10^{-3}$, which gives a correction factor to ω_a of $\sqrt{1+\delta^2} = 1 + (7 \times 10^{-6})$. We plan to improve the experimental limit on the EDM by an order of magnitude by measuring the amplitude of oscillation of the average vertical detection positions of the electrons using detectors with more vertical segmentation. With an order of magnitude improvement on the EDM measurement, the uncertainty in ω_a due to the EDM would be $\sqrt{1+\delta^2} = 1 + (7 \times 10^{-8})$, which is negligible.

4.3.3. General Requirements for the Measurement of a_μ

If we ignore the small term $\beta \cdot \mathbf{B}$ in the expression for ω_a above, (see Eq. (4.3.1)) as well as the small terms just discussed, we obtain the familiar form

$$\omega_{\rm a} = -\frac{e}{2mc}(g-2)\,\mathbf{B} = -\frac{e}{mc}a_\mu \mathbf{B} \qquad (4.3.2)$$

We wish to measure a_μ with an overall error of less than 0.35 *ppm*. We would like to keep systematic contributions small, below 0.1 *ppm*. This requires precision measurements of both ω_a and $\mathbf{B}$. It is important to note that it is these quantities *averaged over the ensemble of detected electrons* which need to be known accurately, not for individual muons.

The experimental value of ω_a comes from the measured frequency of oscillation in the detected electron time spectrum over ten muon lifetimes, for a large number of electrons. The detector system must therefore be capable of producing accurate timing of the decay electrons, averaged over a large number of electrons, to 0.1 *ppm*. If a fit is made to data from 0 to $200\mu s$ after injection, where approximately half of the statistical significance of the data lies, then the timing must be good to about 20 *ps* on average. The timing over the full ten muon lifetimes=640 μs must be good to 64 *ps*. The statistical significance of

data beyond 640 μs is negligible. Of course, the detection times for *individual* electrons can only be measured to an accuracy of a few hundred picoseconds, and in fact we plan to measure them to the nearest 5 ns detector clock cycle. The data are collected in a histogram as a function of time, and a 5 ns bin width is easily small enough for a good fit to the time histogram when compared with the precession period of 4.4 μs. However, on average, the decay electrons must fall into the proper time bin. This means that the boundaries of the 5 ns time bins must be stable to 20 ps on average. This will be discussed below in detail in the detector systematic error subsection.

The **B** field is measured with precision proton NMR probes. This is done by measuring the rate of precession of an NMR proton, ω_p', in the B-field at many points in the storage ring. The NMR proton is at rest, so that its precession rate is

$$\omega_p' = -\frac{eg_p}{2m_pc}B.$$

with a correction ($\sim$ 26 ppm) for the effects of the medium surrounding the proton (see Chapter 14). The NMR probes will be calibrated at LAMPF as described in Chapter 14. The frequency standards for both the NMR system and for the detector system will be stabilized using the same LORAN C 10 MHz time standard module.

The **B**-field seen by an individual muon, averaged over one cyclotron turn, is expected to be uniform to 1 ppm, and the NMR measurements are expected to be accurate to 0.1 ppm. Again, it is only the **B**-field averaged over the ensemble of muons which decay and the decay electrons are detected which must be known to 0.1 ppm. Given the map of the **B**-field from the NMR measurements, and a knowledge of the stored muon distribution (see Chapter 15), the average **B**-field for the ensemble can be determined to 0.1 ppm. It is possible for the muon phase space distribution to change as a function of time after injection, which may affect the average **B**-field, and this must be known. Examples of this are differential decay in the ring and muon losses, and these are discussed below.

4.3.4. Factors Affecting the Mean Field

The magnetic field will be mapped and calibrated with high precision proton NMR and it is expected to achieve an overall accuracy of 0.05 to 0.1 *ppm*.

As explained in Chapter 14, it is intended to monitor the field continuously at some 360 positions outside the vacuum chamber. There will be 12 plunging NMR probes which can be driven radially across the storage aperture. Also the muon runs will be interrupted on a regular schedule and the field measured inside the vacuum chamber. As a result errors due to a drift of the field are expected to be negligible. The usual statistical tests will be applied to estimate the deviation of the true mean from that derived from the many sample measurements.

An accurate map of the field must be folded with the muon distribution to find the mean field for the ensemble of muons that contribute to the determination of the f_a. New techniques are introduced in this experiment to reduce uncertainties in this average.

As explained in Chapter 5, the moments I_a, J_a of the muon distribution can be calculated from the initial conditions at injection and it will be possible to measure them with pickup electrodes, traceback electrons, and fast rotation analyses (Chapter 15). The magnetic field will be averaged in azimuth to give

$$B\left(r,\theta\right) = \frac{1}{2\pi}\int_0^{2\pi} B\left(r,\theta,\phi\right)\, d\phi$$

and $B(r,\theta)$ will be expressed in terms of multipoles

$$B\left(r,\theta\right) = \sum_0^{\infty} \left(C_n I_n + S_n J_n\right)/I_0$$

By using a circular aperture the higher moments of the muon distributions will be kept small and the lower multipoles of the field will in any case be small. Therefore, we expect the error in computing the mean field B for the muon population to be no greater than 0.1 *ppm*.

The stored muons do not contribute equally to the data for f_a. The particles on the inside of the ring contribute more counts than those on the outside because of the detector solid angles involved. The observed muon distributions will be corrected for this bias.

4.3.5. Effect of the Radial Electric Field

If the electric quadrupole field is given by $E = k\frac{\Delta\rho}{\rho}$ where k is the quadrupole constant and ρ is the radius of curvature of the ring at the center of the aperture, it will be equivalent to a magnetic field gradient of field index n if the electric force $eE = ek\frac{\Delta\rho}{\rho}$ is the same as the change of magnetic force due to the magnetic gradient $\frac{ev}{c}nB\frac{\Delta\rho}{\rho}$, where n is the field index.

Hence the effective n-value for electric quadrupole focusing is

$$n = \frac{k}{\beta B} = \frac{2eV}{\beta p_0 c}\left(\frac{\rho}{r_e}\right)^2$$

where V is the voltage applied between the center of the aperture and the horizontal electrode at $\pm r_e$ and p_0 is the stored muon central momentum. One should note that the circular storage region has radius $r_0 = 4.5\ cm$ and the electrodes are at $r_e = \pm 5.0\ cm$.

The effect of the radial electric field on the spin precession is given by

$$\frac{f_a}{f_0} = 1 - \left(\frac{\beta E}{B}\right)\left(1 - \frac{1}{a\left(\gamma^2 - 1\right)}\right),$$

where a is the anomalous magnetic moment of the muon and

$$f_0 = \frac{aeB}{2\pi mc}.$$

For muons whose average radius is at the center of the aperture (average radius ρ and frequency f_0), $a(\gamma^2 - 1) = 1$, and the electric field has no effect on the precession frequency. However, for other radii, γ does not meet this condition and

$$\frac{\Delta f_a}{f_a} = -\frac{2\beta E}{B}\frac{d\gamma}{\gamma}$$

.

If x_e is the displacement of the equilibrium orbit from the center of the aperture, and x the instantaneous position of the particle,

$$\frac{d\gamma}{\gamma} = (1 - n)\left(\frac{x_e}{\rho}\right),$$

and

$$E = k\left(\frac{x}{\rho}\right) = n\beta B\left(\frac{x}{\rho}\right).$$

Hence

$$\frac{\Delta f_a}{f_a} = -2n\left(1 - n\right)\left(\frac{x x_e}{\rho^2}\right).$$

If the horizontal oscillations of the particle about its equilibrium orbit at x_e are exactly sinusoidal, i.e. if the quadrupole field is perfect, the time average value of x is $< x >= x_e$.

Then averaging over all particles

$$\frac{\Delta f_a}{f_a} = -2n\,(1-n)\left(\frac{< x_e^2 >}{\rho^2}\right)$$

For muons uniformly filling the available phase space in a circular aperture

$$< x_e^2 >= \frac{r_0^2}{14}$$

where $2r_0$ is the horizontal aperture, so

$$\frac{\Delta f_a}{f_a} = -Kn\,(1-n)\left(\frac{r_0}{\rho}\right)^2$$

with $K = \frac{1}{7}$. For the planned circular aperture of radius $r_0 = 4.5\ cm$, this correction is $0.69\ ppm$. The electric field *decreases* the experimental $(g-2)$ frequency by this small amount.

For a rectangular aperture of width $2r_0$ the same formula applies with $K = \frac{1}{5}$.

It is desirable to know this correction to about 10%, so the value of n must be known to this accuracy. The distribution of the equilibrium orbits can be found experimentally from the rotation frequency patterns at early times, giving measurements of $< x_e >$ and $< x_e^2 >$. More detailed calculations will be necessary once the exact form of the quadrupole field is known, and allowance must be made for azimuthal gaps in the electrodes. There would appear to be no difficulty in principle in knowing this correction to $0.05\ ppm$.

4.3.6. The Pitch Correction

The theory of the pitch correction in the case of vertical focusing by electric fields has been given by Farley [6] and further discussed by Field and Fiorentini. [7] A nice summary of many of these details appears in the review by Farley and Picasso. [8]

At the magic energy we have $f_a = f_0(1-C)$ where

$$f_0 = \frac{aeB}{2\pi mc}$$

and

$$C = 0.25\chi_0^2\left[1 - \frac{f_0^2}{\gamma^2\left(f_0^2 - f_p^2\right)}\right]$$

Here χ_0 is the angular amplitude of the sinusoidal pitching motion at the angular frequency f_p. In our case, $f_0 = a\gamma f_c$ and $f_p \approx \frac{f_c}{3}$, where f_c is the frequency of the particles in the orbit, so the final correction term inside the brackets is negligible and $C = 0.25\chi_0^2$.

If y is the instantaneous position of the particle above the median plane and λ_v is the wavelength of the vertical oscillation, $\chi_0 = (2\pi y_{max}/\lambda_v)$ and we can write $C = \frac{2\pi < y^2 >}{\lambda_v^2}$

For particles filling phase space uniformly in a vertical aperture of size $2b$, the overall average value of y^2 is

$$< y^2 >= 0.25b^2$$

so, on average over all trajectories

$$C = \frac{\pi b^2}{2\lambda_v^2}$$

for a rectangular aperture.

For a circular aperture of radius r_0,

$$< y^2 >= 0.143 r_0^2$$

In this case,

$$C = \frac{0.0715\left(4\pi^2\right) r_0^2}{\lambda_v^2}$$

With $\lambda_v = (2\pi\rho/n^{\frac{1}{2}})$ this gives finally

$$C = 0.0715n\left(\frac{r_0}{\rho}\right)^2$$

With $r_0 = 4.5$ cm, $\rho = 711$ cm, $n = 0.135$, the correction is 0.40 *ppm*.

Knowing this to 0.02 *ppm* means knowing the value of n to about 5%, and having evidence on the vertical distribution of the stored muons, which comes from the decay electron traceback. Again a more detailed calculation allowing for the gaps in the focusing electrodes will be made to relate χ_0^2 to the observed vertical distribution of particles. There should be no difficulty in establishing this correction to 0.05 *ppm*.

4.3.7. The Differential Decay Correction

The muons of higher momentum near the outside of the storage region have a longer lifetime than those on the inside, so after several lifetimes the mean radius will shift outwards and the mean muon momentum will increase. If $\gamma\tau$ is the dilated lifetime, the shift at time t is

$$\frac{\Delta\rho}{\rho} = \left(\frac{t}{\gamma\tau}\right)\left(\frac{< x_e^2 >}{\rho^2}\right)$$

where x_e is the position of the equilibrium orbit relative to the center of the aperture.

For the phase space distribution in a circular aperture of radius r_0, $< x_e^2 >= \frac{r_0^2}{14}$, so the shift in mean radius will be

$$\frac{\Delta\rho}{\rho} = 0.071\left(\frac{t}{\gamma\tau}\right)\left(\frac{r_0^2}{\rho^2}\right)$$

i.e. $\Delta\rho = 0.02\ mm$ per lifetime.

Again, experimental measurements will be made of the stored momentum distribution (fast rotation) and the positions of decay as a function of time (electron traceback) to confirm predictions for a circular aperture.

In view of the uniformity of the magnetic field the average radius shift with time will produce a negligible effect on the mean field. There will also be a slight shifts in the electric field correction and in the distribution of decay electrons on the front face of the detectors, and also an effect due to the slight spin phase dependence on average storage radius. Given our measured data on the phase space distribution and the predictability of the differential decay, all these will produce a negligible effect on the muon precession frequency.

4.3.8. Particle Losses from the Storage Ring

The stored muons have some probability of missing the aperture defining stops at early times, only to be lost later. Thus, the population inevitably takes some hundreds of turns to settle down to its final level. Furthermore, small irregularities in the magnetic and electric fields give small perturbations of the orbits and may cause particles to be lost at later times. Experience at the CERN ring indicates that continuing losses of about 1% per lifetime can be expected, but this can be reduced to less than 0.1% if the particles near the edges of the aperture are scraped off by deliberate field perturbations at early times.

The lost particles can influence the observed *(g-2)* frequency because they contribute to the precession curve at early times, but not at late times. So if they have a different mean field, or different spin angle than the average there will be an error. Lost particles are inevitably those which pass near the aperture stops, and so in principle are different from the average. Their polarization vector may therefore be different, and we would like to put limits on this effect.

In one muon lifetime (64 μs) there are 15 *(g-2)* cycles, so the total precession angle is 5.4×10^3 degrees. For 0.1% losses per lifetime and a 0.1 *ppm* error in f_a, the lost particles could have a maximum departure from the average *(g-2)* phase by 0.54 degrees, which is a fairly stringent requirement.

There are two factors which determine the phase of the *(g-2)* precession:

a. The average muon spin direction arising from the detailed left-right selection in the $\pi - \mu$ decay process in which the muons are born.

b. The average μ-e decay direction for the electrons which reach the detectors, referred to the muon rest frame.

In the $\pi \rightarrow \mu$ decay process

$$p_\mu = p_\pi \left[0.21 \left(1 + \cos \Theta^*\right) + 0.58\right]$$

A center of mass decay angle Θ^* of 22 degrees gives $\Delta p = 1.6\%$. This is the maximum $p_\pi - p_\mu$ which will contribute a stored muon with pion injection, so the muon spin direction spreads over a 22 degree cone (11 degree half-angle) about the pion direction. If left and right decays are equally probable the mean muon spin angle will still be zero on average. However, when the muons are injected by π-decay in the ring, there are small factors favoring outward over inward decay angles. But if the muons are produced in the straight muon channel, as will be the case for muon injection, left and right decays should be trapped with equal probability. A residual 1% difference between left and right trapping would give a phase shift of 0.2 degrees for the muons which are lost, if, of the 0.1% of lost muons, all are either of the left or right variety. Furthermore [9], with pion injection, the muons with $30 < x_e < 45mm$ are born at a mean azimuthal location of 132°, while those with $-45 < x_e < -30\ mm$ are born on average at 182°. Of course,the muon spin begins to precess as soon as the muon is born. For 0.1% muon losses per lifetime, this gives a phase change of about 0.5 degrees. However, these errors occur only with pion injection. The muons injected into the storage ring during muon injection are born in a straight channel. Thus these errors do not apply for muon injection.

For decay electron detection, there is inevitably a bias in favor of (outward, inward) decays of (μ^+, μ^-) (those electrons which at the time of muon decay have a small negative radial velocity component), in which case the electrons emerge from the magnet rapidly. Outward decays (electrons with initial positive radial velocity components) emitted at the same angle relative to the muon follow a longer path in the magnet before hitting the counters and so have a greater probability of being lost vertically or horizontally. Thus, the mean direction of the muon spin is tipped slightly inward or outward, and this effect is greater for high momentum muons near the outside of the storage region (e.g. larger than the average storage radius) than for low momentum muons. Selective losses at, for example, the outside of the ring would change the phase of the *(g-2)* precession curve. The typical decay direction also depends on the decay electron energy due to the variation of detector acceptance with energy. Calculations of mean muon decay direction give 0.16 degrees from the highest momentum muons and 0.02 degrees for the lowest, a spread of only 0.145 degrees, so the effect will be very small.

It is proposed to test for this effect during the experiment by artificially creating large losses at the extremes of the aperture by moving the aperture defining stop. The *(g-2)* phase will be recorded at early times for the remaining particles, and compared with the normal value. This will yield definitive limits on this error.

Another way to study the effect is to make some runs without scraping (loss level 1%) and to measure this 10-fold larger change in the *(g-2)* frequency. This could be done in about 1% of the running time. On the assumption that the mechanism for losses with scraping are similar, but smaller, a good estimate of the correction will be obtained. We will also measure the number of lost muons using muon monitors placed inside the ring. The muons will be detected as particles which pass in coincidence through at least two successive detector stations, with a small amount of energy deposited in each calorimeter. The muon loss detectors will be calibrated when the losses are 1%. Assuming a similar distribution of losses at the 0.1% loss level, this provides a direct measure of the muon loss rate.

4.3.9. Timing Errors

A systematic difference in timing between the early times when counting rates are higher, and late times when counting rates are lower will give an error in the *(g-2)* frequency. The fit to the frequency is sensitive, in effect, over a time span of 3 lifetimes, 200 μs. So an error of 0.1 *ppm* implies that the required timing accuracy be better than 0.02 ns on average over many events. The timing accuracy and linearity of the *(g-2)* digitrons from CERN III [2] at low rates has been demonstrated to be an order of magnitude better than this with crystal-controlled test pulses, but these tests were not carried out at high rates.

At high counting rates timing errors occur because in a closely-spaced pulse pair the first pulse will register while the second will be lost. With dead time t_d and count rate R the error is $\delta = 0.25\ R\ t_d^2$. If both pulses are rejected there should be no timing error, but a calculable small loss in the count rate. This will affect the measured lifetime to first order, but not the precession frequency. In the experiment the initial counting rate in each calorimeter may be as high as 8 MHz, but the double pulse rejection, using time over threshold and counter segmentation information will reject better than 90% of the double counts. With an electronic dead time t_d=10 ns, for example, the timing error at early times is then 20 ps, which just meets our standards. However, we will measure the time of each decay, therefore, we will know accurately the value of t_d, and we can make corrections accordingly a factor of 3 better than we need. It is straightforward to examine such effects experimentally by putting the signals from several counters into one timing channel, thus increasing the counting rate well beyond the normal, and then calculating the appropriate small correction.

However, the above error can be eliminated with a new method of analysis which becomes possible since we will instrument the calorimeter with a waveform digitizer which digitizes the output voltage from the calorimeter at accurately defined time intervals of 2.5

ns. In this method of analysis, the WFD pulse height is entered into the time histogram. Therefore, the ω_a analysis is done on the WFD time distribution, ie. events$\times$*volts* vs. time, instead of events above threshold vs. time. The pulse height is recorded by the WFD if it is above a hardware electronics threshold. Event overlap causes no error, if the WFD hardware threshold is sufficiently low and if the pulse height measurement is sufficiently linear. A Monte Carlo based calculation [3] indicated the hardware threshold should be below 500 MeV and the linearity should be better than 10%. This calculation assumed a very high probability of overlap of events: 20% at early times in the fill.

The statistical sensitivity of this 'Q' method is inferior to the traditional method of analysis. Briefly, this is because the asymmetry is a strong function of the electron energy, and only the high energy electrons have high asymmetry. The statistical sensitivity for the WFD Q method of analysis [3] is less than the traditional method by about $1/\sqrt{2}$. Therefore, this new method of analysis will be most useful for muon injection. The WFD Q method will be very useful if we exceed our target statistical sensitivity, which may be likely with muon injection.

Apart from the timing logic, errors can occur due to the finite rise times of the primary signals if there are any threshold, gain, or base-line shifts at high rates. With typical rise time of 3 *ns*, [10] these shifts must be less than 0.3% to avoid errors greater than 0.01 *ns*. In addition, the gains must be calibrated to 0.2% on average at early compared to late times in order to hold slewing of electrons into the wrong energy bins to an acceptable level. This is a demanding requirement, but not impossible. With the Q method of analysis employing the WFD, threshold shifts cause no appreciable error if the hardware threshold is below 500 MeV. Small gain changes and baseline shifts also cause no appreciable error.

If one pulse falls on the tail of a previous pulse, the energy measurement of the decay electrons is invalid. As a result, counts belonging to the wrong energy bin with incorrect *(g-2)* phase can be introduced at early times, but this will not happen at late times when counting rates are low. To avoid such effects in the threshold method of analysis, it is essential to reject all pairs of events which occur within say 100 *ns* of each other. This error causes no appreciable error with the new method of analysis with the WFD, if the hardware threshold is below 500 MeV. Another error occurs in the traditional method of analysis if two half energy events occur within say 5 *ns* and pass the double pulse rejection system. This can be minimized in the traditional method of analysis by choosing an energy threshold such that the mean asymmetry A of overlapping events is small, at a small loss of statistical sensitivity. Furthermore, this results in no appreciable error in the WFD Q method of analysis.

Overall, timing errors and *(g-2)* phase errors at early times due to pile up effects will be small. They will be studied at higher rates to measure the correction. Careful electronic

design, fast rising detector pulses, and high speed logic will minimize the effects. The new Q method of WFD analysis is complementary to the traditional method, and will provide a further check.

4.3.10. Summary of the Systematic Errors

Table 4.3.1: A Summary of the Systematic Errors

Source of Error or Correction	**Magnitude of Correction (ppm)**	**Error (ppm)**	**Comments**
Magnet calibration, Averaging **B** over muon population	–	0.1	Continuous monitoring Circular aperture, measured muon distribution
Radial **E** field	0.69	0.03	Rotation frequency to measure distribution of equilibrium orbits
Pitch Correction	0.40	0.02	Measured muon distribution
Differential decay	0	0.01	
a_μ phase change due to muon losses	0.1	0.05	Measured at larger loss levels with no scraping
Timing errors at early times	0.09	0.03	Measured at higher rates by combining signals from several counters
Errors added in quadrature		**0.12**	

The sources of systematic error are summarized in Table 4.3.1. If a correction needs to be made to the final data, then the magnitude of that correction, as well as the expected uncertainty on that quantity is given. The dominant systematic error is the knowledge

of the magnetic field averaged over the muon population. Our knowledge of the muon distribution and the field thus provide the systematic limit for this measurement.

4.3.11. The Detector/Electronics Systematic Error Budget

Recently, after a Detector Team meeting at Urbana-Champaign in October 1994, a list of the systematic errors introduced by the detectors and electronics was drawn up. [11] This is a preliminary list, but is included here to alert the reader that such an accounting exists.

Table 4.3.2: The conversion factor between errors in detector related quantities and a 0.1 *ppm* effect on the measured value of a_μ.

Detector/electronics mistake	Threshold Method	Q Method
PMT gain shift	0.2%	2%
WFD Linearity	NA	10%
Event overlap suppression	$> 10\times$	NA
PMT transit time shift	20 *ps*	20 *ps*
Electronics time slewing	20 *ps*	20 *ps*

The conversion factors which equate detector electronics mistakes to a 0.1 *ppm* effect on the measurement of the anomalous magnetic moment of the muon are given in Table 4.3.2 The first number is for the threshold ("T") method of analysis, [12-13] the second is for the WFD "Q" method. [3] The detailed calculations are given in the *g-2 Notes* by Morse [3], Carey and Miller, [12] and Miller. [13] If no correction is made, the effect given in Table 4.3.2 will give a 0.1 *ppm* shift in the measurement of a_μ. Alternatively, if a correction is made for the effect, an uncertainty on the knowledge of the effect at the above level will lead to a 0.1 *ppm* uncertainty in the measurement. The gain shifts and time slewing are differences between early and late times.

The performance of the detector electronics have recently been documented in *g-2 Notes.* The phototube tests on rate stability, gating and blanking are described in notes 201 and 202, [14-15] and further details on pulse tail effects have been studied by Ouyang. [16] The MTDC is described in note 207, [17] and the performance is described in note 206. [18]

The measured detector/electronics responses are summarized in Table 4.3.3 along with the relevant *g-2 Note* reference.

The error in the measurement of a_μ due to the detector electronics errors is given in Table 4.3.4 In light of the reported shift due to pulse tails which was reported at the Illinois detector meeting, [16] it was agreed that additional study is necessary for pulse shaping, deadtime corrections, etc. to reduce these effects for the threshold method of analysis.

Table 4.3.3: Measured Detector/Electronics Time Shifts.

Electronics error	Measurement	Ref.	comments
MTDC rate dependence	$< 20ps$	[17]	rate = 10 MHz
WFD rate dependence	$< 20ps$	[17]	rate = 10 MHz
PMT transit time shift	$2ps$	[14]	average shift at 5 MHz
Rate dependent PMT gain shift	$< 0.6\%$	[14]	rate = 10 MHz
Blanking PMT gain shift	$< 0.6\%$	[15]	

Electronics error	Threshold Method	Q Method
MTDC rate dependence	< 0.1 *ppm*	NA
WFD rate dependence	NA	< 0.1 *ppm*
Total PMT gain shift	< 0.6 *ppm*	< 0.06 *ppm*
PMT transit time shift	± 0.01 *ppm*	± 0.01 *ppm*
Tail effect ($\delta t < 125ns$) [16]	> 0.1 *ppm*	NA

4.4. References

1. H.N. Brown, Y.Y. Lee, S. Mane, E. Benedict, J. Miller and B.L. Roberts, *Revised Rates for Muon Storage in the (g-2) Ring*, *Muon g-2 Note No. 185*, February 1994.
2. J. Bailey et al., Nucl. Phys. B150,1(1979).
3. W. Morse,*A New Method of Analysis*, *Muon g-2 Note No. 93*, October 1991.
4. W.M. Morse, *What AGS Energy Should We Use for the* $(g-2)$ *Experiment*, *Muon g-2 Note No. 99*, June 1990.
5. S. Mane, presentation to the Beam Dynamics Team on 10 February 1994.
6. F.J.M. Farley, Phys. Lett. 42B, 66 (1972).
7. J.H. Field and G. Fiorentini, Nuovo Cim. 21A, 297 (1974).
8. F.J.M. Farley and E. Picasso in *Quantum Electrodynamics*, T. Kinoshita editor, World Scientific (1990), p. 479.
9. W. M. Morse *Systematic Error Due to Particle Losses*, *Muon g-2 Note No. 147*, March 1993.
10. D. Hertzog, October 1994 Detector Meeting.
11. W. Morse compiled the errors and will update these tables as necessary.
12. R. Carey and J. Miller, *The Impact of Gain and Resolution Shifts on the g-2 Frequency Measurement Muon g-2 Note No. 165,* August 1993.

13. J. Miller, *Discussion of Some Detector-Related Systematic Problems and a Discussion of the Optimum Number of Counters*, *Muon g-2 Note No. 68* February 1991.

14. Jinsong Ouyang and William E. Earle, *Rate and pileup Studies for Photomultiplier Tubes/Bases and Some Electronics*, *Muon g-2 Note No. 201*, June 1994.

15. Jinsong Ouyang and William E. Earle, *Blanking and Flash Studies for Photomultiplier Tubes*, *Muon g-2 Note No. 202*, July 1994.

16. J. Ouyang, presentation at the Illinois Detector meeting in October 1994.

17. W. Earle, E. Hazen, B. Safford and G. Varner, *A Deadtimeless Multihit TDC for the New g-2 Experiment*, *Muon g-2 Note No. 207*, September 1994. Test results show that no time boundary shifts > 20 *ps* occur at input rates up to 10 MHz. Additional details were given by G. Varner at the Illinois meeting..

18. E. Hazen, R.B. Safford and G. Varner, *g-2 MTDC Timing Performance*, *Muon g-2 Note No. 206*, September 1993.

Chapter 5.
The Physics of Muon Storage

Revised August 1994

5.1. Introduction

In the initial year of running for E821, we will begin with the injection of pions into the storage ring. After the muon kicker is ready, we will inject muons directly into the ring. Since pions or muons exit the inflector and enter the vacuum chamber at a radial point which lies outside of the storage volume, a kick is needed to store muons onto a stable orbit in the storage ring. With pion injection, the decay

$$\pi^+ \rightarrow \mu^+ + \bar{\nu}_\mu$$

provides the kick to place muons onto a stable orbit in the storage ring. If muons are injected directly, a fast kicker is necessary, and it is placed one quarter of a betatron oscillation around from the injection point. (Ahn and Lysenko [1] carried out the first thorough study of this option.) There are similarities and differences in these two techniques which are discussed below.

More recently, tracking codes developed by Mane [2-3] have been used to study both pion and muon injection.

One should note that although muons are stored in a weak focussing circular machine, it is not a storage ring in the traditional sense but rather more like a static device such as a spectrometer or a beamline. (See Wiedemann, [4] Edwards and Syphers [5] and the classic treatise by Sands [6] for a discussion of weak focussing, storage rings, etc.)

Because the muon lifetime is 64.4 μs, after 640 μs almost the entire beam has been lost to muon decay. The energy loss per turn from synchrotron radiation is given by [7]

$$\delta E = \frac{4\pi}{3}\frac{e^2}{R}\beta^3\gamma^4 = \frac{4\pi}{3}\frac{e^2}{\hbar c}\frac{\hbar c}{R}\beta^3\gamma^4$$

which with $\beta = 0.99942$, $\gamma = 29.3$ yields $6.2 \times 10^{-10}\ MeV/turn$, which means that after 10 muon lifetimes the beam energy loss totals $2.7 \times 10^{-6}\ MeV$, which is negligible. On the other hand, $e^{\pm}$ which happen to be in the $\pi^{\pm}$ or $\mu^{\pm}$ beam will quickly radiate their energy and spiral inward and be lost from the storage ring

Thus for pion injection without beam scraping, there is no need for RF power or any other dynamic element. (Direct muon injection is discussed below.) While it is true that the electrostatic quadrupoles which provide the vertical focussing are pulsed, the reason for the pulsing is to prevent charge build up and the resulting sparking, rather than having any beam-dynamic function. The only requirement is that the quadrupole high voltage is turned on before the beam arrives, and then is turned off after the muons have decayed. Of course, when the beam is scraped after injection into the ring, the quadrupoles do perform a dynamic function when they are energized asymmetrically to produce a temporary dipole component which kicks the beam.

In the absence of scraping, the beamline-storage-ring system is essentially a beamline-spectrometer system rather than a conventional storage ring. This point will be returned to in Chapter 22, where we discuss commissioning with beam and propose to use the storage ring magnet as a 180° spectrometer.

Even with scraping, where the quadrupole plates will be initially powered asymmetrically, they are turned on before the beam arrives, held constant for a hundred turns, and then brought up over fifty beam revolutions to their final symmetric voltages.

Only when the fast kicker is employed, do we encounter some of the complications of a traditional storage ring, since the kicker needs to be at flattop before the muon bunch enters and off 149 ns later when the beam returns for its next pass.

In the following sections we discuss a few general features common to both injection options, such as the phase space of the ring, etc., and then consider the specifics of the two injection schemes.

5.2. General Features of Muon Storage

In the traditional storage ring, great care is made to match the emittance of the beamline to the Twiss parameters, α, β, γ [8-9] of the storage ring.[†] This is not possible in the $(g-2)$ experiment. With pion injection the random $\pi \rightarrow \mu\nu$ kicks make matching more or less meaningless. For direct muon injection, beam matching would require that the inflector aperture be at least as large as the storage aperture (90 mm). This is not possible without compromising the magnetic field uniformity needed to perform the measurement of a_μ to the desired precision. Instead, the geometry of the inflector magnet was

[†] The Twiss parameters are also referred to as the Courant-Snyder parameters. [9] H. Wiedemann [4] uses Twiss parameters, Edwards and Syphers [5] refer to them as Courant-Snyder parameters, as do Ahn and Lysenko. [1] Sands, avoids the issue altogether.

chosen to roughly match the emittance of the incoming beam, except that an iron-free superconducting design was chosen, [10] rather than the pulsed device used at CERN. [11]

The storage ring is a weak focussing device, with an average field index $n = 0.135$. With the assumption that the vertical focussing is provided by a uniform quadrupole field spread around the storage ring, the horizontal and vertical betatron oscillations obey the equations

$$\ddot{x} + \omega_x^2 x = 0 \tag{5.2.1}$$

and

$$\ddot{y} + \omega_y^2 y = 0 \tag{5.2.2}$$

which are harmonic oscillator equations with the frequencies

$$\omega_x = \omega_c\sqrt{1-n} \qquad \omega_y = \omega_c\sqrt{n} \tag{5.2.3}$$

where ω_c is the cyclotron frequency. For a uniform quadrupole gradient, the field index n is defined by

$$n = -\frac{\rho}{B_{0y}}\frac{\partial B_y}{\partial x}$$

where ρ is the storage ring radius, B_{0y} is the vertical dipole magnetic field, $\partial B_y/\partial x$ is the magnetic gradient term which provides the quadrupole focussing. If both magnetic and electric gradient terms are present, the effective field index becomes [12]

$$n_{eff} = -\frac{\rho}{B_{0y}}\frac{\partial B_y}{\partial x} - \frac{\rho}{\beta B_{0y}}\frac{\partial E_x}{\partial x}$$

In E821, only the electric field term provides vertical focussing since the magnetic field will be the purest dipole field one can obtain. From Eq. (5.2.3) one sees that the requirement for stable orbits is $0 < n < 1$.

For our value of the field index, $n = 0.135$, the betatron wavelength is 1.08 turns horizontally and is 2.72 turns for the vertical motion. In reality, the quadrupoles do not cover the entire ring and the β function is not quite constant around the ring. The geometry is shown in Fig. 5.2.1 and the horizontal and vertical β functions are shown in Fig. 5.2.2. With finite quadrupoles, the restoring force will depend on arc length s as will the β-function, and the motion is only approximately simple harmonic.

The β function indicates the maximum transverse excursion the beam makes, since the maximum excursion is proportional to $\sqrt{\beta(s)}$. The smoother the β function is, the smoother the transverse beam envelope. The CERN ring had a two-fold symmetry, which produced $\sim$ 30% difference in β_{max} and β_{min} which should be compared with the few percent change present in the four-fold symmetry for this experiment. [13]

Figure 5.2.1: The geometry of the $(g-2)$ storage ring showing the vacuum chamber, the inflector, the quadrupoles and muon kicker locations.

Figure 5.2.2: The horizontal and vertical beta functions for the storage ring.

Because of the relatively flat β function, the four-fold symmetry permits rather large gaps between the quadrupoles for the inflector, kicker and beam monitors. The quadrupoles take up approximately a third of the ring, so that the muon decay electrons, on average will shower much less in the quadrupole material than they did in the CERN experiment.

The experiment has now been modelled using Monte Carlo techniques from the proton beam striking the production target through the decay electrons showering in the calorimeters. This is done in three separate stages. First, the pion yield from the AGS proton beam striking a production target is calculated as described in Chapter 6. The pions or muons produced by this calculation are then followed through the beam transport optics, through the inflector exit and input to the ring tracking calculation. Once a distribution of stored muons is obtained, it is input into g2-GEANT which simulates the muon decay and the subsequent history of the decay electrons. The issues relating to the muon decay electrons are discussed in Chapter 16. The issues which are related to the storage of muons are discussed below.

5.2.1. Resonances and Beam Losses

Resonances are always important in storage rings, but here we are only concerned with those which can influence the beam in the first millisecond. If a perturbation in the storage ring occurs in an azimuthal position such that it reinforces the vertical or horizontal betatron oscillations, *i.e.* a driving term of the correct frequency appears on the right hand side of Eq. (5.2.1) or Eq. (5.2.2), it can drive a resonance, thus causing the betatron amplitudes to become sufficiently large to cause particle losses from the storage ring. Such a perturbation usually appears as a field imperfection (multipole) at some point in the ring, which we will quantify below. It is also possible for a perturbation to couple the vertical and horizontal betatron motion, which will produce beating between the two. These phenomena are thoroughly discussed in the literature [14-17] and several $(g-2)$ technical notes have been written on the subject. [18-19]

First a few general statements taken from Ref. 14. An n-th order multipole field can drive all resonances up to n-th order with driving amplitudes that depend on the strength of the multipole, as well as its location within the lattice. All even perturbations, such as quadrupole, octupole, duodecapole, etc., lead to some tune shift or spread, and if the tune spread extends into the stop band (width) of a resonance of the ring, a loss of particles can result. On the other hand, *weak* odd perturbations, *e.g.* dipoles, sextupoles, or decapoles, etc. do not lead to a tune shift [20] and to a loss of particles.Certainly strong odd perturbations, *e.g.* sextupole, can indeed cause a tune shift and losses.

In a circular machine composed of one or more superperiods, the superperiodicity of the lattice is important. For a lattice composed of N superperiods, the Fourier expansion has nonzero coefficients for every N-th harmonic, and thus a high periodicity reduces the sensitivity to resonances. We shall see that this is an added benefit of the four-fold symmetry (superperiodicity) adopted for the $(g-2)$ ring.

Since the primary sensitivity to resonances comes from the non-ideal electric quadrupole field, we follow the discussion of Farley [18] to illustrate the problems which can be encountered from electric multipoles. We adopt the usual coordinate system (x, y, s) [4] where (x, y) are the horizontal and vertical directions transverse to the ideal orbit.

Consider the electric potential Φ given by

$$\Phi = (x + iy)^k \cos N\phi \tag{5.2.4}$$

where ϕ is the azimuthal angle around the storage ring. The potential Φ represents the N-th azimuthal harmonic of the $2k$-pole term. We consider one term of Φ of the form

$$^kC_m \; x^\ell \, (iy)^m \cos N\phi \tag{5.2.5}$$

where

$$^kC_m = \frac{k!}{\ell! m!} = \frac{k!}{(k-m)! m!}$$

is the binomial expansion coefficient of $(x + iy)^k$ and $k = \ell + m$.

The resulting vertical and horizontal electric fields are:

$$E_y = {}^kC_m x^\ell y^{m-1} \cos N\phi \tag{5.2.6a}$$

$$E_x = {}^kC_m x^{\ell-1} y^m \cos N\phi \tag{5.2.6b}$$

If the unperturbed betatron oscillations are described by Eq. (5.2.1) and Eq. (5.2.2) above, with the solutions

$$x = X_0 \cos \nu_x \phi$$

$$y = Y_0 \cos \nu_y \phi$$

one obtains from Eq. (5.2.6) the field values

$$E_x = {}^kC_m X_0^{(\ell-1)} Y_0^m \cos^{(\ell-1)} \nu_x\phi \cos^m \nu_y\phi \cos N\phi \tag{5.2.7a}$$

$$E_y = {}^kC_m X_0^\ell Y_0^{(m-1)} \cos^\ell \nu_x\phi \cos^{(m-1)} \nu_y\phi \cos N\phi \tag{5.2.7b}$$

which, following Farley [18] can be expanded in terms of products of simple sines and cosines;† *e.g.* the leading term for Eq. (5.2.7b) is

$$2^{(-k-1)} \cos\left[\ell\nu_x \pm (m-1)\,\nu_y \pm N\right]\phi. \tag{5.2.8}$$

† Recall that $\cos^\ell(x) \sim \cos(\ell x) + ...$

Thus, if the frequency of the driving term given by Eq. (5.2.8) equals the betatron frequency ν_y, i.e.

$$\ell\nu_x \pm (m-1)\,\nu_y \pm N = \pm\nu_y,$$

then the vertical electric field contains a term which will drive the vertical betatron oscillations at resonance and can be responsible for particle losses. The same argument holds for the horizontal motion.

The general resonance condition can be stated as:

$$\ell\nu_x + m\nu_y = jN \tag{5.2.9}$$

where $\pm\ell$, $\pm m$, and j are integers and N is the superperiodicity of the machine (4 in our case). The order of the resonance is given by $|\ell| + |m|$. One should note that when ℓ and m have the same sign the motion may be unbounded. [5]

One can display this information graphically in the ν_x, ν_y (tune) plane, showing both the resonance lines described by Eq. (5.2.9) and and the (idealized) operating line given by $\nu_x^2 + \nu_y^2 = 1$. Although with discrete rather than continuous quadrupoles, $\beta = \beta(s)$ and the operating line changes slightly, this discussion still gives a good guide for the the resonance behavior.

In terms of the field index n, $(\nu_x, \nu_y) = (\sqrt{1-n}, \sqrt{n})$, which for the field index under consideration, $n = 0.135$ is $(0.93, 0.37)$. In Fig. 5.2.3 we reproduce the resonance diagram taken from Combley and Picasso, [16] and in Fig. 5.2.4 we reproduce a blowup of the tune plane from Ref. 2.

The quadrupole design adopted for E821 employs flat electrodes, rather than hyperbolic ones. This design was adopted because it was felt that with electrodes which have a radius of curvature ($\sim 7112\ mm$), it would be easier and cheaper to fabricate, and to control the tolerances on the electrodes, if their profile was flat in the transverse plane, rather than hyperbolic (See Chapter 11). In addition to the desired quadrupole field, such a geometry produces 12-, 20-, 28-, etc. pole fields. [2]

The 12 pole is eliminated by choosing the correct relationship between between the plate separation and the plate width. [21] The maximum allowable 20 pole content was estimated by Farley [18] to be 5% of the quadrupole term.The flat quadrupoles produce a 20-pole/4-pole ratio of $b_{10}/b_2 \simeq 1.8\%$, which is well within this specification. The tracking calculations discussed below in §5.2.3 included the correct vertical and horizontal focussing effects of the discrete quadrupoles, as well as the twenty-pole term. The losses were well within what is acceptable. The multipoles higher than 20 have not yet been included in the tracking calculations.

Resonances can also be driven by one of a kind or random perturbations at some point in azimuth. A disturbance such as the superconducting inflector fringe field, or

Figure 5.2.3: Resonance lines up to fifth-order in the (ν_x, ν_y) plane taken from Ref. 16. They use the notation (Q_H, Q_V) rather than (ν_x, ν_y). The intersection of the working line $\nu_x^2 + \nu_y^2 = 1$ with each of the resonance lines is indicated by a $\bullet$, and the working point of $n = 0.135$ is also indicated by a $\bullet$.

the gross misalignment of one quadrupole plate, will generate many multipoles and has a superperiodicity of $N = 1$. This type of disturbance presents a double threat to the stability of the beam since it has the potential to drive many different resonances. Fortunately, it is likely that the inflector fringe field can be completely shielded by a passive superconducting shield (see Chapter 10), and the random errors one should encounter from tolerances on

Figure 5.2.4: A small region of the tune plane around the operating point. (Taken from Ref. 2).

the placement of the quadrupole plates should not be serious. The tolerances have been discussed by Semertzidis. [22] Random errors at the level of the stated tolerances on the

positioning of the quadrupole plates have already been included in the tracking calculations described below.

We close this section with a few comments on improvements which E821 will make over the third CERN experiment, which had a superperiodicity of $N = 2$. The late term losses at CERN after scraping were 0.1% per lifetime. In Bailey et al. [11] it is stated:

"These late losses were possibly due to the second harmonic of the octupole component of the field. For non-ideal ratios of the electrode voltages there was an octupole component in the electric field which had a strong second harmonic due to the azimuthal arrangement of the electrodes..."

The resonance referred to is the $\nu_x + 3\nu_y = 2$ line in Fig. 5.2.3 at $n = 0.1261$. There is also the decapole resonance $3\nu_x - 2\nu_y = 2$ at $n = 0.1479$. With the four-fold symmetry of E821, these resonance terms will not be serious. The closest 5-th order resonance with four-fold azimuthal symmetry is $4\nu_x + \nu_y = 4$ at $n = 0.2215$, but this driving term should be absent in the electric field. Several 10-th order resonances are shown in Fig. 5.2.4, the most serious being the $6\nu_x - 4\nu_y = 4$ resonance which occurs at $n = 0.1479$, which was discussed above.

In summary, the superperiodicity of $N = 4$ in E821 has three major advantages over the $N = 2$ geometry at CERN:

1.) The beta function variation over the entire azimuth is reduced from 30% to a few percent;
2.) The fraction of the ring covered by the electrostatic quadrupoles is about 43% instead of 80%, so electron showering in the electrodes is reduced;
3.) The closest low order resonance with $N = 4$ symmetry is at $n = 0.2215$ driven by a decapole term, which is absent from a perfectly symmetric quadrupole. This n value is 60% higher than the value of $n = 0.139$ which is sometimes mentioned, and 64% higher than $n = 0.135$ which has been used in the tracking calculations.

In addition, the magnetic field uniformity will be 1 *ppm* integrated over azimuth compared with 20 *ppm* at CERN so the magnetic multipoles higher than dipole will be substantially reduced from those present in the CERN ring. The situation regarding resonances is clearly improved over the CERN experiment.

5.2.2. The Muon Distribution and the Average Field

In order to compute the average magnetic field [23] which enters into the the expression for a_μ, (see Chapter 2) it is necessary to compute the average field over the storage volume. By "the average field", we mean the integral of the field, weighted by the muon population, over the storage region. If we write the field in the usual multipole expansion

$$B(r,\theta) = \sum_{n=0}^{\infty} r^n \left[c_n \cos(n\theta) + s_n \sin(n\theta)\right] \tag{5.2.10}$$

where (r,θ) are the polar coordinates of the 45 mm radius muon storage region centered at a ring diameter of $\rho = 7112$ mm. This represents a transverse slice of the circular storage region for one value of the azimuth ϕ. This notation is consistent with the coordinate system used in §5.2.1

The muon distribution, $M(r,\theta)$ can be expanded in a similar expansion

$$M(r,\theta) = \sum_{m} \left[\gamma_m(r)\cos(m\theta) + \sigma_m(r)\sin(m\theta)\right] \tag{5.2.11}$$

where the coefficients γ and σ are given by

$$\gamma_0(r) = \frac{1}{2\pi}\int_0^{2\pi} M(r,\theta)\, d\theta \tag{5.2.12a}$$

$$\gamma_m(r) = \frac{1}{\pi}\int_0^{2\pi} M(r,\theta)\cos(m\theta)\, d\theta \tag{5.2.12b}$$

$$\sigma_m(r) = \frac{1}{\pi}\int_0^{2\pi} M(r,\theta)\sin(m\theta)\, d\theta \tag{5.2.12c}$$

To find the mean field we multiply Eq. (5.2.10) by Eq. (5.2.11) and integrate. This gives

$$< B >= c_0 + \frac{1}{I_0}\sum_{1}^{\infty}\left[c_n I_n + s_n J_n\right] \tag{5.2.13}$$

where

$$I_0 = \int_0^R \int_0^{2\pi} M(r,\theta)\, r\, dr\, d\theta,$$

$$I_n = \int_0^R \int_0^{2\pi} M(r,\theta)\cos(n\theta)\, r\, dr\, d\theta,$$

and

$$J_n = \int_0^R \int_0^{2\pi} M(r,\theta)\sin(n\theta)\, r\, dr\, d\theta$$

where R is the storage aperture radius of 45 mm. Note that for a symmetric distribution all J_n are zero.

Thus the contribution to the average field seen by the muon sample is given by the multipole coefficients c_n and s_n multiplied by the corresponding moments of the muon distribution, I_n and J_n. We should note at this juncture, that the choice of a circular aperture was made based on the observation [23] that the sensitivity to higher order multipoles in the magnetic field is greatly reduced with a circular, rather than a rectangular aperture. In addition, the circular aperture has the added benefit that both the electric field and pitch corrections for a circular aperture are decreased, relative to a rectangular aperture (see Chapter 4).

Both the magnetic field $B(r,\theta)$ and the muon distribution $M(r,\theta)$ depend on azimuth (ϕ) as well as (r,θ). Because of the weak focussing nature of the storage ring, the muon distribution is unlikely to change in a complicated way as a function of azimuth, since the β function changes are minimal going around the ring. In fact, because of the weak focussing nature of the ring, in quoting the 1 *ppm* magnetic field uniformity in the error discussion it is implied that this is a uniformity integrated over azimuth.

Much experimental and theoretical work must still be done to develop the prescription of how to combine the information from a field map with information on the muon distribution in the ring in order to determine the average field which appears in Eq. (2.1.7) or Eq. (2.1.8). In fact, the required muon distribution $M(r,\theta)$, must apply to those muons which contribute to the counting data. Therefore it must include corrections for the counting probability as a function of muon radius and electron energy as well.

5.2.3. Particle Tracking Studies and Beam Scraping

As discussed in Chapter 4, muons lost from the storage ring thorough mechanisms other than decay can contribute to the systematic error in $(g-2)$. In the CERN experiment the loss rate per lifetime was about 1%. By scraping the beam, this was reduced to 0.1%. It is clear from the discussion in the previous chapter that it is necessary to improve on this loss rate for the new experiment.

In order to model the ring, new Monte Carlo tracking programs have been developed which explicitly include both electric and magnetic fields. [3,2] The equations of motion in the form proposed by Berz [24] were employed in these calculations. More recently, calculations have been carried out both at Brookhaven [25] and at Boston. [26]

The current ring parameters are:

$\rho = 7.112m$ (Radius of equilibrium orbit)
$p_0 = 3.0944GeV$ (Design momentum)
$B = 3.3356 * p_0/(\rho) = 1.4513T$

The following effects have been taken into account in the tracking program:

1. Multiple scattering in all material
2. Beam loss in entering through the side of Q1
3. The 20-pole content in the electric field plus other random multipoles in the electric and magnetic fields.
4. End effects at the electrostatic quadrupoles
5. Random misalignments in the collimators and quadrupoles to the design specifications.

Two methods of scraping the beam have been proposed: 1. Kicking the beam sideways and vertically as was done at CERN, and 2. Changing the ring symmetry from four-fold to two-fold during scraping, thus blowing the beam up both horizontally and vertically. [27]

After detailed studies [26,28] it was determined that the long term losses were minimized by employing method 1. above.

Although a $(g-2)$ technical note has not yet been written, Mane [29] has reported promising results on scraping the beam.

Nine collimators were placed around the ring. In his calculation Mane used aluminium ring shaped collimators, 15 mm thick to the beam, with an inner radius of 45 mm and outer radius of 55 mm placed in Q2, Q3, and Q4 as shown in Fig. 5.2.1 at Q2 and labelled by "C". For mechanical reasons, in the experiment we will use copper collimators of the equivalent number of radiation lengths. This higher Z collimator should improve things further since it has been argued that multiple scattering is the most efficient process for collimating the beam. [30]

The collimator aperture is chosen to be the desired storage region radius, rather than larger, to minimize the kick needed to scrape the beam on the collimators. This improves the injection efficiency, since it has the minimal impact on the β function of the ring.

A variation of the scheme employed at CERN, of powering opposite plates in the quadrupoles with different voltages was employed in the calculation. Horizontally Mane used a voltage difference between the plates of 0.07 (7%) during the scraping period. Unlike CERN, the voltage differences were held constant for 100 turns, and then brought up to the (symmetric) operating voltages over the next 50 turns.

5.3. Pion Injection

In the pion injection option, pions of momentum slightly higher than the magic momentum are brought into the storage ring. As the pions cross the storage region, some of them decay, and some of the decay muons have a (vector) momentum compatible with the transverse and momentum acceptance of the storage ring. The Monte Carlo calculation obtained a capture efficiency of 26 *ppm* for pion injection and furthermore, the calculated loss rate per lifetime obtained for pion injection was 2×10^{-5}. This loss rate estimate was based on $\sim$2 losses from the stored sample. This loss rate is considerably better than the 0.1% obtained at CERN, and should eliminate any uncertainty in the $(g-2)$ value from muon losses. We note that with the scraping scheme employed here one would expect a cleaner beam. At CERN, there was one adjustable rectangular collimator in the storage ring, plus the quadrupoles to scrape the beam on. We have 9 collimators, and in principle an additional three semicircular collimators could be added in Q1 if necessary. (Recall that the inflected beam must enter through one plate of Q1, and a full circular collimator would remove the incident beam.)

The number of stored muons has been presented in the previous chapter, along with the experimental statistical error for various running scenarios.

This injection efficiency is in agreement with the crude calculation of Morse. [31] Furthermore, the calculations of Benedict [26] obtained capture efficiencies in agreement with Mane in the scraping scenario described in Note 145, [27] which increases one's confidence in these calculations.

Because of the diffuse nature of the kick provided by pion decay, it being roughly equally probable throughout the region where the pion beam passes across the storage region, the phase space of the storage ring is uniformly filled.

There are two unfortunate side effects of pion injection: the low efficiency of actually having a muon stored for a given pion injected, and the large background (generally referred to as "the flash") associated with pions, which do not decay in the ring, hitting various obstructions and causing a large background for the electron detectors immediately after injection.

5.4. Muon Injection

Direct muon injection into the storage ring is far more efficient in producing stored muons, and the hadronic background associated with many pions interacting with the storage ring material is absent. An efficiency of muon storage of 7% was obtained in the calculations for muon injection. The loss rate per muon lifetime was 4×10^{-6}, almost an order of magnitude better than that obtained in the pion injection calculations. Furthermore, although the number of pions per muon could be as large as 2:1, this is orders of magnitude fewer pions (which can cause a "flash") than will be obtained with the pion injection option.

Because of the inflector acceptance, the phase space of the storage ring is not filled uniformly in muon injection, as is shown in Fig. 5.4.1. This should not present a problem to the measurement, since the muon distribution will be monitored on a pulse to pulse basis, as well as averaged over the fills that contribute to the data.

Figure 5.4.1: The vertical and horizontal phase space from muon injection. The circle shows the acceptance of the ring, and the scatter plot shows the actual particle distribution. The particles outside of the circle will be lost on the collimators during the scraping procedure.

5.5. References

1. Hyo E. Ahn and Walter P. Lysenko, *The Muon Injection Option*, *Muon g-2 Note No. 46, February 1989.*
2. S.R. Mane, *Particle Tracking with Flat Quadrupole Electrodes*, *Muon g-2 Note No. 107*, March 1992.
3. S. Mane, *Electrostatic Quadrupole Design*, *Muon g-2 Note No. 103*, February 1992; *Solutions of Laplace's Equation and Multipole Expansions with a Curved Longitudinal Axis*, *Muon g-2 Note No. 91* November 1991; *Particle Tracking of Muons: Tests of the Programs*, *Muon g-2 Note No. 88*, August 1991.
4. H. Wiedemann in *Particle Accelerator Physics, Volume 1*, Springer-Verlag 1993.
5. D.A. Edwards and M.J. Syphers, *An Introduction to the Physics of High Energy Accelerators*, J. Wiley & Sons, Inc. 1993.
6. M. Sands, *The Physics of Electron Storage Rings*, SLAC–121, 1970.
7. Particle Data Group, Phys. Rev. 45D, III.44 (1992).
8. R.Q. Twiss and N.H. Frank, Rev. Sci. Instr. 20, 1 (1949).
9. E. Courant and H. Snyder, Ann. Phys. 3, 1 (1959).
10. F. Krienen, D. Loomba and W. Meng, Nucl. Inst. and Meth. A238, 5 (1989) and *Development of Non-Ferrous Superconducting Magnets*, *Muon g-2 Note No. 63*, November 1990, and W. Meng, Ph.D. Thesis *Non-Ferrous Superconducting Magnets* Boston University, December 1990.
11. J. Bailey et al. Nucl. Phys. B150, 1 (1979).
12. F. Combley and E. Picasso, *op. cit.*, p. 43.
13. Y.Y. Lee, *Lattice and Injection Kicker Considerations for the g-2 Ring*, *Muon g-2 Note No. 77*, April 1991.
14. H. Wiedemann, *op. cit.*, pages 248 - 256.
15. Edwards and Syphers *op. cit.*,Chapter 4 and pages 166-170.
16. F. Combley and E. Picasso, *The Muon (g-2) Precession Experiments: Past, Present and Future*, Phys. Reports C14, 1 (1974).
17. W. P. Lysenko, *Nonlinear Betatron Oscillations*,Particle Accelerators, 5, 1 (1972), and Ph.D. thesis, Yale University 1972.
18. F.J.M. Farley *Some Calculations on resonance excitation in the g-2 ring*, *Muon g-2 Note No. 106 (Revised)* May 1992.
19. William Morse and Francis Farley, *Magnetic Resonances*, *Muon g-2 note No. 116*, June 1992.

20. H. Wiedeman, *op. cit.*, p. 252.

21. The elimination of the 12 pole by the appropriate choice of geometry, while obvious now, was first suggested by P. Thompson.

22. Y. K. Semertzidis, *Quadrupole Tolerances, Rails and More*, *Muon g-2 Note No. 149*, April 1993.

23. F.J.M. Farley and W.P. Lysenko, *The Muon Distribution and the Average Field*, *Muon g-2 Note No. 23*, September 1985.

24. Nucl. Inst. Meth., A298, 473 (1990).

25. S. Mane has completely revised his version ofthe code to run faster. The current code has not yet been documented..

26. Eric Benedict and B. Lee Roberts,*Tracking Studies – Injection Efficiency and Scraping Studies I:*, *Muon g-2 Note No. 183*, January 1994.

27. S. Mane, *A Study in Scraping*, *Muon g-2 Note 145*, March 1993.

28. S. Mane, Private Communications at various Beam Dynamics Team Meetings.

29. S. Mane, Beam Dynamics Team meeting 10 February 1994. These results are summarized in the *Semester Report*, *Muon g-2 Note No. 199*, June 1994.

30. F.J.M. Farley, *Best Material for Beam Defining Aperture Stops in g-2 Ring*, *Muon g-2 Note No. 170*, September 1993.

31. W.M. Morse, *Muon Capture Efficiency for Pion Injection*, *Muon g-2 Note 146*, March 1993.

Chapter 6.
Pion/Muon Beam and Monitoring

Revised February 1995

6.1. Introduction

In the basic injection scheme used in the CERN experiment, [1] a pion beam was formed and directed parallel to, but just outside of, the muon storage region by means of a pulsed inflector. As the pions executed their first oscillations about their respective closed orbits in the ring, they crossed the storage region and a fraction of them decayed and emitted muons within the transverse and momentum acceptances of the ring. The remaining pions were lost on the focussing electrodes or on the inflector structure after one turn, and produced the "flash" following injection which presented such a challenge to the muon decay electron detectors.

We will use this same method for the initial phases of the experiment, employing a DC superconducting inflector as described in Chapter 10.

An alternative procedure, which we also plan to use, is to allow the pions to decay into muons in a long transport channel which will retain a fraction of the muons. After separating the residual pions by means of a tight momentum selection, the muons will be injected through the inflector into the storage ring and be kicked onto a stable orbit by a fast kicker. This technique of direct muon injection has two benefits:

i) the number of stored muons per fill is increased by an order of magnitude over pion injection

ii) the flash following injection, which is caused by pions which do not produce stored muons, is greatly reduced.

The placement of the storage ring in the former 80″ Bubble Chamber building makes it possible to construct a secondary beam channel which can be utilized for either of these injection methods.

6.2. Proton Extraction and Targeting

During each AGS pulse, it is proposed that 1 to 8 (or 12 depending on the mode of AGS operation) proton bunches be extracted by firing a one-bunch kicker magnet at intervals of about 40 msec. Within the 40 msec intervals, the precession of the muons produced by one proton bunch is measured by the electron counters for a time interval of 10 muon lifetimes, or about 640 μs. In principle, the interval between injections could be much less than 40 ms, but then recharging the kicker's energy storage capacitors becomes more difficult. Hence, a new multi-pulsing kicker power supply has been designed by the AGS Department.

The H10 straight section in the AGS ring has been chosen as the point of ejection of the proton bunches. This is where extraction to the existing Fast External Beam to the neutrino experiment target is accomplished, and where transfer of Heavy Ions to the RHIC will begin. Thus, duplication of much extraction equipment will be avoided. No changes need be made which will compromise normal operation of these other transport lines.

Fig. 6.2.1 illustrates the region of the AGS complex where, after exiting from the AGS at H10, the primary proton beam is carried around the 4 degree bend in the U line to the dipoles VD3,VD4 where it is deflected about 3.0 degrees westward. This allows it to exit into the new targeting area which is under construction. The beam is carried to and then focussed on the "V" target by VQ9- VQ12. This target station will have standard instrumentation for proton beam monitoring, including radiation monitors to monitor beam losses at crucial points in the proton transport line.

The target proper must be designed to withstand high peak and high average beam heating for intensities up to 6×10^{13} protons per AGS pulse. It is not critical that the pion source be sharply defined vertically. Hence, a low density heat sink, such as aluminum or water, could be in direct contact (vertically) with a heavy target such as platinum or copper, letting the incident beam size largely determine the vertical source size. The horizontal target width should be well defined for good momentum resolution.

The list of beamline elements needed for the "V" proton beamline is given in Table 6.2.1.

Figure 6.2.1: Proton Extraction at H10 and Transport to the "V" Target

Table 6.2.1: Equipment required for proton transport from the U-line to the "V" target. The key to the abbreviations is: Q = Quadrupole, D = Dipole, P = Pitching Dipole, hs = Horizontal steering dipole, vs = Vertical steering dipole, SWIC = Segmented Wire Ionization Chamber for beam profile measurement, IONCH = Ionization Chamber for beam pion/muon intensity measurement, SEC = Secondary Emission Chamber for proton intensity measurement.

Magnet	Type	B(kG)/G(kG/in)	$L_{eff}(in)$	I (kA)	R ($m\omega$)	V (V)	P (kW)
VD3	12C100	9.6400	102.00	1.25	21.0	26.	33.
VD4	12C100	9.6400	102.00	1.25	21.0	26.	33.
vs1	4x6d24	1.2000	28.00	-	-	-	-
VQ9	4Q26.5	2.8000	28.5	.310	93.0	28.	9.
hs1	4x6d24	1.2000	28.00	-	-	-	-
VQ10	5Q36	3.1390	37.50	0.7440	97.5	72.5	54.
VQ11	5Q36	3.1390	37.50	0.7440	97.5	72.5	54.
VQ12	N3Q36	7.9130	37.50	1.7820	12.0	21.4	38.
vs2	4x6d24	1.2000	28.00	-	-	-	-
SEC		-	-	-	-	-	-
SWIC	1mm	-	-	-	-	-	-
TARG	Cu	3 mm dia	150 mm				
				Total	"V" Line	Power	221.

6.3. The Secondary Pion and Muon Beam

The secondary beamline is designed with a 72 m straight section so that a substantial fraction of the pions can decay to muons, thus providing either pions or muons to inject into the storage ring.

6.3.1. Pion Collection and Momentum Definition

The secondary beam layout is included in Fig. 6.3.1 and the beam envelopes and momentum dispersion are shown in Fig. 6.3.2. Quadrupoles V1Q1 and V1Q2 collect pions within a solid angle of 1.5 msr (32 mrad horizontal $\times$ 60 mrad vertical) and with accepted emittances of $42 \times 10^{-6}\pi\ m$ and $56 \times 10^{-6}\pi\ m$ respectively. The pions are focused on the momentum defining apertures near V1Q4-V1Q5, where the dispersion due to V1D1 and D2 is $0.42''/percent$. The desired pion momentum band is about 2.0% base width. Dispersion in the selected pion beam is then removed by the action of V1Q3-V1Q6 and V1D3 and D4. Primary protons bend only 2.1 degrees in V1D1, miss D2 and are subsequently absorbed in the beam stop.

Figure 6.3.1: The secondary π/μ Beam to the Muon Storage Ring

Figure 6.3.2: Envelopes and Dispersion of the π/μ Beam

Table 6.3.1: Equipment for the "V1" line. The key to the abbreviations is: Q = Quadrupole, D = Dipole, P = Pitching Dipole, hs = Horizontal steering dipole, vs = Vertical steering dipole, SWIC = Segmented Wire Ionization Chamber for beam profile measurement, IONCH = Ionization Chamber for beam pion/muon intensity measurement, SEC = Secondary Emission Chamber for proton intensity measurement.

Mag	Type	B(kG)/G(kG/in)	L_{eff}(in)	I (kA)	R ($m\omega$)	V (V)	P (kW)
V1Q1	8Q48	3.3578	52.00	2.7790	35.0	97.	270.
V1Q2	8Q32	2.6384	36.00	2.1180	25.6	54.	115.
V1D1	6x18D72	14.8940	75.00	0.8500	46.0	72.	114.
V1D2	6x18C72	14.8610	75.00	1.3000	35.0	46.	61.
V1Q3	4Q16	3.1036	18.00	0.2799	183.0	51.	14.
V1Q4	4Q16	3.4065	18.00	0.3072	183.0	56.	17.
V1Q5	4Q16	3.4065	18.00	0.3072	183.0	56.	17.
V1Q6	4Q16	3.1036	18.00	0.2299	183.0	51.	14.
V1D3	3x18D72	14.8610	75.00	0.9120	46.0	33.	24.
V1D4	3x18D72	16.1320	75.00	0.9900	46.0	36.	30.
V1Q7	8Q24	2.0263	28.00	1.5918	21.4	34.	54.
V1Q8	8Q24	2.1306	28.00	1.6759	21.4	35.	60.
vs1	4d16	0.6100	16.00	0.0300	500.	15.	.5
V1Q9	4Q24	1.0288	26.00	0.1306	30.4	4.	.5
V1Q10	4Q24	1.2356	26.00	0.1568	30.4	4.	.7
hs1	4d16	0.6100	16.00	0.0300	500.	15.	.5
IONCH1		-	-	-	-	-	-
SWIC1	3mm	-	-	-	-	-	-
V1Q11	4Q24	0.9658	26.00	0.1226	30.4	3.	.5
V1P1	5D22	4.9859	36.00	0.6760	40.0	27.	18.
SWIC2	3mm	-	-	-	-	-	-
V1Q12	8Q24	0.9658	26.00	0.1226	30.4	3.	.5
hs2	4d16	0.6100	16.00	0.0300	500.	15.	.5
SWIC3	3mm	-	-	-	-	-	-
V1Q13	4Q24	0.9658	26.00	0.1226	30.4	3.	.5
vs2	4d16	0.6100	16.00	0.0300	500.	15.	.5
SWIC4	3mm	-	-	-	-	-	-
V1Q14	4Q24	0.9658	26.00	0.1226	30.4	3.	.5
V1Q15	4Q24	0.9658	26.00	0.1226	30.4	3.	.5
V1Q16	4Q24	0.9658	26.00	0.1226	30.4	3.	.5
V1Q17	4Q24	0.9658	26.00	0.1226	30.4	3.	.5
vs3	4d16	0.6100	16.00	0.0300	500.	15.	.5
V1Q18	4Q24	0.9658	26.00	0.1226	30.4	3.	.5
hs3	4d16	0.6100	16.00	0.0300	500.	15.	.5
V1Q19	4Q24	0.9658	26.00	0.1226	30.4	3.	.5
vs6	4d16	0.6100	16.00	0.0300	500.	15.	.5

Table 6.3.2: Table 6.3.1 continued

Magnet	Type	B(kG)/G(kG/in)	$L_{eff}(in)$	I (kA)	R ($m\omega$)	V (V)	P (kW)
V1P2	5D22	4.9859	36.00	0.6760	40.0	27.	18.
SWIC5	3mm	-	-	-	-	-	-
V1Q20	4Q24	0.4829	26.00	0.0613	30.4	1.	.1
V1D5	3x18D72	20.1635	75.00	1.2000	45.8	55.	66.
V1Q21	4Q24	0.8668	26.00	0.1100	30.4	3.	.4
V1Q22	4Q24	1.2184	26.00	0.1546	30.4	4.	.7
vs4	4d16	0.6100	16.00	0.0300	500.	15.	.5
hs4	4d16	0.6100	16.00	0.0300	500.	15.	.5
IONCH2		-	-	-	-	-	-
V1Q23	4Q24	1.4267	26.00	0.1811	30.4	5.	1.
V1Q24	4Q24	1.2184	26.00	0.1546	30.4	4.	.7
V1Q25	4Q24	0.8668	26.00	0.1100	30.4	3.	.4
V1D6	3x18D72	20.1635	75.00	1.2000	45.8	55.	66.
vs5	4d16	0.6100	16.00	0.0300	500.	15.	.5
SWIC6	3mm	-	-	-	-	-	-
V1Q26	4Q24	0.7105	26.00	0.0902	30.4	2.	.2
V1Q27	4Q24	0.3104	26.00	0.0394	30.4	1.	.1
vs6	4d16	0.6100	16.00	0.0300	500.	15.	.5
V1Q28	8Q24	2.5596	28.00	2.0322	21.4	43.	88.
V1Q29	8Q24	2.8110	28.00	2.2549	21.4	48.	109.
SWIC7	3mm	-	-	-	-	-	-
IONCH3		-	-	-	-	-	-
hs5	4d16	0.6100	16.00	0.0300	500.	15.	.5
				Total	"V1" Line	Power	1170.

A list of the necessary beamline elements for the "V1" beamline is given in Table 6.3.1 and Table 6.3.2.

6.3.2. π/μ Transport Channel

Quadrupoles V1Q7, V1Q8, V1Q9 and V1Q10 then match the pion emittance to a regular FODO transport channel composed of V1Q10 through V1Q20. The phase advance per cell is 90 degrees.

The floor of the 80″ Bubble Chamber building is 7 feet below grade, which will put the plane of the muon ring at or about 2 feet below grade. The necessary 6.9 foot drop from the AGS plane can be accomplished by inserting a 2.41 degree downward pitching magnet near V1Q12 and recovering to the horizontal with an upward 2.41 degree pitch near V1Q20. The 360 degree phase shift between these two vertical deflections will act to remove any residual vertical momentum dispersion caused by this translation of level. The peak

vertical momentum dispersion between the pitching magnets is only about $0.15''/percent$ and leads to virtually no loss of beam.

The beam transport elements will be housed in a combination of a concrete block house, portable buildings, corrugated steel pipe tunnels, and poured concrete "cellars". The latter two are now completed.

6.3.3. π/μ Momentum Spectrometer

Dipoles V1D5 and V1D6, bending 21 degrees each, and the quadrupoles V1Q21-V1Q25 form an adispersive momentum spectrometer. When the pion injection scheme is used, then V1D1-V1D6 are simply set to pass pions slightly above p_μ (by about 0.5%) through to the ring. For direct muon injection, the residual pions in a 2.0% band centered at 3.152 GeV/c are separated from the useable muon band centered 1.8% lower at the magic momentum p_μ=3.094 GeV/c.

At this momentum, the pion decay length is 174 m. As a pion beam, the effective length is from the target to the tangent point at the storage ring, or 122 meters, so the fraction of pions which survive is 0.496. As a muon forming beam, the effective length is from the pion selecting slit at 8.7 m to the pion rejection slit at 97.5 m. Thus, the fraction of the original pions at the target, which decay within this region, is $[e^{-8.7/174} - e^{-97.5/174}] = 0.380$.

6.4. Matching Through the Inflector to the Ring

Table 6.4.1: Pion and muon fluxes at the inflector exit.

Particle	# per TP on Target	Mean Momentum	Mean Polarization
π^+	1.8×10^7	$3.11 \pm 0.32\%$	–
μ^+	7.1×10^4	$3.0944 \pm 0.43\%$	0.918 ± 0.026

Quadrupoles V1Q26-V1Q29 match the transverse beam emittances to those which will allow passage through the hole in the back leg of the ring magnet, through the strong vertically focusing storage ring fringing field, the inflector, and into the storage volume. The requirements for pion and muon injection are very similar, and so these four quadrupoles will provide enough flexibility. Note that, because the inflector aperture is immersed in the storage ring but is necessarily substantially smaller than the storage aperture, one cannot match the incoming beam to the ring's Twiss parameters without sacrificing intensity.

Figure 6.4.1: The geometry of the inflector exit and the muon storage region. The storage volume is the 90 mm diameter circle, and the muon beam enters through the "D" shaped beam channel to the left (larger radius side) of the storage region. The vacuum chamber and cryostat all have to fit within the pole piece profile.

This situation is quite different from the conventional storage ring where great care is taken to match the beamline, which feeds the ring, to the acceptance of the ring. In the conventional storage ring the beam is kept on orbit by a number of discrete elements with drift spaces in between. In a drift space it is quite simple to introduce an external beamline of the same aperture as the storage ring. However, this technique is counter to the demands of this experiment, *viz.* that the storage ring field be as uniform a dipole field as it is possible to produce.

We have gone to great trouble and expense to design and construct a monolithic "C" magnet, with no gaps in the yoke or pole pieces. The geometry of the inflector exit is shown in Fig. 6.4.1. A break in the storage ring magnet at the injection point would destroy the ability to perform the precision measurement for which this ring is designed. Thus, the conventional approach of phase space matching is not an acceptable solution for this experiment. Instead, we must take the design as shown in Fig. 6.4.1 and make the best of it.

As was discussed in Chapter 4, the instantaneous detector counting rates following muon injection push the limits of detector technology, so the lost beam could not be used anyway. While it is true that the intensity of stored muons from pion injection is an order of magnitude lower than with muon injection, because of the pion induced flash it is not clear that the backgrounds which would be associated with an increase of pion flux would be manageable, even if more flux were available.

Particle fluxes have been calculated by a Monte Carlo beam tracing program which uses the empirical Sanford-Wang formula [2] for pion production at the target. The fluxes obtained at the inflector exit are given in Table 6.4.1, assuming that the beam travels through vacuum from the production target through the inflector, except for scattering in 6 SWIC/Ion-Chamber units spaced along the pion decay channel and in the superconducting coil material at each end of the inflector.

6.5. Vernier Steering and Diagnostic Instrumentation

The customary primary proton beam control and monitoring will be required in the "V" Line and at the "V" target, including the usual radiation monitors in the proton beam tunnel.

A total of about 11 small (5 mrad) vernier steering magnets will be needed along the pion/muon line in order to ensure good beam alignment. Three of them will be wanted in the final matching section, two vertical pitch verniers and one horizontal yaw vernier (in addition to V1D6), for accurate steering through the inflector and onto the ring tangent.

About 6 SWICs (Segmented Wire Ionization Chambers) will be provided to check beam profiles and centroids for proper channel matching and for injection matching just before entry into the ring's back-leg. Three ionization chambers will be needed for monitoring the beam intensity, one at V1Q9 just outside the primary shielding, one preceding the final momentum analyzing slit, and one just before entry into the storage ring. In addition, two scintillating fiber hodoscopes will be available between V1D6 and the ring to continuously monitor the low intensity muon beam not detectable by the SWICs.

6.6. Summary

Table 6.6.1: Summary of Beamline Elements in "V" and "V1" Lines

Element	"V" Total	"V1" Total
Quadrupoles	4	29
Dipoles	2	6
Horizontal Steering	1	5
Vertical Steering	2	6
Pitching Dipole		2
SWIC	1	7
SEC	1	3
Ion Chambers		3

The fast proton bunch extraction, the production target, and the secondary beam transport line is fairly standard for the AGS. The H10 extraction point will be able to serve *(g-2)*, RHIC or a neutrino experiment without conflicts. A summary of the beamline elements needed is given in Table 6.6.1.

6.7. References

1. J. Bailey et al., *Final Report on the CERN Muon Storage Ring Including the Anomalous Magnetic Moment and the Electric Dipole Moment of the Muon, and a Direct Test of Relativistic Time Dilation*, Nuclear Physics B150 (1979) pp 1-75.

2. J.R. Sanford and C.L. Wang, *Empirical Formulas for Particle Production in P-Be Collisions Between 10 and 35 GeV/c*, AGS Internal Report JRS/CLW-1 March 1967.

Chapter 7.
The Experimental Hall

Revised March 1994

7.1. Introduction and Overview

The former $80''$ bubble chamber building will house the muon $(g-2)$ storage ring. Its position is ideal for the experiment, allowing either pion or muon injection options. The high bay is $73' \times 62'$, which is large enough for the ring which has a $54'$ outside diameter. The floor is constructed in three sections. The central $20'$ wide strip is $5'$ concrete thickness, with the two outer sections being $1'$ thick. There was concern that the floor might need to be augmented for stability, however loading and survey studies have been carried out which indicated sufficient stability. The floor level is $6'$ below grade, so that the pion/muon beam will be pitched down to about $3'$ below grade. The ground will then provide useful shielding for radiation. The building includes a 40 ton overhead crane, an adjacent control room and work areas, and an adjacent compressor room, all of which will be used for the experiment.

The hall is not large enough to allow for both coil construction and the construction of the ring. These will therefore be phased. The three coil packages (4 coils total) will be each wound in the hall, then stored outside adjacent to the hall. To do this, a slot was built into the south wall of the hall to pass the 14 m diameter coils to and from storage.

Fig. 7.1.1 shows the hall with the $(g-2)$ ring in position. the ring will be placed to the south end to allow for a $12'$ high wall of concrete shielding to protect people in control room area ($6'$ light concrete equivalent, 335 tons, will be sufficient for this). The building will be fenced on the other sides to limit access for radiation protection.

The building and control room are now being used by the $(g-2)$ engineering and physicist staff for design, construction, R&D work on the magnet shimming and measurements, and on the development of the quadrupole and ring vacuum design.

Figure 7.1.1: A plan view of the beamline and experimental hall.

7.2. Building Foundation Study

The floor of the $(g-2)$ building was loaded on 1 August 1988 to match the ring loading, with survey measurements of elevation and floor expansion taken each week until 12 April 1989. [1] Fig. 7.2.1 shows the distribution of several of the elevations and Fig. 7.2.2 shows the distribution of the measurements across the diameter of the storage ring. Accuracy was estimated by considering the spread of several measurements taken at the same time. We have observed a $0.010''$ maximum fluctuation in elevation and a $0.060''$ maximum spread in the diameter.

The elevation tolerance is set by effects on the muon population which would change the storage volume or the effective field integral seen by the muons, as well as by mechanical considerations. Tilts of the field are more important for the muon populations than displacements. A tilted field creates a vertical force which must be offset by the much weaker quadrupole field. For example, a 0.2 $mrad$ radial tilt of the entire ring (0.5 mm relative to the center) results in a 1 cm displacement of the muon population. This would reduce the effective storage region by 40%. There is a negligible effect on the spin motion and a small additional uncertainty (0.1 ppm) in the correction for the average orbit circumference in determining the total field integral seen by the muons. The effect is considerably less if the tilts are randomly distributed. Thus a ± 0.5 mm tolerance ($\pm 0.020''$) has been adopted relative to the reference plane. The floor stability, Fig. 7.2.1, is better than this. It is also planned to monitor tilts with electronic bubble levels and elevations with periodic surveys.

The observed diameter variations have let to a base design which is not tied to the floor, see Chapter 8 for details.

7.3. Radiation Shielding

Radiation estimates from the ring have been made assuming pion injection (for muon injection the radiation levels are much less), with 10^8 $pions/fill$ and three fills per AGS cycle of 1.2 seconds. Pions (and protons for positive beam injection) are 2% higher momentum than the ring setting, and will hit one or more constrictions in the storage aperture (quadrupoles, collimators and vacuum tank walls) after about one turn. Most will then lose energy and spiral to the inside of the ring, ultimately striking one of the 24 electron calorimeters. Approximately 20% of the pions will have decayed before striking material. We assume that 10^7 $\pi/fill$ strike each calorimeter. We consider 24 sources of radiation (the calorimeters) which are partially shielded vertically and radially to the outside of the ring by the iron return yoke.

Figure 7.2.1: Elevation change for for a 4.5 month period.

Figure 7.2.2: Diameter variations over 14 m for a 4.5 month period.

An empirical formula for estimating side shielding gives about 16 $mrem/hr$ just outside the iron at the midplane. At the control room area, which is not shielded by the yoke for radiation from across the ring, we estimate 0.4 $mrem/hr$ just outside $6'$ of light concrete.

It is important to realize that the weight of the shielding will affect the floor settling. It will be intolerable to adjust the shielding empirically since a year of careful shimming will have preceded the first beam. A $6'$ thick wall represents a very conservative plan, compared to the AGS experience in the C1 line for example. Muon injection would require no shielding.

The other three sides of the $(g-2)$ building will be fenced at an appropriate distance.

7.4. Refrigerator Building

The R&D refrigerator has been moved to a concrete pad on the east side of the $(g-2)$ building, housed in existing temporary buildings.

7.5. Ring Thermal Enclosure

The ring iron must be held at a constant temperature, to within $\pm 1^{o}C$. We plan an inner thermal box of height $10'$ above the floor. Removable insulated panels will be installed on an aluminum frame which will span the width of the $(g-2)$ building. Sides will include three building walls and a wall on the control room side. Access from the control room, which is about $6'$ above the experimental floor, will be from a platform above the ring, with a stairs into the ring center. Sketches of the plan are shown in Fig. 7.5.1. We plan to build the thermal enclosure with a heating/cooling system after the first pion injection run in 1996.

Figure 7.5.1: The thermal enclosure.

7.6. References

1. A. Pendzick, F. Karl, J. Mills, J. Sullivan, $(g-2)$ *Building Floor Stability*, *Muon* $(g-2)$ *Note No. 39*, May 1989.

Chapter 8.
Storage Ring

Revised March 1994

8.1. Introduction

8.2. Magnetic Design and Field Calculations

8.2.1. Conceptual Approach

8.2.2. Computer Aided Refined Pole Designs

8.3. Design Considerations

8.3.1. Yoke

8.3.2. Coil Design

8.3.2.1. Coil Motion

8.3.2.2. Loads and Stresses

8.3.2.3. Tolerances

8.3.3. Cryostat

8.4. Magnet Yoke

8.4.1. General Design

8.4.2. Steel Composition

8.4.3. Critical Machining

8.4.4. Pole Pieces

8.4.5. Magnet Support Stability

8.4.6. Magnet Yoke Assembly and Alignment

8.4.7. Final Alignment and Installation of Reference Plates

8.5. Coil Assemblies

8.5.1. Conductor

8.5.1.1. Physical Characteristics

8.5.1.2. Insulation

8.5.1.3. Electrical Characteristics

8.5.2. Mandrels

8.5.2.1. Design Criteria

8.5.2.2. Outer Mandrel

8.5.2.3. Inner Mandrel

8.5.2.4. Mandrel Fabrication

8.5.3. Coil Cooling

8.5.4. Coil Insulation

8.5.4.1. Turn-to-Turn Insulation

8.5.4.2. Ground Plane Insulation

8.5.4.3. Ground Plane Epoxy

8.5.5. Coil Winding Process

8.5.6. Cure Operation

8.5.7. Coil Stack Modulus and Shimming

8.6. Cryostats

8.6.1. Vacuum Chamber and Insulating Vacuum

8.6.2. Coil Location

8.6.2.1. Coil Suspension

8.6.2.2. Coil Positioning

8.6.3. Thermal Insulation

8.6.3.1. Heat Shields

8.6.3.2. Superinsulation

8.6.4. Plumbing and Power Leads

8.6.4.1. Coil Assembly Cooling

8.6.4.2. Electrical Leads

8.6.5. Attachment to Yoke

8.7. Controls and Instrumentation

8.8. Tooling

8.8.1. Coil Winding Machine

8.8.1.1. Coil Winding Fixture

8.8.1.2. Conductor Feed Device

8.8.1.3. Conductor Feed Device Layout

8.8.1.4. Caterpillar Drive Unit

8.8.1.5. Insulation Wrapping Mechanism

8.8.1.6. Insulation Test Stand

8.8.1.7. Conductor Guides A, B, and C

8.8.1.8. Transfer Plate, Hold Down Roller and Vertical Support

8.8.1.9. Feeding Table

8.8.1.10. Control, Instrumentation and Calibration

8.8.1.11. Coil Winding Procedure (Overview)

8.8.1.12. Winding

8.8.2. Conductor Cleaning Station

8.8.3. Mandrel Weld Fixture

8.8.4. Lifting Rig and Coil Transport Tracks

8.9. Assembly Plan

8.10. References

Chapter 9.
Cryogenic System

Revised June 1994

9.1. Introduction

9.2. Heat Loads and Refrigeration Duties

9.3. Two Phase Helium Cooling

9.4. The Refrigerator and Control

9.5. Cryogen Delivery and Control

9.6. Three Cooling Circuits

9.7. Gas Cooled Electrical Leads

9.8. Cryogenic Control

Table 9.9.1: The $(g-2)$ Magnet Parameters

9.9. Quench Analysis

The quench analysis is given in $(g-2)$ Note No. 159. [1] and is briefly reviewed here. The magnet parameters relevant for the quench analysis are given in Table 9.9.1. The conductor parameters are given in Table 9.9.2. An important consideration is the cold aluminium mandrel which supports the conductors (see Fig. 9.9.1). A changing magnetic flux enclosed by the mandrels generates an emf which induces current to flow within the mandrel such that it opposes the change in magnetic flux. If the flux changes rapidly enough, the energy dissipated by the eddy currents in the mandrel will drive the entire

Table 9.9.2: The $(g-2)$ Magnet Superconductor

Figure 9.9.1: Quench Protection System

coil normal. This is called "quench-back". Quench-back is desirable if a quench should develop. Since the entire coil goes normal, the heat is dissipated over the whole coil/mandrel assembly. Thus temperature differences are minimized.

The design goals are to cause quench-back quickly once a quench is detected, but to maximize the time constant with which the energy is extracted. The latter requirement is to minimize eddy currents in the iron. These are conflicting requirements. The quench analysis has resulted in a design which gives an acceptable solution for both of these requirements.

The eddy currents generated in the iron [2] create a magnetic field which effectively remains confined to the iron. Therefore, in some places it opposes the main magnetic field, and in other places it reinforces it. It is the latter case that causes a potential problem, since the enhanced magnetic field will put the iron in a new position on the **B** *vs* **H** curve. We can get an estimate of the size of the above effect from the CERN experience. After a power breakdown, the magnetic field changed by 55 *ppm* when the magnet was turned on again. [3]

However, when a turn-on cycling procedure was used [4], the magnetic field was reproducible at the 1.4 *ppm* level. The L/R time constantfor the CERN magnet was $\tau = (0.3H/0.1\Omega) = 3s$. During the cycling procedure, the magnet was ramped to 110% of full current in 100 seconds, and then ramped down in 100 seconds. This was repeated three times. Finally, the current was slowly cycled above and below the set point.

We have chosen a quench protection resistor with a resistance of 0.01Ω based on the above considerations. A schematic of the electrical circuit is shown in Fig. 9.9.1. The current will then decay with a time constant of about 29 seconds. The current and energy ratios as a function of time after quench are shown in Fig. 9.9.2. This time constant is about ten times longer than the CERN value. Therefore the eddy currents in the iron should be about ten times smaller. The effects on the reproducibility of the magnetic field should be acceptable based on the CERN experience. Calculations of the effects of the iron eddy currents with the magnetic field analysis program OPERA are proceeding. We have allotted time for quench-back and field reproducibility studies during the magnetic field shimming process (see Chapter 21). If power is lost, the current will decay with a time constant [5] of about 800 sec. The maximum voltage developed during the quench is:

$$V_m = NA\frac{dB}{dt} = (48)\left(25m^2\right)\frac{1.5T}{29s} = 62\ V$$

The insulation has been tested to over 1 KV.

As can be seen in Fig. 9.9.2, over 60% of the magnet stored energy will be dissipated by the 0.01Ω resistor. The 29 second time constant dominates over the other quench time constants (see Table 9.9.3). The hot spot temperature will be less than $100^{\circ}K$. The criteria

Figure 9.9.2: Current and Energy Ratios During a Quench

Table 9.9.3: Time Constants

is that the hot spot temperature remain less than $300^{\circ}K$. Quench-back will occur in less than 2 seconds. This makes every quench effectively identical.

9.10. References

1. M.A.Green, *Muon g-2 Note No. 159, Design Parameters for the g-2 Solenoid Power Supply and Quench Protection System*, May 1993.
2. K. Halbach, Nucl. Inst. and Meth. 107, 529 (1973).
3. CERN Logbook 2, 33 (1974).
4. H. Drumm et al., Nucl. Inst. and Meth. 158, 347 (1979).
5. W. Morse, *Minutes of April 13, 1994 Energy Extraction Workshop.*

Chapter 10.
The Superconducting Inflector

Revised March 1994

10.1. Introduction

The inflection of a particle beam into a storage ring is usually done with a pulsed magnetic inflector, which locally cancels the field of the main magnet, so that the beam enters the storage region as close as possible, and almost tangent to the equilibrium orbit of the ring. Further manipulation of the beam with a full aperture kicker would assure the permanent acceptance or storage of the inflected beam. A problem with a pulsed inflector is the persistence of the magnetic stray fields. In the third CERN $(g-2)$ experiment, a coaxial structure pulsed inflector was used. The skin depth of the copper determines the initial magnitude of the pulse which propagates as a wave away from the device. In the storage region, the fringe field from the pulsed inflector is several hundred gauss at 1 μs and decreases to about 20 gauss at 600 μs, the time when data collection ends.

Fig. 10.1.1 shows the cross section of the CERN device, and Fig. 10.1.2 shows the time dependent fringe field pattern.

In the present experiment (E821), the injected beam is pulsed up to 12 bunches per AGS cycle (It may be changed to 8 bunches). The AGS cycle is from 1.4 seconds to 3 seconds depending on the extraction mode used for sharing protons between E821 and the rest of the physics program. Ideally, when the experiment is ready to collect data, all 12 (or 8) bunches in the AGS would be used, with as short a cycle time as possible. The major difficulty in using a variation of a CERN pulsed design is that CERN's device was pulsed only once per CERN PS cycle (2.3 seconds); E821 would require up to 12 (or 8) times per AGS cycle. Extensive studies on a pulsed inflector for E821 were carried out, including material heating-stress, solid state switches and ignitrons [1]. The study concluded that a pulsed inflector for E821 would be very difficult to accomplish.

A direct current non-ferrous superconducting septum magnet may overcome the above problems. It will be shown that current distributions and their combinations can be used to reduce the fringe field. The integrated fringe field will be dominated by the end of the septum near the storage area, but it allows at least static shimming and precise

Figure 10.1.1: The CERN Inflector

measurement of the numerical correction to be applied. Since the cross section of the inflector is constrained by the limited space between the muon storage region and the superconducting coils of the storage ring magnet, it is impossible to make the field near zero everywhere along the injection trajectory. An optimum path has been selected to minimize the amount of inflector aperture used up by this curvature in a straight channel[2].

The requirements of the DC $(g-2)$ inflector are: (1) to produce a homogeneous dipole magnetic field 1.5 T over the length of 1.7 m, in order to essentially cancel the integrated fringe field of the storage ring; (2) to keep its own stray field low enough and acceptable for the magnetostatic shimming.

The conceptual design of the inflector was completed by Boston University; detailed design and construction have been carried out by Boston, BNL, and Japan KEK.

Figure 10.1.2: The Time Dependent Fringe Field From the CERN Inflector

10.2. Design Principle

10.2.1. Double Cosine Theta Distribution

The Magnetic configuration for the device is developed from the well known cosine theta distribution of surface current, where in cylindrical coordinates at a certain radius R, a surface current K is applied, which is modulated according to

$$K = \hat{K} \cos(N\theta) \tag{10.2.1}$$

$\hat{K}$ is the amplitude of the distribution of dimension A/m, θ is the polar angle and N is an integer. N = 1 creates a pure dipole field inside the circle of radius R, N = 2 creates a pure quadrupole, and so on. Since K does not depend on the axial coordinate, the magnetic field is two-dimensional, so that one can introduce profitably complex potentials

which depend on the variable z = x + iy. For instance, the vector potential $\vec{A}$ has a single component A(x,y) pointing in the axial direction. Thus we would write for N = 1:

$$A^{int} = -\left(\mu_o \hat{K} R/2\right)(\mathrm{x}/R) = -\left(\mu_o \hat{K} R/2\right)\ R_e\,(z/R) \qquad |z| < R \quad (10.2.2)$$

$$A^{ext} = -\left(\mu_o \hat{K} R/2\right)(\mathrm{x}R)\,/\,(\mathrm{x}^2 + y^2) = -\left(\mu_o \hat{K} R/2\right) R_e\,(R/z) \qquad |z| > R \quad (10.2.3)$$

The complex potential of this system would be:

$$\zeta^{int} = A^{int} - iG^{int} = -\left(\mu_o \hat{K} R/2\right)(z/R) \qquad |z| < R \quad (10.2.4)$$

$$\zeta^{ext} = A^{ext} - iG^{ext} = -\left(\mu_o \hat{K} R/2\right)(R/z) \qquad |z| > R \quad (10.2.5)$$

where the imaginary part of ζ, G, is the current related potential. Magnetic flux lines follow lines of constant A, which close upon themselves, whereas lines of constant G, which are orthogonal to those of A, provide the direction of the force on axial current elements. Lines of constant G are discontinuous on current boundaries in magnitude and direction and are most useful to lump in optimal fashion a distribution of surface currents into a distribution of line currents, making thereby the device physically realizable.

10.2.2. Truncation

One may modify the shape of the useful volume if a circle (or ellipse) on which the surface current is projected, does not satisfy the geometrical requirements. Charged particle beams may require a channel which is narrow but quite high. In this case one uses only part of the field plot associated with the $\cos\theta$ distribution, i.e., the field is truncated. The truncation is invariably along a line of constant A. On this line can be projected a surface distribution of current, which nullifies the field on the outside but leaves unaltered the field on the inside. The boundary condition in this case would be:

$$\vec{n} \times \vec{B}^{int} = -\mu_o \vec{K} \quad (10.2.6)$$

$\vec{n}$ is the outward unit vector normal to the truncation, $\vec{B}^{int}$ is the flux density on the inside of the truncation and $\vec{K}$ is the surface current density on the truncation.

Fig. 10.2.1(a) shows the principle for a dipole septum (upper half). The cosine theta distribution is now limited to the circle segment 1. The truncation consists of a straight line segment 2, the septum, on which the current density is K/2, or half the amplitude of the cosine distribution on segment 1. The septum boundary is closed by the circle segment 3, on which the surface current density equals $|B|/\mu_o$. The useful dipole field is contained in the area between 1 and 2, the dead space (for return flux) is between 1 and 3, and the

Figure 10.2.1: The Principle of the Truncated Double Cosine Theta Septum Magnet

area outside 2 and 3 is field free. The total current in 1 is opposite and equal to the sum of the currents on 2 and 3.

The truncated DOUBLE cosine theta septum has the purpose to reduce drastically the dead space encountered in a single cosine theta distribution. To this end we consider the magnetic field produced by two concentric cosine theta distributions, $(\hat{K}, R)$ and $(\hat{K}',\ R')$, creating three regions where the potential differs:

$$\zeta_1 = -\left(\mu_o \hat{K} R/2\right)(z/R) - \left(\mu_o \hat{K}' R'/2\right)(z/R') \qquad |z| < R \tag{10.2.7}$$

$$\zeta_2 = -\left(\mu_o \hat{K} R/2\right)(R/z) - \left(\mu_o \hat{K}' R'/2\right)(z/R') \qquad R < |z| < R' \tag{10.2.8}$$

$$\zeta_3 = -\left(\mu_o \hat{K} R/2\right)(R/z) - \left(\mu_o \hat{K}' R'/2\right)(R'/z) \qquad |z| > R' \tag{10.2.9}$$

It is noticed that under circumstances ζ_1 may be made zero, creating a field free region inside R. Likewise one may find the condition for which ζ_3 is zero, creating a field free region outside R'. Useful as this may be for certain applications, the objective here is to reduce the overall size of the dipole septum. In the case of Fig. 10.2.1(a), we have the relation $pq - R^2 = 0$, in which p is the distance from origin to septum, measured on the x-axis, and q is the distance from origin to boundary 3, also measured on the x-axis. Clearly, q can be quite large, dependent on the aspect ratio of the useful dipole region. But the double cosine theta distribution allows one to squeeze the return flux at will, albeit at the expense of more ampere turns for the same useful dipole strength. Fig. 10.2.1(b) shows an example, scaled to give the same useful dipole region as shown in Fig. 10.2.1(a), but a second virtual cosine theta distribution $K' = \hat{K}' \cos\theta$ is applied on circle 4 of radius $R' > R$. The dipole area has the boundary 5 and 6 and the area outside 6 and 7 is field free. The generating currents on 4 are virtual, since they are not physically present in the device. However 7 is uniquely determined by specifying K' in addition to K, R and p. Since boundary 7 follows a line of constant A, its value equals the potential of septum 6: $A_6 = A_7$, or:

$$A_6 = R_e\left(\zeta_1\right)_{\mathrm{x}=p} = -\frac{1}{2}\mu_o p\left(\hat{K} + \hat{K}'\right) \tag{10.2.10}$$

$$A_7 = R_e\left(\zeta_2\right) = -\left(\frac{1}{2}\mu_o \hat{K} R^2\right)\ \mathrm{x}/\left(\mathrm{x}^2 + y^2\right) - \left(\frac{1}{2}\mu_o \hat{K}'\right)\mathrm{x} \tag{10.2.11}$$

$$\hat{K} R^2 \mathrm{x}/\left(\mathrm{x}^2 + y^2\right) + \hat{K}'\mathrm{x} = \left(\hat{K} + \hat{K}'\right)p \tag{10.2.12}$$

$$\hat{K} R^2/q + \hat{K}' q = \left(\hat{K} + \hat{K}'\right)p \tag{10.2.13}$$

Eq. (10.2.12) is the equation for boundary 7 and Eq. (10.2.13) is the equation for the end point q. The parameters leading to the construction of Fig. 10.2.1(a) and Fig. 10.2.1(b) are shown in Table 10.3.1, in relative units.

It is noticed that the squeezing of the return flux by a factor of 2 in Fig. 10.2.1(b), reduced the dipole field by 10%. The equation for boundary 7 reads:

$$y^2 = 10x/(x+3) - x^2 \tag{10.2.14}$$

Fig.	$\hat{K}$	$\hat{K}'$	R	p	q	B(dipole)
1	1	0	1	1/3	3	1
2	1	-0.1	1	1/3	2	0.9

Table 10.2.1: Relative Parameters of Fig. 10.2.1(a) and (b)

10.2.3. Line Currents

Assuming that the superconductors have a relatively small superconducting core, embedded in a much larger stabilizing matrix, the continuous surface current must be concentrated in what one could call a distribution of line currents. It will be shown how to determine the optimum location of each line current, and how to study the effect of the granularity on the quality of the dipole field, i.e., the amount of stray field adjacent to the septum.

The method consists of constructing an arithmetical series of the complex potential. The real part is constant and equals the value of A on the current boundary. The imaginary part of the series has a progression proportional to the current in the wire: $G_{j+1} - G_j = \pm\mu_o I$. Since $G = 0$ in the median plane, $y = 0$, the first G in the series would be $G_1 = 0$ for an odd number of turns and $G_1 = \mu I/2$ if the number of turns is even. Having established the series of ζ, one may solve for z. Fig. 10.2.1(c) shows an example. The cosine theta distribution segment 8 can be made discrete if the conductor density vs. y is constant, by virtue of the cosine law. One should preferably select an even number of layers, since the number of conductors on the septum 9 is somewhat less than half the number on 8. This ensures a reasonable and uniform packing density on the septum, where the conductors must be evenly spaced according to the relation

$$\zeta_1 = -\mu_o \left(\hat{K} + \hat{K}'\right) z/2 \tag{10.2.15}$$

The equation for ζ_2 applies to boundary 10. As this equation can be solved for z, and the discrete series of ζ_2 is known, the position of the conductors is:

$$z = \{-\zeta_2 \pm \left(\zeta_2^2 - \mu_o^2 \hat{K}\hat{K}' R^2\right)^{\frac{1}{2}}\} / \left(\mu_o \hat{K}\right) \tag{10.2.16}$$

Figure 10.2.2: The Conductor Arrangement

The second root in the solution is due to the analytical continuation of G_2 and A_2.

Fig. 10.2.1(c) shows that near the intersect of boundary 8, 9 and 10, physical interference of some conductors could occur. These conductors must be deleted in a pairwise fashion as shown in Fig. 10.2.2. In the present example the cosine theta distribution lost one turn, so that the return conductors on the septum and the closing boundary should be reduced by one turn. In this case an enhancement of the stray field and impurity of

the harmonic content of the dipole field may occur. Small perturbations of the position of adjacent conductors will reduce either enhancement.

Fig. 10.2.2 is the first version of the inflector. The parameters for this version are shown in Table 10.3.2, and the harmonic contents are shown in Table 10.3.3, which were calculated using an algorithm developed at Boston University[3].

Table 10.2.2: Preliminary Parameters of $(g-2)$ Inflector.

R = 50 mm	Number Turns = 50	B Dipole = 1.5 T
p = 15 mm	Number Cosine Wires I = 50	I/Wire = 5200A
q = 93 mm	Number Septum Wires II = 22	J= 550 A/mm^2
h = 61 mm	Number Rear Wires III = 28	Channel = 18x 45 mm
	K_1=2400 A/mm	$K_1{}' = -360$ A/mm

Table 10.2.3: Harmonic Expansion of the Inflector Field.

Order of Multipole	(a) Center of Pion Channel x = 30 mm, y = 0 R=12.5 mm	(b) Center of Muon Channel x = -45 mm, y = 0 R=50 mm	(c) Center of Pion Channel x = 30 mm, y = 0 R=80 mm
N	Na_N/R(gauss)	Na_N/R(gauss)	$\bar{\kappa}_N(A/m)$
1	-15064	1.1	0.5657E-02
2	-7.6	5.1	0.1092E-02
3	-0.5	6.7	-0.8858E-03
4	1.2	5.2	0.5153E-03
5	-0.1	2.2	0.5031E-02
6	-0.3	-0.6	-0.1320E-02
7	0.6	-2.1	-0.2269E-02
8	-1.3	-2.3	0.1154E-02

10.3. Physical Realization

After August 1989, a new $(g-2)$ inflector was designed in order to accommodate an existing superconductor, to be supplied by Japan KEK. This conductor has been fully developed for the ASTROMAG (Particle Astrophysics Magnet Facility) project and therefore has no development cost.

10.3.1. The Conductor

The KEK aluminum stabilized superconductor consists of multi-filament; there are 3050 NbTi/Cu filaments in the core. The basic parameters are listed in Table 4.

To investigate the detailed electric and magnetic properties of the conductor, short sample measurements were taken at the BNL Accelerator Development Department. We thank Bill Sampson for that. Fig. 10.3.1 shows the test result. In the upper right corner, B_a stands for the applied magnetic field in the test dipole magnet; B_p stands for the peak field, in which the self field is taken into account; and I_c is the critical current at the peak field. The result is scaled to the temperature of 4.224 K.

10.3.2. Field Calculation

Together with the insulation and the fiber glass tape, the apparent sectional area will be $2.3 \times 3.3 mm^2$. Due to the improved granularity, the field quality inside the channel will be almost perfect and the stray field almost absent. This allows one to delete two pairs of conductors, and to relocate some conductors so that the bending radius around the ends of the inflector would be increased. The revised distribution is shown in Fig. 10.3.2. There are 88 turns; the operating current is 2850 A. The channel width is 1.8 cm and the height is 5.6 cm. The flux plot and the harmonic components are shown in Fig. 10.3.3.

If the storage ring magnetic field is superimposed, fields are eliminated inside of the device channel, and enhanced in the return flux region. By considering the self-field effect (2.5 gauss per ampere), some particular portions of the superconductor windings have to stand peak fields up to 3.5 tesla.

Figure 10.3.1: Short Sample Tests of the Conductor

Figure 10.3.2: The Revised Conductor Distribution

Figure 10.3.3: Flux Plot and Harmonic Content

10.3.3. Magnetic Force

According to the 2D calculations, the components of the force per unit length, $\vec{F}_{jk}$, on wire k due to the field produced by wire j, may be shown[4]:

$$(F_k)_x^i = \sum_j \left(F_{jk}\right)_x \qquad j \neq k \tag{10.3.1}$$

and

$$(F_k)_y^i = \sum_j \left(F_{jk}\right)_y \qquad j \neq k \tag{10.3.2}$$

where the superscript i stands for "internal", and later on, e for "external".

If the wire system is immersed in an external magnetic field, the forces on the wires contain the additional terms:

$$(F_k)_x^e = -I_k B_y^e, \quad (F_k)_y^e = I_k B_x^e \tag{10.3.3}$$

where the components of B^e are to be evaluated at the location x_k, y_k.

Either $(F_k)^i$ or $(F_k)^e$ are transmitted to the supporting body on which the conductors are positioned, but whereas $\sum(F_k)^i = 0$, there can be a residual $\sum(F_k)^e$ and a torque M, if the external field is not uniform.

Based on the two dimensional calculation, Fig. 10.3.4(a) and Fig. 10.3.5(b) show the magnitude and the direction of forces on each conductor, in the cases of without and with the storage ring field, respectively. The magnitude of the forces is of the order of several thousand newton per linear meter.

In reality, the inflector is a three dimensional device. One end is located in the homogeneous storage ring magnetic field and the other end is located in the storage ring fringe field; therefore the external field is not uniform. Three dimensional forces have been calculated, and the total residual forces are shown in Fig. 10.3.6.

Figure 10.3.4: (a) Forces on the Conductors - No Storage Ring Field

Figure 10.3.5: (b) Forces on the Conductor - With Storage Ring Field

Figure 10.3.6: Residual Forces

10.3.4. The Critical Surface

The critical current density, critical temperature and critical field are related to each other by the critical surface in $BJ\theta$ space, which is characteristic of the material in use. Superconductivity prevails everywhere below this surface with normal resistivity everywhere above it. Fig. 10.3.1 actually shows the profile of the critical surface at the temperature of 4.224 K. The critical current at this temperature is 4350 A.

Two phase helium cooling option has been chosen for the superconducting inflector. The operating temperature is 4.6 K. Critical currents at different temperatures are calculated [5] as following:

$I_c = 3890A \ at \ \theta = 4.6K \ and \ B = 3.5T$

$I_c = 3000A \ at \ \theta = 5.5K \ and \ B = 3.5T$

The inflector will be operating around 73% of the full load.

10.3.5. The Configuration of the Inflector Ends

The fringe field of the inflector is dominated by two ends. By measuring the fringe field of a room temperature wire model, it became clear that to close the downstream end would reduce the fringe field by a factor of 6 (integrated dipole component). From an engineering point of view, if both ends are closed, it will be much securer for force support and quench prevention (Table 10.3.1). In this case, incoming particles (pions or muons) must penetrate superconductor layers. Table 10.3.2 lists the calculation results of muon storage ratio for all three options. It shows that if one leaves the upstream end open, the experiment running time would not have a significant reduction; therefore, closing both ends is the best choice.

10.3.6. Engineering Design and Construction

The detail engineering design was completed by KEK. The inflector body consists of three parts (Fig. 10.3.7):

a)inner coil (one winding on the aluminum mandrel);

b)outer coil (two windings on the aluminum mandrel);

c)housing jacket (aluminum) with two liquid helium tubes.

The inner and outer coil will be wound separately; the housing jacket will be shrink-fitted and constrain the two mandrels firmly. The end loops will be confined by end caps (Fig. 10.3.8). The whole assembly will be epoxy impregnated and cured, becoming one integrated solid.

Table 10.3.1: Summary of the meeting with A. Yamamoto on July 29, 1991 to discuss the inflector design and development.

A liquid nitrogen heat shielding is proposed by KEK. Fig. 10.3.9 shows the upstream case: two squared nitrogen tubes are attached on the shield plate, which surround the inflector assembly.

Several test windings have been done at KEK. A superconducting prototype with shortened length (0.5 meter long) has been constructed and tested in KEK (March 1993) and

Table 10.3.2: Muon Storage Comparison for Open and Closed Inflector Ends

Figure 10.3.7: The KEK Inflector Body

Figure 10.3.8: The Inflector End Loops

Figure 10.3.9: KEK Design with Heat Shield

in BNL (March 1994), with and without the external field, respectively. The construction of the full length superconducting inflector will be completed by the end of 1994.

10.3.7. Cryostat and Beam Chamber Complex

10.3.7.1. The Location of the Inflector in the Storage Ring

Fig. 10.3.10 shows the location and the orientation of the inflector in the storage ring magnet. The injection beam line is 1.25 degree from the tangential reference line. The inflector is aligned along this tangential reference line and its downstream end is positioned at the injection point which is 12.35 degree west from of southerly axis of the building.

10.3.7.2. Integrated Inflector Cryostat and Beam Chamber

Due to the limited space, the inflector cryostat is being designed together with one of the beam vacuum chamber section of the storage ring to form an integral structure but with two different vacuum zones. It is an aluminum structure sealed with aluminum welding for vacuum integrity. Viton O-rings will be used in the flange area. Vacuum quality better than 10^{-5} torr will be achieved for cryogenic insulation.

Fig. 10.3.11 shows the integrated structure of the inflector cryostat and beam chamber. The shaded area is the 1.7 meter long inflector body. The injection point is 76 mm outside the tangent point of the muon orbit and tangential reference line.

A beam window in the upstream end is designed for injection beam to come in. Another beam window in the downstream end is designed for the inflected beam to enter into the storage region. These windows will be made of 1 mm aluminum plate to let most of the muons pass through. The inflector is supported in the two ends with accessing flanges for installation and adjustment. A penetration hole in the upstream end through the outer coil and the yoke, is designed for the beam pipe to bring the beam in. Another penetration hole in the downstream end is designed for the connection of power leads and cryogenic tubes.

Figure 10.3.10: Inflector Location

Figure 10.3.11: Inflector/Beam Vacuum Chamber

10.3.7.3. Cryostat in the Downstream (Injection Point)

Fig. 10.3.12 shows the cross section view of the inflector in the downstream end where the inflector is very close to the storage region. To overcome the space limitation, the partition wall (shown in Fig. 10.3.13) which is 0.5 inch thick at the top and the bottom, is designed with a thin wall near the mid-plane, to serve following functions:

a) to separate vacuum zones between the inflector and the beam chamber;

b) to keep structure integrity under vacuum condition even when only one side is in vacuum; c) to provide at least 7 mm space between the inflector and the partition wall, because the inflector will be operated in 4.6 K, space is needed for thermal insulation;

d) to keep a minimum clear space of 48 mm radius for muon storage region in the injection point area.

The top or bottom plate (0.5 inch thick) has a 5 mm undercut to make enough room for thermal insulation. The thickness of the two outside vertical plates is 0.75 inch. Under vacuum condition the deflection of the top or bottom plate is about 0.5 mm, which is acceptable.

10.3.7.4. Cryostat in the Upstream

Fig. 10.3.14 shows the cross section view of the inflector in the upstream where the end of the inflector cut into the outer cryostat. In order to make room for inflector steering and thermal insulation, a concave wall has been designed in the outer cryostat and a 45 degree chamfer was cut in the coil cover.

10.3.7.5. Inflector Support and Steering Adjustment

The two supports of the inflector have been designed to provide steering and shifting capability for injection beam adjustment. The downstream end support (shown in Fig. 10.3.15) is designed as a pivot to keep the end of inflector in the injection point. The upstream end support (shown in Fig. 10.3.16) is designed as a slide with a motion feed through. The slide is to compensate the shrinkage of the inflector when it is cooled down. The motion feed through is to provide $+/-$ 4 mrd steering adjustment for the injection beam without losing vacuum. The two supports can shift the inflector toward upstream end, up to 1.5 inch.

Figure 10.3.12: The Downstream End of the Inflector

Figure 10.3.13: Inflector Partition Wall

Figure 10.3.14: Upstream End of the Inflector

Figure 10.3.15: Downstream End Support

Figure 10.3.16: Upstream End Support

10.3.7.6. Beam Divergence and Downstream End Window

Fig. 10.3.17 shows the gradually increased width of the exit beam from the inflector. Due to the beam divergence and the range of the steering angle, a beam window will be designed to fit into a tapered partition wall without interfering with the beam.

10.3.7.7. Penetration through the Outer Coil and the Yoke

Fig. 10.3.18 shows the beam line penetration through the outer coil and the yoke. A slot will be cut in the back leg of the yoke. A beam tube will slide through the yoke and the outer coil to bring the beam into the inflector. In the downstream end, another penetration tube will be designed to support and guide the lead conductors and cryogenic tubes to a lead pot in the back of the yoke. The locations of these two penetration holes have been carefully positioned to pass through the space between tension bolts.

10.4. References

1. V.Badea et al. "Pulsed Inflector Study", Muon $(g-2)$ Note No.32, October 16, 1989.
2. H.Brown "Inflector Path into the $(g-2)$ Storage Ring", Muon $(g-2)$ Note No.29, 58, 76.
3. F.Krienen et al. "The truncated double cosine theta superconducting magnet", NIM A283(1989)5-12.
4. F.Krienen et al. "Development of Non-ferrous Superconducting Magnets", Muon $(g-2)$ Note No.63.
5. Provided by W.B. Sampson, Brookhaven National Laboratory, March 1992.

Figure 10.3.17: Beam Divergence and Window

Figure 10.3.18: The Penetration Through the Coil and Yoke

Chapter 11.
The Electrostatic Quadrupoles

Revised February 1995

11.1. Introduction

For a muon focusing field index (see section 2 of chapter 5) of $n = 0.139$ the required theoretical voltage on the electric quadrupoles is 10.63 kV/f where f is the fraction of the $(g-2)$ ring occupied by the quadrupole. With an azimuthal coverage of 39° in each quadrant

$$f = \frac{39^\circ \times 4}{360^\circ} = 0.43 \qquad (11.1.1)$$

(see Fig. 11.1.1), the required voltage on the electrodes is ±24.5 kV. A POISSON calculation with the actual flat electrode geometry (see section 2 of this chapter) gives ±23.6 kV. Two adjacent vacuum tanks will share unequally 1/4 of the total electrostatic quadrupoles. The four fold symmetry of the quadrupole position in the $(g-2)$ ring eliminates certain groups of resonances. [1]

The quadrupoles will be fabricated in modules each 13° in azimuth, approximately 1.6 m in length. One tank will be filled with 2 modules, 26° (3.22 m) long electrostatic quadrupoles and the next one will contain 1 module 13° = 1.6 m long. This assures that every electrostatic segment will be completely contained in one vacuum tank leaving the transition piece (bellows) free. Every tank will be an independent unit, i.e. it will have its own set of four feedthroughs, one support cage, etc.

Figure 11.1.1: The $(g-2)$ ring (view from top) and the quadrupole locations.

11.2. The Quadrupole Structure

The dimensions of the plates, cage, insulators etc. are shown in Fig. 11.2.1. S. Mane studied the flat electrodes and found that they "almost yield a pure quadrupole potential" [2-3], which makes them appropriate to use in theexperiment. The material is aluminum and care will be taken so that no sharp metal points will be at high electric field regions. The diameter of the tubes at the end of the plates will be 3 mm and the total width of the plates 4.7 cm. The distance between the plates will be 10 cm as shown in Fig. 11.2.1. Special care will be taken so that no impurities with high magnetic susceptibility are present in the insulators. The material used thus far is MACOR which passed the magnetic susceptibility tests by Kim Woodle (the Susceptibility Sherif). The side plates require 3 support insulators each, in order to assure proper alignment and secure fastening. The diameter of the horizontal insulators used in the tests was 0.75 inches, but it will be reduced to half of this. This will reduce the absorption of the pions which enter the $(g-2)$ ring. [4] Each quadrupole segment will be powered from feedthroughs upstream in the vacuum chamber.

The feeding leads shown in Fig. 11.2.2 will be of aluminum tubing; care will be taken so that the minimum distance everywhere between the leads is 4 cm. The geometry of the feeding leads is such that the trapped electrons are driven out of the quadrupole region and discarded. [5] The feedthroughs can nominally withstand 30 kV DC electrical potential, so that DC tests and measurements are possible.

The positioning of the vacuum tank relative to the magnet yoke will be accurate to 1 mm. [6] Inside the vacuum chamber there willbe marks for the proper position of the cage that holds the electrostatic quadrupoles. The assembly of the cage with the electrostatic quadrupole plates will be done outside the vacuum tank. The tolerances on the plates and the stand off insulators are 0.5 to 0.75 mm. The positioning of the cage in the tank will be done outside the $(g-2)$ ring. There will be set screws which will allow fine adjustments to the cage position relative to the vacuum tank. The overall position of the electrostatic quadrupoles should be accurate to 1 mm relative to the center of the muon storage region.

Figure 11.2.1: Cross section of a quadrupole with its housing cage. The rails are used for the transport of the beam tube trolley and E-field quality.

Figure 11.2.2: Quadrupole feeding leads. The high voltage lead geometry is such that it releases the low energy trapped electrons. [6]

11.3. High Voltage

The high voltage will be approximately 25 kV and pulsed. It needs to be on for about 12 muon lifetimes (i.e. for about 800μs) after pion/muon injection in the ring. This will help to minimize the effect of the electron trapping and avoid breakdown. [5,7] The high voltage on some electrodes [8] will come up to full voltage after the beam is stored in order to displace the muon beam for scraping. The proposed electrical connections are shown in Fig. 11.3.1. The thyratron switches [9] have been tested and performed adequately. The voltage must be stable and known to 2%. [10]

The total capacitance of each long electrostatic quadrupole contained in one vacuum tank is of the order of 1 nF and 0.5 nF of the short ones. We plan to use high voltage storage capacitors of 75 nF.

11.3.1. Quadrupole Control Electronics

The four quadrupole high voltage pulsers are on the floor, more or less in the center of the ring. This is necessary to minimize the capacitance of the high voltage cables going to the vacuum chamber. Four electronics racks will be necessary. The start and stop pulses will be generated with "GG200" type NIM modules. We require a prefill and fill pulse from the AGS. The prefill pulse should come $100 - 200\,\mu$s before the fill (switch S1 in Fig. 11.3.1 will be triggered by it). The time jitter should be less than about $10\,\mu$s. The fill pulse should come with a well defined time relationship with the beam (switch S2 will use this). The time jitter should be less than 30 ns. We also require a signal from the vacuum system if the muon chamber pressure rises above a preset level. This will inhibit pulsing the quadrupoles until the vacuum has recovered.

Each quadrupole high voltage pulser will have a voltage divider for monitoring the actual high voltage waveform. This will go to an oscilloscope, and an ADC. The ADC will be read out by the host computer. If any of the four signals are not correct (presumably due to a high voltage discharge), this will be recorded in the data-stream (perhaps the entire fill will be rejected), and the host computer will issue a warning message.

Figure 11.3.1: Electrical connections for the pulsed high voltage on the quadrupoles. The final timing will be determined by the beam dynamics team.

11.4. R & D Tests

The charge accumulation in the quadrupole region during the high voltage pulse is a consequence of the mixing of the electric field, due to the quadrupoles, and the magnetic field, due to the main magnet. It turns out that it is more severe when negative muons are stored in the ring, [5,7] and therefore we setup a system where we performed tests in order to establish the requirements and limits for various parameters (i.e. residual gas pressure, pulse duration, smoothness of the quadrupole plates, durability, etc.).

11.4.1. Negative Muon Polarity Test

First we tested the negative muon polarity with a pressure in the tank of 5×10^{-7} Torr at the quadrupole position. [5] The pulse duration was 3 ms which is more than three times needed. The applied voltage was +19 kV to the side plates, and −27.7 kV to the top and bottom ones. In the last test the distributed ion pumps (DIP) were operating next to the quadrupole plates providing also a convenient way to read the pressure at the quadrupole site. The magnetic field was always about 1.5 T.

The voltage was pulsed at 1 Hz for more than a day continuously and a more than 100 thousand pulses were accumulated without a single spark. Afterwards we let air in the vacuum chamber keeping everything else the same. The first spark appeared at 2.5×10^{-6} Torr pressure.

We have also applied DC high voltage to the system and the following were limiting values (i.e. the pressure was moving up after a certain point):

-11 kV, +10.5 kV

-19 kV, 0 kV

0 kV, +12.5 kV

each raw representing a separate test. On the left is the voltage applied to the top and bottom plates and on the right that applied to the side ones. The DC voltage in this polarity is limited by the fact that some of the trapped electrons hit the insulators which support the side electrodes and cause secondary emissions. However, the "venting" mechanism is very efficient in preventing critical space charge accumulation and sparking.

11.4.2. Positive Muon Polarity Test

Again the pressure was 5×10^{-7} Torr, and the pulse duration 3 ms. The applied high voltage was +19 kV to the top and bottom plates, and −27.3 kV to the side ones and many pulses were collected with no breakdowns. The limiting pressure was found to be 1.4×10^{-4} Torr (Townsend Limit), by bleeding outside air into the vacuum chamber.

We have also applied DC high voltage of ±20 kV limited only by the rating of the scope probes and not the plates. The pressure was moving down when the DC high voltage was on which means that the release of the trapped electrons is complete in this polarity. In this polarity the trapped electrons do not encounter any insulators before they are released.

11.4.3. DC High Voltage and Its Applications

We were able to see the resonant frequencies of the trapped electrons when DC high voltage was applied to the plates in the negative muon polarity configuration. [5] The frequency of the trapped electrons depends only on the electric field that exists between the plates:

$$\omega = \left(\frac{eV}{m_e d^2}\right)^{1/2} = \left(\frac{ek}{m_e}\right)^{1/2} \tag{11.4.1}$$

where ω is the angular resonance frequency of the electrons, e is the charge of the electron, V the applied total voltage on the plates, m_e the mass of the electron, d the half separation of the plates, and k multiplied by the coordinate x gives the electric field at that point, *viz.* $E = -kx$.

In Fig. 11.4.1 we show the resonance frequency versus the applied high voltage which follows the square root law of Eq. (11.4.1).

The fact that the plates can hold DC high voltage means that the electron trapping is minimized by our design of the feeding leads and the accumulation of space charge is quenched. The fact that we observe the expected frequency of electron oscillations for a quadrupole field means that the electric field is not influenced to a measurable degree (at the level of 0.5% for a DC field) by trapped electrons. The resonance frequencies can be used to equalize the electric field on all the quadrupoles which helps to minimize muon losses due to asymmetries. It also gives the opportunity to study whether the electron trapping creates any magnetic field. Since it is DC it can be measured by the NMR probes that are located above and below the plates. This will set very strict limits to spurious magnetic fields coming from the trapped electrons, but it needs a homogeneous magnetic field not available at the time of the tests.

Figure 11.4.1: Resonance frequencies of the trapped electrons versus the applied total DC high voltage. The solid line is the fit to the data and follows the square root law implied by Eq. (11.4.1).

11.5. References

1. Y.Y. Lee, private communication.
2. S.R. Mane, *Muon (g-2) note #103*, 1992.
3. S.R. Mane, *Muon (g-2) note #107*, 1992.
4. W.M. Morse, *Muon (g-2) note #146*, 1993.
5. Y.K. Semertzidis, *Muon (g-2) note #169*, 1993.
6. Lou Snydstrup, private communication.
7. W. Flegel and F. Krienen, Nucl. Inst. and Meth. 113, 549 (1973).
8. Eric Benedict and B.L. Roberts, *Muon (g-2) note #183* and references therein, 1994.
9. EEV Electronics, Chelmsford, Essex CM1 2QU, England.
10. W.M. Morse, *Muon (g-2) note #118*, 1992.

Chapter 12.
The Muon Kicker

Revised September 1994

12.1. Introduction and Overview

Direct muon injection into the storage ring is accomplished by giving the muon beam a 10 milliradian kick at a quarter of a betatron wavelength from the inflector. The muons produced by pion decay in the transport channel are selected by the momentum slit near the end of the beam line.

Three different kickers have been considered, since the kick can be accomplished either by electric, magnetic or a combination of these two fields. Each technique has its difficulties and implications on the measurement of $(g-2)$ due to the residual fields after the kick.

The advantages of the muon injection into the ring are that it reduces the initial flash which the detectors see by many orders of magnitude, while producing over an order of magnitude more stored muons per fill than can be achieved with pion injection. [1]

Initial calculations for a somewhat idealized ring [2] estimated that up to a third of the muons transported through the inflector can be stored. For the actual storage ring with the present geometry, the quadrupole system and π/μ beam transport system, tracking calculations indicate that a 5 to 10% injection efficiency seems achievable. The most recent calculations say that compared to pion injection, a factor of ten more muons can be stored per fill with direct muon injection, compared to pion injection.

The disadvantage of direct muon injection is that one must deal with the effect of the residual magnetic field of the fast muon injection kicker due to the eddy currents in the vacuum chamber. The effect of the residual field on the measured value of $(g-2)$ was estimated to be about 0.3 *ppm* [1], if a magnetic kicker is employed.

A new dynamic calculation using the sophisticated computer program `PE2D/TR` shows that the effect on the measured $(g-2)$ frequency is about 0.1 *ppm*, but the details depend on the exact pulse shape. [3]

Moreover, the residual field can be measured using the Faraday effect. Since the effect of the residual field is small and also measurable, the choice of the kicker was made based on the reliability and the cost.

We have chosen the magnetic current loop kicker as the kicker of choice. The length of the kicker is limited by the space between the quadrupoles and the maximum is about 5 meters. An electrostatic kicker needs on the order of 400 kV to accomplish the kick. A magnetic kicker with a current loop requires less than 70 kV if the kicker is divided up to four sections. The electrostatic kicker [4] requires some state-of-the-art research and development. On the other hand, the magnetic kicker can be accomplished with the present engineering experience at BNL.

12.1.1. The Pulser

The pulser for the muon kicker will be made up of a number of sections to enable available thyratrons or spark gaps of standard ratings to be employed. A lot of experience exists in the AGS with these types of systems. The booster extraction and the AGS fast extraction are the prime examples. Synchronization of the modules can be readily accomplished and maintained over a large number of cycles in those systems.

Each module will consist an energy storage capacitor, a discharge switch (thyratron or spark gap), a crowbar switch, an energy-dissipating resistor and a short transmission line to connect the module to its vacuum feedthrough. The initial part of the pulse is formed by triggering the discharge switch and resonating the capacitor and the inductance of the kicker. As soon as the capacitor voltage reverses, the crowbar switch is triggered and the second half of the pulse is formed primarily by the kicker inductance and the resistor time constants. All necessary axillary timing and control circuits will be constructed. A common high voltage power supply will be used to charge the modules in parallel. Therefore, all capacitors will have the same initial stored charge. Individual delays will be required to make the initial adjustment of delay differences between simultaneously operated switching devices. Lately we are looking into the possibility of using a critically (or near-critically)-damped R-L-C circuit. The advantage of this scheme is that is pulses the kicker with only one switch (a spark gap) and the rest of the pulse is naturally taken care of by the damping resistor. Since this circuit requires only one switch instead of two, the pulser should be more reliable. The disadvantage is that a small residual kick exists during the first two turns. Mane had investigated the effect of a residual kick with up to 20% of the primary pulse amplitude after the first turn and 15% after the second turn. He found no noticeable effect was seen in the injection efficiency or in the subsequent beam losses. Another disadvantage of the critically damped scheme is that a somewhat higher pulser voltage is required than for the other scheme.

The switching device can be either a commercially available thyratron or a spark gap. A thyratron is known to have lifetime exceeding the life of the $(g-2)$ experiments but

with a higher internal inductance. Recently we have been looking into the possibility of using commercially available spark gaps and we learned of the possibility of obtaining units which would be suitable for our application which have an expected life of over a million shots. Because of low internal inductance (< 40 nH) we may be able to construct the kicker with three modules.

12.1.2. The Electrodes and Feedthroughs

The material chosen for the magnetic field generating current loop is $.02''$ thick titanium sheet which will provide both mechanical stability and good high voltage properties. The top and bottom ends of the sheet will be welded to titanium channel which will also serve as the rail for the field mapping trolly. The end of the sheet as well as the titanium channel shall be rounded to withstand voltage up to 100 kV. The channels and sheets are supported on MACOR insulators.

The kicker will be constructed in three or four modules to reduce the voltage required to overcome the inductance of the module. The current connections through the vacuum walls will be made via high current coaxial feedthroughs in order to reduce stray inductance. The feedthroughs will be modeled after the feedthroughs utilized in the extraction and injection kickers in the AGS ring.

12.1.3. Calculation of the Residual Fields

Since the walls of the $(g-2)$ vacuum chamber are several tens of the skin depth of the kicker pulse, the effect on to the magnetic yoke is expected to be nil. However, the eddy current created in the vacuum chamber by the fast rising and falling magnetic field would have some effect on the $(g-2)$ measurement. An analytical calculation for a simple electrode geometry and current pulse shape was carried out by Farley, [1] who estimated the effect to be 0.3 ppm.

Dynamic calculations for a magnetic loop kicker, [3] and for a stripline kicker [5] using the computer program `PE2D/TR` showed that the effect on the $(g-2)$ frequency is about 0.1 ppm at 20 μs and 0.04 ppm at 100 μs. Additional calculations are under way for the planned kicker geometry and pulse shape, since the residual eddy currents are somewhat dependent on the geometry as well as the pulse shape. Though the residual field is small, we are planning to measure and to correct for it. The method to measure the field is described by Semertzidis, et al. [6]

12.1.4. Measurement of the Transient Fields Induced by the Kicker

The transient field produced by the kicker will be measured by the Faraday effect. A test setup has been built [6] which has shown the feasibility of measuring transient **B** fields of the magnitude expected from the kicker, and to a precision better than is needed for the $(g-2)$ measurement. Since knowing the effect of the kicker on the muon spin precession frequency is crucial to the success of the experiment, the laboratory test setup for measuring eddy currents and the results are described below.

For muon injection the particles need to be kicked by 10 $mrad$ outwards at about 90° around from the inflector exit so that they are stored in orbits that have the same center as the $(g-2)$ ring. The integrated magnetic field needed is $B \cdot L = 0.1\ Tm$ or $B = 330\ G$ for $L = 3\ m$. If the electrostatic kicker is used, the required field is of the order of 10 MV/m.

The muons take about 150 ns to go around the ring and therefore the kicker field should be off before that time. However, this high transient field has the potential to create eddy currents in the vacuum chamber walls. As discussed above, this is particularly true for the magnetic kicker [3] and less true for the stripline [5] kicker.

The integrated main dipole magnetic field is about 65 Tm and there is a need to know the average **B** field to 0.1 ppm. For 3 m of kicker length this translates to about 22 mG of Remnant Magnetic Field (RMF). The estimated magnetic field at the center of the storage region induced by these eddy currents for both the magnetic and stripline kickers is calculated [3,5] to be of that order 20 μs after muon injection, which is when data collection will begin. Therefore, for both those kickers there is a need to measure the induced magnetic field to 50% and to study its time dependence.

12.1.5. The Faraday Effect

A measuring device for that purpose has been developed at BNL based on the Faraday effect: Polarized light that propagates in a dielectric material in the presence of a magnetic field has its polarization state rotated by an angle

$$\theta = VB\ell \tag{12.1.1}$$

where V is the Verdet constant of the material, B is the magnetic field along the light propagation direction and ℓ is the total light path in the material. The sense of rotation given by Eq. (12.1.1) depends only on the direction of the magnetic field and not on the direction of the light propagation. The rotation follows the rotation of a right-handed screw that moves in the direction of the magnetic field.

By detecting the angle θ as a function of time we can estimate the changing magnetic field when V and ℓ are known. The merit of this method is that there are no metallic

parts present but only dielectric materials so that the measuring instrument itself does not influence the RMF. In addition, this technique has a large dynamic range and its time response is very short, limited only by the time constants of the detection electronics. The large static external dipole magnetic field does not contribute anything since this method is only sensitive to time-varying magnetic fields.

12.1.6. The Test Setup

The setup used for the tests is shown in Fig. 12.1.1. A green laser, which provided $\approx 50\ mW$ of continuous wave (CW) Ar^+ laser light with $\lambda = 514.5\ nm$ was polarized by the polarizer P. The polarized light then enters a TGG crystal † which is surrounded by a coil that generates a magnetic field along its axis. The light is reflected back by the mirror $M1$ and retraces itself through the crystal. The mirror $M2$ catches the returning ray and directs it to the analyzer A which is set for best extinction, σ^2, where for crossed polarizers, extinction is defined as the ratio of the light that escapes the second polarizer, over the light intensity before the second polarizer.‡

The photodiode on the back of the analyzer monitors the light intensity that escapes it. The light intensity I on the photodiode is

$$I \;=\; I_0 \left[\sigma^2 + (\alpha+\theta)^2\right] \;=\; I_0 \left[\sigma^2 + \alpha^2 + 2\alpha\theta + \theta^2\right] \qquad (12.1.2)$$

where I_0 is the light intensity before the analyzer and $\sigma^2 = 10^{-5}$ to 10^{-6} for the polarizer crystals used in the tests. The angle θ (see Eq. (12.1.1)) is the Faraday rotation to be measured and α is the static rotation introduced to the system in order to linearize the effect and to improve the signal to noise ratio. For the best signal to noise ratio and shot noise limit it turns out that $\alpha \;\geq\; \sqrt{\sigma^2}$. In practice we used $\alpha \;=\; \sqrt{\sigma^2}$.

Following the laser there is a periscope (PS) for adjusting the height of the laser beam, and a Galilean telescope (GT) for minimizing the light spot size at the TGG crystal site.

---

† A TGG crystal is an artificially grown crystal with a big Verdet constant, i.e. for the same magnetic field you get large rotation without compromising the laser light quality (see Eq. (12.1.1)). The crystal used in the tests was provided by: Optics For Research, Box 82, Cadwell, NJ 07006.

‡ The first polarizer polarizes the light to a high degree. The second polarizer when rotated relative to the first (in which case it is also called the analyzer) extinguishes the light. However, in practice, there is always light that is transmitted and one uses extinction to quantify it. The analyzing power of a system depends heavily on how good extinction is.

Figure 12.1.1: The experimental setup. The symbols are: PS - periscope, M - mirror, A - polarization analyzer, P - polarizer (see text).

Figure 12.1.2: The circuit used to generate the time-varying magnetic field in the tests.

12.1.7. The Time-Varying Magnetic Field

The coil (C) simulates the magnetic field to be measured. The circuit used is shown in Fig. 12.1.2. The coil was capable of delivering a magnetic field

$$B = \mu_0 I \frac{N}{2L} cos\beta \tag{12.1.3}$$

where I is the current that flows, $2L = 3.5''$ is the coil length, $N = 1135$ is the number of turns, and the tangent of the angle β is the ratio of the diameter to the length of the coil which for our case was $cos\beta = 0.96$. For the coil used, $B = 154\ G$ per ampere.

The inductance of the coil was measured to be $L = 9.2\ mH$ and its resistance was $9\ \Omega$. A resonance circuit was used to create a fast-changing magnetic field by placing a capacitor ($C = 10\ nF$) in parallel to the coil. The resonance frequency is given by

$$f = \frac{1}{2\pi\sqrt{LC}} = 16{,}600\ Hz \tag{12.1.4}$$

12.1.8. Results of the Test Measurements

The extinction achieved with the TGG crystal in place was 2.6×10^{-5} and was limited by its inhomogeneities. With the TGG crystal removed, and everything else the same, the extinction was measured to be 4.4×10^{-6}. The DC level on the oscilloscope was 163 mV, therefore I_0 (see Eq. (12.1.2)) corresponds to 6250 V.

Fig. 12.1.3 shows the results with 1000 measurements vector-averaged. The trigger that is sent to the base of the transistor to close (i.e., to pull point C of Fig. 12.1.2 to ground), also triggers the digital oscilloscope for data taking. Curve 2 of Fig. 12.1.3 is a single measurement of the voltage at point C of Fig. 12.1.2 and curve 1 corresponds to the vector average of the output of the charge preamplifier that follows the signal photodiode. In these measurements the voltage at point D was 3.25 V.

The polarization rotation angle (see Eq. (12.1.1)) induced by the time-varying magnetic field was

$$\theta = \frac{I}{2\alpha I_0} = \frac{58\ mV}{2 \times 5 \times 10^{-3} \times 6270\ V} = 9.2 \times 10^{-4}\ rad \qquad (12.1.5)$$

The company that furnished the TGG crystal provided a value for the Verdet constant of ($V = 219\,Tm$). The crystal length is 1.3 cm (i.e. total light path 2.6 cm), so the measured rotation given in Eq. (12.1.5) corresponds to a transient magnetic field amplitude of 1.6 G. The signal-to-noise is very large in that case.

If one analyzes the circuit, the expected field is 1.1 G, which is $\sim 30\%$ less than the measured value. Because of time pressures to finish these measurements, it was not possible to completely explore the sources of this discrepancy. There are several possible sources of this difference, and they will be studied in detail later in 1994.

With the same setup and the light to the photodiode blocked, the signal looks like trace 1 of Fig. 12.1.4 which corresponds to a maximum noise of 6 mG after 20 μs of the trigger. This is well below the required sensitivity.

In the real setup data should be taken with the crystal in and out of the light path in order to study the effects of spurious signals.

Figure 12.1.3: Storage oscilloscope result of the measurement (see text).

Figure 12.1.4: Storage oscilloscope measurement with the photodiode blocked (see text).

12.1.9. Conclusions on the Transient Measurements

In laboratory tests it has been shown that a determination of a fast-changing magnetic field with 1000 measurements at 1 Hz is possible to a level that is 3 times more precise than the required accuracy for the $(g-2)$ experiment.

The 1.6 G signal is quite large (as is the signal to noise) compared to the 22 mG we need to measure in the $(g-2)$ experiment. The low level measurement is shown in Fig. 12.1.4 where the noise 20 μs after the trigger corresponds to 6 mG. The laser light noise was much less than the equivalent of 6 mG, and the main problem was pickup, presumably ground loops or other noise through the trigger electronics to the preamplifier, or the oscilloscope itself.

In the real setup the power supplies for the receiving electronics will be isolated, which should eliminate this problem. Furthermore, successful isolation of the electronics should permit measurement of the stray field on a pulse-to-pulse basis.

Because of time constraints, and a failure of the laser tube, it was not possible to investigate the isolation issue, nor was it possible to apply a static 1.5 T external magnetic field on the apparatus in order to study its effect on the measurements. In principle, the external field should have a negligible effect, since the Faraday effect only depends on a time-varying magnetic field. Both isolation studies and the external field test will be carried out in the future on the magnetic kicker prototype under construction.

12.2. References

1. J.M. Bailey and F.J.M Farley, *Muon Injection and the Initial Flash*, *(g-2) Note #13*, October 1987.
2. H.E. Ahn and W.P. Lysenko, *The Muon Injection Option*, *(g-2) Note #46*, February 1989, and also K. Ishida, *Note on Injection Scheme*, *(g-2) note #27*, February 1989.
3. Y.Y. Lee, W. Meng, and W. Feng, *Eddy Current Study for the Non-HV Muon Injection Option*, *Muon g-2 Note No. 153*, April 1993.
4. F. Krienen, *The Electrostatic Muon Kicker*, *Muon g-2 Note No. 84*, September 1990 and addendum July 1991.
5. W. Feng and E.B. Forsyth, *Eddy Currents Induced in the Muon Storage Ring Vacuum Chamber Due to a Stripline Fast Kicker*, *(g-2) note #152*, April 1993.
6. Yannis K. Semertzidis, Francis J.M. Farley, Richard Larsen, William M. Morse, Joe Yelk, *Test Setup for Measuring the Magnetic Field Due to Kicker Eddy Currents*, *(g-2) note #168*, August 1993.

Chapter 13.
The Vacuum System

Revised February 1994

13.1. The Vacuum Chambers

A plan view of the assembled vacuum chamber ring is shown in Fig. 13.1.1. The vacuum chamber ring includes twelve 28 degree chamber sectors, the bellows adapters (2 degrees) between sectors, and the support frames which are installed inside the sectors. There are nine sectors which have the same geometric features and three sectors which have special features. The similar sectors, which are referred to as "standard" sectors, are shown in Fig. 13.1.2. The special sectors are the inflector, trolley garage, and the traceback chambers. The kicker will also require a special design, but it will not be installed at the time the experiment is first commissioned.

The chambers have a scalloped shape on the inside to accommodate the twenty-four electron detectors while minimizing the showering in the vacuum chamber walls[1]. There are two detector regions per vacuum chamber sector. The detector region is shown in Fig. 13.1.3. The vacuum wall adjacent to the calorimeter is only 3 mm thick to allow the detector to be as close to the storage region as possible. The calorimeter is inclined at an angle of 70 mrad, which is the mean angle of electrons with high analyzing power (actually NA2) which miss the outer edge of the detector and hit the next detector. The outside wall of the chamber is at a radius of 721 cm to allow free space for the incoming pion or muon beam.

The inflector, which is installed in chamber 1, cancels the field for the incoming particle beam, and directs (i.e., inflects) the beam tangentially into the storage region. The kicker will be located approximately 90 degrees clockwise from the inflector end. Two sets of beam monitors determine the particle distribution at approximately 180 degrees and 270 degrees from the inflector end. There are four regions in the vacuum chamber ring for electrostatic quadrupoles: Q1, Q2, Q3, and Q4. Each region has 39 degrees of electrodes mounted in standard chambers for a total azimuthal coverage of 156 degrees. The trolley garage is at the chamber 10 position, and the electron traceback detector is at the chamber 11 position.

Figure 13.1.1: Plan view of the storage ring vacuum system.

Figure 13.1.2: Plan view of the standard vacuum chamber.

Figure 13.1.3: Plan view of detector station. There are 23 such stations around the ring.

The vacuum chamber sectors are a welded fabrication of aluminum alloy 6061 plate. The standard chambers have 5 conflat flange ports with a 203 mm outside diameter and a 124 mm inside diameter facing radially inward. These flanges are available for the quadrupole electrical feedthroughs, beam monitors, vacuum pump connections, for removal of the distributed ion pumps (DIPs), for access when installing the quadrupole feedthroughs, and for positioning of the internal support frame. There are 30 fixed NMR probes per chamber which are mounted in grooves in the upper and lower chamber plates. These grooves are on the outside faces of the plates, external to the vacuum.

The support frame inside each chamber sector serves primarily to provide rails for the NMR trolley cable car. The support frame is shown in Fig. 13.1.4. The quadrupole electrodes are mounted to the support frame. To ensure accurate frame assembly and precise positioning of the rails and electrodes, 3 mm upper and lower plates of the frame are CNC machined to the exact radius for a 28 degree arc. A short aluminum bellows adapter is placed between each vacuum chamber section. The bellow adapter facilitates installation and removal of a sector, provides for any angular misalignment of chamber end flanges, allows expansion for small temperature differences between the yoke iron and aluminum chamber ring, and allows independent, and therefore more precise, setting of chamber radial position. The rectangular end flanges of the sectors and bellows adapters are sealed with viton O-rings. NMR plunging probes and collimators (scrapers) will be installed in the bellows adapters.

The accurate positioning of the NMR trolley rails and quadrupole electrodes which are mounted on the support frame is critical to the experiment. The alignment of internal components of the vacuum chamber will be accomplished in the following steps: assembly of the support frame on a very flat surface using gauging and tooling, machine chamber upper and lower surfaces to a flatness of .010 inch (.25 mm) to serve as a datum for support frame positioning, installation and alignment of the support frame in the sector relative to end flanges and sector upper and lower surfaces, and finally positioning and alignment of the sector in the magnet gap.

To minimize electron trapping and high voltage breakdown at the quadrupole electrodes[2], a pressure of 10^{-7} $Torr$ is required for the storage ring vacuum. The total gas load of the storage ring vacuum system is estimated to be 1×10^{-3} $Torr - \ell/s$ 24 hours after roughing down. To reach pressure of 5×10^{-7} $Torr$ in 24 hours, a pumping speed of $\simeq 2000\ell/s$ is needed.

Figure 13.1.4: The support frame which goes inside of the vacuum chamber to support the trolley rails and the electrostatic quadrupoles.

13.2. Vacuum Pumps, Pumping Speeds and Outgassing

A prototype vacuum chamber has been constructed which is identical to the standard vacuum tank section. In the prototype sector chamber, an outgassing rate of $1 \times 10^{-9}\ Torr - \ell/s\ cm^2$ was reached 24 hours after roughing down. The outgassing of twelve sector chambers with an internal surface area of $5 \times 10^5\ cm^2$ will therefore be $\sim 5 \times 10^{-4}\ Torr - \ell/s$ or 50% of the estimated gas load. The quadrupole electrodes will contribute a gas load of $2 \times 10^{-4}\ Torr - \ell/s$ or 20% equivalent. The 24 Viton O-ring seals will add a gas load of $\sim 1 \times 10^{-4}\ Torr - \ell/s$ from both outgassing and permeation. The remaining 20% of the gas load budget is set aside for other vacuum components, such as kicker, profile monitors, etc. With careful selection and evaluation of the material used in each component and proper cleaning and handling, the total gas load shall not exceed the estimated $1 \times 10^{-3} Torr - \ell/s$ 24 hours after pumping down.

Turbomolecular pumps will be used to rough the ring vacuum from ambient to $\sim 10^{-5}\ Torr$ before the high vacuum pumps can be started. The turbopumps can also be used as high vacuum pumps when the need arises. Identical turbopump stations will be used to maintain the insulating vacuum of the cryostats of the magnet coils and the inflector.

Sputter ion pumps, which provide clean, vibration free vacuum, have been chosen as the high vacuum pumps for the storage ring vacuum system. Instead of lumped ion pumps, distributed ion pumps(DIPs) mounted inside the vacuum chambers will be used here. With the existing bending field and vacuum chambers, only Penning discharge cells are needed. These on-the-spot pumps eliminate the conductance restriction of the manifolds associated with the lumped pumps. The other major advantage of using DIPs in the $(g-2)$ storage ring vacuum is the absence of permanent magnets of the lumped ion pumps, which might disturb the 1 *ppm* field uniformity requirement. The absence of pump manifolds also frees up the space in the storage ring midplane and simplify the chamber design.

Two areas of $5\ cm \times 50\ cm$ at the inner radius of the sector chambers, as shown in Fig. 13.2.1, have been identified[3] to be outside the trajectories of the decaying electrons and will be used for positioning the DIPs. The DIP will be installed and retrieved through the down stream Conflat port. The maximum allowable cross section of the DIPs through the port is approximately 5 cm wide and 10 cm high. The DIP design is shown in Fig. 13.2.2. It consists of two sections, each with three layers of anode elements. Flexible braids are used to joining the anode elements together. Both the anodes and the cathodes of the DIPs are made of titanium therefore they will not disturb the uniformity of the magnetic field at the muon storage region.

Figure 13.2.1: A sample of muon decay electron trajectories showing the optimum location inside the vacuum chamber for the distributed ion pumps.

Figure 13.2.2: A schematic view of the distributed ion pump elements.

The pumping speed of the sputter ion pumps is a function of the geometry of the Penning discharge cells and the magnetic field intensity. The lumped ion pumps, using permanent magnets, usually have a field intensity of $\leq 1.5\ kG$. The magnetic field at $(g-2)$ DIP locations ranges from 12 kG to 15 kG. At this high field, DIPs with anode cell radius around 6 mm have been found[4] to have the highest pumping speed of approximately 0.4 ℓ/s per cell. The pumping speeds drops off with decreasing and increasing cell radii. Each $(g-2)$ DIP will have over 270 cells, therefore a pumping speed over 100 ℓ/s. A total pumping speed of 2000 ℓ/s can be obtained with 20 DIPs distributed around the ring.

13.3. Monitoring the Vacuum

To monitor the vacuum level, the storage ring will be instrumented with a few sets of vacuum gauges. Due to the distortion of the electron orbits inside the gauge heads by the fringe magnetic field, hot filament ionization gauges will not function correctly. Cold cathode gauges will be used instead. The effect of the fringe field on the cold cathode readings will be negligible if the gauge heads are located more than 1.5 meters away from the storage region where the fringe field is less than 50 G. Alternatively, the gauge discharge can be sustained by the storage ring magnetic field if the gauge is positioned near the storage region and the permanent magnet is removed. The gauge readings will supplement the pressure readings derived from the discharge current of the DIPs. With over twenty DIPs distributed around the ring, an accurate pressure profile will be readily available for interlock and trouble shooting.

13.4. References

1. F. Krienen and D. Brown, *(g-2) Note No. 62*, April 1991.
2. Y.K. Semertzidis, *(g-2) Note No. 169*, August 1993.
3. S. Hou, Private Communication, August 15, 1992.
4. H.C. Hseuh, M. Mapes, L. Snydstrup, Proc. 1993 PAC, IEEE 93CH3279, 3897.

Chapter 14.
The Precision Magnetic Field

Revised July 1994

14.1. Introduction

Two quantities must be measured precisely to determine a_μ to 0.35 *ppm*. These are the $(g-2)$ precession frequency ω_a and the storage ring magnetic field **B**. The goal in precision for determining **B** is 0.1 *ppm*. Actually it is not **B** at each point in the storage ring that is needed to evaluate a_μ but rather the azimuthal average of B (vertical) around the ring, weighted by time and by the spacial distribution of muons. We designate this average by $\overline{B}$.

The principal specifications placed on the magnetic field of 14.5 kG in the muon storage volume are the following:

(1) Homogeneity of **B** over the storage volume to 1 *ppm*.
(2) Constancy of **B** with time to 0.1 *ppm*.
(3) Measurement of **B** by NMR to 0.1 *ppm* so that the relevant **B** average over the storage ring volume is determined to 0.1 *ppm*.
(4) Absolute calibration of the NMR system to 0.05 *ppm*.

In Chapter 8 the design of the conventional muon storage ring was presented in detail. In this chapter we describe the plans for shimming the field to the required homogeneity for measurement of the field and for its control to 0.1 *ppm* and for absolute field determination.

14.2. Shimming the Storage Ring Magnetic Field

14.2.1. General Considerations

To achieve the required homogeneity of 1 *ppm* over the muon storage volume several techniques of shimming are planned as follows:

(1). Iron pieces on the yoke.

(2). Tilting of the pole faces.

(3). Iron pieces in the air gap between the pole face and the yoke.

(4). Adjustable Rose or edge shims.

(5). Current loop shimming on the pole faces.

Grinding the pole face surfaces is one approach that was used in the CERN experiment but our initial shimming plan does not include grinding.

A special shimming trolley with NMR probes will be used during the shimming process. Field mapping at about 10^5 points (spacing $\sim$ 2 cm) will be done in a complete map with the trolley in a period of 4 to 8 hrs. It will be useful to describe the field in terms of its harmonic expansion. A measured set of field points can always be so represented for a 2-dimensional case and the harmonic description is useful for shimming and also for analysis of the errors due to field inhomogeneities. At present we plan to deal with the real 3-dimensional problems empirically. A program will provide rapid off-line analysis to represent the field in its harmonic components and with this information a decision can be made about what changes to make in the shimming configuration. In general it will be necessary to turn the storage ring magnetic field off to make changes in the iron shims.

A cross section of the pole face region is shown in Fig. 14.2.1 including the pole face edge shims.

The muon storage volume where a precise knowledge of $\mathbf{B}$ is required is indicated. After construction and assembly we anticipate inhomogeneities of $\mathbf{B}$ over the storage volume of several parts in 10^4. These arise inevitably from imperfections in the mechanical configuration of the superconducting coil and iron within the allowed tolerances and from inhomogeneities in the iron. We note for example that a change of 25 μm (1 mil) in the size of the gap between the pole faces results in approximately a 100 *ppm* change in $\mathbf{B}$. The capacitance transducer from Capacitec is a very useful tool to make spacing measurements. Transducer HPB-150 has a linear range of 25 mm and specified repeatability of 0.25 μm.

We plan to reduce long wavelength azimuthal variations of $\mathbf{B}$ by placing iron pieces on the outside of the yoke. We will reduce shorter wavelength ($\sim$ 10 cm) azimuthal and radial variations of $\mathbf{B}$ by placing iron wedges inside the 2 cm air gap.

Figure 14.2.1: The Magnet Pole Region.

The final shimming technique which should allow us to improve from the 10 *ppm* to the 1 *ppm* homogeneity level will be pole face current loop windings. The distribution of the currents will of course depend on the inhomogeneity of the magnet. Current loop shimming on magnet pole faces is a well known technique which has been widely used

commercially for precision electromagnets for NMR studies. We plan to use printed circuit board techniques for the current windings.

The shimming techniques will all be done with an iterative approach involving field measurement, calculation, shimming and then remeasurement. The calculation to predict the shimming required to improve the field will depend on the particular shimming technique being employed and on the character of the inhomogeneity. There is no accurate code for solving the three dimensional Poisson equation, but only for the two dimensional case, including the two dimensional case with cylindrical symmetry. Hence during the initial phase of mechanical shimming when azimuthal field variations may be considerable the calculation will involve a qualitative estimate together with extrapolation and interpolation of measured values. When the two-dimensional Poisson equation is applicable, it has been found by full calculations that the effects of perturbations due to iron distributions or permeability variations and due to changes in current distribution can be accurately and usefully computed by perturbation methods to the 0.1 *ppm* level. We anticipate that such calculations will be very useful in the final stages of current loop shimming. Shimming for the inflector region is discussed later in this section.

During the shimming process field measurement will be done with NMR probes on a movable shimming trolley. Tests of various aspects of the shimming techniques will be made with the test magnet at Brookhaven before the storage ring is constructed. A beam tube trolley will be used to obtain a complete field map and to carry up to 25 NMR probes around the muon beam path when the beam chamber is present.

14.2.2. Iron Shimming

14.2.2.1. General Approach to Static Iron Shimming

Static iron shimming will be used to improve field homogeneity [1,2] up to the limit where temporal, thermal, cyclical, and vibrational variations require current shimming capable of active control, based on ongoing measurements of the field to the necessary accuracy.

The field shape, as computed, can be realized by adequate control of dipole, sextupole, plus 10-pole even power moments and of quadrupole plus octupole odd power moments. It is judged that this will also be the case for actual magnet operations including routine environmental influences. Perturbations of moments can be practically introduced using iron, based on computed shimming perturbations of the magnet geometry.

Note that material inclusions in pole pieces and pole surface irregularities are not present in these computations. Very high purity vacuum-formed iron pole stock is being used to minimize local "*pot holes.*" Any additional pole surface measures that may be taken are beyond the scope of the present discussion and must await further experience and ongoing development.

This basic magnetic design approach of the $(g-2)$ magnet with its floating pole, shaped to give the necessary good field uniformity on paper, was made by Danby and Jackson [1] and has been extensively reviewed by them and checked by other members of the collaboration.

The capacity to perturb the magnet was designed to allow practical corrections for what were believed to be the *"real world"* deviations to be expected when the magnet is actually constructed and operated. It is expected that large corrections of low order moments will be required initially but that iron shimming of moments higher than 10-pole will not be necessary.

14.2.2.2. Even Moments

The tables in Sections 14.2.2.2 through 14.2.2.4 give the multipole field contributions $\Delta B_n/B_o$ at r=4.5 cm for different conditions.

Sextupole and 10-pole moments can be eliminated on paper while reducing higher moments to levels smaller than 1 *ppm* by varying the bump height of the Rose shims.

Table 14.2.1: Field perturbations of symmetric moments due to bump height of rose shims. $\delta = 46\mu$m change in bump height.

$\Delta B_n/B_o$ (4.5 *cm*)	Bump Height 0.2854 cm	Bump Height 0.2900 cm	δ (46 μm)
n = 1 (quad)	-252.0 *ppm*	-252.2 *ppm*	+ 0.2 *ppm*
2(sext)	- 14.1	- 7.1	+ 7.0
3	- 34.1	- 34.2	- 0.1
4 (10-pole)	+ 1.3	+ 2.6	+ 1.3
5	-3.8	- 3.8	0.0
6	- 1.4	- 1.3	+ 0.1

Table 14.2.1 gives the calculated perturbations of different moments due to several different heights of the Rose shims with a width of 3.0 cm (see Fig. 14.2.1). Only the symmetric moments are significantly changed.

For the real magnet, based on measurements, perturbation by symmetric adjustment of the pole edge shims can make the 10-pole moment zero. Any residual sextupole will be small compared to correction coil capabilities. Since the sextupole moment is a dominant dynamical field term, current correction of this moment will be required in any event.

Table 14.2.2: Field Perturbations of Moments at r=4.5 cm due to Permeability Changes. Δ B 1001 pole = 0.1% (pole only); ΔB yoke $\approx$ 7%.

$\Delta B_n/B_o$ (4.5 cm)	(Yoke + Pole, 1006 μ = 1006	1006 Yoke + 1001 Pole μ = 1006/1001	1006 Yoke + 1001 Pole 1006/1001
n = 1	+ 0.1 *ppm*	- 6.1 *ppm*	-5.8 *ppm*
2	-7.9	+ 19.9	+ 20.1
3	- 0.2	+ 1.0	+ 1.0
4	+ 1.5	+ 2.1	+ 2.1
5	- 0.1	- 0.1	- 0.1
6	- 1.4	- 1.4	- 1.4
7	-0.1	-0.1	-0.1
8	-0.3	- 0.3	-0.3
B_o(G)	14,418.398 124 *kAT*	14,432.529 124 *kAT*	14,422.984 less current

Table 14.2.2 shows the effect of realistic μ changes on the moments. From calculations with pole pieces from 1006 iron and 1001 iron (as actually planned) we can judge the influence of a change in the properties of the iron pole faces as given in the μ tables. The sextupole contribution changes by 28 *ppm*. Other low order terms are affected slightly. All of these perturbations are well within the range of the edge shim height adjustments only and the air gap shimming. Actual permeability variations in pole pieces can be a significant fraction of the changes given in Table 14.2.2. This change of pole iron properties leads to a 0.1% higher dipole field for the better 1001 material. Control of the dipole field is discussed later. The third column, at reduced current, shows that the changes in sextupole and other field components are due to the better permeability and not due to the slightly higher central field in column two.

14.2.2.3. Odd moments

Table 14.2.3: Field moment perturbations due to asymmetric heights of Rose shims.

$\Delta B_n/B_o$ (4.5 cm)	Pole bumps $\Delta\pm$ 0.047 cm	Pole bumps $\pm$ 0.000 cm	δ
n = 1 (quad)	+ 0.1 *ppm*	-87.7 *ppm*	-87.6 *ppm*
n = 2 (sext)	-10.4	-9.7	+ 0.7
3	-0.4	-36.6	-36.2
4	+ 0.9	+ 1.1	+ 0.2
5	- 0.1	- 3.8	- 3.7
6	- 1.4	- 1.4	0

For the actual magnet, the octupole component can be made zero, based on field measurements, by asymmetric adjustment of the pole edge shims (see Table 14.2.3). Note that δ only effects quadrupole series and this unequal bump is used to correct especially octupole due to asymmetric C magnet [$\Delta = \pm.0185''$ for the chosen geometry.]

Combinations of small symmetric and asymmetric changes of the edge shims can be used, after initial measurements, to eliminate the octupole and 10-pole aberrations.

Table 14.2.4: Perturbing air Gap Behind Pole.

$\Delta B_n/B_o$ (4.5 cm)	Pole Gap Slope $\pm$ 0.4 cm	Pole Gap Slope $\pm$ 0.5 cm	$\delta = \pm$ 1 mm
n = 1 (quad)	- 20.2 *ppm*	+ 10.1 *ppm*	+ 30.3 *ppm*
2 (sext)	- 11.6	-9.8	+ 1.8
3	-0.2	-0.6	-0.4
4	+ 1.0	+ 0.9	- 0.1
5	- 0.1	- 0.2	- 0.1
6	- 1.4	- 1.4	0.0

The quadrupole component can be rendered zero by a wedge-shaped air gap between the poles and yoke pieces. (See Table 14.2.4) This perturbation is used principally to correct the quadrupole term. A change of ± 33 μm in width across the entire pole width gives $\pm$ 1 *ppm* change in the quadrupole field component.

Table 14.2.5: Pole Surface Tilt Computations

$\Delta B_n/B_o$ (4.5 cm)	Base	Tilt Pole Surface & Bumps $\mp$ .010 cm	δ
n = 1 (quad)	-252.2 *ppm*	- 19.2 *ppm*	+ 233.0 *ppm*
2 (sext)	- 7.1	- 7.4	- 0.3
3	- 34.2	- 34.2	0.0
4	+ 2.6	+ 2.6	0.0
5	- 3.8	- 3.8	0.0
6	- 1.3	- 1.3	0.0

The entire pole could also be tilted as a whole to eliminate the quadrupole component, but with about 100 times greater sensitivity. Calculations of the effect of tilting the poles are given in Table 14.2.5.

To summarize, with a tilt of $\pm$ 50 μm across the entire pole width, the quadrupole change is 120 *ppm*. By contrast, a tilt of $\pm$ 50 μm across the entire pole width, but in the air gaps, gives a quadrupole change of 1.5 *ppm*. Since the pole surface tilt is ultra sensitive, it is planned to shim the pole supports at the quarter points to a desired precision value and then leave them alone. The air gap will then be used for adjustments.

14.2.2.4. Static Iron Dipole Shimming

The dipole amplitude results from the first order total reluctance of the magnet circuit.

Variations of the geometrical tolerances and the properties of materials will produce very large azimuthal variations of the dipole field, even with the decoupling improvements of an air gap and floating pole pieces. Before shimming considerably more than 100 *ppm* inhomogeneity will no doubt occur, including quite short wavelength effects. (Note that $10^{-4} \times 10$ *cm* air gap is a very small number.) Also see §8.2.2 and Tables 8.2.1, 8.2.2 and 8.2.3.

Because of the bolted assembly and the accumulated tolerances, the effective total air gap between the pole faces plus the two air gaps behind the poles is estimated to vary by up to 200 μm.

Table 14.2.6 shows the computed effect of a change in each air gap behind the poles by 1 mm (1000μm). This is then 10 times as large as the expected worst case experimental air gap variation.

Table 14.2.6: Air Gap Variation

$\Delta B_n/B_o$ (4.5 cm)	Base (Gap) = 1.0 ± 0.4667 cm	(Gap) = 0.9 ± 0.4667 cm	δ (Gap) =-0.1 cm	δ (Gap) = 1.1 ± 0.4667 cm	δ (Gap) = +0.1 cm
n=1	- 13.5	- 14.0	-0.5 *ppm*	-12.7	+ 0.8 *ppm*
2	- 1.8	- 4.9	- 3.1	+ 1.1	+ 2.9
3	+ 0.1	- 0.1	- 0.2	+ 0.2	+ 0.1
4	0.0	- 0.2	- 0.2	+ 0.3	+ 0.3
5	0.0	0.0		0.0	
6	- 1.0	- 1.0		-1.0	
7	0.0	0.0		0.0	
8	- 0.2	- 0.2		-0.2	
B_o(G)	14556.698	14656.784	100.086	14455.652	-101.046

Table 14.2.6 shows that the expected variation should effect only the dipole moment. Note the wedge angle of ± 0.467 cm over the 56 cm wide pole is unchanged as the average air gap is changed.

Table 14.2.7: Perturbation Due to Vertical Movement of Pole Pieces

	Base	Pole Toward Yoke 0.1 cm	δ
n = 1 (quad)	+ 0.1 *ppm*	+ 5.9 *ppm*	+ 5.8 *ppm*
2 (sext)	- 10.4	- 21.5	- 11.1
3	- 0.4	- 0.9	- 0.5
4	+ 0.9	- 1.5	- 2.4
5	- 0.1	- 0.2	- 0.3
6	- 1.4	- 1.7	- 0.1
B_o(Gauss)	14422.491	14417.475	- 5.016 Gauss

Next, in Table 14.2.7 the pole pieces were moved vertically so that the sum of all air gaps is constant. Note that translation of the pole pieces produces a very small change compared to that of a change in total air gap.

Note that the simple description of the field in terms of moments transverse to the azimuthal (or beam) direction is realistic only if azimuthal field gradients are very small. With azimuthal symmetry $\nabla \cdot B = 0$ occurs in a plane normal to the azimuthal axis. Computations are made in 2D rectangular or polar coordinates or in 3D cylindrical coordinates.

An approximate method of treating the three-dimensional problem when the field varies in azimuth has been proposed. [3]

We desire to obtain knowledge of the field to 0.1 *ppm* as rapidly as practical from the minimum number of fixed point on-line measurements. The quality of the experiment will depend on making the field as uniform as practical to enhance both the measurement and particle orbit accuracies.

Fortunately it has been shown that large dipolar field perturbations can be made in the air gap without producing other moments. This correction should be performed azimuthally with a "wavelength" approximately equal to the pole thickness of about 4 inches.

In Fig. 14.2.2 and Fig. 14.2.3 are shown a system to provide simultaneously localized dipolar correction and also quadrupole correction. This system performs this dual function with wedges or "shingles" that are inserted in a parallel air gap. The pole can be machined with parallel horizontal surfaces, which is mechanically attractive. The tapered wedges provide the wedge angles computed to eliminate the large field gradients. After measurement of the field, one iteration of angle should be sufficient.

Each 10^o pole piece section would contain 12 shingles, each of 4 inch width. Moving the wedges radially affects the dipole, but not the gradient, permitting a very short wavelength dipole correction which is essential for azimuthal uniformity.

The wedge or "shingle" gives about a 50/1 demagnification of the dipole perturbation, that is a horizontal screw adjustment of 50 μm corresponds to - 1 μm of vertical thickness change of either air gap. A 1 μm change in both air gaps results in about a 7 *ppm* dipole change so that good azimuthal uniformity is practical. Then the transverse approximation, probably integrated over 10^o (48 inches), can be used for perturbing the various moments.

A detailed engineering design has been made for the radially adjustable wedge structure. The wedge shingles will be 1 cm thick at r = 0, with a wedge angle of $\pm$ 0.467cm /28cm. In fact, the wedge shingles will be 1 cm narrower than the 56 cm wide poles. This will allow for use of non-magnetic fixtures to hold the shingles and to allow a travel of $\pm$ 0.5 cm horizontally. Construction of the wedges has been largely completed.

The distance of travel corresponds to about 100 μm of gap adjustments on each pole, which is enough to compensate for the estimated 200 μm total gap variation of the magnet as assembled. For locations where the dipole field is quite different when initially assembled, the shingle thickness can be adjusted such that the horizontal travel range is reduced. As was shown in Table 14.2.6 the effect of a 1 mm change of the air gap, which is equivalent to a 10 times larger shingle translation than planned, gives a very large (local) dipole change with only the sextupole moment being above 1 *ppm*. For the expected changes, which are

Figure 14.2.2: A pole piece, which covers 10° of arc, showing the wedge configuration in the air gap.

very small compared to these computed values, negligible multipoles will occur and the correction is a pure dipole.

Table 14.2.8 shows the computed effect of making the wedge shingles 1 cm narrower on each edge. A quadrupole change of 2.6 *ppm* occurs, which requires a very slight modification of the gradient design angle. All higher terms are completely unchanged. Table 14.2.8 results are for a two centimeter narrower wedge shingle, twice the reduction planned. The last column shows this has no adverse effect other than requiring slightly higher current to regain 19 Gauss. Cutting from the outer and inner edges separately in the computations was done only as an example of linear superposition in the computed results.

Figure 14.2.3: The pole piece cross section showing a wedge in the air gap.

Table 14.2.9 actually shows the computed results for the planned wedge shingle width and for a very large radial adjustment. It is clear that it produces very pure (local) dipole adjustment. After the first iteration of the magnet air gap shims, any additional fine adjustment should indeed be dipole only so azimuthal variation in the central orbit field should be quite small.

Table 14.2.8: "Shingle" Edge Variation.

$\Delta B_n/B_o$ (4.5 cm)	Base	-1cm Inner Edge	δ inner	-1cm Outer Edge	δ outer	- 1 cm Both Edges	δ
n=1	- 13.6	- 18.9	- 5.3 *ppm*	- 11.0	+ 2.6 *ppm*	-16.2	- 2.6 *ppm*
2	- 2.0	- 2.7	- 0.7	- 1.5	+ 0.5	- 2.1	- 0.1
3	0.0	0.0		0.0		0.0	
4	0.0	0.0		0.0		0.0	
5	0.0	0.0		0.0		0.0	
6	- 1.0	- 1.0		- 1.0		- 1.0	
7	0.0	0.0		0.0		0.0	
8	- 0.2	- 0.2		- 0.2		- 0.2	
B_o(G)	14557.341	14550.726	- 6.615G	14544.936	-12.405G	14538.285G	-19.056

Table 14.2.9: Shingle Radial Movement.

$\Delta B_n/B_o$ (4.5 cm)	- 0.4 *cm*[a]	$\delta 1$	"BASE"	$\delta 2$	-0.4 *cm*[b]
n=1	- 20.8	- 4.5	- 16.3	+ 3.7	- 23.6
2	- 3.0	- 0.9	- 2.1	+ 0.7	- 3.6
3	- 0.1	0	- 0.0	0	- 0.1
4	+ 0.1	0	+ 0.0	0	+ 0.1
5	0.0	0	- 0.0	0	+ 0.0
6	- 1.0	0	- 1.0	0	- 1.0
7	- 0.0	0	- 0.0	0	- 0.0
8	- 0.2	0	- 0.2	0	- 0.2
B_n(Gauss)	14.54573	+ 7.89G	14.53784	-8.15G	14.54976

[a] - Shingle moved toward back leg yoke.

[b] - Shingle moved away from back leg yoke.

14.2.3. Shimming with Currents

As remarked in §14.2.1 the final shimming from a homogeneity level of 10 *ppm* or 0.15 *G* to the level of 1 *ppm* or 15 *mG* will be done with current loop pole face windings. The final configuration of the coils is not yet fixed [4,5,6] but currents up to about 1 *A* are in the coils are to be provided.

Current shim coils are a set of 2 $\times$ 160 wires at 0.1 inch pitch which go all the way around the storage ring and are fed at one point with a constant current. Top and bottom coils will have separate power supplies. currents through the coils will be set after a vacuum trolley map and kept at these fixed values.

Current shim coils will be placed on the pole pieces (total number = 72) copper conductors on G-10 will be etched or milled. Length of the current shim coils will be equal to the average pole piece. Connections beetween different current shim coils will be made by staple type connectors.

Dipole corenctions coils are designed to keep the field constant in 10^o section of the storage ring magnet. The main source of the variation is expected to be the local temperature variations around the ring. This results in small changes int he air gap resulting in magnetic field variation. The dipole correction coils currnets will be actively feedback by the NMR to keep the dipole field constant.

Dipole correction coils are pancake design 50 turn coils, wound with a rectangular 9 mils $\times$ 90 mils copper magnet wire and mounted between the pole pieces and yoke. There are a total of 72 dipole correction coils. Top and bottom dipole correction coils are connected in series to 36 constant current power supplies.

14.2.4. Shimming in the Inflector Region

The design of the inflector was based on the truncated double cosine principle which minimizes the fringe field by the cancellation of current distributions. In the physical realization, the designed surface current distributions must be replaced by the SC windings and hence the cancellation will not be complete due to the discrete wires and manufacturing tolerances. Furthermore, the winding of the inflector coils will introduce end effects. To investigate the residual fringe field of the inflector wire models were made and the fringe field was measured and studied at room temperature by supplying 4 ampere dc current.

The fringe field is a very rapidly varying function of position containing high order harmonic components and perturbs the integral of the field around the storage ring by about 7 *ppm*. To shim this large fringe field, two methods have been studied: the conventional shimming and the superconducting shielding. The conventional shimming is based on compensation with iron. Due to the requirement of high vacuum in the storage region, the iron must be located outside the vacuum chamber and hence it would be quite difficult to correct a fringe field with high gradient. The superconducting shielding is based on the magnetization property of the type II hard SC material. According to the recent shielding tests, the SC shielding method appears encouraging. [7]

14.3. Field Measurement

14.3.1. General Considerations

The basic method of field measurement will be the well-known NMR technique which will permit the absolute measurement of a local magnetic field to a precision of 0.1 *ppm*, with respect to the proton magnetic resonance frequency. The NMR technique will be used for shimming the magnet as well as for measuring and controlling the field during the experiment.

A movable NMR trolley, equipped with up to 25 probes, will be used at frequent intervals (perhaps about once a week, depending on the stability of the field) to provide a detailed map of the magnetic field in the actual storage volume. In addition, 360 fixed probes will provide a continuous readout of the field in the vicinity of the beam tube and thus give an on-line monitoring of the field stability. Some of the fixed probes will also be used in a feedback loop (sec. 14.4) for field control during data-taking. Cross calibration of the two systems will be provided by a set of several "plunging probes" capable of insertion into the vacuum beam pipe at appropriate intervals. These plunging probes will be carefully constructed to serve as secondary standard calibration probes.

14.3.2. NMR System

The experiment will employ the technique of pulsed NMR for the magnetic field measurement. The main advantage of this method over field modulation, which was used in the CERN experiment, is that no perturbations of the magnetic field are introduced. The pulsed NMR system is also simpler and more sensitive than the frequency and field modulation techniques. Several different kinds of NMR probes are needed for the field measurement:

(1) fixed probes along the ring for field regulation and field monitoring purposes. (2) probes mounted on a movable trolley - both a shimming trolley and a beam tube trolley, with the latter movable in vacuum. (3) a few plunging probes as secondary standards for checking the trolley and fixed probes and for absolute calibration of the beam tube trolley probes. A system for absolute calibration of NMR probes will be discussed in Sec. 14.3.5.

The pulsed NMR system has been developed at the University of Heidelberg [8] and tested at LAMPF. The system for absolute calibration of the NMR probes is being provided by Yale. The Free Induction Decay (FID) signal and its Fourier transform NMR signal have been observed and studied. Fig. 14.3.1 shows a free induction decay signal from a

Figure 14.3.1: Free Induction Decay NMR Signal of a water sample.

water sample doped with $CuS0_4$ and obtained with an RF pulse peak power of 10 watt and pulse width of about 4 μs. Its characteristic relaxation time T_2^* is approximately 30 ms and the signal to noise ratio is 320 to 1 at the beginning of the signal. The Fourier transform signal (Fig. 14.3.2) is observed at approximately 62 MHz. The linewidth is less than 40 Hz (about 0.6 ppm) which is mainly due to the relaxation time of the sample.

The NMR probe consists of a water sample in a glass tube, surrounded by an NMR coil and a tuning arrangement with a variable capacitor and a choke. The water is doped with paramagnetic salts to reduce the relaxation time T_1. Each probe must be shielded from the other NMR probes. The time for each measurement will take less than 100 ms.

Figure 14.3.2: The NMR signal in the frequency domain.

The NMR probes are shown in Fig. 14.3.3. A typical signal from a shimming probe is shown in Fig. 14.3.4.

The overview of the NMR magnetic field measurement system is shown in Fig. 14.3.5. A block diagram of the special VME module and a timing diagram are shown in Fig. 14.3.6. Multiplexing of the RF pulses and the signal detection is essential to keep the system practical and elegant. The frequency standard is a LORAN-C receiver with long time

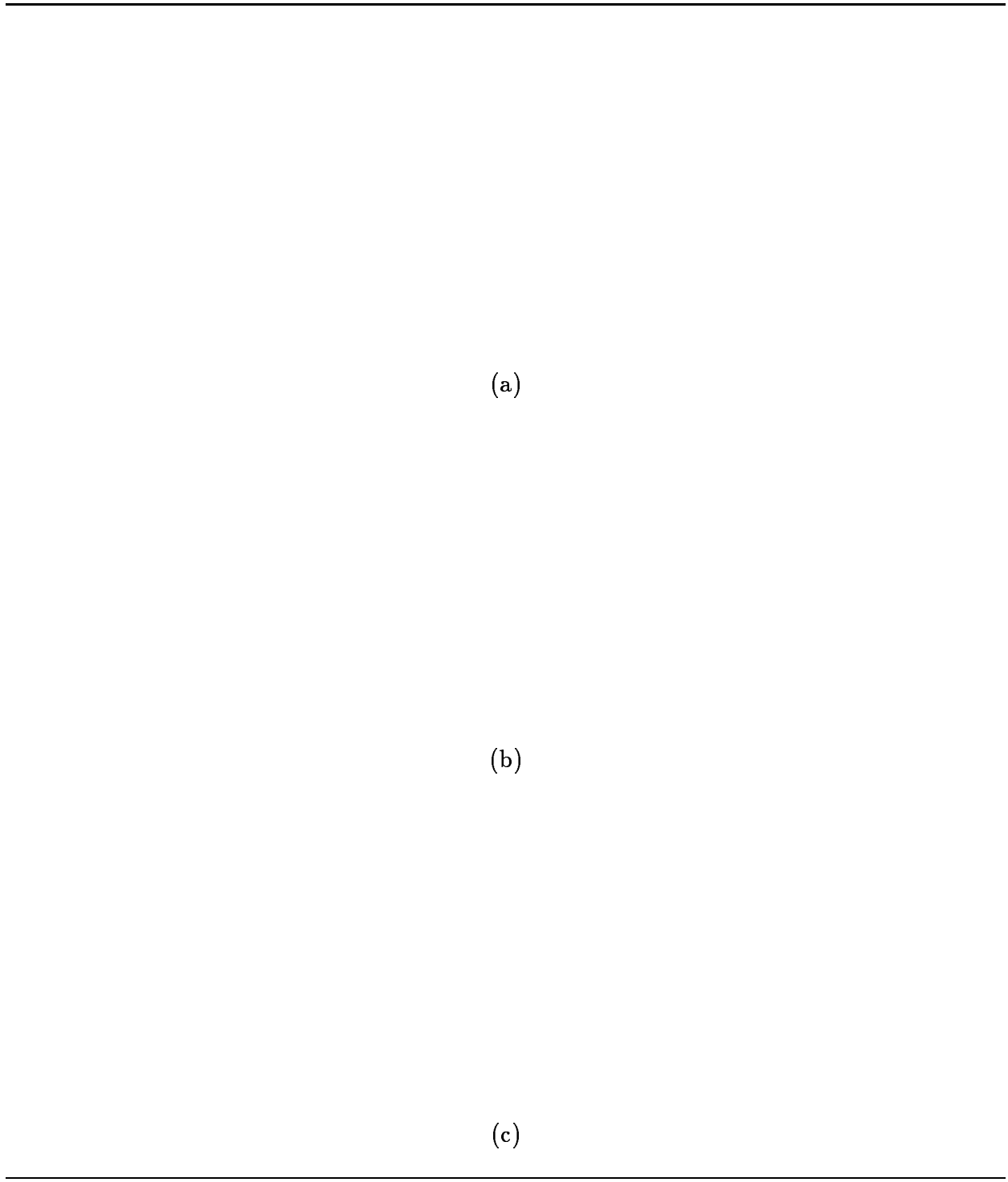

Figure 14.3.3: (a) An NMR probe for the shimming trolley. (b) A fixed NMR probe. (c) A plunging probe.

Figure 14.3.4: Typical signal from a shimming probe. (a) Full signal showing the Free Induction Decay. (b) Enlarged display of the first 5 ms. (c) Noise recorded. (d) Distribution of free noise.

stability of 10^{-12} and short time stability of 10^{-10} (or better). The NMR measurement is carried out by counting zero crossings of the FID signal in a well measured period of time. A short (10μs) RF pulse of 3 watts is used. The preamplified FID signals will be brought by cables (of arbitrary length) to the signal detection and data acquisition electronics where the FID signal will be mixed (hetrodyned) down to the 10 to 50 kHz range. Provision will be made for the recording of the full FID signal simultaneously for several proves with flash ADC's. Fourier transformation of FID signals will be done in an independent process of the system's single board computer (68000 series) which runs

Figure 14.3.5: Overview of the NMR magnetic field measurement system.

Figure 14.3.6: Block diagram of NMR specific units and timing diagrams.

inside a multitasking operating system (059 at present). The NMR data histograms are made in the VME computer memory at any time during the measurements. The raw data will be transferred to a Microvax using TCP/1P protocol.

The NMR specific unit shown in Fig. 14.3.6 receives the basic clock frequency of 62 MHz from the synthesizer which itself is locked to the LORAN-C frequency standard. It further receives from the computer a logic pulse FP (stands for "fire pulse"). It sends to the computer a logic pulse SM (start measurement), the phase sensitively detected and therefore oscillating FID signal and a signal corresponding to the envelope of the FID called FIDE. This signal is used by the computer to decide for how long a time it should count the number of oscillations of the FID and measure their period. All FIDs sent to the computer with the same initial phase are ensured by SYNC. All components needed for the single sideband generator (SSG), including quadrature hybrid, four-quadrant multipliers, power splitters/combiners, have been purchased and two 31 kHz bandpass filters with identical insertion loss and phase characteristics have been built. The four quadrant multipliers (Analog devices, model AD 834) have been tested and found to work very well. The RF-gate consists of a double balanced mixer. A duplexer mimicking quarter wave cable has been built and tested. This duplexer protects the signal preamplifier from the strong transmitter pulses and prevents the NMR signal from flowing back into the transmitter instead of into the preamplifier. The insertion loss in the NMR signal path is only 0.3 dB. The low signal level isolation from the transmitter is 27 dB. Two 1P6T microwave relay switches model SR-6C-H for switching between different probes seem to work reliably. The NMR signal amplifier assembly has an overall gain of 60 dB. The duplexer, switches and signal amplifier will all be moving around the magnet together with the shimming trolley which carries the NMR probes. Long low loss cables with high quality shields will connect the duplexer with the transmitter, and the signal amplifier with the mixing and FID circuitry housed in a rack outside the ring. The FID signal containing a mixed down frequency in the range of 10 kHz to 50 kHz will be measured by an NMR counter circuit.

The NMR system has been tested extensively [9] using the Los Alamos superconducting solenoid running in persistent mode (drift $< 10^{-8}$/h) at a field of 1.7 T where the NMR signal occurs at approximately 72 MHz. The signal to noise ratio exceeds 320 and the characteristic relaxation time T_2^* is approximately 13 ms which is close to the 30 ms intrinsic relaxation time expected for the water sample with the concentration of Cu SO_4 used. For the probes tested (shimming, fixed and plunging) the distributions of single measurements appear to have a standard deviation of below 1.1 10^{-8} of the center NMR frequency.

The diamagnetic and paramagnetic properties of the carefully chosen materials used in the probes and probe holders still lead to significant corrections to the measured NMR

frequencies. The probes of the shim system, tested at LAMPF in 1993, differ by up to 0.3 *ppm* when measuring the same magnetic field. The influence on neighbouring probes by an individual probe at a distance of about 2 cm is at the level of 0.1 *ppm*. The complete shim matrix changes the magnetic field measured by a single probe by up to 1 *ppm*. Therefore further systematic studies will be done prior to the absolute calibration of the probe system to achieve magnetic field measurement at the 0.1 *ppm* level.

14.3.3. The NMR Trolley

A shimming trolley for the muon $(g-2)$ ring magnet will be used during the field shimming process when the beam tube and electrodes are absent. A test shimming trolley has been made to fit the BNL Test Magnet so that we can test a probe-package and its electronics. After the shimming the complete beam chamber will be installed.

Our final plan is to map the magnetic field in situ during the experiment in order to obtain the necessary precise and detailed measurements of the field throughout the muon storage region to a precision of 0.1 *ppm*. To this end we will use a beam tube trolley carrying 25 NMR probes around the muon beam path when the chamber is under vacuum. In this manner we will obtain a map of the magnetic field over the beam cross-section at any azimuthal position. We envisage having a field map of a 2 cm x 2 cm grid. The trolley carrying the NMR probes and the associated electronics is shown schematically in Fig. 14.3.7. The beam tube trolley is designed so that it fits the space without hitting the potential barriers such as electrodes, inflector, detectors, tracking wire chamber, and kicker. It will also make the full 360^0 around the ring. The trolley when parked will be completely out of the vacuum beam pipe using a gate valve for vacuum isolation. Because of the beam tube design and the positions of the detectors, the trolley length will be 50 cm.

Fig. 14.3.8 shows the schematic drawing of the externally driven NMR trolley. It will be moved using a long 50 Ω coax cable which runs around the ring. The cable will be driven by two piezo electric motors operating two drums onto which the cable will be wound. Vacuum compatibility and mechanical strength of the cable were tested and are considered satisfactory. The trolley garage is shown in Fig. 14.3.9.

Electric power and NMR data can be transferred using the driving cable, which will be electrically split at the trolley. NMR data will be collected serially, which means that only one of the probes will be running at any given time. Data acquisition and data transmission will be controlled by a microcomputer on board the trolley. The NMR data will be fully digitized and transmitted via one of the coax cables. The reference frequency needed for the precise NMR measurements and the necessary 5 V dc power will be brought to the

Figure 14.3.7: NMR Beam Tube Trolley.

trolley on the second cable. Voltages of -5 V and 12 V will be generated on the trolley using coils with nonmagnetic components. For precision monitoring of the azimuthal position, an optical encoder reading a bar code on the bottom of the mounting frame will record the position to better than 1 mm.

Figure 14.3.8: The drive system for the beam tube trolley. A coaxial cable is used to drive the beam tube trolley. In addition to providing dc-power for the on-board electronics, the cables are used to communicate the reference frequency and the NMR measurement results between the trolley and the control room. Both ends of the cable are used.

14.3.4. Radial Field Measurement

In order to achieve a dominantly vertical magnetic field, to limit the vertical excursions of the beam, and for the measurement of the muon electric dipole moment, the radial field in the ring will be shimmed to be smaller than 50 *ppm*. Corrections to the radial field will be made by tilting the pole pieces and by using the pole face current shims.

We will measure the radial field with a vertically oriented search coil mounted on a rotatable platform on the shimming trolley. The platform will be leveled with spirit levels (both "bubble" and electronic). The radial field will be measured by integrating the search coil voltage while it is rotated 180 degrees about a vertical axis. The coil does not need to be precisely vertical as long as the rotation axis is vertical which is achieved by precise leveling of the platform using the spirit levels.

The search coil will have an area of 100 cm^2 and about 15 turns giving the required 10^{-6} volt sensitivity for a 50 *ppm* radial field. We are testing electronic spirit levels which have 12 μrad resolution and should allow us to measure the radial field to about 10 *ppm*.

Figure 14.3.9: The trolley garage.

14.4. Field Monitoring and Control

14.4.1. General Considerations

The field will be monitored continuously with the fixed probes and under the supervision of the NMR computer. A software algorithm will be used to derive the average NMR frequency around the ring using the readings from the probes. Part of the algorithm shall have some digital filter for noise reduction. If this average is different from a preset value, then an error signal is generated to change the main coil current to bring this error to zero. This software error signal is converted to an analog signal by loading the amplitude and sign of the error signal into a digital to analog converter (DAC). The DAC output is connected to the regulating winding of a power supply transductor. This transductor measures the main coil current and generates a proportional voltage to regulate the main coil power supply. Twelve dipole correction coils, each with its own power supply for every magnet sector, will be used to make dipole changes for individual magnet sectors. A pick-up coil will be used to monitor the rapid field variations.

The inductance of the superconducting solenoid is 0.4 H. The impedance is 2.4 Ω at 1 Hz or 0.24 Ω at 0.1 Hz. For a 2 mV voltage ripple at 1 Hz, the current ripple is 1 mA or 0.2 *ppm* for a total current of 5 kA. Therefore the field ripples for 2 mV 1Hz and 0.1 Hz voltage ripples are 0.2 *ppm* and 2 *ppm* respectively. Because of the low magnet inductance,

it is difficult to keep the current stable to 0.1 *ppm*. The random fluctuations will make the ripple effect smaller.

Figure 14.4.1: PIN diode switch for multiplexing 1:20 fixed probes.

We will use some level of multiplexing of the fixed probes to reduce the amount of electronics. (See Fig. 14.4.1) This will reduce the cost of the system but increase the measurement time. An overall measurement time of about one second will be quite adequate for our system.

14.4.2. Main Power Supply for the Storage Ring

The power supply (mfg. by Bruker) for the storage ring coil will be twelve phase rectifier output derived from two six phase units in parallel, see Fig. 14.4.2. This is followed by a passive filter and a series linear transistor bank regulator (504 transistors). An internal dc current transductor (DCCT) is used to measure and feedback a current signal to the transistor regulator. Low noise cabling, layout and dc reference techniques are employed to achieve precision and drift values specified at the level of <1 *ppm*. An external DCCT (mfg. by Danfysik) will be used to measure the output current independently with a precision of 1 *ppm*. The internal DCCT has an extra winding on its cores to enable an external NMR (nuclear magnetic resonance) correction signal. This will permit average field regulation for the storage ring.

The power supply operates in constant current mode with an adjustable voltage limit. The output voltage range can be from 1 to 5 volts. During charging of the magnet, a fixed voltage of 3 volts will be applied to the magnet coil. On reaching the desired current level,

Figure 14.4.2: *The*$(g-2)$ main magnet power supply and quench detection/protection system.

the power supply voltage will reduce and the supply will operate in its constant current mode. The NMR field input can be implemented at this time. On normal turn-off a set of reverse connected diodes (free wheeling diodes) will conduct the decreasing magnet current to zero.

The following are some of the specifications of the power supply:

Output Current:

6500 amperes, maximum

Local, remote and computer control with 10 *ppm* resolutions

Isolated external analog feedbhack range is +/- 100 *ppm*

Current Regulation <0.3 *ppm* - 30 minutes

Current Regulation <1.0 *ppm* - 8 hours

Noise < 0.1 *ppm* - 0.0 to 10 Hz

Output Voltage:

5 volts, maximum. Adjustment range 1 to 5 volts.

Output negative terminal will be grounded through a Ground Detection circuit.

Power Supply Interlocks:

Safety Loop - uses computer set temperature and current limits

Direct Loop - has overtemperature and overcurrent limits which are tied directly to the main contactor circuit.

Quench Protection:

A DC interrupter switch on the output will isolate the power supply from the magnet in case the magnet goes normal. The interrupter will be rated 6500 amperes at >300 volts and will be capable of being triggered by an external signal. In this case, the magnet current will be diverted through a 10 milliohm resistor in series with a high current diode, connected across the magnet terminals. The interrupter trigger will be derived from monitoring electronics that determine voltages across the various sections of the magnet windings and the cryogenically cooled magnet leads.

14.5. Absolute Calibration of NMR Probes

It is imperative to have a reliable method for absolute calibration of the NMR probes [10]. We will accomplish this with a few plunging NMR probes as secondary standards which can be moved in a plane normal to the muon beam direction under vacuum using a combination of a rotary vacuum feedthrough driving a worm gear and a linear translation feedthrough. A calibrated plunging probe will be inserted into the vacuum chamber through slot-shaped airlocks and into azimuthal gaps in the electric quadrupole electrodes. In this manner we will be able to locate the plunging probe to any of the positions occupied by one of the trolley probes in an azimuthal plane and make a comparison of their resonance frequencies. The plunging probe can be extracted from the chamber and calibrated in a straightforward way against laboratory standards [7]. Figure 14.5-1 shows the design of the standard probe.

Ultimately the absolute field value must be known in terms of the free proton resonance frequency. Care in construction of a standard probe to realize a spherical geometry and to avoid magnetic impurities may be adequate. The value for the ratio of the proton magnetic moment in a spherical sample of H_2O to the magnetic moment of the free proton is well known [11]. This diamagnetic shielding factor is $25.689(15) \times 10^{-6}$. The temperature dependence of this quantity is about 10 ppb/^0C [12].

Figure 14.5.1: Design of the spherical water probe for absolute calibration.

It should be noted that if the same standards are used at LAMPF [13] in determining μ_μ/μ_p form the muonium Zeeman effect, any errors in absolute calibration will be largely reduced in the determination of a_μ.

Conceptually the free proton is attractive and its magnetic moment is a fundamental constant. However, the magnetic moment of a free proton has not been measured directly with high precision. In general, when an external magnetic field H_o is applied on an atom or molecule, the magnetic field at the atomic nucleus, H_n, is modified by the electrons in an atom or molecule

$$H_n = (1 - \sigma) H_o$$

where σ is the diamagnetic shielding factor. Using a H maser and NMR a value of the proton moment (measured in water) in Bohr magnetons of μ_p'/μ_B has been determined and the shielding constant for water has been found to be [11]

$$\sigma (H_2O) = 25.790 (14) \times 10^{-6}$$

for a spherical sample of water at 34.7^{o}C. The temperature dependence of the diamagnetic shielding correction for proton NMR in a spherical pure water sample has been measured directly as $10.36(30) \times 10^{-9}\ {}^oC^{-1}$ (Ref. [12]). Therefore, a spherical H_2O sample can be used as a standard. The accuracy is limited to about 0.02 *ppm* due to the uncertainty of the measurement of $\sigma(H_2O)$.

The demagnetization effect of a sample depends on the susceptibility χ of the sample and also its shape:

$$(4\pi/3 - \varepsilon)\chi$$

where ε is a shape parameter. For a spherical sample the value of ε is $4\pi/3$ so that the shape correction is zero. The shape correction for a long cylindrical sample ($\varepsilon = 2\pi$) is 1.5 *ppm*. Therefore a spherical sample is preferred as a standard probe. It is difficult to make a small spherical sample which is completely filled with water. A tiny bubble may cause correction of about 10^{-8}. Variation in the diameter of a spherical probe by 1% will shift the NMR frequency by 0.024 *ppm*. Spherical probes have been constructed and tested for sphericity with an optical comparator. The magnetic field shift and field gradient caused by paramagnetic and diamagnetic material nearby have to be measured and calculated.

We also need a setup for calibrating various probes (plunging probes and trolley probes) calibration. Most of the potential sources of error are due to the problem of assuring that both the standard probe and the probe be calibrated experience the same magnetic field. We can calibrate NMR probes directly against a standard probe in the MRI superconducting solenoid at LAMPF which operates in persistent mode. It has a usable inner bore diameter of 70 cm. The field homogeneity is better than 1 *ppm* over 20 cm DSV and the stability of the field is better than 10^{-8}/hour. It is an ideal environment for the probe calibration.

Several standard probes have been constructed with an accuracy expected to be better than 0.1 *ppm*. The combined error in absolute calibration of an NMR probe should be 0.05 *ppm*.

14.6. References

1. G.T. Danby and J.W. Jackson, Muon ($g-2$) Note No. 001 (1987).
2. G.T. Danby and J.W. Jackson, Muon ($g-2$) Note No. 180 (1993).
3. K. Woodle, Muon ($g-2$) Note No. 123 (1992).
4. F. Krienen, Muon ($g-2$) Note No. 054 (1990).
5. W. Morse and K. Woodle, Muon ($g-2$) Note No. 065 (1990).
6. M.J. Fischer, Muon ($g-2$) Note No. 114 (1992).
7. G.T. Danby, W. Meng, W.B. Sampson, K. Woodle, Muon ($g-2$) Note No. 191 (1993).
8. U. Haeberlen, K. Jungmann, R. Prigl, G. zu Putlitz, P.v. Walter, Muon ($g-2$) Note No. 078 (1991).
9. R. Prigl, K. Jungmann, G. zu Putlitz, P. v. Walter, X. Fei, V.W. Hughes, M. Janousch, W. Liu, W. Schwarz, Muon ($g-2$) Note No. 161 (1993).
10. X. Fei, V.W. Hughes, Muon ($g-2$) Note No. 131 (1992).
11. W.D. Phillips et al., Metrologia 13, 179 (1977).
12. B.W.Petley and R.W.Donaldson, Metrologia, 20, 81 (1984).
13. V.W. Hughes, et al., LAMPF Experiment 1054.

Chapter 15.
Monitoring of the Stored Muon Beam

Revised August 1994

15.1. Introduction and Overview

The muon decay electron detectors provide substantial information on the beam inside of the storage ring. At early times the beam is bunched, with a base width of less than 10 ns, and a cyclotron period of $\sim$ 150 ns. Each detector reports counts for a brief period each time the bunch goes around the ring (the 'fast rotation' structure). Eventually the bunch spreads out After the initial injection, particles of lower momentum, which are at smaller radii, get ahead of those at higher momentum at larger radii, the beam debunches and fills the ring uniformly. The de-bunching is of interest, since one gains information on the mean radius by measuring the fast rotation frequency and information on the momentum distribution from the debunching process.

This method was used in the third CERN experiment [1] and the computer code developed by Hattersley [2] forms the core of the E821 fast rotation analysis. This method only provides information on the momentum distribution during the first 20 μs, since the fast rotation signal disappears once the beam has debunched. Should the muon distribution change significantly after the debunching time, using the distribution obtained from the fast rotation would introduce an error into the electric field correction which must be made to obtain ω_a.

More recently, Orlov and Soffer [3] have proposed measuring the distribution of rotation frequencies, and thus the muon momentum distribution, by Fourier analysis of the electron time spectra. They claim that with sufficient statistics, the momentum distribution at all times can be measured.

In addition to the electron detectors, there will be several other devices which will monitor the muon beam in the storage ring. Scintillating fiber monitors will be used to measure the beam profile during injection studies, and each time the storage ring is brought back on after a shutdown. Pickup electrodes will measure the moments of the distribution from injection until the beam debunches. In one non-standard vacuum chamber section, a set of wire chambers will measure the decay electron trajectories, and permit us to infer the muon distribution in the ring.

Each of these techniques is discussed in more detail below.

15.2. Scintillating Fiber Monitors

Scintillating fiber monitors to measure the beam profile in the storage ring are being designed and constructed at KEK. [4] A schematic of the overall system is given in Fig. 15.2.1, and sketches of the x and y planes are given in Fig. 15.2.2.

These monitors will be used to monitor the beam immediately after injection into the storage ring, especially during the commissioning of the ring, and when the experiment is brought on in the successive years for running. These monitors will be retractable, and will be removed from the storage region during normal data collection.

There will be two sets of $x - y$ monitors in the ring, one set at 180^0 and one at 270^0 (relative to the inflector exit) around the ring. See Chapter 22, §22.3 for a discussion of their use during commissioning.

The fibers in each plane are equally spaced in a "harp" configuration as can be seen in Fig. 15.2.2. Since the light output of each of the fibers will depend on the number of muons in the bunch passing through that fiber, the pulse height will be proportional to the beam intensity at the fiber location. For example, if 2×10^4 muons are stored in the 90 mm diameter storage aperture, a single fiber of 0.5 mm thickness will see about 40 muons in one revolution, which corresponds to 40 photoelectrons. Each fiber will be read out by a separate photomultiplier, since cross talk problems were encountered with multi-anode phototubes. [4]

Because cross calibration of the relative light yields of the different fibers is essential to obtain an accurate beam profile, it is necessary to have a procedure which can be carried out inside the storage ring. By rotating the "harps" by 90^0, it will be possible to place each fiber just downstream of the next, thus presenting the same portion of the beam to all fibers in a plane. This calibration position is shown in Fig. 15.2.2 for each plane.

These monitors will be quite useful during the intial injection studies, and also when the muon kicker is commissioned, since they will provide a pulse to pulse picture of the beam profile in the storage ring.

Two types of planes are being prepared, planes with seven 0.3 mm thick fibers, and planes with six 0.5 mm planes. Since the fibers are thin, ≤ 0.5 mm, and there are only a few fibers in each plane, the multiple scattering is small and one can monitor the beam for some number of turns before the beam is seriously degraded by these monitors. The beam lifetime from multiple scattering in the fibers is shown in Table 15.2.1, which should

Figure 15.2.1: Schematic View of the Fiber Monitor System

(.a)

(.b)

Figure 15.2.2: **(a)** The x profile monitor showing both the measurement position (upper) and the calibration (lower) positions. **(b)** The y profile monitor showing both the measurement position (left) and the calibration (right) positions.

Table 15.2.1: Beam lifetime τ_{sf} from multiple scattering in the scintillating fiber monitors.

Fiber Thickness (#)	# of planes	τ_{sf} due to scattering
$0.3\ mm\ \times (7)$	one	$1.3ms$
	two	$0.65\ ms$
$0.5\ mm \times (6)$	one	$0.56\ ms$
	two	$0.29\ ms$

be compared with the muon decay lifetime of $\gamma\tau = 64.4\ \mu s$ and the data collection time of $10\gamma\tau = 644\ \mu s$.

15.3. Monitoring of the Muon Beam with Pickup Electrodes.

15.3.1. Introduction to the Pickup Electrode Principle

The Pickup Electrodes will provide a real time picture of the moments of the muon distribution during data collection, in a non-destructive way. As discussed in Chapter 5, §5.2.1, in order to determine the average magnetic field seen by the circulating muons, it is necessary to know the moments of the muon distribution. [5] A scheme which was proposed to measure the muon moments [5] involves pickup electrodes which form a cylinder with its axis along the muon beam's path. The cylinder consists of 8 independent plates 1 m long, each of which is connected to a separate charge preamplifier. The signals are Fourier analyzed around the cylinder's azimuth in order to determine the moments of the muon distribution up to $N = 4$ for the cosine term and $N = 3$ for the sine term.

Figure 15.3.1: Cross section of the pickup electrode geometry

15.3.2. Hardware

The pickup electrodes will occupy a total of 120 *cm* of the $(g-2)$ ring azimuth. The design of the plates is intimately connected to the beam tube trolley design, and a final geometry will be possible only after the trolley design is finished. The cross section of the pickup electrodes is octagonal. There are eight plates, each $\sim$ 100 *cm* in length, four of the which resemble the quadrupole electrode geometry with the four others occupying the corners. In two of the corners, trolley rails will be added as needed (see Chapter 14). A cross section of the pickup electrodes is shown in Fig. 15.3.1. The supporting cage will be very much like the one used for the quadrupoles. [6] To lower the capacitance of the plates, the trolley rails will be non-metallic.

Figure 15.3.2: The low noise charge pre-amplifier design scheduled to be used in the readout of the pickup electrodes.

15.3.3. Electronics

The charge preamplifier was designed by the BNL instrumentation division, (see Fig. 15.3.2), and the signal to noise ratio for the prototype electronics was found to be adequate on a small prototype. The capacitance of the prototype plates was measured to be about 90 pF total. A full size model has been constructed and will be tested.

The prototype electronics showed promise of being able to resolve the muon distribution in real time, rather than having to average over a number of fills. The charge preamplifiers will be located in the vacuum chamber very close to the plates from which they pick up the charge, which is possible since they had sufficiently low magnetic susceptibility to be approved for use in the main field by the Suceptibility Sheriff. However, the packaging must be changed to meet the outgassing requirements of the ring vacuum system.

The signal from the preamplifier will be transferred to the voltage amplifier with semi-rigid, low loss high bandwidth solid copper coaxial tubes in order to minimize electronic pickup. These second-stage voltage amplifiers will be optimized for the best signal to noise ratio, and will be placed on the outside of the vacuum chamber for more flexibility.

A charge-integrating ADC (Analog to Digital Converter) and a personal computer will read, average, Fourier analyze and display the signals.

15.4. Muon Decay Electron Traceback

The electron traceback system consists of a set of wire chambers which measure the trajectory and momentum of decay electrons in one section of the storage ring. The goal is to propagate the electron back along its trajectory up to the point where its radial component of motion is zero. Leaving aside experimental errors for the moment, the distance of this point to the actual site of the muon decay is typically about 1 mm in the radial and vertical directions. As discussed in Chapter 4, §4.3, a knowledge of the muon phase space distribution is essential for performing the pitch and magnetic field corrections. Furthermore, it provides additional information to supplement the fast rotation data in determining the electric field correction.

Several guidelines have been observed in designing the chambers:

1. The chambers themselves should be made of low Z material to minimize multiple scattering. And, since the chambers themselves cannot be placed in the vacuum, whatever exit window the electrons must pass through before striking the chambers must likewise be made of some low Z material.
2. The arrangement of the chambers should be optimized for decay electrons with energies between 1.5 GeV and 2.5 GeV, where the traceback is most accurate. The highest energy electrons must be traced back the farthest (in fact the traceback distance becomes asymptotically infinite as the electron energy approaches its endpoint) which maximizes the destructive effect of errors caused by multiple scattering.
3. There is an inverse relation between the acceptance of the system and the separation of the chambers, but a direct relation between the accuracy of the momentum measurement and the separation.
4. The outer edge of the exit window should be placed at as large a radius as possible. Electrons which exit from the vacuum tank into the traceback chamber system at the largest radius have traveled the shortest distance and can be traced back with the greatest accuracy.

5. The acceptance of the traceback system will depend on the energy of the electrons, their initial radius and, to a small extent, their initial vertical position.

The accuracy of the traceback technique in obtaining the muon phase space distribution has been investigated with G2GEANT, our GEANT-based simulation program and TRACENON, which uses a slightly modified version of CERN's GEANE package to perform the traceback. The simulations have considered the effect of multiple scattering in the vacuum exit window and the chambers themselves, the effect of the intrinsic position resolution of the chambers, and the effect of the electron selection. The electron selection is determined by the positions and sizes of the exit window and the chambers. The exit window must be thin (0.5 mm) mylar or kapton foil. Each of the chambers must have a position resolution of 100 μm and have a thickness equivalent to no more than 200 μm of mylar. To reconstruct the (approximately) helical path at least three radial (horizontal) and two axial (vertical) coordinates are needed. To provide redundancy, four measurements of each coordinate are planned.

A diagram of the traceback system layout is shown in Fig. 15.4.1. The four chambers are separated by about 25 cm each. The last lies in front of a calorimeter station. The first lies directly behind a chamber exit window which is anchored by an aluminum flange. The window is 14 cm high and its edge extends outward to a radius of 701 cm and inward to 692 cm. Pushing the edge out further in the radial direction would require that the flange obstruct the tracks of high energy electrons headed for the next calorimeter station downstream. The vacuum wall is 2 cm thick as drawn, although this thickness has not been optimized. The thinner the vacuum wall, the more useful will be the data from the calorimeter station which lies just beyond the traceback system. A thinner vacuum wall will also mean a more difficult engineering job.

Although the exact results depend on the parameters of our chamber design and the choice of electrons in the sample, the typical reconstruction error in the vertical and radial directions is 3 mm. To obtain the muon phase space distributions we must also make acceptance corrections with the help of our simulation. Generally, the corrections are not large and their success should be limited by our knowledge of the fringe field and of the precise location of the various obstacles and detector components. Finally, we will need to model the betatron motion of the muons in order to deduce from this local measurement where the muons would be found elsewhere in the storage ring.

We have decided to make the traceback measurement with drift chambers, a well established technology which can provide the required position resolution. (The principal competition, the silicon microstrip detector, has excellent position resolution, but is too thick. The typical thickness is 300 μm, which is equivalent to 1000 μm of mylar. The traceback system requires four radial and four axial measurement planes: smaller (10 $cm \times$

Figure 15.4.1: Traceback system layout

15 cm) in front of the exit window and larger (25 $cm \times 15$ cm) in front of the calorimeter.

These dimensions make no particular demands on the construction of the drift chambers; in fact, the traceback system is not large. Although there are many different varieties of drift chambers, ones of the straw tube geometry may be appropriate. This type of chamber has typically a position resolution of 100 μ for a tube diameter of 10 mm. Straw tubes can be made from aluminized mylar with a wall thickness as small as 25 μm. Thus a stack of straw tubes can have the required resolution and thickness. The four horizontal and vertical planes require a system of about 400 tubes. Straw tubes have the advantage of a simple electric field configuration and independence of the tubes in a stack. The problem of the "right-left" ambiguity, in which the measured drift time can correspond to two positions, can be resolved by using a stack of tubes, the minimum number of layers in the stack is, of course, two. The non-uniform electric field, which results from the cylindrical geometry of the tube, implies that the relation between the drift time and the position of the track is very non-linear. As with other drift chamber geometries, the calibration of straw tubes requires careful consideration. In the traceback application there may be no method of calibration in place, since neither the momentum nor the vertex of the track is known a priori. Thus the calibration of the system must be done in a test beam, a less satisfactory situation.

Another major consideration in the design of the traceback chambers is the magnetic field. The uniform field extends only to a radius of 695 cm, but the traceback chambers must extend to a radius of 681 cm. Thus approximately half of the volume of the drift chambers lies in a highly non-uniform magnetic field. On the median plane outside the uniform field region, the field gradient is of the order of 500 G/cm at the position of the traceback chambers. Seven centimeters off the median plane the radial component of the field is as large as 500 G, and the direction is of the order of 20^o away from the vertical. These are unfavorable conditions for the operation of a drift chamber due to variation in the magnitude and direction of the drift velocity of the electron ionization.

For the measurement of the horizontal coordinate, the sense wires in the drift chamber run vertically, and the drift field lies in a horizontal plane. The drifting electrons then experience a Lorentz force which effects the direction of their drift. This phenomenon is well known in drift chambers and is described by the Lorentz angle, the angle between the velocity vector of the drift electrons and the electric field. Chamber gases with high (low) drift velocity tend to have large (small) Lorentz angles. Since the Lorentz angle and the electron mobility depend, in general, on both the electric and magnetic field, in a non-uniform magnetic and electric field, the relation between the track position and direction and magnitude of the drift velocity is complicated. The same problem arises in the measurement of the vertical coordinate where the sense wires run horizontally, and the drift field is in a vertical plane. Off the median plane the radial component of the

magnetic field again causes a Lorentz force. Thus the relation between drift time and the track coordinate will depend on the location of the track. As the design of the traceback chambers continues, the drift time in the non-uniform magnetic field will be simulated.

The effect of the non-uniform magnetic field can be minimized by the choice of chamber gas. A "slow" chamber gas, e.g. CO2-isoC4H10, has a small Lorentz angle regardless of the fields. With a "slow" gas the maximum drift time in a 1 cm straw tube will then be of the order of 500 ns. The estimated number of calorimeter hits per spill for muon injection is 240. The probability of more than one hit within a 500 ns gate, 20 microseconds after injection, is 30%. This is not a large probability; however, for successful track reconstruction, there must be few extraneous hits in the chambers. As mentioned above, extraneous hits are expected from decay electrons which shower in the wall of the vacuum tank, an effect which will be investigated in some detail with our simulation program. The calibration of the traceback system must be done in a non- uniform magnetic field, and, ideally, the field profile should be identical to the field profile of the ring. Thus the fringe field of the ring must be mapped and a test beam magnet must be constructed to reproduce this field. Position resolutions of 100 μm and better have been reported for drift tube systems with **B** fields as non-uniform as our own, but obtaining such accuracy with this chamber system will undoubtedly be challenging.

One should note that if the chambers can be made to work at early times (perhaps by reducing the intensity) we can study the debunching directly with the traceback system.

15.5. Measurement of the Muon Momentum Distribution

Precise knowledge of the muon momentum distribution is needed to calculate the largest correction in the $(g-2)$ experiment, the error caused by the electric field in the presence of a spread of muon momenta. This correction is 0.69 ppm and we need to know this correction to about 10% to eliminate its influence on the systematic error on ω_a (see Chapter 4 §4.3.6). The CERN experiment used the fast rotation of the unbunched beam to study the momentum distribution which has been documented by Hattersley. [2] More recently it has been proposed that a Fourier analysis of the time spectra from the electron detectors can provide better information on the momentum distribution.

Fourier analysis is a powerful tool to extract the frequency content from a signal, and the techniques are well understood numerically. [7-9] However, one should be aware that Fourier analysis, while widely used in signal processing, does have its limitations. [10] Fourier analysis works best when a few discrete frequencies are present. When the situation is more complicated, it is a general practice to make a model of the signal and to try to

fit the signal directly in the time domain. This technique avoids the bandwidth problems associated with the Fourier spectrum, as well as problems associated with going from a continuous to a discrete transform (see Ref. 8). This is, of course, the tack taken in the fast rotation analysis, where one assumes a model for the radial distribution and then calculates the observed time spectrum of decays during the debunching. While it is true that numerical Fourier techniques are both very powerful and well understood, [8,9] one must take care to understand the limitations of the technique in each specific application. [10]

15.5.1. The Momentum Distribution I: Fast Rotation Analysis

15.5.1.1. The Fast Rotation: General Principles

The bunch of particles injected into the storage ring has a radial distribution over the whole of the aperture but a very narrow time width ($\sim 10\ ns$) which is much less than the rotation time (149 ns) of the particles in the ring. Since all particles travel at essentially the speed of light, those at inner equilibrium radii will get steadily ahead of those at outer equilibrium radii. Thus the time distribution of particles on subsequent turns exhibits an ever increasing width which is directly related to the initial distribution, and which depends mainly on the initial radial distribution. The effect of betatron oscillations can be neglected. If we call the betatron deviations r_B and z_B, the linear r_B/R term is averaged after the first 10 turns, and the quadratic terms $\left(r_B^2 + z_B^2\right)/R^2$, are very small.

The assumption that the radial distribution is constant in time is not true for genuine data; there is an exponential fall-off due to muon decay, which gives a reduction in rate of about 15% over the analysis time, and there is also the ω_a modulation. The analysis program, REVFR, [2] is set up to deal with a constant average rate in the analysis, so the number of counts is multiplied by $e^{t/64.4\mu s}$ to correct for muons lost by decays. In addition, the data are smoothed to bring the general level down to that at the end of the analysis period, which results in a small overestimate in the statistical errors.

With these assumptions and with a know input distribution, it is easy to calculate the time distributions of muons seen in each subsequent revolution of the muon bunch in the storage ring. The distribution is divided into radial bins and from the known rotation time the relative positions (that is the bunch lengths) are calculated on subsequent turns. After a number of turns, the inner edge will have caught up with the outer edge of the previous turn; the peaks will overlap, the picture will be more confused and the time-histogram will tend to smear out. However, the calculation is still quite possible – the only difference being that two (and eventually 3,4, etc.) radial bins will contribute to some of the time

bins; the contribution of any radial bin to any time bin is still directly calculable. The time limit comes in principle when a radial bin starts to overlap itself; however the information content in the time histogram is very small long before this occurs, and in practice it seems that it is only worth analyzing data to about twice the overlap time.

The reverse calculation, *i.e.* the determination of the input distribution from the time-histogram, is not so straightforward. Firstly, one must make some assumption as to the input time shape; this fortunately appears not to be critical. Secondly, the final results are needed in the process of calculation; however, by an iterative procedure it is possible to get successively better approximations and in practice it turns out that only one repetition is necessary to reach the accuracy warranted by the data.

The output of REVFR is a parameterization of the input radial distribution normalized to the maximum bin. In order to compare the output distribution with that originally put into the Monte Carlo data generation program, the mean radius is found, together with its standard deviation and the rms width of the distribution. The input and output histograms are also compared directly: an agreement factor is given which consists of the sum of the squares of the deviations weighted according to statistics, and the change in ω_a due to the distribution is given, together with the error in comparison with the input distribution.

15.5.1.2. The Mathematical Details

For the fast rotation analysis, we suppose that the storage aperture is divided into I radial (momentum) bins with the suffix i. Let the contents of the radial bins be f_i; it is this distribution f_i which we want to determine.

We observe the histogram in time and we denote the time bins with the suffix j. Let the counts we observe in bin j be N_j, which form the input data.

The expected contribution from radial bin i to the counts in time bin j is

$$f_i \beta_{ij} \tag{15.5.1}$$

where β_{ij} is a geometrical factor which can and must be calculated separately for each combination of i and j. [11]

We must choose the population of the radial bins, f_i to give maximum agreement between the expected counts, C_j, and the observed counts, N_j, in all time bins. For each time bin j. The expected number of counts is

$$C_j = \sum_{i=1}^{I} f_i \beta_{ij}.$$

We wish to minimize χ^2 where

$$\chi^2 = \sum_j \frac{(C_j - N_j)^2}{Z_j} = \sum_j \frac{(\sum_i f_i \beta_{ij} - N_j)^2}{Z_j}.$$

Z_j is a weighting factor which should equal the expected counts in bin j. Since the Z_j are initially unknown, we replace them by the N_j in the first pass, taking precautions when they are zero. With the f_i so obtained we carry out a second pass with

$$Z_j = \sum_i f_i \beta_{ij}$$

Experience shows that a third pass does not appreciably alter the results, provided the process converges at all.

To minimize χ^2 by adjusting the $f_n (n = 1, 2, ...I)$ we require

$$\frac{\partial \chi^2}{\partial f_n} = 0$$

for each n. In differentiating χ^2 we assume that the denominators, Z_j are constant, which is not strictly true. However, since the numerators change much faster with f_n than the denominators, it is a good approximation.

We get

$$\frac{\partial \chi^2}{\partial f_n} = \sum_j \left[\frac{[\sum_i f_i \beta_{ij} - N_j] \beta_{nj}}{Z_j} \right] = 0$$

Hence

$$\sum_j \left[\frac{\sum_i f_i \beta_{ij}}{Z_j} \right] = \sum_j \frac{N_j \beta_{nj}}{Z_j}$$

which, upon reversing the order of summation gives

$$\sum_i f_i \sum_j \left[\frac{\beta_{ij} \beta_{nj}}{Z_j} \right] = \sum_j \frac{N_j \beta_{nj}}{Z_j} \qquad (15.5.2)$$

Eq. (15.5.2) represents a set of equations, one for each n, *i.e.* we have I equations for I unknown values of f_i. We solve the equations iteratively to obtain the f_i. The procedure can be represented schematically as:

1. first pass, with $Z_j = N_j$
2. second pass, using the f_i of the first pass and $Z_j = \sum_i f_i \beta_{ij}$.

The I values of f_i can then be used in the so-called electric field corrections, which corrects ω_a for the fact that not all muons have energies which correspond to the magic gamma.

15.5.2. The Momentum Distribution II: Fourier Analysis

From the basic formula,

$$\vec{\omega}_a = \frac{e}{mc}\left[a\vec{B} - \left(a - \frac{1}{\gamma^2 - 1}\right)\vec{\beta} \times \vec{E}\right], \tag{15.5.3}$$

where $\beta = v/c$, we can derive the expression for the electric field correction:

$$\frac{\Delta\omega_a}{\omega_a} = -2\langle\frac{\gamma - \gamma_m}{\gamma_m}\frac{p - p_0}{p_0}\rangle\frac{1}{2\pi}\int_0^{2\pi}\psi\left(\theta\right)n\left(\theta\right)d\theta, \tag{15.5.4}$$

where $\gamma_m = \left(\frac{a+1}{a}\right)^{1/2}$ is the magic energy; p_0 is the muon momentum corresponding to the central orbit with the radius R_0, $E(R_0) = 0$; $n(\theta)$ is the actual (not average) field index as a function of azimuth θ,

$$n\left(\theta\right) = |\left(\frac{R}{\beta B}\right)\left(\frac{\partial E_R\left(\theta\right)}{\partial R}\right)|\ ; \tag{15.5.5}$$

$\psi(\theta)$ is a familiar function in accelerator physics, defining the equilibrium orbit vs. momentum:

$$\frac{R\left(\theta\right) - R_0}{R_0} = \psi\left(\theta\right)\frac{p - p_0}{p_o}; \tag{15.5.6}$$

$$\overline{\psi\left(\theta\right)} \equiv \frac{1}{2\pi}\int_0^{2\pi}\psi\left(\theta\right)d\theta = \alpha \tag{15.5.7a}$$

$$\frac{\Delta L}{L} \equiv \frac{\overline{R\left(\theta\right) - R_0}}{R_0} = \alpha\frac{p - p_0}{p_0} \tag{15.5.7b}$$

and α is the compaction factor, which relates the momentum spread Δp to the circumference spread ΔL, and is defined by [12]

$$\frac{\Delta L}{L} = \alpha\frac{\Delta p}{p_0}$$

which appears in Eq. (15.5.7b). Bars designate kinematic averages over some intervals of the ring, and brackets designate statistical averages.

The integrand in Eq. (15.5.4) is non-zero only inside a focusing quad. Let n_Q, ℓ_Q, $\psi_Q(\theta)$ be the internal field index, length, and ψ-function of a quad. Then,

$$\frac{1}{2\pi}\int_0^{2\pi}\psi\left(\theta\right)n\left(\theta\right)d\theta = n_Q\frac{\ell_Q}{\ell_Q + \ell_F}\overline{\psi_Q} = \frac{\overline{n}}{\ell_Q}\int_0^{\ell_Q}\psi d\ell = \overline{n}\overline{\psi_Q}, \tag{15.5.8}$$

ℓ_F is the interval between quads. Note that $\overline{\psi_Q} > \overline{\psi(\theta)} = \alpha$ because the ψ-functions inside a focusing lens are always bigger than between lenses. We can now rewrite Eq. (15.5.4) in the form

$$\frac{\Delta\omega_a}{\omega_a} = -2\overline{n}\overline{\psi_Q}\langle\frac{\gamma - \gamma_m}{\gamma_m}\frac{p - p_0}{p_0}\rangle, \quad \overline{n} = \frac{1}{2\pi}\int_0^{2\pi}n\left(\theta\right)d\theta. \tag{15.5.9}$$

In the muon $(g-2)$ experiment, the value $1/\gamma^2$ is much less than the accuracy needed to correct the error $\Delta\omega_a/\omega_a$. For this reason, in Eq. (15.5.9) let $\beta \cong 1$, $pc \cong \gamma$, and for muon revolution frequencies,

$$f = 1/T = v/L \cong c/L, \quad L = 2\pi\overline{R}, \tag{15.5.10a}$$

$$\frac{\Delta f}{f} = \frac{\Delta v}{v} - \frac{\Delta L}{L} = \left(\frac{1}{\gamma^2} - \alpha\right)\frac{\Delta p}{p} \cong -\alpha\frac{\Delta p}{p} = -\alpha\frac{\Delta\gamma}{\gamma}. \tag{15.5.10b}$$

Thus, in Eq. (15.5.9) we can use γ instead of p, and vice versa; also, we can let $\gamma_0 = \gamma_m$ in the denominator. From Eq. (15.5.10) we get another expression for $\Delta\omega_a/\omega_a$:

$$\frac{\Delta\omega_a}{\omega_a} = -2\overline{n}\frac{\overline{\psi}_Q}{\alpha^2}\langle\frac{(f-f_m)\,(f-f_0)}{f_m^2}\rangle$$

$$= -2\overline{n}\frac{\overline{\psi}_Q}{\alpha^2}\left[\langle\left(\frac{\Delta f}{f_m}\right)^2\rangle + \langle\frac{\Delta f}{f_m}\rangle\frac{f_m - f_0}{f_m}\right] \tag{15.5.11a}$$

$$= -2\overline{n}\frac{\overline{\psi}_Q}{\alpha^2}\left[\langle\left(\frac{f}{fm}\right)^2\rangle - \langle\frac{f}{f_m}\rangle\left(1 + \frac{f_0}{f_m}\right) + \frac{f_0}{f_m}\right], \tag{15.5.11b}$$

where $\Delta f = f - f_m$ with f_m, the frequency associated with the "magic momentum" as the central frequency. Again, we can use L instead of f, and vice versa.

Approximately (but only for evaluations),

$$\overline{\psi}_Q/\alpha^2 \sim (1-\overline{n})\,. \tag{15.5.12}$$

Here f_m is the frequency associated with the "magic momentum", f_0 is the frequency associated with the actual central momentum. The difference between f_m and f_0, which is not desired, can occur if the central magnetic field is not correctly set.

We plan to use (and compare results of) two methods of measuring $\langle\frac{f}{f_m}\rangle$ and $\langle\left(\frac{f}{f_m}\right)^2\rangle$.

1. The CERN approach [1,2], which was described in the previous section, is based on the observation of the muon debunching in the storage ring. This observation is possible only during a rather small part of the muon lifetime, namely, after the scraping and before the actual spreading of the bunch over the ring, some 50 turns compared with the 400 turns per muon lifetime of 64.4 μs.
2. The new method [3] described below which employs a weighted Fourier analysis of the decay electrons. This method can be applied to the whole period after scraping ($\sim 10\tau$); the longer the duration of the analyzed signal, the better, because the phenomenon on which this method is based is a resonance in a specific sense.

The general theory of this method is given in Ref. 3; here we present a qualitative explanation.

Figure 15.5.1: Schematic of a ring with only one counter.

For clarity of the physical picture, let us consider an initially short bunch of muons injected at time zero onto azimuth $z_0 = 0$, where a single counter C is placed (Fig. 15.5.1). We can assume that after injection, the muons are decaying either outside the counter (which has effective azimuthal size, $\pm\delta z$) and, therefore, are not counted at all, or at point $z_0 = 0 \pm \delta z$, and only in that case are counted. In reality, of course, the counter gathers electrons from some area upstream of the ring. There are two points to note. First, the decay electrons are moving so closely to the muon trajectories ($v = c$ and $\varphi \ll 1$, see Fig. 15.5.1) that their signals come almost simultaneously with those from muons decaying just at $z = z_0$. Second, the average difference in time can be computed and the appropriate correction incorporated into the results; third, and most important, this time difference represents merely a general shift of the time axis and is not essential *if* we measure a distribution of electron signals in time always relative to the first electron signal at C. (For a more detailed definition of time zero for the Fourier analysis of decay electrons, see Ref. 3.)

Thus, every time t_n that an electron hits the counter, we can take the case as a signal from a muon passing the counter (only once in its lifetime).

Figure 15.5.2: Signals from different muons having the same special frequency

Obviously,

$$t_n = Tn_{\rm rev} = n_{\rm rev}/f, \tag{15.5.13}$$

where $n_{\rm rev}$ is the number of the muon's revolutions before its decay, and f is its individual frequency. The Fourier analysis in this case includes calculation of the product of the muon signal, $\delta N_\mu(t_n)$ which is the number of muons giving a signal after n revolutions, and a harmonic function $\cos\omega t_n$ with some arbitrary ω. One then calculates the sum, $F(\omega)$:

$$F\left(\omega\right) = \sum_{n=0}^{n_{\max}} \delta N_\mu\left(t_n\right) \cos\omega t_n\,. \tag{15.5.14}$$

In our case, $t_{\max} = n_{\max}T \sim 10\gamma\tau$, where $\gamma\tau = 64.4\ \mu s$ is the muon lifetime.

Muon signal $\delta N_\mu(t_n)$ contains, in general, a sum of signals from different muons with different momenta p, i.e., with different revolution frequencies f. Among them there can exist the special frequency (relative to the given ω):

$$f = \omega/2\pi q, \quad T = q\frac{2\pi}{\omega} \tag{15.5.15}$$

where q is an integer.

Figure 15.5.3: Signals from different muons having the same non-special frequency

Signals from different muons having the same special frequency are summarized in Eq. (15.5.14) with the same phases of $\cos \omega t_n$, see Fig. 15.5.2.

$$[F(\omega)]_{f=\frac{\omega}{2\pi q}} = [\delta N_\mu(0)]_{f=\frac{\omega}{2\pi q}} \sum_{n=0}^{n_{\max}} e^{-nT/\tau} \approx \frac{[\delta N_\mu(0)]_{f=\omega/2\pi q}}{\left(1-e^{-T/\tau}\right)} \tag{15.5.16}$$

where the assumption has been made that $n_{max} \to \infty$.

Signals from different muons having the same <u>non-special</u> frequency are summarized with <u>different</u> phases of $\cos \omega t_n$ (see Fig. 15.5.3, where $T < T_{\text{res}}$). In the general case, when $T = 2\pi q/\omega + \delta T$,

$$[F(\omega)]_f = [\delta N_\mu(0)]_f \cdot \sum_{n=0} e^{-nT/\tau} \cos \omega n T \tag{15.5.17a}$$

$$\cong \frac{[\delta N_\mu(0)]_f}{\left(1-e^{-T/\tau}\right)} \left[\frac{1+e^{-T/\tau}\omega^2 \delta T^2/2\left(1-e^{-T/\tau}\right)}{1+e^{-T/\tau}\omega^2 \delta T^2/\left(1-e^{-T/\tau}\right)^2}\right] \tag{15.5.17b}$$

the approximation in Eq. (15.5.17b) being valid for $\omega \delta T << 1$. Far from the special frequency, $\mid \delta T/T \mid \gg 1/\omega\tau$, or equivalently $\omega \delta T >> T/\tau$, Eq. (15.5.17) gives

$$\frac{[\delta N_\mu(0)]_f}{\left(1-e^{-T/\tau}\right)} \cdot \frac{T}{2\tau} \to 0 \text{ when } \tau \to \infty. \tag{15.5.18}$$

since $\delta N_\mu(0) \sim T/\tau$ also.

We should compare Eq. (15.5.18) and Eq. (15.5.16). Note that $T/2\tau \sim 10^{-3}$. Thus, for $|\frac{\delta f}{f}| \gg \frac{1}{\omega\tau}$, the non-special frequencies will be averaged and $F(\omega)$ will be proportional to the relative number of muons with revolution frequencies $f = \frac{\omega}{2\pi q}$. That is the main idea of this method.

However, the accuracy of the reconstruction of muon momentum (or frequency) distribution is limited by the finite muon lifetime. Two spectrum lines, f_1 and $f_2 = f_1 + \delta f$ can be separated only if

$$|\frac{f_2 - f_1}{f}| \gg \frac{1}{\omega\tau} = \frac{1}{2\pi q f \tau}, \tag{15.5.19}$$

with $f\tau \approx 400$. If $q = 1$, for example, the errors of reconstruction exceed 30%. The use of the highest q's (i.e., highest ω's) for the Fourier analysis needs much bigger statistics.

The solution of this problem is to analyze a weighted signal $\delta N_\mu(t)$. If, instead of $\delta N_\mu(t)$, we use

$$e^{+t/\tau}\delta N_\mu(t),$$

then the limitation Eq. (15.5.19) will be eliminated. As a price for this we will need bigger statistics because the relative fluctuations of $\delta N_\mu(t)$ (not shown in Fig. 15.5.2 and Fig. 15.5.3) grow exponentially in time and our factor $e^{t/\tau}$ increases the level of those fluctuations.

Also, we need to use an additional weight function in order to eliminate from our spectrum the side bands created by spin precession which modulates the electron signal intensity at the counter. We can clearly see these FM side bands in Fig. 15.5.4a (the result of simulation). They distort the tails of the distribution we have sought.

Simply stated, any components such as the exponential decay or the $(g-2)$ modulation which make the background over the time region to be analyzed not flat, need to be taken out before the Fourier analysis is carried out to obtain the distribution of rotation frequencies. This is the purpose of the weighting function given below.

The final weighted signal that we will analyze will be

$$S(t) = \frac{e^{t/\tau}\delta N_\mu(t)}{1 + A\sin(\omega_a t + \phi)} = W(t)\,\delta N_\mu.(t) \tag{15.5.20}$$

where A and ϕ will be taken from the very earliest results of $(g-2)$ measurements. Fig. 15.5.4b shows the spectra for different q's, and Fig. 15.5.5 a result of a simulation for $q = 1$, $A = 1/3$, $\phi = 0$. The full number of muons N was equal to 10^8 with 24 counters over the ring. The initial bunch had the azimuthal length 6m and the (arbitrary) muon frequency distribution used in the simulation was deliberately chosen to be complicated and asymmetric. Zero time corresponds to the condition,

$$\langle \sin\theta_{0k} \rangle = 0, \tag{15.5.21}$$

15.6.4a

15.6.4b

Figure 15.5.4: **a** The frequency spectrum showing the side bands from the muon spin precession. **b** The frequency spectrum for different q's.

Figure 15.5.5: The result of a simulation for $q = 1$, $A = 1/3$, $\phi = 0$.

where θ_{0k}, $k = 1\ ,\ \ldots\ , N$, are initial azimuths of different muons. The accuracy of the reconstruction of the initial revolution frequency distribution is about 0.3%.

15.6. References

1. J. Bailey et al., Nucl. Phys. **B150**, 3036 (1982).
2. Peter Hattersley of the CERN3 collaboration has kindly provided us with a copy of his fast rotation code.
3. Y.F. Orlov and A. Soffer, *Precise Measurement of Muon Momentum Distribution Using Fourier Analysis of Decay-Electrons*, *Muon g-2 Note No. 128*, 1992.
4. Yoshihiko Mizumachi and Takahiro Sato, *Concept of a Muon Profile Monitor with Scintillating Fibers*, *Muon g-2 Note No. 192*, April 1994.
5. F.J.M. Farley and W.P. Lysenko, *The Muon Distribution and the Average Field*, *Muon g-2 note No. 23*, September 1985.
6. Y.K. Semertzidis, *Minutes of the Quadrupole Meeting of August 18, 1993*, *Muon g-2 Note No. 169*, August 1993.
7. Ronald N. Bracewell, *The Fourier Transform and Its Applications*, second edition, revised, McGraw-Hill, Inc. 1986.
8. E. Oran Brigham, *The Fast Fourier Transform*, Prentice- Hall, Inc. 1974.
9. William H. Press, Brian P. Flannery, Saul A. Teukolsky and William T. Vetterling, *Numerical Recipies, The Art of Scientific Computing*, Cambridge University Press, 1989.
10. T. Miller, private communication, 1993.
11. For the details of the calculation see R. Carey, *The Fast Rotation Analysis*, *Muon g-2 Note* in preparation summer 1994.
12. See D.A. Edwards and M.J. Syphers, *An Introduction to the Physics of High Energy Accelerators*, J. Wiley & Sons, 1993, p. 89-91.

Chapter 16.
Electron Detectors

Revised July 1994

16.1. Measurement Overview

The muon anomalous magnetic moment, $(g-2)$, is determined from the measured precession rate of the muon spin $\omega_a = 2\pi f_a$ in a uniform magnetic field, by fitting to the time distribution of detected muon decay electrons in a given energy bin. The useful time span is ten muon lifetimes, or 640 μs.

Muons are held in the storage ring at the "magic" momentum of 3.1 GeV/c ($\gamma = 29.3$). The average spin polarization magnitude is better than 95% and is initially directed anti-parallel(μ^+) or parallel (μ^-) to the muon momenta. The ring radius is 711.2 cm and the B field is 1.45 T. The spin rotates with a frequency $f_s = 6.944$ MHz about the vertical magnetic field direction, while the cyclotron frequency is $f_c = \frac{eB}{\gamma mc} = 6.715$ MHz. The net rotation of the muon spin relative to its momentum ($(g-2)$ precession frequency) is $f_a = f_s - f_c \approx \frac{aeB}{mc} = 0.229$ MHz, where $a = \frac{g-2}{2} \approx 1 \times 10^{-3}$ is the muon anomaly. In the decay process, the electron (or positron) will have energies between 0 and 53 MeV in the muon rest frame(hereafter called *"CM"*). Since the lab energy ranges from 0 to 3.1 GeV, almost all decay electrons will be swept by the magnetic field to smaller storage radii, where they can be detected.

The time distribution averaged over all decay electrons is a pure exponential, but if the detected decay electron data are divided into energy bins, the exponential will be modulated at the precession frequency

$$N = N_0 e^{(-t/\gamma\tau)}\{1 + A\cos(\omega_a t + \phi)\} \tag{16.1}$$

where $\gamma\tau = 64.4\mu s$ is the dilated muon lifetime, $\omega_a = 2\pi f_a$, and A is the energy-dependent asymmetry. To see how these oscillations come about, consider for example a band of the highest energy electrons, $E(lab) > 2.5$ GeV. These can only be produced by electrons with CM energy $E(CM) > 43$ MeV and with directions $\Theta(CM)$ within 52 degrees of the muon momenta. Because the direction of electrons with $E(CM) > 43$ MeV is highly correlated

Figure 16.1.1: The magnitude of the decay electron asymmetry, A, versus energy.

to the muon spin direction, the number of electrons with $E(lab) > 2.5$ GeV oscillates with a frequency f_a as the spin precesses with respect to the muon momentum.

The overall asymmetry parameter A is the product of the stored muon polarization (which in our case is better than 95%) and the average asymmetry in the detected muon decay electrons. The asymmetry depends on the lab energy of the electron, being a maximum of 1 for the highest energy electrons, dropping to zero at about 1.2 GeV in the lab frame, and decreasing to $-\frac{1}{3}$ at $E = 0$ (see Fig. 16.1.1).

The statistical error in the measured $(g-2)$ frequency, when data are collected over many lifetimes, is given by:

$$\frac{\Delta\omega_a}{\omega_a} = \frac{\sqrt{2}}{A\omega_a\gamma\tau\sqrt{N_e}} \tag{16.2}$$

where N_e and A are the total number of detected decay electrons and their average asymmetry, respectively, in a given energy band. The statistical weighting of an ensemble of

Figure 16.1.2: The relative number of decay electrons per unit energy, N, versus energy.

decay electrons for determining ω_a is thus given by $N_e A^2$. The detector design goal, then, is to choose a detector system which maximizes $N_e A^2$ over the ensemble of detected electrons, within reasonable cost constraints. In Fig. 16.1.1, Fig. 16.1.2, and Fig. 16.1.3 we show the differential asymmetry, the relative number of electrons, and differential $N_e A^2$ as a function of the lab electron energy. $N_e A^2$ reaches a maximum at about 2.6 GeV, with a broad peak ranging from about 1.6 to 3 GeV. The detector system was designed for optimum acceptance and energy resolution in this energy range, although only about 14% of all decay electrons fall above 1.6 GeV. Note that there is a secondary peak in $N_e A^2$ at low electron energies. However, the average asymmetry is low while the relative number of electrons is high. Detecting such low energy electrons efficiently would require a much more expensive detector: much larger geometric coverage of the inside of the storage ring, good energy resolution at these lower energies as well as at higher energies, and higher rate capability. As is discussed later in this document, pileup and time and pulse height

Figure 16.1.3: The differential NA^2 for decay electrons, which gives their relative statistical significance, as a function of electron energy.

stability are potential problems at very high rates. We have chosen to design a system which has good acceptance for the high energy electrons, where the quality of data per electron is highest. The approach in the CERN III experiment was similar; they combined all electron data for $E_e > 1.8$ GeV. The integral distributions of A, N_e and $N_e A^2$ for all electrons above a given energy threshold versus threshold are shown in Fig. 16.1.4 and Fig. 16.1.5. These plots show curves for various radial widths of the calorimeter, with our current design having a width of 22.5 cm. The outer radial side of the calorimeter should be as close to the storage region as possible in order to minimize the number of electrons which miss the calorimeters altogether and to minimize the average time for the electron to arrive at a calorimeter. [1]

Since the highest-energy electrons have the highest average asymmetry, we could in principle gain additional statistical precision by dividing the data above about 1.6 GeV into smaller energy bins, and fitting for the precession frequency for each bin. Only modest

Figure 16.1.4: The number of decay electrons detected versus the energy threshold on the calorimeter. This is given for several widths of the calorimeter. N = relative number of electrons above threshold.

energy resolution is required, and with the expected detector energy resolution of around $11\%/\sqrt{E}$, we expect about 15% statistical improvement with energy binning of the data. However, dividing the data into smaller bins increases the potential systematic error in $(g-2)$ due to rate-dependence in the electron energy measurements.(see Ref. 1). High energy electrons travel farther in the ring and therefore have a longer "drift time", the time interval between muon decay and electron detection, than low energy electrons. If the energy gain of the detectors varied from early to late times in the spill, then, for a given electron energy bin, the true average energy in the energy bin will be slightly different at early and late times, the average drift times will be slightly different, and a timing error will be introduced. In order to minimize this problem, it is most likely that we will combine the data into one large bin, above about 1.6 GeV, in which case gain shifts need to be

Figure 16.1.5: The integral value for NA^2 (= relative statistical significance) as a function of the energy threshold on the calorimeter. This is given for several values of the detector width. Note that NA^2 vanishes for all electrons at zero threshold, but does not vanish for detected electrons, since the detectors preferentially miss low energy electrons.

controlled to about 0.2%. [1] The average asymmetry for these electrons is about 0.4, and as noted previously, the fraction of all decays detected would be about 14%.

Ultimately, the frequency of muon precession must be compared to the spin precession frequency of a proton (NMR probe) in the same magnetic field. The ratio of the clock frequencies for the detector and that of the NMR system must be kept very stable. Furthermore, the clocks which drive the electronics must themselves be stable to better than 0.1 ppm at all times. The electronics clock will be a highly stable oscillator, phase-locked to the same LORAN-C module as the NMR probes.

16.1.1. Measurement Apparatus

In order to reach our goal of 0.35 ppm measurement of $(g-2)$, we must detect about 2×10^{10} electrons above 1.6 GeV, which will require about 1×10^{11} stored muons. We must restrict systematic errors in the average detection time of the electrons to 0.1 ppm in order to keep their contribution to the overall error small. This implies that we must keep the systematic error in timing below 20 ps for any 200 μs segment of decay data, and below 60 ps over 10 lifetimes (64.4 μs=1 lifetime), after which there are very little data.

It is worth emphasizing that in order to control systematic errors in our $(g-2)$ measurement, we must avoid shifts in timing at early muon decay times compared to late decay times, *on average*. For example, individual electron arrival times will be measured to the nearest 5 ns time bin, which is the TDC+derandomizer least count. But the time of arrival averaged over a very large number of decays must be good to 20 ps. This means we must have excellent control over rate dependent shifts in the averages for PMT transit time, discriminator response, and time boundaries in our clock system. If all of these were to shift by a small constant amount from one spill to the next, it would not affect the measured $(g-2)$ frequency. Such a shift would simply introduce a shift in phase for that spill, but not a shift in the measured $(g-2)$ frequency. However, a systematic effect from early to late times in the spill would lead directly to an error in the $(g-2)$ frequency.

For the case of pion injection, a 10 ns wide bunch of about 10^7 pions is injected into the ring. Some decay into muons, but most are lost to collisions with the vacuum chamber, quads, inflector, etc. This produces an intense "prompt flash" in the detectors which can blind the PMTs. Therefore, we have designed special bases which greatly reduce the PMT gains during the flash. The gain must return to normal within a few microseconds so that timing and energy measurements can begin as soon as possible after injection. The CERN III experiment experienced, in addition to the "prompt flash", a fairly substantial "delayed flash" which produced a large DC offset in the PMT output lasting tens of microseconds after injection. They attributed the delayed flash to the effect of secondary neutrons bouncing around the area of the detectors. In pulsed beam studies by our group at BNL we saw a large long-lived tail following the flash when the PMT was directly in the pion beam, but the tail was absent when the PMT was pulled out of the beam, whether the scintillators or lightguides were directly in the beam or not. In separate tests, we found that the PMT analog signals had long tails when placed near a strong radioactive source, indicating that the PMTs themselves are quite sensitive to passing radiation. We expect to conduct further tests with pulsed test beam in August 1994 with our "final" prototype detector elements. We also plan to place the PMTs in E821 so as to minimize their exposure to traversing charged particles.

At injection time, the muons are bunched spatially over about a 20 degree arc in the ring, corresponding to the 10 ns time width of the injection pulse. Owing to the momentum range of stored muons, the muons spread out around the ring, and the bunching structure is gone after about $40\mu s$. We plan to measure the rate of debunching in order to deduce the momentum distribution of stored muons. In order to make an effective measurement of the muon momentum distribution, we must begin timing of the muon decays within 5 μs, before there is overlap between bunches. Therefore the PMT's must have recovered from gating at ~ 5 μs or less after injection, before muons at smaller radii (lower momentum) overtake those at larger radii and the beam becomes debunched. The measurement of f_a will begin at about $20\mu s$ after injection, when the PMT gains have stabilized, muon losses have subsided, and after most of the bunch structure of the stored muons is gone.

Because the average rate of electrons incident on a single calorimeter, $20\mu s$ after injection, is about 6 MHz for muon injection, we must prepare the counters to handle the very highest rates. In addition, at the end of 10 muon lifetimes this rate has decreased to a few hundred per second, so the detectors must be stable against shifts in timing and pulse height over a very wide dynamic range(10^4). The detectors will be segmented to reduce the early-time rates per PMT, and considerable effort has gone into developing PMT and base combinations capable of stable operation at elevated rates. We have found that our base and PMT combinations are very stable at the highest rates anticipated in our measurement. One reason we are able to drive the tubes at such a high rate is that this high rate is not sustained, but instead decreases rapidly over a couple of hundred microseconds. This means that we do not exceed the manufacturer's specification for maximum average anode current. The instantaneous currents are low enough and sufficiently transient that space charge does not have time to build up in the PMTs.

For the calorimeter, a lead-scintillator combination has been chosen because of its speed, short radiation length, fairly good energy resolution, and high level of light output. The light output is large enough to have long light guides, allowing the placement of the PMT's well below the plane of the ring, where problems from the flash will be much less severe. High light levels also reduce potential background problems due to Cerenkov light produced in the lightguides by errant charged particles. The good time and energy resolution of the detectors makes it easier to monitor the rate stability and to handle pileup, which is essential to controlling systematic errors.

We are developing two different methods for recording the time of the electrons. The "T" method will use the conventional approach, used by CERN III, of recording the timing from discriminated pulses in a multi-hit time-to-digital converter (MTDC). In the "Q" method, the electron pulse height from the calorimeter is recorded at 2.5 ns intervals over the decay period using a waveform digitizer, data from all injections are added together,

and the resulting spectrum, total calorimeter pulse height versus time, is fit for the precession frequency. [2]

We also plan a subsidiary measurement to establish a new limit on the muon electric dipole moment (EDM) which requires that we detect the oscillation in the average vertical component of the decay electron momenta. This can be achieved by vertically segmenting the electron detectors, as discussed below and by Miller et al. [3].

16.2. Detector Specifications

We have settled on a design where 24 detector stations are placed at equal (1.8 m) intervals around the ring (see Fig. 16.2.1). This maximizes the acceptance of the high energy electrons, which carry the most useful information on the $(g-2)$ frequency. The short radiation length of our design allows us to contain the electromagnetic showers with a short counter, and also reduces the number of undesirable side entering electrons, which tend to have much lower average energies and $(g-2)$ frequency information but larger shower leakage than front entering electrons. If the side entering electrons are not vetoed, then they are a potential source of pileup on top of the front-entering electrons, particularly when we operate at the highest rates. We have not yet determined whether we will need to veto side entering electrons (see below for the discussion of the side scintillator detector, SSD).

Each detector station will consist of a calorimeter and a horizontal array of five scintillator paddles on the front face of the calorimeter (Front Scintillator Detector, FSD) Fig. 16.2.2. Leading-edge timing for the $(g-2)$ precession frequency measurement would be taken from the FSD, and the time over threshold measurement of the discriminated FSD signal would provide information for pileup rejection, with both measurements utilizing the MTDC. For timing purposes, the FSD signal has the advantage over the calorimeter signal since the pulse height is independent of the electron energy. Pulse height and an additional measurement of the average time for a given event would come from the calorimeter and waveform digitizer (WFD).

At least one detector station will be a so-called "superstation", and will have, in addition, a scintillator along the side of the calorimeter closest to the storage region (Side Scintillating Detector, SSD), and a Position Sensitive Detector(PSD), or hodoscope, on the front of the calorimeter. The SSD would be a veto for electrons entering the side of the detector. The PSD is a scintillator fiber hodoscope with 0.7 cm segmentation in x and y. Its spatial information will be used for additional pileup suppression and to

Figure 16.2.1: Plan view of the detectors.

Figure 16.2.2: Calorimeter design.

provide information on the entrance point of the electron into the calorimeter. The vertical position information from the SSD or the PSD will provide the necessary data to place an improved upper limit on (or measurement of!) the muon electric dipole moment. The SSD performance will be evaluated for its pileup rejection capabilities, and may be incorporated at all stations for the high rate situation expected with muon injection. The PSD may be implemented at more stations if the unit cost can be reduced, mainly by finding a cheaper PMT and readout.

16.3. Proposed Detector System- Design Details

As previously mentioned, the detector system for the $(g-2)$ experiment will consist of 24 detector stations positioned at 15 degree intervals around the storage ring. Their height is limited to less than 18 cm by the pole gap. Part of the detector will be in the full magnetic field;the remainder will be in the fringe field. The task of each station is to provide a high-quality determination of the time of arrival and energy of decay electrons. The design is influenced by the high rate in the muon-injection phase of the experiment. Therefore segmentation is introduced into both the timing counters and the calorimeter. Scintillator fluors are chosen to be fast with fast decay constants. The calorimeter is physically compact to reduce the number of side-entering decay electrons (proportional to its length). Additionally, a side veto counter option (SSD) is provided, as is a highly segmented front hodoscope (PSD) to mark the entrance position of the electrons into the calorimeter. Each detector package is fully self-contained and is designed to permit detectors to be positioned as near as possible to the vacuum chamber walls of the storage ring while keeping all photomultiplier tubes and bases well out of the influence of the ring's magnetic field and out of plane from the initial flash caused by the decaying pions at injection. For ease of installation and handling, and to ensure proper and repeatable alignment, each detector package will ride in a carriage mounted on a set of precision rails. An N_2 laser-based calibration system will be implemented to illuminate all detectors with a pulse of UV light coming from a common source and, most importantly, at a common time. Laser illumination of the scintillator provides for complete system integration, a measurement of relative gain stability and a good timing standard.

An overall view of the detector package is shown in Fig. 16.2.1 The baseline plan provides for a four-fold segmented calorimeter at each station and a five-fold segmented set of front scintillator detectors (FSD). One "superstation" will include such enhancements as an SSD and a PSD.

A full prototype of the system was built and tested in the summer of 1993 (see below) from which final design changes have been made. At the time of this writing (3/94), many of the components are well under way to final construction and plans are firm for a 1994 beam test of the final design, including a mock-up of the storage ring magnet. The detector subsystems of the final design will be discussed in turn in the sections which follow.

16.3.1. Calorimeters

The calorimeters are made of 1 mm scintillating fibers embedded in a lead block. The construction of these Pb/SCIFI calorimeters consists of placing stretched "nets" of evenly spaced fibers on top of grooved lead/antimony (6%) plates. The fiber nets are held in the grooves by an optical epoxy. For the $(g-2)$ experiment, modifications have been made compared to our earlier work which results in a shorter radiation length, i.e. the detectors are more dense. This has been achieved by increasing the thickness of the lead plates while keeping the fiber-to-fiber spacing the same. An indirect consequence of this change has been the need to develop a somewhat revised assembly procedure including a new custom air-cylinder press facility which has recently been fabricated. On the whole the design of the calorimeters is based on our considerable experience with such devices and therefore represents a minimum of new or risky development. [4]

Each $(g-2)$ calorimeter is 22.5 *cm* wide $\times$ 14 *cm* high $\times$ 15 *cm* deep, with a radiation length of about 1 cm for a 35% packing fraction (35% plastic by volume). It is made of four separately-constructed modules which are then machined smooth and glued together to form the complete block, see Fig. 16.2.2. The fibers are oriented radially with in the storage ring coordinates which implies that the electrons enter nearly orthogonal to the direction of the fibers. The depth of approximately 15 radiation lengths is sufficient for reasonable containment of the showers, however slightly better resolution could be achieved by lengthening the blocks a few cm. This is not warranted in our application as the increase in the number of side-entering electrons and the need for larger light couplers offsets the slight resolution gain. It is expected that the resolution will be about σ = 10-13%/$\sqrt{E}$, in the final configuration. Test results on linearity and resolution are shown in Fig. 16.3.1 and Fig. 16.3.2.

One concern with the four-fold physical segmentation is the inevitable crack between modules. In the prototype version, one crack was oriented horizontally at the detector midplane. A noticeable gain loss and resolution degradation was seen there, and although a blemish in an otherwise uniform detector, we hasten to point out that it would have no direct effect on the measurement of $(g-2)$. However, substantial improvements have been made on two fronts. First, the machining and assembly procedure has reduced the effective

Figure 16.3.1: Calorimeter linearity.

Figure 16.3.2: Calorimeter resolution.

crack by a factor of three; it is equivalent to the absence of one row of fibers. Further, we have devised a method to machine oversized Pb/SCIFI blocks at 4 degree angles so that the crack now does not run horizontally, but rather, at a 4 degree pitch. From front to back, no straight-through particle path now exists.

Solid acrylic light couplers have been designed to gather the light from the inside radius of the flat and diamond-machined ends of the calorimeter and bring it to a two-inch round acrylic light pipe. The light coupler / mixer has been measured to have a uniform acceptance to approximately 1% across the entrance face. [5] Four such couplers, each $7.5 \times 8\ cm^2$ are glued to the Pb/SCIFI detector and, together with the calorimeter, are housed in a light-tight plastic box securely mounted and aligned to the detector carriage. The two-inch light pipes extend from the light couplers to the PMTs located approximately 48 inches away. Each light pipe undergoes a precise 90 degree bend having a 10 inch radius.

An important design parameter for $(g-2)$ is uniform light output, independent of the entrance position of the electron into the calorimeter. This can be problematic in a Pb/SCIFI detector because of light attenuation in fibers. For example, 2 GeV electrons entering at large and small radii will look somewhat different. We have studied this effect and determined that the detector's radial uniformity must remain better than 20% over the 23 cm width. The measured response is found to be about a factor of two better than this, as we now discuss. The attenuation length of scintillating fibers has two components; a short component (usually ignored) is thought to be associated with the trapping of light in the cladding, while the longer component is an intrinsic one dependent on the choice of fluor. In our application, light trapped in the cladding is soon lost to the lead plates through the optical epoxy which surrounds each fiber. The long component, measured by us to have an attenuation length of approximately 1 m, still yields a considerable change over the 23 cm-wide front face. We have had several iterations of fiber choice with Bicron, finally settling on a BC-404 based formula modified for our needs and embedded for the first time in a fiber. BC-404 is a known "fast" scintillator and is commonly used in timing applications.

Furthermore, attenuation length is wavelength dependent; short wavelengths are absorbed faster than long ones. Accordingly, we have studied the use of wavelength cutoff filters just before the PMT. A good compromise between light transmission and extended attenuation length is a Kodak #2E Wratten filter with a transmittance of 9% at 420 nm and 50% at 430 nm. This causes a 58% reduction in light from an unfiltered detector but doubles the attenuation length. The detector is uniform at the 10% level or better from the inside to the outside radius. With the configuration described, the light output corresponds to approximately 520 pe/GeV (1235 pe/GeV without filters).

16.3.2. Front Scintillation Detectors (FSD)

The FSD system consists of 5 radially oriented scintillator fingers each made of 3/8 inch BC-404 scintillator and measuring $2.8 \times 23\text{cm}^2$. Together, the five fingers cover the entire front face of the calorimeter. (See Fig. 16.2.1.) The light couplers for this system consist of three parts which ultimately, as for the calorimeters, result in the light being piped to PMTs situated near the floor more than 1.5 m away. In this case, 1 inch stock acrylic is used which matches the PMT choice, giving approximately adiabatic matching of the lightguide pieces. Care is taken to wrap them as a group and to ensure their alignment with the calorimeter and carriage. Accordingly, physical slots are prepared in the plastic light-tight box housing the calorimeter which extend to align the FSD system. Provision is made for a quartz fiber which will be attached to the front of each slab for calibration purposes.

16.3.3. Position Sensitive Detector (PSD)

The position sensitive detector (PSD) is basically a scintillator hodoscope composed of one x and one y plane each with 7 mm segmentation. Since the calorimeter has little inherent position information and the FSD provides only 5-fold segmentation in the vertical plane, a PSD is also planned for at least one station. If the unit cost can be brought down sufficiently, we may upgrade all detectors at some point in the future. The PSD provides rejection of spatially separated hits which occur within the same 2.5 ns time window, a more precise measurement of up-down asymmetry in the precession plane in the analysis of the electric dipole moment limit, redundancy in the muon distribution measurement when used in conjunction with the traceback chambers, and may be a general calibration tool to understand any non-uniformities or leakage problems in the calorimeter. In order to employ it properly as a calibration tool, the PSD should be portable and each calorimeter station should be designed to accommodate one PSD. This also allows for a possible upgrade to additional PSDs during muon injection when rates may require better pileup rejection than that achieved by the FSDs alone.

Three main considerations drive the present design: (1) Due to the segmentation, the PSD is inherently a more costly device to read out and therefore a multi-channel photosensor is the appropriate choice to keep the per channel cost low, (2) there is barely 2 cm between the top of the calorimeter and the bottom of the magnet pole tip in which to extract the light from the vertical strips, and (3) the photosensor must be removed from the midplane and placed more than a meter away from the PSD, necessitating a long light pipe. Considerations (2) and (3) imply some sort of fiber light guide with small cross

Figure 16.3.3: PSD.

sectional area and flexibility. In addition, the small size of the pixels on a multi-channel phototube also force one to abandon any simple adiabatic light guide solution. The highest light yield solution to the area reduction problem (detecting light generated in scintillator strips of cm^2 cross section by mm^2 pixels) is to use wavelength-shifting fibers. The original PSD designs used "pencil fibers" from Kuraray, so-called because the core (or lead of the pencil) was a green wavelength fiber embedded in a second, larger diameter blue fiber (the wood of the pencil). These have very good photon capture efficiency, but the mechanical problems of mating them to clear plastic light guides for transmission to the phototube outweighs the advantages. Since Kuraray has discontinued their manufacture, we have designed and built our own hodoscope elements. Each strip is formed by cutting a groove down the center of two 7mm $\times$ 4mm Bicron 404 scintillator strips, placing a 1mm diameter Kuraray multi-clad Y11 green wavelength-shifting fiber in the groove and then gluing the two halves together to form a 7 mm wide $\times$ 8 mm deep element. Each strip is individually wrapped in teflon sheeting and the bottom of the fiber is mirrored. The length of the horizontal strips is 23 cm and the length of the vertical strips is 14 cm. A custom optical coupler mates each of the green central fibers to 1.5 meter long clear plastic light guides of the same diameter. This optical connector enables one to disconnect easily or interchange the tube and light guide assembly from the PSD active elements. Fig. 16.3.3 shows an engineering drawing of the PSD assembly and mechanical support.

The PSD is a threshold device whose 53 channels will be read out by two 27-channel MTDCs. Since a typical hit in the PSD produces only a handful of photoelectrons, PSD performance is determined by how well these hits can be separated from ambient noise. Tests using a triple coincidence trigger with a Sr^{90} source have consistently shown 15 photoelectrons at the end of the light guide, as observed by a Hamamatsu R1332 photo-multiplier tube which has 12% quantum efficiency in the green. This is adequate for 99% efficient sensing of minimum ionizing particles (which is what the electrons are to the thin PSD). However, any reduction in the quantum efficiency of the photosensor will lead to inefficiencies.

The commercially available multi-channel tubes have some disadvantages which make them marginal in this application. There are only two manufacturers of such devices: Philips and Hamamatsu. The Philips tube has generally poor quantum efficiency in the green, averaging 4-10%. The Hamamatsu tube has better quantum efficiency (12%), but its energy resolution is worse by a factor of 5. The poor resolution cancels out the improved sensitivity, since a broader peak due to gain dispersion is just as bad for a threshold sensing device at low light levels as a peak broadened by poor quantum efficiency. All these tubes suffer from crosstalk at the 2-5% level. However, a new multi-channel hybrid tube being developed by a member of this collaboration (P. Cushman) is well-suited to this application.

It is a proximity-focused tube with a segmented avalanche photodiode as the target. The total gain of up to 10^6 comes in two stages: from the acceleration of photoelectrons across the 6 mm gap (to which 10 kV has been applied) and an additional gain from the avalanche produced within the reverse-biased diode. Crosstalk is $< 0.1\%$ between the 64 1mm square pixels. The S20 photocathode typically yields 20% quantum efficiency in the green and we have made several Gallium Arsenide tubes with 40% quantum efficiency in the green. Read out with GaAs photocathodes, the number of detected photoelectrons at the end of the light guide will be 50. At these light levels, it is possible that the timing measurements from the PSD will surpass those from the FSD, since the hybrid tube has been measured to have a time jitter of less than 50 ps.

16.3.4. Side Scintillation Detectors (SSD)

A side veto counter system (SSD) has been developed, and may be important in attempts to keep pile-up from affecting the accurate determination of an electron's energy. The idea is to eliminate any event where a substantial amount of energy is deposited by an undetected side-entering electron entering in time with an ordinary front-entering electron. A 1/8 inch fast scintillator placed along the outside radius of the calorimeter can serve this purpose. Simulations show that electrons entering the side of the calorimeter cross this thin scintillator at such a glancing angle so as to leave a considerable energy deposit. This is in contrast to shower electrons leaking from the calorimeter itself which typically leave a small pulse height.

An SSD was incorporated into our 1993 test beam and provision for it is included in our detector carriage design. However, we were not convinced from the test beam results that the distinction between side-entering and leakage electrons could be made as reliably as we had hoped from the simulations. Accordingly, we will only provide an SSD on the superstation in time for the 1996 pion run and will continue to study its possible use.

Note that the SSD is coupled to a two-inch PMT through another adiabatic light transport system, this time through two 90 degree bends, one to turn radially, the second toward the floor.

16.3.5. PMTs and Bases

For the $(g-2)$ experiment, we need phototubes for both the front scintillation detectors (FSDs) and the electron calorimeters. Based on a series of rate, gating, and flash tests on different phototubes, the Hamamatsu R1355 and R1828-01 were selected for the FSD and the calorimeters, respectively. The R1355 is a 10-stage tube with a 28.5 mm active diameter, a 2.0 ns rise time, and a 23 ns transit time. R1828-01 is a 12-stage tube with a 53 mm active diameter, 1.3 ns for rise time, and 28 ns transit time. The transit time spread (FWHM for single photoelectron state) is about 650 ps for the R1355 and 550 ps for the R1828-01. So if the number of photoelectrons seen by the PMT is 200 for the R1355 and 500 for the R1828-01, then the transit time spread will contribute about 46 ps for R1355 and about 25 ps for R1828-01 to the FWHM of the timing histogram.

The PMT bases for both the R1355 and R1828-01 were designed by the Electronics Design Facility (EDF) at Boston University. The voltage distribution ratios were chosen from the options suggested by Hamamatsu. Different voltage distribution ratios give different rise times, gains, and linearities. The voltage distribution ratios finally used give the fastest rise time and reasonable gain and linearity for both tubes. It was necessary choose a transistorized base in order to hold the dynodes voltages stable at the highest rates. A zener diode was added between the photocathode and the first dynode to give the best possible timing stability. A transistorized switchable circuit gates off the R1355 (R1828-01) by switching the voltage on dynode 5 (dynode 7) to the same value as on dynode 2 (dynode 4). These dynode combinations were found to optimize the gain reduction and speed of tube recovery when the PMTs are switched off and on.

The output of the phototubes also poses problems. Even if the impedance of the cable and electronics input are 50 Ω, reflections at the few percent level can still be found if there is only one output from the anode. This small reflection may cause a timing shift or multiple discriminator pulsing. One way to solve this problem is to have two very short coaxial cables coming out of the anode and use a 50-Ω terminator to terminate one of the outputs so that all the reflection from the electronics gets absorbed properly by the terminator. In this way, we can have a clean signal, although its amplitude will be cut in half.

The issue of whether to clip the PMT analog signals is still under investigation. CERN III had problems with a decaying DC offset in the PMT signal just after pion injection. A short clipping stub, shorted to ground, would greatly reduce this DC offset problem. However, in tests employing a fast pion beam at BNL, we attributed the DC offset to the direct response of the PMT to traversing charged particles. By placing the PMTs out of the plane of the ring, we hope to eliminate this problem. Thus, we may be free to place

a resistor at the end of the clipping stub, and to adjust the resistance and the length of the clip line until the natural tail from an individual pulse is cancelled. This will greatly reduce the time shift of a pulse which would otherwise have been sitting on the tail of the previous pulse, a circumstance which may be a significant problem at the high rates of muon injection.

16.4. Detector Electronics

16.4.1. System Architecture

The heart of the $(g-2)$ measurement is the precise, rate-independent measurement of muon-decay electron arrival times. In addition, electron energies must be measured with modest resolution, in order to to select those of highest energy (which have the highest asymmetry) and to bin the data according to energy. Both timing and energy measurement systems must operate at peak rates of up to 8 MHz per calorimeter for muon injection, and must digitize as many as 400 events per calorimeter during the 1 ms muon storage time. During the 1 or 2 seconds between AGS storage ring fills, data must be transferred to mass storage and any on-line calculations necessary for monitoring the experiment must be performed. In addition to the calorimeter and FSD readout, data must be acquired at similarly high rates from PSDs and the muon phase space reconstruction systems. Finally, data from the on-line calibration system and from the NMR magnetic field measurement system must be included in the data stream and stored for later detailed analysis. Precision field measurement and precise decay-time measurements must also be coordinated through a common high-stability clock and its associated clock signal distribution system.

Our baseline detector electronics system is built around a few modular components, a multi-hit time to digital converter (MTDC), a "derandomizer", and a wave form digitizer (WFD), each of which has a prototype currently under test. The readout electronics for the calorimeter and FSD systems are illustrated schematically in Fig. 16.4.1.

The MTDC records the times of the leading and trailing edges of logic pulses with 1.25 ns accuracy. A prototype of this device has been developed at Boston University in collaboration with the DUMAND experiment. A VME version with on-board memory is being developed at BU. The key element within this device is a new Gallium Arsenide-based ASIC (Application Specific Integrated Circuit) running with a split-phase 400 MHz clock.

Figure 16.4.1: Schematic illustration of E821 readout electronics system architecture.

The MTDC registers the time of the leading and trailing edges of the input logic pulses. If the logic pulse is time over threshold from the PMT's, then the width of the pulse can be used for pileup suppression. It also identifies piled-up pulses with small temporal separation (plus tagging anomalously wide pulses resulting from nearly simultaneous piled-up events- the width is deduced since the time of trailing edge of the logic pulse is also recorded) for each of up to 27 independent input signals. Data from the FSD and calorimeter will be read out by separate channels of the MTDC so that correlation of data from each of these devices may be readily achieved.

A $(g-2)$ prototype of the MTDC is now being tested, and the functionality of the ASIC chip has been proven. For the time being, the device sits inside a large rack-mount box along with its power supplies and an interface board. As there is no large on-board memory, the MTDC is read out into a 128 Kbyte LeCroy 1190 VME memory module. We have recently begun using our $(g-2)$ decay pulser (which produces a spectrum of pulses with the timing characteristic of our experiment, but no modulation) to exercise the MTDC and have successfully read out hundreds of pseudo-spills with UNIDAQ and VxWorks, the data acquisition and operating systems, respectively, which we expect to use in the real experiment. The MTDC ASIC, its interface and memory will be repackaged into a triple width 9U VME card in late summer 1994. We expect that much of the original design can simply be transferred to the new one, and that the VME interface can be borrowed in large part from that for the WFD, which is described below.

A second component of our electronics is a "de-randomizer" circuit which will unambiguously associate asynchronous discriminator transitions from the FSD with synchronous clock cycles. In fact, we plan to use a single 200 MHz clock for the derandomizer, MTDC, and WFD, so that they are all in phase. The MTDC board would have a x2 frequency multipler to provide the necessary 400 MHz. The derandomizer is housed in a NIM module, with 4 channels per station. Its input will be the logic pulse from a discriminated FSD signal and its output, a logic pulse whose leading edge has been shifted to the center of the proper clock pulse, which is then fed into the MTDC. The time boundaries of each 5 ns bin must be stable on average to 20 ps over 200 μs, i.e. 0.1 ppm. The derandomizer is necessary since the MTDC is not designed to be free of systematic errors to 0.1 ppm. The de-randomizer circuit will only be used for those channels requiring high-stability timing, corresponding to discriminated FSD outputs in our baseline design. By separating the functions of high stability pulse synchronization (with the derandomizer) from the time scaler (with the MTDC) we hope to isolate and minimize any sources of systematic error.

A derandomizer prototype was produced by the BNL instrumentation group, and was delivered to BU in February of 1993 but, owing to early problems with the MTDC ASIC, we have just begun to examine its performance. It was tested and certified as rate independent

in isolation from the rest of the detector electronics. In particular, we have moved a pulse very slowly (fractions of a ps per step) across a clock boundary and verified that the derandomized signal moves cleanly and suddenly from one time bucket to the next and that it does so in a rate-independent manner. Naturally, this test must be repeated for a variety of ambient rates and the transition between buckets should look the same in all cases. We also plan to perform the so called synchronous random phase test, developed by by the CERN III experiment, to measure the linearity of our counters.

For the calorimeter energy measurement, we have constructed a two phase 400 MSPS (Mega-samples per second) zero-suppressed waveform-digitizer (WFD) system. The WFD was developed by the BU electronic design facility in collaboration with the BU MACRO group. The WFD is a VMEbus slave module designed to digitize and store analog input data at a rate up to 200 MHz. With a pair of channels operating 180 degrees out of phase on the same analog pulse, we will effectively sample at 400 MHz. We have indicated the internal operation of a WFD channel schematically in Fig. 16.4.2. There are four independent WFDs per VME motherboard. Each channel has in turn four analog inputs, corresponding to the four PMTs on each calorimeter. The sum of the four analog signals is digitized by a 300 MHz, 8 bit flash A/D converter, while each of the four inputs is separately discriminated. In zero-suppress mode no data throughput occurs unless at least one of the discriminators has fired. After every four conversions, the digitized data are stored as a parallel group of four bytes, allowing a 50 MHz rather than 200 MHz data storage rate. At the time each group of 4 data bytes is stored, a 16 bit time word (incremented every 5ns) plus 2 bytes of discriminator information are also stored, resulting in a total of eight bytes of information being stored at a rate up to 50 MHz. Each channel of the module is allotted 64 Kbytes of storage: 32K for pulse samples and 32K for time and discriminator data.

The MACRO version of the current motherboard is about to go into production. Any modifications for $(g-2)$ will be minor. The front end amplifier card of the WFD, a daughter card which is mounted, in turn, on the 9U mother board, is being modified for the needs of the $(g-2)$ experiment. Specifically, it should be capable of handling high rates and fast phototube signals and have good linearity characteristics. The new front end should be ready for testing in the late summer 1994.

We tried out a second generation prototype WFD card in the July 1993 beam test. The WFD worked the first time we plugged it in. The energy resolution curves were identical to those produced using conventional charge-integrating ADCs. We also tested two-phase operation by splitting the linear signals, delaying one copy and sending it off to another input channel. That, too, was a success.

Figure 16.4.2: Schematic illustration of waveform digitizer internal operation.

Several critical tests remain. We have made preliminary tests of the pulse height stability with rate which look promising, but we won't have a truly definitive answer until the new amplifier front end arrives. The same goes for the stability of the time response.

In addition to event-by-event determination of electron energies and the detection of anomalous pulse shapes (for pileup rejection), the WFD system is being incorporated into an alternative system for measuring the muon precession frequency with the same calorimeter pulses, termed the "Q-method". In the Q-method, waveform digitized calorimeter pulses are digitally summed across many fills, and the resulting pulse height/timing pattern fitted to a sinusoidally modulated decaying exponential. The timing versus rate stability and linearity requirements for the WFD system are more demanding than for the conventional energy-threshold technique (the "T-method"), and we are in the process of determining whether our WFD meets Q-method requirements for linearity and rate-independence in its digitization of pulse heights.

The baseline DAQ electronics system described thus far is for a general detector station. In addition we expect to instrument between 1 and 4 "superstations". As mentioned above, superstations will include Position-Sensitive Detectors (PSD) and Side Scintillator Detectors (SSD) for additional pileup rejection, as well as additional calibration, monitoring, and pulse measurement capabilities. Although there is no provision for waveform digitization of FSD signals from general stations, for example, our modular design allows us to outfit a superstation with this capability if we so choose, and to thereby make informed decisions on potential future electronics upgrades. The modular DAQ electronics system design allows this and other variations on the baseline design to be explored at superstations.

16.4.2. Calorimeter Readout

Each of the four PMTs on a calorimeter is split into calibration and WFD signal paths (Fig. 16.4.1). Resistive splitters are used in our conservative baseline design, but we will characterize the rate independence of commercial active splitter modules as well. Our baseline design for standard stations includes only a 2-way split, while superstations might use a further split to form analog sums of the calorimeter PMT signals. These summed signals would then be discriminated and accurately timed in the same manner as FSD signals (as discussed below). For standard stations, we will use the WFD as a multiple-hit ADC which samples the pulse height of the sum of the four PMT signals every 2.5 ns, and Lecroy CAMAC-based FERA ADCs will be used for calibration and monitoring. The purpose of the calibration ADC is to provide a high-resolution measurement of the calorimeter PMT response to a laser calibration pulse. This pulse will be generated once

per storage ring fill, at varying time positions relative to injection, to monitor any gain or time shifts from early to late decay times. For our baseline design (if funding allows), we plan to have a separate FERA calibration channel for each PMT in the experiment.

Our baseline design also calls for an MTDC for the time correlation of calorimeter signals with those from the FSD. Input to the MTDC is provided by the discriminators in the WFD. Superstations may discriminate each PMT individually and record separate times to the MTDC and may also include de-randomizers on discriminated outputs of either fanned-in or separate calorimeter PMTs. This implementation will require sufficient rate-independence from the calorimeter PMTs and might also require the use of constant-fraction discriminators (or a software correction) to eliminate the correlation between pulse-amplitude and the time of the discriminator pulse. However, the rate dependence of CFDs tested (see §16.4.3) was unsatisfactory, so this correlation will have to be corrected in software.

If the calorimeter signals are to be used to provide a second precision timing system for the superstations, it will be necessary to include more high-resolution calibration TDC channels of the type discussed below.

16.4.3. Front Scintillator Detector (FSD) Readout

The FSD system provides the precision timing measurement for the determination of $(g-2)$. As discussed earlier, we plan to isolate rate-dependent effects within the electronics to the PMT, base, and "de-randomizer" circuit. Error-free recording with the MTDC system should then be straightforward. The input to the de-randomizer will be provided by a single channel from a leading edge discriminator; initial tests are currently being carried out with a Phillips 704 300 MHz Quad leading edge discriminator. The use of constant-fraction timing would minimize the correlation between timing and pulse height from the PMTs, but the rate-dependence of a candidate CFD, the Phillips model 714, is too large at the highest rates expected in our application. By contrast, the Phillips model 704 leading edge discriminator displays no rate dependence at or beyond the highest rates anticipated in the experiment. In spite of the merits of CFD timing, we have decided to use leading-edge discriminators in the experiment. We note that the variation in the electron pulse heights in the FSD is not large and tests have shown excellent gain stability in our candidate PMTs which facilitates the use of leading edge discriminators for timing.

The direct and de-randomized FSD discriminator outputs will be sent to separate MTDC inputs. The purpose of this partially redundant readout is to preserve the 1.25 ns resolution of the MTDC for the leading and trailing edge timing of the direct discriminator output, since the derandomized pulses will only be timed with 5 ns resolution. The fine

time resolution on the MTDC will be used to reject pileup through analysis of temporal and spatial hit patterns. Two pulses too close together in time could be rejected, or two pulses nearly on top of each other will produce a discriminator pulse which is over threshold too long compared to a single pulse. For superstations, we will implement precision TDCs which will monitor the FSD timing response to calibration laser pulses. The calibration TDC will be a LeCroy 2228 8-channel TDC, with 50 ps resolution. This fine time resolution permits calibration and monitoring with many fewer calibration pulses than with the coarser MTDC timing. The calibration TDCs will be operated at a low constant rate to maximize their stability. The superstation FSD readout system may also include fanning out the analog signal to a waveform digitizer and calibration ADCs.

16.4.4. SSD and PSD Readout

The side scintillator detector (SSD), which will be found only in "superstations", is used to reject decay electrons entering through the side of the calorimeter. The SSD is read out with a leading-edge discriminator whose output is fed into the MTDC system. The threshold would be set so that the discriminator fires on the large pulses from side-entering electrons but not on the smaller pulses from electrons leaking from the shower of a front-entering electron. An alternative implementation of the superstation SSD readout might include fanning out the signal to waveform digitizer and calibration ADC systems of the type used for the calorimeter signals.

The PSD is read out with the MTDC, like the FSD but without the derandomizer. The sparse nature of the PSD data is well-matched to the MTDC 27-input design. For our baseline, we have assumed that each PSD will require two MTDC modules, which will record threshold-crossing times for the summed-anode output provided by the PSD multianode PMT and/or a synchronization signal. The 1.25 ns resolution time of the MTDC system is smaller than required for the PSD and sufficient for accurate correlation of PSD, FSD, and calorimeter information. For our baseline, we plan to use Phillips model 706 100 MHz 16-channel leading edge discriminators, although an integrated preamplifier/discriminator system such as the 16-channel LeCroy 2735DC is another possibility.

16.4.5. Clock Distribution, Calibration and Test Electronics

The $(g-2)$ Clock and its distribution system are indicated schematically in Fig. 16.4.3. Our baseline precision clock for the $(g-2)$ experiment is a temperature-controlled and highly stable 200 MHz oscillator which is phase-locked to the LORAN standard. For historical reasons we still sometimes refer to this as a "frequency synthesizer", as in the figure. From this standard we must generate both a 400 MHz clock for the MTDC as well as 200 MHz signals for all the WFDs and derandomizers. We will therefore require a clock fan-out distribution system, which is currently under development. Low-dispersion cables will be used in the clock signal distribution to preserve the clock pulse integrity, and both the cabling and the fan-outs (housed in RF-shielded NIM modules) will be well-shielded from such sensitive circuits as the NMR field measurement system. The NMR system will also be locked onto LORAN, and the maintenance of a constant ratio between the frequencies of the two clocking systems will require careful verification. For testing the stability of our precision timing circuits against rate changes and other effects, we will use a precision frequency generator which can be beat against the master clock. This Synchronous Random Phase Test, developed by the CERN $(g-2)$ group, is one of many tests we will perform on the system. In connection with these tests, we have constructed two custom modules: 1) a "flight simulator", which can faithfully deliver a train of pulses similar to that expected in the detectors, and 2) a device (described earlier) which produces a logic pulse with varying time relative to the clock, in order to test the stability of the derandomizer near a clock boundary.

16.5. Calibration System

We anticipate performing PMT analog-signal calibration with our laser-based and LED-based calibration systems. The laser will be fired once per $(g-2)$ storage ring fill, with the delay between injection and laser firing controlled by a programmable pulse generator (such as the HP 8112A). The intensity of the pulse will be monitored by an isolated independent PMT. Emphasis will be placed on detecting any shifts in pulse height or timing as a function of time after injection, which appear as a direct systematic error in our $(g-2)$ measurement. The LED calibration system will be used for tests at high rates, and will require computer control over pulse amplitude and timing, whether used in single pulse or high-rate mode. It will also require LED driver pulse fan-outs to provide an LED signal at each PMT. Finally, it will be very important to analyze the pulse shapes

Figure 16.4.3: Schematic illustration of E821 clock and clock distribution system architecture.

Figure 16.5.1: Laser calibration system.

produced by both to decay electrons and the laser light source with a 1 GHz digital storage oscilloscope.

Our high-precision measurement relies heavily upon accurate calibration in order to measure those systematic effects which cannot be reduced below the 0.1 ppm level. For timing shifts which vary as a function of time after injection, a 0.1 ppm error limit corresponds to a less than 20 ps systematic timing shift over a 200 μs period, the time over which we establish half the statistical significance of our experiment. These time-shifts are expected to come mainly from rate-dependent gain effects on the PMT. In order to hold the centroid of a time distribution produced by a CFD constant to 20 ps, the gain on a PMT which slews at 0.1 V/ns must be corrected to 0.3%.

Measurement of such small shifts requires large numbers of calibration events, since we need 2500 pulses measured with a timing precision of 1 ns to measure a mean time to within 20 ps. It is clear that good time resolution would facilitate the calibration, and we expect to obtain a resolution of around 300 ps, which would require only about 200 counts per calibration point. Furthermore, calibration must be performed during actual data taking, in order to take account of the prompt and delayed flash and changes in ambient rate.

A laser calibration system designed to meet these needs is shown schematically in Fig. 16.5.1. There are two separate calibration subsystems, one laser- and LED-based, since the capabilities of these two methods are complementary. Laser pulses are very useful for time-synchronizing calorimeter channels, for generating narrow pulses (similar to an electron shower), for monitoring rate dependent time shifts, and for exciting the emission of fluorescence light from scintillating fibers. The UV laser pulses are injected into the scintillating fibers at the end of the fiber bundle farthest from the PMT, which therefore calibrates the readout system as a whole unit. The laser system will consist of 2 independent UV lasers with relatively low command jitter (1-2 ns). Each laser will have a separate vacuum photodiode monitor viewing a portion of the light for an absolute time difference and start time measurement. The lasers will be fired relative to each other at precisely measured times (using both a channel of the data electronics and an independent CAMAC system). Typically this will occur early (few μs) and late (500 mus) into the data taking to measure relative shifts in the time offset of the rate-dependent gain. A set of reference cables will be supplied to calibrate the time system. The amplitude of the laser pulses is independently adjustable.

The LED system injects light directly into the photomultiplier tube via a short coupling lucite cookie. LEDs are useful for measurements at high pulse rates, for simulating pulses from light sources with arbitrary time patterns (such as for simulating the flash), and for

distributing calibration light to a large number of calorimeter channels nearly simultaneously. The LED's additionally provide an independent check of the PMT performance, as separate from the calorimeter, and are used to measure the absolute photoelectron gain via the statistical method. It is likely that the LED system will be replaced by laser diodes at the time of the experiment, which have superior temporal properties to LED's, in order to use the LED/laser diode system with a flight simulator output that directly simulates the optical pulses from the experiment. In any case, a pulser system based on avalanche transistors which can produce pulses as short as .5 ns, will be constructed for each channel.

The laser calibration system begins with pulsed nitrogen lasers (0.3-0.6 ns FWHM) as a source of UV light, which is transmitted through a collimator into a high-power UV transmitting optical fiber. From here, the laser light is directed onto four major segments which are remotely enabled by shutters; these correspond to the 4 calorimeters at each measuring station. The 4 fibers are then split into 25 quartz fibers, using a commercially available 1:25 fiber optic splitter with 3db variation in intensity between output channels and 6 dB loss overall. Each quartz fiber is 8 meters in length, and extends from the laser splitter located at the center of the storage ring to a calorimeter on its circumference. On the calorimeter, each laser fiber will excite a custom UV diffusion chamber (simple UVT lucite box) which will then distribute light by short fibers to each of the calorimeter segments, the FSD, and the SSD. The light is injected by more UVT lucite boxes or prisms using teflon reflectors. Tests have shown good uniformity (10% across a face) and low time dispersion (less than 1 ns). A time-offset on each calorimeter is anticipated to be less than 0.5 ns. Finally, one of the quartz fibers is routed to a reference PMT which is well-shielded from radiation in the ring, so that it is not subject to a rate-dependent environment. The reference PMTs provide a standard against which rate-dependent gain and time shifts are measured.

The absolute energy calibration is transferred from test beam data to the experiment using radioactive sources An 18 gauge stainless steel tube (hypodermic needle) will be inserted into each calorimeter. Each of these channels will be oriented transversely to the incident electron trajectories and to the scintillating fibers. Sealed miniature ^{60}Co sources on wires will be inserted into the channels at various depths in order to illuminate different sections of the calorimeter. A radioactive source of strength 100microCurie will be used during down times to provide an absolute energy shape in the calorimeters, which will correspond to testbeam data. Fiducial marks are provided on the counters to use the sources externally.

16.6. Expected Detector Performance

16.6.1. Results of Simulations

The design of the electron calorimeters and their readout has been carried out with the aid of a chain of computer simulation programs. The flow chart for this process is shown in Fig. 16.6.1. We first generate stored muons from injected pions. Large data sets of muons and pions have been generated in the past year and have been used in studies of the muon loss monitor and the flash, as well as of the decay electrons and their motion through the storage ring. S. Mane has provided the detector group with data files which are essentially a snapshot of the bunch at 22.4 μs and at other set times, as well as the phase space coordinates of these same muons at birth. However the muons are chosen, they are propagated through the ring using a simple parameterization of their betatron motion and spin rotation until they decay.

The decay electrons are then turned over to the GEANT-based simulation and propagated through the magnetic field, a map of which was calculated using POISSON. If they strike a calorimeter, PSD, quadrupole electrode, or other obstacle, the shower is simulated as well. The magnitude and spatial pattern of energy deposition in the four calorimeter segments then serves as input to several post-processing routines, which simulate the resulting pulse waveforms and the response of the data acquisition electronics. The output of the simulation includes data banks which look like those produced by the MTDC and waveform digitizer.

Given the enormous numbers of events we will collect and the small errors that we are trying to understand, the full Monte Carlo, with a complete electromagnetic shower simulation, will not be capable of delivering the number of events that we need in order to see very small systematic problems. There is considerable flexibility in the level of detail performed by the Monte Carlo, but even in its simplest useful form, it is still far too slow to generate 30 billion events. However, it may help in indicating what those problems might be. For example, a particular systematic effect can be studied with far fewer events if it is exaggerated and the effect from a much smaller systematic problem can be estimated by extrapolation. We have attempted to parameterize the results of the full Monte Carlo in a very fast and very simple Monte Carlo capable of delivering the needed number of events, but it is still largely untested.

After simulating the shower within the detectors, the next step is to simulate the time and energy response of the data acquisition electronics. The response parameters for these electronics (pulse width, energy resolution, etc.) can then be varied to find the resultant

Figure 16.6.1: Flow chart for detector simulations.

response to electron showers and pairs of nearly coincident electron showers. Preliminary studies have been completed. A phototube pulse corresponding to the energy left by a

1.5 GeV electron in a calorimeter with perfect resolution was modeled, with adjustable scintillator and phototube pulse-shape time-constants. Simulated energy measurements were made using an 8 bit 200 MHz wave-form digitizer and the corresponding 400 MHz device, where two FADCs sample the waveform at two phases of a 200 MHz clock. In each case, an FADC samples the pulse height at 4 ns intervals. Naturally, the measured resolution depends on the number of flash ADC samples taken during each pulse, and resolution improves with increasing pulse width. The results indicate that at 200 MHz, for a high packing-fraction (30%) calorimeter, with underlying resolution of 11.6% at 1 GeV, we need a phototube decay time constant of more than 6 ns, if we wish to keep the electronics' contribution to the overall resolution to less than 10% of the total. At 400 MHz, even with an uncertainty in phase of .5 ns between the two clocks, the time constant can be as little as 3.5 ns, which will make our calorimeter signals more useful for rejecting pileup. As described elsewhere, the WFD has been used on electron signals at the BNL test beam and its resolution performance was comparable to conventional charge integrating ADCs.

The second problem, that of rejecting overlapping pulses, has also been addressed in our simulations. As mentioned above, there are two approaches to pileup rejection: using geometric information from the PSD or segmented FSD, or using pulse height or pulse width measurements from a slab of scintillator (FSD) placed before or on the side of the calorimeter. Using the former method, with an algorithm which demands separate hits on two fingers of each plane in the PSD (where each finger is about 1cm wide), we obtain a rejection power, (how often it distinguishes overlap events) of about 85 %, consistent with a simple geometric estimate. Unfortunately, as we do not expect to outfit each detector station with a PSD, this approach is of limited utility. The segmented FSD could be used in much the same way. With a five-fold segmentation, we would expect a rejection power of close to 80 percent.

The alternative approach to overlap rejection involves measuring the width of photomultiplier pulses from the FSDs, that is how long the pulse remains over a carefully chosen threshold. Single particle events are expected to be narrower; overlap events, wider. The MTDC, now being developed at BU performs exactly this job: sampling an input waveform at 800 MHz and writing to a large buffer the times at which the signal rises above and falls below threshold. The results of simulation, mainly the rejection power vs. single particle efficiency, depend somewhat on the threshold chosen, but at one plausible threshold and pulse width cut, 93% of the double particle events (where the two particles arrived within 8 ns of each other) were rejected while 90% of the single particle events were retained. We have chosen to use the pulse width of the FSD signal as our primary means of rejecting pulse pileup. Hardware tests of this method have just begin at Boston University.

We have decided to install a veto counter (side slab detector, SSD) on the outside radial edge of only one of the detectors ("superstation"), at least for the time being. There are a couple of reasons why we would like to reject side entering electrons. One, these electrons carry little $(g-2)$ frequency information, since their average energy is low. Two, they are a source of signal pileup in the calorimeters, and if we do not detect them, we cannot correct for this problem. An SSD would also help give a good understanding of the level of pileup, which is needed in order to adequately model the expected shape of the time spectrum. However, this turns out only to be a significant problem at the highest rates. Therefore we have decided to leave open the possibility of running with an SSD for muon injection, but until then, to do without.

The final set of simulations uses the effects of pileup thus derived to modify the distribution of higher-energy electrons as a function of time after injection in the same way as will be the data from the future experiment. Without specifically accounting for pileup, the function would be of the form

$$f(t) = Ne^{(-t/\gamma\tau)}\left[1 + A\cos\left(\omega_a t + \phi\right)\right] \tag{16.6.1}$$

Perturbations in the timing spectrum $f(t) \rightarrow f'(t)$ resulting from pileup or other effects operate upon the muon count rate distribution to produce perturbations in the measured muon $(g-2)$ precession frequency $D \rightarrow D'$. By requiring that D and D' agree to within 0.1 *ppm*, we can place a constraint on the maximum permissible magnitude of the perturbation f→f'. It is the ERROR in our knowledge of the magnitude of the perturbing effect $f \rightarrow f' \pm \Delta f'$ which determines the ultimate $(g-2)$ error $D \rightarrow D' \pm \Delta D'$, since one can, if necessary, subtract the known systematic errors in D'.

The fitting procedure is performed through minimization of χ^2 with t varying across all time bins and p over the n $(= 5$ in Eq. (16.6.1)) parameters in the fitting function.

16.7. Rate and Pileup Studies for PMTs and Bases

16.7.1. Introduction

As mentioned above, in order to control systematic errors in the measurement of $(g-2)$ to better than 0.1 ppm, we must measure the average electron arrival times in any 200 μs interval to 20 ps and over the whole measurement time, 640 μs, to 64 ps. In addition, we must know the relative average energies of the electrons to 0.2%.

Event rates in the PMTs are as high as several MHz shortly after muon injection and decrease to hundreds of Hz at the end of the decay period (ten muon lifetimes). The large range of rates can lead to gain and timing changes in the PMTs and discriminators from early to late decay times.

In this subsection, we report the results of time stability measurements on our candidate PMTs and discriminators. We have found their time stability to be at least as good as the specification at the highest rates expected, but gain stability is about 0.4%, or twice the specification. Both gain and timing will be carefully monitored to the desired accuracy during the experiment (see §16.5 on the laser calibration). Corrections will then be applied to the gains and, if necessary, to the times, in order to meet specifications.

16.7.2. Description of the Rate and Pileup Tests

Two types of measurements were performed on candidate PMTs.

1) The timing and pulse height of the last pulse in a burst of between 100 and 2000 uniformly spaced LED pulses was measured as a function of time between the pulses in order to detect shifts which depend on average rate. Successive pulse trains were separated by 200 ms.

2) The timing and pulse height of the second of a pair of LED pulses was measured as a function of the time between the pulses. This test is a measure of shifts which depend on the spacing between a pair of pulses, e.g. pileup effects. Shifts in timing could come from a shift in the electron transit time of the PMT, or from effects of the tails of previous pulses. We will distinguish between these two effects.

We tested two different tubes: a Hamamatsu R1828-01 2 inch PMT for the calorimeters and a Hamamatsu R1355 1 inch PMT for the FSDs. These tubes are designed for high rates and fast timing.

If the gains on these tubes were set so that a typical pulse produced 200 mV into 50 Ω, then the average current through the anode for a continuous, 5 MHz, 15 ns wide pulse would

be around 2 mA, far in excess of the maximum anode current ratings. Fortunately, our application does not require operating PMTs at sustained high rates. If the instantaneous rate in a detector at early decay times were 5 MHz, then the total number of electrons detected in 10 lifetimes would be 320. In order to perform realistic testing, we test timing following a burst of between 100 and 2000 closely spaced pulses, which simulates more nearly the high rate situation which we will encounter, and also does not approach the maximum rated average anode currents.

The first set of tests consisted of measuring the times between pulse "B" and a delayed pulse B in the PMT, with and without a burst(pulse train "A") in between them. To solve the problem of irrelevant long term drifts in the PMTs and electronics, we fired the B pulse every event, but the A pulse train only every other event. Thus, the time comparison, with and without the high rates produced by A, could be made over a much shorter time scale, in this case every other pulse, (0.2 Hz). This improved the stability of the measurements dramatically, and precision timing and pulse height studies became possible. For convenience, when alternate pulsing was used to measure time shifts, we will refer to it as "method 1".

One other problem was solved in a similar manner. If we note time or gain shifts in the B pulse as a function of rate, we would like to know whether they are due to transit time shifts in the PMT, or whether they are due to the fact that pulse B is sitting on the tail produced by pulse train A. Therefore, we set up 4 different kinds of triggers:

1) A and B- simulates the full high rate environment for test pulse

2) B only- test pulse only, response when rates are low, no tail from pulse train A

3) A only- tail from pulse train A only

4) no pulse - pedestal only

Obviously, when B does not fire, there can be no timing. However, an ADC will still monitor the integrated area in the same time region, so that we can know the size of the tail relative to the pedestal, and, with a knowledge of the shape of the leading edge of the PMT analog signal, we can model the expected time shift. We refer to measurements obtained using these four different triggers as "method 2".

16.7.3. Setup for PMT tests

The setup we used for rate and pileup studies is shown in Fig. 16.7.1. The idea is to let a very low rate light source (pulse "B") define the timing and pulse height(strictly speaking the area under the pulse) and then to measure the timing shift and pulse height changes in B by firing a burst of light pulses at a high rate before B (pulse train "A"). All the signals are synchronized. A pulse generator (PG in Fig. 16.7.1) is running at about 5 Hz and one of its outputs is connected to a module (AP in Fig. 16.7.1) which generates one logic output pulse for every other input pulse. The outputs from AP were used to start a time-to-digital converter (TDC), externally trigger an LED pulser which is used to fire the low rate LED, and as an input to a pattern register which is used to tag the type of event. The other output from the PG was sent to a module (DP in the Fig. 16.7.1)which only generates logic pulses for the first two of every four input pulses. The output from this module is sent to an HP 8130A 300 MHz Pulse Generator which is used to drive the high rate LED (pulse train A) and is an input to another pattern register. A gate for the ADC (a Lecroy FERA), timed to the low rate pulse position, was driven by PG.

We used a Phillips model 704 300 MHz quad leading-edge discriminator to provide the logic signal to the TDC. This unit has very good rate stability, introducing less than a few ps timing shift at the highest rates in our tests. The octal model 708 showed equally good timing stability.

The TDC was a Lecroy model 2228A CAMAC module. Its start was derived from the gate driving the slow LED, pulse B. Its stop was derived from discriminated PMT signals. The analog input to the discriminator included both pulse train A as well as pulse B. The pulses in burst A were set to be smaller than pulse B. The discriminator threshold level was set to fire only on pulse B. This was done in order to limit the rate of pulses into the TDC, which was found to have some rate dependence. While the pulse height differed, the areas of the PMT pulses from both LEDs were about the same.

Figure 16.7.1: Part of the setup used for rate and pileup studies. PG is a pulse generator, AP is a module which generates one logic pulse every other input pulse, DP is a module which, for every four input pulses, generates two logic pulses on the first two and nothing on the second two. HP 8130A PG is a pulse generator which can generate bursts of between 1 and 10000 equally spaced pulses.

16.7.4. Results of PMT Tests

Now we describe the results of our PMT tests.

The test of timing stability was performed by using 100 signals in a burst (pulse train A) with a uniform spacing of Δt. The low rate signal (pulse B) was placed Δt after the end of the burst. For example, with a burst rate of 5 MHz, we generated 100 signals with 200 ns between the neighboring signals and placed the low rate signal 200 ns after the last signal in the burst. This required that the low rate signal be delayed by about 20 μs relative to the start of the burst. The jitter caused by this delay is about ± 4 ns, which is acceptable compared to the 200 ns or larger period between pulses. This is why we chose to limit the high rate burst to 100 successive signals; more would have introduced an unacceptable jitter of pulse B relative to pulse train A. Nevertheless, we did some tests with 2000 pulses in the burst, which we will also describe. Recall for comparison that the expected maximum total number of electrons per calorimeter per ring injection is a few hundred.

For the R1355 tube, the signal from the PMT was fed into the Phillips Scientific 704 Leading Edge Discriminator directly. For the R1828-01 tube, the signal was first led to an attenuator set at 30% before going to the discriminator. The number of photoelectrons for each high rate signal was about 300 for the R1355 and 690 for the R1828-01. The high voltage was 1325 V for the R1355 and 2300 V for the R1828-01. The parameters for the low rate and high rate signals from both tubes are listed in Table I.

Table 16.5.2-1 Signals used for rate and pileup studies: All parameters were measured by averaging over 64 pulses using the Tektronix DSA 602A Digitizing Signal Analyzer with band width set at 1 GHz. The signal from the PMT was connected by a 35 ns RG 58 cable to the scope. LD refers to the leading edge, TD the trailing edge as observed on the scope. Both LD and TD are measured from 10% to 90%.

Signals	LD [ns]	TD [ns]	FWHM [ns]	Amplitude [V]
Low Rate/R1355	2.13	2.20	2.87	2.47
HighRate/R1355	2.73	12.17	7.57	0.78
Low Rate/R1828 − 01	1.68	4.35	2.37	7.83
HighRate/R1828 − 01	2.36	11.78	7.26	2.81

Fig. 16.7.2 shows a typical timing histogram, in this case for the low rate LED with no high rate LED, indicating the intrinsic time resolution in our measurements. The peak is mainly broadened by the Poisson distribution of photons of the low rate light source and the jitter of the electron transit time in the PMT. For the rate tests here, $\sigma = 60.2 \pm 0.7$ ps for the R1355 and $\sigma = 33.5 \pm 0.7$ ps for the R1828-01. The positions of the peaks were

Figure 16.7.2: For a constant rate, this shows the time resolution on the low-rate pulse in the typical case, using a green LED under reverse bias. There are about 46 ns per TDC channel.

calculated by averaging over all the events in the peak. Timing shifts were calculated using

$$\Delta t = \bar{t}_{rate} - \bar{t}_{free} \ ,$$

where $\bar{t}_{rate}$ was the averaged time of the low rate LED when both the high rate LED and low rate signal were firing and $\bar{t}_{free}$ was the averaged time when only the low rate LED was firing (method 1).
Fig. 16.7.3 shows the timing shift for both R1355 and R1828-01 tubes at different rates up to 20 MHz. We can see that there is a weak rate dependence, but the shift is less than 20 ps at all rates.

Before we reach any conclusions, there are a few questions we need to answer.

(i) Is 100 signals in the burst enough for the $(g-2)$ rate test ?

(ii) For the timing shift above, how much does the tail from the previous pulse contribute (hereafter "the tail effect") and how much does the shift of the electron transit time in the PMT contribute?

(iii) In the actual experiment, pulses will not be uniformly spaced. How much does the timing shift as a function of the spacing between two successive pulses?

As mentioned above, for most of the tests, only 100 signals were used in a burst in order to minimize the time jitter in the low rate pulse relative to the end of the pulse train. But we also tested at 10 MHz with about 2000 signals in the burst. Both the R1355 and the R1828-01 were tested. The timing shifts are -14 and -18 ps for R1355 and R1828-01, respectively. The timing shifts were found to be almost a constant value if the low rate signal was placed anywhere within a couple hundred μs after the end of the burst. These tests were conducted at average rates well beyond those expected in the $(g-2)$ experiment.

The timing shift shown in Fig. 16.7.3 can be caused by the tail effect or by the rate dependence of the electron transit time. This becomes clear if we use Method 2 in Fig. 16.7.1, where we measure the both the timing and the integrated charge (over a 200 ns gate): of the low rate pulse, of the low rate pulse plus the tail contribution from the burst, of the tail contribution alone, and of pedestal events in successive triggers. Measuring the pulse heights concurrently allows us to determine their effect on the timing shifts. We define

$$\lambda = \frac{\bar{A}_{tail} - \bar{A}_{ped}}{\bar{A}_{free} - \bar{A}_{ped}} \times 100 \ ,$$

where $\bar{A}_{rate}$ is the measured low rate pulse height when both the high rate and low rate pulsers are firing, $\bar{A}_{tail}$ is the measured tail contribution when only the high rate pulser is firing, $\bar{A}_{ped}$ is the measured pedestal when neither the low rate nor the high rate is firing, $\bar{A}_{free}$ is the measured low rate pulse when only the low rate pulser is firing. In the case where the low rate pulse was absent, the gate falls over the same time region relative to

Figure 16.7.3: The timing shifts Δt of the R1355 and R1828 PMTs as a function of rate, by method 1: a high rate burst of pulses followed by the test pulse.

the high rate pulses. As previously mentioned, we monitored the low rate signal, the tail

Figure 16.7.4: Δt versus λ, indicating the relative importance of the tail in the timing shift as a function of rate. The tube was an R1828-01 with high voltage at 2300 V. A leading edge discriminator was used to measure the timing shift. The upper set of data points corresponds to the case where the low rate pulse was placed after a 100 signal burst of varying rate. For the other set, the low rate pulse was placed 140 ± 40 ns after 2004 signals at 10 MHz. For the 100-burst data, the timing shift Δt has a linear relationship to the size of the tail, λ, suggesting that shifts are dominated by the tail effect. The three points corresponding to 2004 signals in a burst do not lie on this line, suggesting that another mechanism has come into play, namely a shift in the electron transit time in the PMT.

contribution, and the pedestal contribution to the ADC at almost the same times, with a repeating pattern of four different triggers. To register pulse areas, we used the Lecroy Fast Encoding and Readout ADC (FERA) 4300B, which showed good stability at high rates.

Fig. 16.7.4 plots the timing shift Δt versus λ. We can see there is some correlation between Δt and λ when there are 100 pulses in the burst at different rate. This means the timing shift as a function of rate, shown in Fig. 16.7.3, arises mostly from the tail effect (The Lecroy 428F Linear Fan-in/Fan-out was found not to cause extra timing shifts at different rates). Fig. 16.7.4 also shows three data points measured by firing 2004 pulses in a 10 MHz burst. With the low rate pulse placed about 140 $\pm$ 40 ns after the end of burst (the $\pm$ 40 ns jitter is caused by the long delay), we can see that, 1) the shift is repeatable, and 2) the three data points associated with the 2000+ pulse bursts do not fall on the previous curve. Since the observed shift was larger than that expected from the tail effect alone, we concluded that a significant portion was caused by a shift of the electron transit time. Fortunately, this timing shift is small. In zero resistance clip line studies, the timing shifts for 100 pulses in the burst are always found to be positive, which is consistent the fact that the reflected pulse gives a positive tail. The electron transit time shift was found to be about constant from the highest rates down to a few hundred kHz. Our conclusion was that in contrast to the 100 burst data, we were beginning to see a transit time shift in the 2000 burst data, although the shift was still within the specification of < 20 ps.

In order to measure the change in pulse height with rate, we define

$$R = \left(\frac{\bar{A}_{rate} - \bar{A}_{tail}}{\bar{A}_{free} - \bar{A}_{ped}} - 1 \right) \times 1000 \ ,$$

Fig. 16.7.5 shows R as function of rate. The total error from the FERA measurement can be estimated by examining the data points in the figure. The total error (standard deviation) should be less than 1.63 for R1355 measurements and less than 1.16 for R1828-01 measurements. Similar to the timing test, we put 2000 pulses in 10 MHz burst and placed the low rate pulse about 150 ns after the end of the burst. The ratio was measured to be 3.41 for the R1355 and 4.36 for the R1828-01. This is two times larger than the specification $R < 2$, and a correction based on calibration data may be necessary during the experiment.

For the pileup studies, the setup is the same as that for the rate tests. Instead of a high rate burst, a single pulse (pileup pulse) was placed before the low rate signal, and the time shift was measured as a function of spacing between the pulse pair. Again the threshold of the leading edge discriminator was set high enough to block the pileup signal

Figure 16.7.5: The ratio R as a function of rate for the R1828 and R1355 PMTs, indicating the shift in the measured pulse height for bursts of pulses at varying rate.

from going to the TDC. The timing shift Δt is defined in the same way except $\bar{t}_{rate}$ is replaced by $\bar{t}_{pile}$.

In order to get an idea of the systematic error for the timing shift measurement, we used an R1828-01 with high voltage at 2300 to test 41 continuous runs with a time separation between pulses of 14.8 ns. The standard deviation on our measurement was 3.34 ps.

Fig. 16.7.6 shows the timing shift as a function of the time separation between the low rate and the pileup pulse (measured from the peak position). Again, as in the rate test, we needed to understand any shift caused by the discriminator, the electron transit time and the tail effect. To test the discriminator, we again put an adjustable attenuator before the Phillips 704 discriminator and adjusted the attenuator setting from 10% to 100%. The maximum change for the timing shift was found to be about only 6 ps for a time separation of 15.5 ns using the R1355 tube.

The analysis of the tail effect is more complicated. It is reasonable to assume that the timing shift from the tail effect is linear with the size of the tail. If the timing shifts are due mainly to the tail effect, then with a reasonable delay and multiplying factor, a pulse height curve of the tail from the first pulse should follow the time shift data points.

The timing shifts as shown in figure Fig. 16.7.6 and a plot of the tail of the first pulse are overlaid in figure Fig. 16.7.7 by multiplying the tail pulse height by 930 and shifting it 2 ns to the right. The scaling and offset factors are consistent with the pulse parameters listed in Table 16.5.2-1 and the discriminator threshold we used. The wave form was taken with a Tektronix DSA 620A Digitizing Signal Analyzer (DSA). It fits the data very well. This gives us confidence that the timing shifts we saw in Fig. 16.7.6 arise mostly from the tail effect.

We used the same setup for the pileup pulse height stability measurement as for the timing rate test. R is defined in the same way except $\bar{A}_{rate}$ is replaced by $\bar{A}_{pile}$. Fig. 16.7.8 shows the results. R for some of the data points is found to be close to 1% and the reason is not clear. The shift is larger for the R1355, and is larger than 0.2% for pulse spacing less than about 50 ps. It is believed to be due to the fact that the FERA is not able to measure the tail contribution accurately, perhaps due to baseline instability. However, since the probability of two pulses being within 50 ns at 4 Mhz (the expected rate at early times in the FSD,) is about 0.2, the effect is again at about the level of 20 ps.

Besides the PMTs and bases, we also studied the timing shift caused by the Lecroy 428F Linear Fan-in/Fan-out, the EG&G 50-Ω splitter, and a long cable under high rate and pileup. They were found to be rate independent but do add to the tails of the pulses and therefore increase the timing shift caused by the tail effect.

Figure 16.7.6: Timing shifts from pileup vs pulse separation for the R1355 and R1828-01. The separation is the time between pairs of pulses. The lines are to guide the eye.

Figure 16.7.7: The line represents the pulse height of the tail from ADC data (suitably scaled and shifted) overlaid with timing shifts from pileup. Data points are for the R1355 as shown in Fig. 16.7.6. The waveform was recorded by a digital scope with a 1 GHz bandwidth.

Figure 16.7.8: R as function of separation for both tubes: the relative shift of the pulse height as a function of the time spacing between a pair of pulses.

The studies above help us understand many issues about timing stability at the several picoseconds level and pulse stability at the several 0.1% level for different devices. From the measurements, we reach the following conclusions:

(a) The electron transit time shift for both R1355 and R1828-01 is less than a couple of picoseconds firing a 100-pulse burst at rates well in excess of those expected in $(g-2)$. The parameters for the tested signals are given in Table 16.5.2-1.

(b) The pulse height change is less than 0.4% at different rates for evenly spaced pulses.

(c) When a pair of pulses are brought together(as close as 10 ns), the resulting timing shift in the second pulse is almost purely due to the presence of the tail from the first pulse.

(d) When a pair of pulses are brought as close as 10 ns apart, the pulse height change from the photomultiplier tubes is less than 1%.

16.8. Data Stream

In this section we discuss the word structure coming from the various electronic elements and the initial on-line event building.

As mentioned earlier, we expect to mount the $(g-2)$ experiment in two phases: first a lower-rate (maximum about 1 MHz/calorimeter immediately after injection) data run at our proposed intensity using pion injection, followed by a later high-rate (8 MHz/counter immediately after injection, 6 MHz after 20 μs) high-statistics data run with muon injection. We anticipate that the online data stream will also make a transition between these phases, from initial logging of all data in a raw format (while compression algorithms are being developed) to later logging of mostly "compressed" events and a small percentage of "raw" events.

The bulk of the data will come from the WFDs and MTDCs. Each of the 27 channels in an MTDC module accepts logic inputs from a discriminator. An output word is generated for the current clock cycle whenever a leading or trailing edge in the input logic pulse is encountered. The output format consists of a 10 bit time field, a 5 bit channel number, and one up/down flag bit. The output words are packed in pairs and are combined with parity data to give 40 bits/pair. We are designing a 256 Kbyte on-board memory to store all of the timing information for a single ring injection. The memory would be read out between injection pulses. We plan to assign one MTDC module per two calorimeter stations. For each detector, there will be five discriminator (up and down logic transitions) and five derandomizer (1 leading edge transition) inputs from the five FSD elements, and one of each from the sum of the wfd signal as well, Typically there will be a total of two transitions recorded per electron, the calorimeter plus one FSD element. Each pair of level-transitions (rising or falling discriminator threshold-crossings) on at least one of 27 parallel inputs results in a 5-byte output record into fast memory (80ns cycle time). We therefore expect 10 bytes per decay electron from the MTDC. Compression is achieved by co-ordinating arrival times between the 4 devices and the calorimeter WFD information, and by encoding pile-up rejection information from the FSD into flag bits. As with the WFD system above, experience with off-line raw data compression in early running will be used to develop algorithms for on-line compression and ultimately hardware pre-processors for in-line compression.

Each WFD consists of 4 analog inputs. For the calorimeter, these would correspond to signals from each of the four PMTs on the calorimeter. Each input has a separate discriminator; if one or more cross a threshold, then output is generated. The analog signals are summed internally and input to two FADCs. The two FADCs are operated at 200 MHz with their relative phase shifted by 2.5 ns, to give ADC values every 2.5 ns. The

output consists of information from a 20 ns time slice: 16 bits of time, 4 successive 8 bit ADC values spaced 5 ns apart and 4x4 bits of discriminator patterns. There are two 32 Kbyte memory banks, one for the times, and one for the pulse heights. Like the MTDC, the memory is large enough to store data for a single ring injection, and would be read out between injection cycles.

We anticipate 20 bytes of raw MTDC data and another 32 bytes of raw WFD data per pulse with our baseline system, yielding 2.5 kByte/fill/cal from the 50 hits/calorimeter/fill in our lower-intensity mode. Multiplying this by 24 calorimeters, 12 fills/AGS cycle, and an AGS cycle frequency of 0.6 Hz, we obtain an average raw data rate of 500 kbytes/s. An additional 25% should be added to this for the readout of PSDs and the wire chamber system (5 PSDs x 48 channels + 112 wires implies 15 additional MTDC modules).

While the calorimeter systems will contribute the bulk of the data stream, provisions must be made for reading out PSDs, wire chambers, the calibration system, the NMR magnetic field data, environmental records of ambient experimental conditions, high voltage monitoring, etc. Muon losses will also be measured as coincidences between scintillation detectors (SD) and/or wire chambers accompanied by small coincident energy deposits in a pair of calorimeters. While this analysis will initially be carried out off-line, it may well be necessary to implement it on-line before final high-intensity running proceeds.

In summary, since it is impossible to anticipate all the subtle uses of the mass of raw data we will accumulate, we are developing a modular and easily upgradable system of data acquisition electronics with a flexible on-line data processing system. For our first engineering and physics runs, this system will be capable of a maximum sustained event rate of 1 MHz/calorimeter, corresponding to our proposal conditions. For later higher-statistics and high-intensity running, the baseline front-end data acquisition electronics will be capable of 6 MHz/calorimeter operation, while the second-level VME on-line and in-line processing system will require minimal upgrading. Upgrade capability for additional instrumentation of either calorimeters or SD systems, and for the introduction of a complete set of PSDs, is provided for in a straightforward and cost-effective manner. Further developments await our experience with prototypes of our baseline DAQ system, and ultimately our experience with muon decay electrons in the storage ring.

1. R. Carey and J. Miller, *The Impact of Gain and Resolution Shifts on the* $(g-2)$ *Frequency Measurement*, *Muon g-2 Note No. 165.*.
2. W. Morse, *A New Method of Analysis*, *Muon g-2 Note No. 93*, October 1991.
3. J. Miller, R. Carey and E. Hawk, *Measurement of the Muon Electric Dipole Moment in E821*, *Muon g-2 Note* in preparation.
4. D. Hertzog et al., Nucl. Inst. and Meth., A294, 446 (1990).

5. D. Simon et al., Nucl. Inst. and Meth., A335, 86, (1993).

Chapter 17.
Data Acquisition and Online Software

Revised March 1994

17.1. Summary of the DAQ Baseline

The design of the data acquisition architecture is determined by the following characteristics of the g-2 fill structure:1) high instantaneous rates (6 MHz) at the input of each of the detector stations 5 μsec after injection,2) 10-50 msec intervals between fills, and3) high total data rate (5.3 MByte/s) from all 24 detector stations averaged over one 2 second AGS cycle.During pion injection, the rates are not as challenging, but the DAQ must be designed with an architecture that can handle the eventual muon injection rates with a simple staging scheme.

In order to handle the high instantaneous rates, the front-end electronics digititizes the waveform information every 2.5 ns and clocks discriminator transitions every 1.25 ns. This information is buffered internally and can then be either read out between fills or after all 12 fills have been completed (roughly 600 msec), but before the next set of 12 fills which occur 1.4 seconds later. In order to be able to keep these transfer rates low enough across the VME backplane during muon injection and to perform compaction algorithms on the data, there are distributed VME crates around the ring with local intelligence. Each crate services 4 calorimeter stations. These crates are linked to a central VME crate in a star formation by a fast VME interconnect (MXI-bus). During pion injection, the central crate CPU pulls the data through the MXI between cycles and controls all crate functions. During muon injection, CPU's can be added to the six distributed crates in order to buffer the data between fills since there is not enough local memory in the front-end electronics. These CPU's will also compact the data before presentation to the event builder in the central crate and would be linked to the event builder CPU by ethernet, but data transfer would still take place over the dedicated MXI highway.

The event builder CPU is also linked to a host computer in the control room via ethernet. Start/stop run commands and relevant slow control data is passed from the host to the event builder and detector data is passed back to the host at a preassigned sampling frequency. The full detector data is written directly to tape via SCSI bus from the event builder without passing through the host. The host is a workstation which monitors all

aspects of the experiment that would be of interest to the general user and is loaded with the same graphical interface as the slow control system. Specific slow control functions that are to be managed by the experts are available only on the relevant PC or Workstation which controls that subsystem (see section on Slow Control). The host is also a server for additional workstations, such as a dedicated offline analysis workstation with its own exabyte drive to do rapid offline analysis in the control room. A diagram illustrating the general architecture of the DAQ system as outlined above is presented in FigDAQ.

17.2. Hardware Organization

17.2.1. Front-end Electronics and VME Backplane Rates

To understand the rate requirements, I here review the relevant numbers for muon injection. Pion injection rates are a factor of 11 times less. Each calorimeter station detects approximately 391 electrons with energy above 800 MeV per fill. If the tubes are turned off for the first 5 μsec after injection to protect them from a burst of particles caused by residual pions hitting the sides of the ring, then this number becomes 362. Assuming that the WFD is run in interleaved mode and each event is sampled over 60 ns, this gives 3 $\times$ (8 bytes/20 ns) $\times$ 2 interleaves = 48 bytes/event/detector station. For estimates based on the MTDC, let's assume we use both leading and trailing edges for time-above-threshold measurements for both calorimeter and one (and sometimes two) hit FSD segments, as well as a single transition for each time-above-threshold measurement. On average, we expect 6 transitions $\times$ 4 bytes = 24 bytes/event/detector station. Although each PSD requires one MTDC per plane, only one or two channels per plane are ever active during an event. In addition, it is not necessary to use both leading and trailing edges. Each PSD therefore adds 2-3 hits $\times$ 4 bytes = 8-12 bytes of data.

The highest expected instantaneous event rate with muon injection is 6 MHz per calorimeter 5 μsec after injection, or roughly one event every 170 ns. Since the WFD is sampling every 2.5 ns and the MTDC every 1.25 ns, the overlap of two pulses poses no insuperable problems, particularly with the additional rejection provided by time-above-threshold and position information. Instantaneous rates in the photodetectors are reduced by subdividing the detectors (calorimeter into 4 parts and FSD into 5). The instantaneous data rate from the WFD and MTDC, however, is quite formidable since each WFD and MTDC services two calorimeter stations. Using the event size derived above, the highest

rate expected is 6 MHz $\times$ 2 $\times$ 48 bytes = 576 MB/s from the WFD and 6 MHz $\times$ 2 $\times$ 24 = 288 MB/s from the MTDC, which, of course, falls off rapidly as the muons decay in the ring. Data cannot be transferred over the VME backplane at such rates and must therefore be buffered internally in the WFD and MTDC themselves.

Each WFD can store internally $\sim$ 2,600 60-ns samples or 1,300 typical electrons events when two calorimeter stations are in the same WFD. In pion injection there are only 34 detected events/fill/station, so the WFD can easily store all 12 fills in its buffer and then transfer the events to the event builder during the 2 seconds between cycles. During muon injection, however, the WFD data must be transferred between fills because storage is not sufficient for the 362 electrons $\times$ 12 fills = 4344 detected events/cycle/station. The MTDC will store 128,000 transitions, which is the equivalent of 21,222 six-transition events or 10,666 electrons hitting both input calorimeter stations. This is sufficiently large for a 12-fill store in either pion or muon injection mode, but for ease of event concatenation will be transferred in the same way as the WFD data. If we have 50 msec between fills (as is the current thinking at the AGS) and there are 4 calorimeter stations in each of the distributed VME crates (i.e. 2 WFD and 2 MTDC), then the total data rate on the backplane must be 2 MB/s to transfer all the data to a buffer in the local CPU. The WFD and MTDC need to be able to transfer data at these rates, but the MVME167 and VME backplane do not limit us. This has been demonstrated in measurements made at the SSClab (Romero and Dunning, June 1992) using a 25 MHz MVME167 CPU communicating with a DRAM Memory Module (MVME224A-2), which achieved sustained data transfer of 10.6 MB/s during VMEbus read cycles and 19.07 MB/s during VME write cycles. Similar rates have been achieved at Boston University.

17.2.2. VME-VME Fast Interconnect

The data will be transferred to the event builder after the 12 fills are completed, in the remaining 1.4 seconds of the cycle. The average rate per link will be 900 kB/s, which necessitates either a fast VME interconnect or a factor of $>$4 data compression to bring the rate comfortably within the range of ethernet. Unlike most other VME interconnects, Ethernet is not limited to short cable lengths. It would also imply that the distributed CPU's must be there from the start, whereas a VME interconnect could hold off the expense of additional CPU's until the start of muon injection. Ethernet is also less immune to noise than most VME interconnects. Our baseline is therefore a dedicated data highway between VME boards, augmented during muon injection with local intelligence for buffering and compaction. Any ethernet connection under this scheme is used to download compaction algorithm software and for status communication. We are studying

both lossless compaction as well as algorithms for online reduction of the data. If we are convinced that the lossless compaction on its own will give us the needed factor of four AND tests indicate that ethernet will not have problems in the noisy environment of the ring, we will install the CPU in the ring from the start and use ethernet for data transfer as well as communication.

In evaluating which fast VME interconnect would best match our requirements for a dedicated data highway, we examined many options. The simplest and cheapest solution are simple bus extenders of which there are numerous varieties on the market. The least expensive, passive bus repeaters, have problems with reflections and noise immunity. The next class of extenders are systems which convert VME protocol to their own in one crate and then translate at the other end. Some examples of this are MXI by National Instruments, Bit3, and VICbus by CES. With an advertised transfer rate of 8 MB/s (15 MB/s with new ASIC in 1995) and the fact that it needs no special software driver, MXI will fulfill our needs. Measurements of DMA transfers across MXI to a DRAM Memeory Module (MVME224A-2) using a 25 MHz MVME167 CPU were performed at the SSC lab (Romero and Dunning, June 1992) and showed a sustained rate of 3 MB/s. Since the maximum cable length is 20 meters, the system will require two MXI interface modules in the central crate, each fanning out to 3 of the distributed crates. This necessitates putting the central VME crate on the experimental floor and bringing the SCSI link to tape (now, per force, differential SCSI) from the event builder to the control room where the tape drive will be located. VICbus has a 100 meter cable length limit, but is almost three times more expensive than MXI and involves a larger investment in software development.

17.2.3. Central VME Crate

The job of the event builder is to collate the information coming from the 6 distributed crates. It is more properly called a spill builder, since it takes a 12-fill spill record from each of the calorimeters and concatenates. Calibration information gathered by the FERA ADC's and scalars which reside in CAMAC represents another spill record which must be properly synchronized with the VME information. Two CAMAC crates are sufficient for all FERA's and scalars. The two Kinetic 3922 crate controllers will be daisy-chained together and a Kinetic 2917 interface will reside in the VME crate. The expected data rate is 33 kB/s, far below the 2 MB/s that this CAMAC-VME link can deliver. Summary information from other subsystems which is to be written to tape, e.g. average field calculated from the NMR trolley and fixed probes or average vacuum in the storage ring, must be sent to the event builder over ethernet from the host computer at regular intervals.

The Host controls this process, as well as general startup and shutdown procedures, and sends them as header records for each run rather than interrupting the main data flow.

The total data rate in the central crate represented by the sum of all 6 streams of uncompacted muon injection data is 5.4 MB/s. In principle the VME backplane can still handle these rates. It now becomes a question of how fast the event builder CPU can concatenate and write to tape. Since exabyte tapes can hold 5 gigabytes of data and are so common that every University owns a number of drives, they are the most economical choice even though their writing speed is lower than other forms of mass storage. Their reliabilty is also greatly improved when operated in streaming mode. For uncompacted pion injection data, the average data rate is 495 kB/s which can be handled by one exabyte tape drive, provided a buffering scheme is used to present data to the tape at exactly 500 kB/s such that it can be operated in streaming mode. For muon injection it is possible to envision a farm of exabyte tapes with an appropriate buffering/pipeline scheme.

This is not, however, the way we would prefer to run. It will require an additional several gigabytes of buffer disks and a data manager to distribute events from the various spills onto the several tapes (to insure that the fast rotation data, for example, has all calorimeters represented in each tape). This methode still ends up with a large number of exabyte tapes which take just as much time to read as they did to write. If we write all this raw data to tape, we will need to write 2000 exabyte tapes to get down to 0.3 ppm statistical accuracy. We believe that we can easily reduce the amount of data written to tape (and make the rate more manageable as well) by a factor of 2-3 using lossless compaction in the front-end CPU's. We are also interested in performing online data reduction in these modules and are presently measuring the total computation time involved in sample algorithms. If we do such reduction during muon injection, we must take great care that biases are not introduced into our data. We would practice data reduction in one CPU during the pion injection run and be able to make offline comparisons between analysis of raw and reduced data. We would also insure that during muon injection, approximately 5% of the data collected from each calorimeter would not pass through the reduction process, thus providing an online monitor. Another factor of 3 reduction using these algorithms combined with the lossless compaction would get us back to one exabyte every 3 hours, or 200 exabyte tapes in all.

17.3. Online Software Organization

17.3.1. Overview

The following guidelines have been used to determine the structure for our online software package. There will be 2 different operating systems within the online-environment. A real-time operating system with good interrupt capabilities is a natural choice for the processors which deal immediately with the data. Therefore, the event builder MVME167 and the distributed CPU which are responsible for data compaction and buffering will be running the VxWorks Operating System by Wind River, Inc. The host computer, on the other hand, will be a standard UNIX workstation, running the X-windows and MOTIF graphic packages. To maintain ease of software development and reduce user confusion, the same online software should be able to run in both operating systems. Eventually we expect that the offline software will flow naturally from the online analysis packages, which should therefore be modular and easily transportable. In light of this, it makes economic sense not to require non-standard or expensive ancillary software licenses, since development and analysis will take place at a number of different University sites. The online software should be easily expandable, to include software in the front-end CPU's for the muon runs. The host computer also serves as a monitor for the slow control system, so any online software package should be easily integrated with whichever slow control graphical interface will eventually be chosen. At the moment our group favors DataViews which has a hefty educational discount and drivers which have been developed by CEBAF for use with their supported DAQ package, CODA. We have determined that the software package which meets the above-stated needs, which will require the minimum programming investment and which shares a philosophy of minimal additional licensing is UNIDAQ, which will be described in more detail below.

17.3.2. The UNIX Host Computer

The UNIX computer will serve as the host for the VxWorks platforms, which means that the VxWorks machines (MVME167) will be booted from the UNIX computer. In addition, the host computer provides the link between slow control and the data acquisition stream without actually interrupting the writing of data directly to tape by the event builder CPU, so it should be able to easily handle the Slow Control software.

The DataViews package, which we are considering for Slow Control, would require on the order of 16 MB of memory (depending on the application), while UNIDAQ would require about 10 MB to run, in addition to about 6MB of shared memory for the buffer manager. Additional memory will be needed for the operating system and possible X-terminals. With a total of about 64 MB of memory, the UNIX station will be well equipped to perform its tasks, even if a more memory intensive slow control package is chosen.

In order to be able to function in stand-alone mode, the workstation will need an internal disk capable of storing its operating system, the slow control package, the online software and the VxWorks system. A standard disk of about 500 MB would be sufficient. If necesary, this can be expanded using external SCSI drives.

Along with the UNIDAQ user interface and a slow control user interface, an online analysis program (part of UNIDAQ) will run on the host computer. This requires data transfer from the event builder crate to the UNIX host, using ethernet. The CPU performance of modern workstations will not be a limiting factor for running the experiment, especially since there will be an additional high performance workstation dedicated to quick turn-around offline analysis in the control room as well, connected to the host ethernet hub. However, since the host machine will also be used for offline analysis between running periods, it makes sense to keep the overall CPU performance high within budgetary constraints.

17.3.3. The VxWorks operating system

Two real-time operating systems were evaluated, VxWorks and LYNX-OS. The center of gravity of LYNX-OS tends to be at CERN and several accelerator control systems in this country. VxWorks, on the other hand, is supported by CEBAF and the SSClab (which, though no longer in a position to manage code (!), has spawned numerous University groups with VxWorks expertise, including RHIC collaborations), as well as many business applications. VxWorks is POSIX compliant without being a full UNIX kernel, which has advantages in terms of lower overhead and faster throughput for data handling. It also has a better interrupt latency than the competing system. Interrupts can be handled by

regular C-code, thus allowing for flexible communication between the interrupt and task level. The VxWorks operating system is designed to be used as a real-time partner of UNIX. For example, the TCP/IP standard can be used for communication between UNIX and VxWorks. In the development cycle, code is written and compiled on the UNIX host. Afterwards, the code can be loaded into VxWorks, and executed. There are VxWorks equivalents to the most important UNIX inter-process communication mechanisms, which simplifies porting UNIX processes to VxWorks.

17.3.4. Online packages

We have considered both the UNIDAQ (developed by SSClab, U. Michigan, LBL and KEK) and CODA (developed by CEBAF) packages for our online software. Both systems are tested to work on HP-UX, ULTRIX, and VxWorks platforms. UNIDAQ is tested to run on SUN-OS and IRIX, platforms to which CODA is not ported.

Within CODA, the RunControl manages the DAQ subsystems. Communication between the subsystems uses RPC's (remote procedure calls). This allows a CODA based online system to run on multiple machines. Within CODA, the Read Out Controller (ROC) may run in VxWorks, while the event builder and event recorder are implemented in the UNIX host. The CODA RunControl is written in Eiffel, an object oriented language. It is loosely coupled to a DataViews based slow control, meaning that the operator can have both slow control and online data in the same window.

Within UNIDAQ, processes may run in a single machine or on multiple machines. In the first case, communication between the processes is based upon standard UNIX/VxWorks message queues and shared memory, while this is expanded using RPC's when UNIDAQ is run in multiple machines. The idea behind UNIDAQ is to reduce the overhead as much as possible. One may run UNIDAQ as a simple two process system plus a buffer manager, or as a multi-process system spanning several machines. The collector process, event builder and recorder processes may run in VxWorks or UNIX. No effort has been made yet to integrate a slow control package within UNIDAQ.

Within a CODA dataflow one may have multiple ROC's, running on different machines sending data to the UNIX host event builder. This is TCP/IP based and relatively independent of the underlaying hardware. Events are formatted using the CODA data-format. The UNIDAQ dataflow is based upon the NOVA buffer manager, which runs both on UNIX and VxWorks. Buffers are transferred from machine to machine using a NOVA network deamon; this is all TCP/IP based. With this scheme it is possible to transport buffers between UNIX and VxWorks platforms, and also between two VxWorks platforms. It is also possible to fan out data (e.g. from one VxWorks platform to a a UNIX and a

VxWorks platform) or collect data from multiple machines into a single machine. A header is added to the events, but no event structure is imposed. New processes can be based upon a skeleton, provided within the UNIDAQ distribution. All UNIDAQ processes are implemented in C, to ease the installation. The user interface is based upon Tcl/TK, an X-based package developed at the University of California, Berkeley, that can be obtained free of charge. As an alternative, a simple X-based user interface can be used.

In general, the UNIDAQ package provides more VxWorks support, and it seems easier to interface UNIDAQ with different (slow control) packages. An example of interfacing UNIDAQ with other packages is the interface between UNIDAQ and MURMUR, an error logging package supported by FNAL. A special process (logbook) is written as an interface between the packages. Furthermore, UNIDAQ provides less overhead and seems better structured for the needs of the g-2 experiment.

17.3.5. UNIDAQ for g-2

The UNIDAQ process can be divided into two categories, data handling processes and control processes. We will first discuss the configuration of the data handling processes. In general, the software configuration depends on hardware choices that need to be made. If there are no front-end CPU's during pion injection, then the buffer manager, the collector and the recorder processes will run in the event builder CPU. The collector process will pull data from the front-end crates across the MXI bus, while the recorder writes it all to tape. The collector will also read data from the CAMAC crates, receive the slow control data from the UNIX host, and perform the event builder tasks. Another process running in the event builder crate will be a sampler process, which transfers a sample of all data to the UNIX host. The UNIX host will run the buffer manager, a process receiving the data from the event builder crate, which acts as a data collector on UNIX, an online analyzer program and additional debugging tools.

During muon injection, front end CPU's will be added. The collection of data from a single crate over the entire spill can be accomplished by each of the distributed CPU's. The front end collector processes may also be used to perform data compaction algorithms before the data is sent to the event builder crate. The event builder CPU will run a dedicated event builder process instead of a combined collector/event builder as in the previous case. The data can either be pushed to the event builder by the front end crates, or pulled by the event builder. This last option resembles the situation in which there are no front end CPU's best, and can be seen as a logical extension of that situation. The remainder of event builder and UNIX processes are similar as discussed above.

The online analyzer process receives data buffers from the buffer manager (it actually receives a pointer to the buffer in shared memory). The number of events received will depend on the parameters of the event sampler. The parameters of each event routed to the UNIX host will be stored in histograms defined in the analyzer process. The analyzer process allows the user to dynamically link fortran routines, in which histograms can be defined and filled. The analyzer process is linked to the CERN libraries so that standard HBOOK routines can be used for this purpose. This dynamic linking procedure allows one to add and remove histograms while taking data. The interface to the analyzer process has the look and feel of PAW. One has the option, with the help of KUIP macros, to define interactively and fill histograms, for on-line monitoring of the data collected by by the dynamically linked routines.. Additional commands are provided to link and remove FORTRAN routines from the analyzer process.

In addition to the data-taking processes, there are control processes such as RunControl, and the XPC (which checks if all processes are alive), a user interface (operator) and several (debugging) tools. The functionality of the RunControl and Operator processes are determined by input files and can be changed on the fly.

The Operator process combines UNIDAQ with the Tcl/TK package. The functionality of this process is determined by a standard tcl-script file. For UNIDAQ, some additional tcl commands are defined which allow processes to communicate directly to other UNIDAQ processes without using the UNIX shell. Furthermore, commands to receive data from the buffer manager are implemented. These additional commands provide all the tools necesary to display information relevant for running g-2. It also provides the tools to create an event display based upon Tcl/TK. Using TK buttons, commands can be sent to RunControl (or other processes) to perform complex tasks like starting or stopping a run. The advantage of using an X-based package for event and statistics displays (that can be part of the operator process) is that these displays can be viewed on any X-based workstation, or X terminal that has an internet connection to the host computer. UNIDAQ has a built-in safety lock which guarantees that only one of these processes may issue commands at a given time.

Errors and other messages will be reported to a logbook process, which stores these messages to a disk file. This file can be displayed using the logview tool. When using the MURMUR package (for which an interface exists) automatic actions can be taken, depending on the error code.

Chapter 18.
The E-821 Slow Control System

Revised March 1994

18.1. Introduction

The $(g-2)$ muon storage ring is more like a small accelerator than an experiment in an extracted beam. There is a need for a more automatic presentation of device status, and a more central initiation of control signals, than is usually the case in a beam line. These requirements imply that the data acquisition systems for the hardware status, and the software for display, be fully integrated at the planning stages, rather than separately matched. An efficient way to take advantage of an integrated approach is to buy commercial plant-floor type monitors and their associated software packages. These customize easily to various industrial applications, and they seem to be applicable to the muon storage ring as well, even though it is not quite like a plant floor.

There are architectural considerations in an experiment that one would not confront in industrial applications. These differences make the $(g-2)$ control system not quite a plug and play toy, but careful consideration of how various ring subsystems interact should make the continuous operation of the ring fairly painless. The main idea in this architecture is that all hardware subsystems operate in a high-priority, local control loop, but talk to the slow control system when they can. The slow control system then logs status information or trouble reports. The local control loops also have priority over control signals sent down to them from the slow control system. This is to prevent the human operator of a system from helplessly losing control to the slow control system.

At the level of the actual hardware, the slow control system will communicate to modular industrial controllers. These controllers are microcomputers, generally configured to operate scanning analog to digital converters or standard industrial signal conditioners. They exist as self-sufficient processors, and have the ability to run the local control functions easily. The ones that E-821 will use will be Allen-Bradley PLC's (Programmable Local Controller's), or their equivalents. They are nearly ubiquitous in plant floor environments, and they have sufficient communications ability to fulfill the reporting requirements for the slow control system. The newest versions also allow ethernet connections, which simplifies their integration into an E-821 network.

The whole control system will use an ethernet network to communicate among its parts, and to communicate at a higher level to the data acquisition host. It will also have a hidden network strictly for automatic control purposes and free of any monitoring responsibilities. The experiment will have its own subnet on the internet, but will be accessible in only a limited fashion to the rest of the internet. This will prevent an anonymous user in a far-off place from running a portion of the experiment in an unforeseen way. However, the ability quickly to communicate news items or experimental data is quite feasible and appropriate.

18.2. The Local Controller Hardware

The controllers for the muon $(g-2)$ experiment will be Allen-Bradley PLC-5 or AEG Modicon controllers. These controllers have a small complement of memory with a battery backup, some communications ports, the ability to scan several hundred to several thousand input or output circuits, and options for EEPROM program backup. Basically, they are scanners that read to or write from a bank of circuits. Separate modules determine the identity of these circuits, and the types of signals they process. The controller simply reads channels and stores them in its memory. It then provides the channel information to a display, which can be just a screen with a display of status indicators, or a highly integrated front end of a control system.

The communications channels that the controllers use come in three types, two quite useful and one less so. There is the proprietary Data Highway, which connects all the PLC's, and which has a reasonably high capacity. There is an ethernet link, which exists independently of the Data Highway, and has about twenty times its transmission capacity. And finally, there is an RS-232 port, useful as a debugging tool, on each PLC.

The controller has all the characteristics of a small, dedicated computer. There is some data handling ability, interrupt capability, status flags, and the ability to run multiple control programs. Their use in E-821 will be to run local control loops for the major subsystems, and to pass news reports back up to the slow control host computer.

The controllers themselves do not have the ability to process raw input signals from various devices. Specialized input modules will handle these tasks. As an example, the controls for the liquid helium refrigerator require temperature readings from junction sensors. A specialized module linearizes and buffers these junction signals before passing them on to the processor, which likes to see only well-conditioned, standard industrial inputs. Other electronic front ends perform similar conditioning in their respective environments.

This separated function design of the electronics also minimizes confusion in the field wiring to the processors. All wiring from the front end modules to the processors is on

terminal strips, and is identical with respect to wire type and termination. The specialized input wiring we will segregate by function onto the appropriate electronics. This input bundling is easier to maintain and repair than just running wires in sequential channel order, heedless of their functions.

18.3. The Network

Devices and computers in the muon $(g-2)$ experiment will communicate with each other via an ethernet network. The PLC-5 controllers have an internal ethernet interface, requiring, however, an external transceiver. The data acquisition (DAQ) host computer and slow control computer, if they are not the same, will both have ethernet capabilities. Allen-Bradley software, running on the slow control computer, will handle the communications between controller and the ethernet. This network should handle easily the data transmissions from ring subsystems and file transfers from the DAQ host.

In addition to the ethernet connections, the PLC's will communicate with each other via the proprietary Allen-Bradley Data Highway (actually, Data Highway+, or DH+), a custom network for their PLC interconnections, but well-supported by other PLC vendors. This second "shadow network" increases the slow control reliability by isolating the important control loops at the major subsystem level from the pure news-gathering functions of the ethernet. The Data Highway provides a way for automatic controls to function separately from the slow control system, though one could also activate devices through slow control, with the approprate priority and privileges. Since the two networks share nothing, failure of the slow control system or the ethernet does not compromise the operation of the ring subsystems.

The Data Highway transmission rate is 57.6 kbaud, in contrast to the much faster ethernet rate of 10 Mbits/sec. However, the Data Highway carries much less in the way of actual data than the ethernet. The Data Highway interconnection is responsible for carrying the control signals, global flags, and small blocks of data among the PLC's. The detailed description of these transmissions among the PLC's is actually imbedded in the design of the subsystem control loops, which will be described later. This "hidden" network remains invisible to the ethernet network, so the ethernet must also carry some of the same information. This redundancy is fortuitous, increasing the reliability of the transmissions at no cost, since E-821 requires the ethernet and Allen-Bradley supplies the Data Highway as standard equipment.

Figure 18.4.1: The E-821 Slow Control ArchitectureThe host computer and DAQ host are one computer in this figure. The host communicates with the PLC's on the ethernet, using Interchange software. The Data Highway is strictly for the use of the automatic controls.

18.4. The General Architecture

The basic idea of a slow control system is to provide a monitor on the $(g-2)$ ring function. It should allow the free transfer of data from ring subsystems, unencumbering the extant automatic controls. These automatic controls and their self-linkages are not properly in the realm of the slow control system. However, there is a connection between automatic and slow control systems. It's probably best to describe the entire ring heirarchically, from the controller, at the base, to the slow control monitor, at the apex.

Fig. 18.4.1 illustrates the basic architecture. The PLC controllers share automatic control among themselve on the Data Highway, and they pass news reports up to the slow control host on the ethernet. Note that the only common point between the two networks is at the PLC. From there on, the networks separate permanently. The ethernet network includes the slow control computer, here shown as part of the DAQ host. This may not be the case in the actual implementation, since there may be a temporal advantage to

obtaining a separate slow control host. If this were the case, the DAQ host would simply be another ethernet node.

The host computer runs the proprietary Allen-Bradley Interchange software, which allows the host to communicate directly to the PLC's over the ethernet. At this point, the slow control system has gotten access to data and/or news reports from the controllers. It is a collection of "unedited" data packages from the controllers. It will be the function of some higher level software to integrate and present these reports in graphical form. The host computer monitor will display a picture or schematic of some subsystem, and variables or parameters that are changing will appear in graphical form. For example, the helium level in the cryostat would appear on the screen, if that screen were selected. The cryostat, filled with helium, would appear as part of a cartoon illustrating the refrigeration system. The software that drives these displays is a commercial product whose only purpose is to generate graphics such as these. There are several commercial options for the slow control graphics software, as well as non-commercial options such as Los Alamos' EPICS. These are all under evaluation.

The central tenet of the slow control system is that it monitor and control the E-821 subsystems without disrupting the local control or feedback of that subsystem. To achieve this non-interference, it is necessary to assign priorities to any operations which may affect the running of a particular subsystem. Fig. 18.4.2 illustrates, in a schematic way, the loops that may exist in the control structure. A local process, for instance, a power supply, has inherent feedback control, and may have setpoints and software controls, as well. The loop labelled "Control" in Fig. 18.4.2 corresponds to the full set of these local device controls. They have the highest priority, being interruptible only under conditions set forth by the designer of the local loop.

Next higher in priority is the pathway labelled "Triggers," which represents a way that the slow control operator (*i.e.* an E-821 "Control Room" operator) could trigger a switch to control a device, or process. As a garish example, there could exist a "Quench" button, which would activate an energy dump from the magnet (at half-field, of course!). Since these priorities are lower than the local loop priorities, the triggers are easy to disable intentionally at the hardware level.

At the lowest priority is the passing of reports up to the operator console, which displays them. The requirement here is for an update rate of perhaps once per second for preformatted reports. This should be slow enough that the PLC's have no problem keeping up with requests from the slow control system, even though they are executing their own set of instructions in the local loops. The slow control software handles the initiation of requests and processes the replies from the PLC's. No request for news ever slows down the automatic control system, since these requests are both of the lowest priority, and

Figure 18.4.2: The Slow Control LogicControl loops indicate the automatic controls. They have top priority. Next in priority are the triggers, which can be locally disabled, which the enable line indicates. Last in priority are the news transmissions. The connection to DAQ is for completeness only.

are travelling on the ethernet, not the Data Highway. The only mechanism for slowing any control functions will be the processing of requests by the PLC's, or the operation of triggers. If the news report from the PLC exists in a predetermined format, of constant length, the delay caused by its transmission becomes a bookkeeping problem. This just means that it becomes part of the local loop, simply another task for the PLC.

Chapter 19.
Offline Analysis

Revised April 1994

19.1. Introduction

The goal of the offline group is to provide the g-2 collaboration with a set of tools for doing analysis, including easy access to the data and a common framework for developing managing and distributing analysis code. The offline code will not be as complicated as that required for the typical high energy physics experiment because of the limited number of physics goals and the relative simplicity of the cuts needed to form each dataset. g-2 is a minimum bias experiment in the truest sense. In order to conserve resources, however, it is imperative that as much of the offline package as possible be obtained from somewhere else, in particular from CERN. While not perfect, CERN code is coherent, well supported and runs on all the platforms needed by g-2: HP-UX, SGI IRIS, SUN SPARC DECstations and VAX/VMS. Furthermore, CERN software packages exist for nearly all our major software requirements - most of the offline work should involve the integration of this contributed code.

Listed below are the principal tasks of the offline group.

1 Set coding standards
2 Define data bank structure
3 Define analysis framework
4 Establish code management
5 Provide code distribution
6 Provide standard user interface
7 Set up database (geometric and calibration)
8 Provide histogramming and display capabillity: PAW/HBOOK/HPLOT/HIGZ etc.

The first item includes choosing the languages we will use and the coding standards we hope to enforce, selecting a databank manager for input and output, and setting up a code verification strategy. The analysis framework is a general means for integrating user code. With input and output standardized in terms of well-defined data banks (item 2) the user instructs the analysis manager to execute a set of routines on each data unit (presumably

one spill in one calorimeter), each of which reads from standard input banks and writes to standard output banks.

The code manager should allow a community of users to develop code together, keep histories and restrict access. A related issue is code distribution, how to dessiminate this information to the far-flung users. Some of the code managers provide natural tools for distibution as well as an entire code development environment, including access to the editor, compiler and librarian. Of course someone must write the code itself, not only for final analyses but also a multitude of utility routines for developing calibrations and checking the basic health of the hardware, as well as simulation routines of various sorts.

g-2 will need a fairly modest database which should include both static information (where this is, how long that is, how many channels of those are there?) and time varying information like calibration constants and magnetic field maps. Finally there is the question of finding the correct hardware with which to perform all these tasks.

The formulation of the offline package is in its early stages. A basic framework will be established by the time data taking begins. By making wise choices at the design stages, we can minimize later difficulties. The following sections describe the steps that need to be taken.

19.2. Coding Standards

19.2.1. Programming guidelines

A set of basic standards must be established. For example:

1 Code should be written Fortran 77 (with the usual VaX extensions) or C.

2 IMPLICIT NONE is required. The IMPLICIT NONE statement is itself platform dependent but it must be implemented in some form, either in the code itself or in the compilation directive.

3 Parameters should be used whenever possible. These include physical constants such as the mass of the muon, the mean radius of the ring or the speed of light as well as offsets into data banks. The data bank specification should include a list of integer parameters which specify the offsets to various entries. Values of parameters should be stored in an include file or CMZ sequence.

4 Code should be commented. Particularly important is a statement of what the routine does and a specification of its input and output.

5 Use meaningful variable names but obey fortran typing conventions in doing so. Failing to observe the Fortran conventions requires the user to constantly refer back to the declaration headers. Describe the role of the variable in comments near its declaration.
6 No GOTOs. Use subroutines for repeated code. Indent DO/IF THEN bodies consistently and label endpoints of the longer ones.
7 Code should be device independent at least to the extent that it run on VMS and the standard UNIX workstations (DecStation, SPARC, HP, SGI). Device dependences arise mainly in file I/O and can be dealt with.
8 Limit the use of common blocks to control functions. Use of standard banks for input and output will make it easy to interface analysis subroutines. Any common blocks should be maintained by CMZ or some other automated code manager.

19.2.2. Code Verification

It will be the responsibility of the offline coordinator to ensure that production code meets the above standards. It is the job of the experts who write the code to ensure that it works. However, global code verification strategies will be developed to doublecheck the experts. One way is to exercise the analysis chain with simulated data and check to make sure that the answer is consistent with the input data. Successive releases of the offline code will be tested on the same sets of input data and any differences in the output histograms will be fully understood.

19.3. Data Banks and Bank Manager

As indicated above, the use of standard data banks facilitates input and output. However, Fortran 77's inability to allocate and deallocate memory for data storage at run time requires the help of a bank manager such as CERN's Zebra package. Using Fortran 90 would save us the trouble of having to deal with a data bank manager, but the code would be incompatible with many of the software packages of which we hope to take advantage and require an enormous education effort within the collaboration.

Zebra is the obvious choice for a bank manager but it is far from perfect. The bookkeeping overhead per bank is larger than much of the competition and the code which one ends up writing often ends up looking far from transparent. At the same time, it is CERN supported, it lies at the heart of HBOOK, CMZ and other CERN products, it does allow the user to transfer files between machines of different binary data format, and experiments in the HEP community *have* written utility routines to make it more user friendly.

Another possiblity is the use of TYPES, from the Supercomputer Computations Research Institute, which can be called from Fortran 77, runs on all the standard platforms and provides a much more effective, object-oriented solution to memory management than Zebra or YBOS(the CDF standard). In addition to built-in protection against memory overwrites, TYPES, through its data type definitions, provides encapsulation of the sort of linked list/pointer code which makes prospective Zebra users rightly shudder. While it runs on all the required platforms, TYPES, like Fortran 90 would require the offline group to do a considerable amount of public education.

Whatever the choice of bank manager, to encourage good coding practice, the offline group should provide template modules which demonstrate how to perform input and output in the g-2 analysis framework, as well as the good general programming style described above.

19.4. Data Banks

The standard I/O banks should be defined as quickly as possible in order that code now under development not have to be later transformed. The raw data banks should look much as the data comes from the hardware and the processed banks should contain information derived from the raw banks. For example, a raw bank might consist of all the WFD information and a set of processed banks derived from it might each contain (among other things) an electron energy and arrival time. The entries within each processed bank should be addressed with integer offsets. An include file of such parameters should be associated with each bank.

19.5. The analysis manager

The basic job of the analysis manager software package is to provide the user with the necessary hooks to interface a series of analysis modules. It should be possible for the user ability to include and remove modules in the execution path both at link and run time. User code provides entry points for the various stages in the analysis of an event or set of events (begin run,end run,define histos,event), which are called by the manager. The manager should also provide utilities for reading and writing (or NOT reading or NOT writing) groups of banks. Although basically intended for batch use, the analysis manager can also be useful in an interactive environment, where for example, the last routine in the execution path is some sort of graphical display.

We have not yet decided on a package for integrating the execution of the various modules. All the major HEP experiments have either written their own or borrowed from elsewehere and we have a wide range of choices. However we will avoid the use of PATCHY, which while powerful and flexible is stubbornly arcane and is porly documented. But again, whatever the choice of analysis manager, it should be promulgated within the collaboration as quickly and as vigorously as possible.

19.6. User Interface, Histogramming and Graphics

We should take KUIP as our user interface. KUIP runs on all kinds of machines, from dumb terminals to workstations running the Motif window manager. Its heierarchecal menu structure should be familiar to most physicists, as it provides the user interface to PAW. KUIP runs in both batch and interactive mode and can learn a set of instructions and save it as a macro. Menus are easy to write. The use of a menu-driven user interface with on-line help not only makes code more user-friendly, the standard presentation of choices allows skills acquired while mastering one package to be transferred to another.

We will use PAW/HBOOK/HPLOT/HIGZ package for histogramming, and basic data manipulation and presentation. There seems to be no serious competition.

19.7. The analysis code

Much of the code has already been written in some form or another, although none has been incorporated in the as yet unspecified analysis framework. Several analyses require minimal processing. The basic muon g-2 spectrum, the number of decay electrons observed vs. the time after injection, can be formed directly from the derandomized FSD channels of the MTDC, once the energy of the electron is obtained from the corresponding WFD data. Algorithms for forming the electron energy on line are now being written - presumably the same algorithms can be used offline for the pion injection data. Once the time histograms are filled, they can be fit with the help of G2MIN, a menu driven interface to Minuit, the standard CERN fitting package.

Other analyses concern themselves with the systematic corrections. Several programs designed to determine the distribution of muon equilibrium orbits (for the electric field correction) have already been written. The CERN III fast rotation code, which takes uses the evolution of the bunched structure of the beam at early times to extract the muon momentum distribution has been resuscitated and is now interfaced to the G2GEANT Monte Carlo. The code for a fourier transform analysis of the fast rotation has been distributed but has not been tested anywhere but Cornell.

The code for two other systematic analyses: the pitch and magnetic field corrections, is fairly mature. We have modified the CERN GEANE package to perform the electron traceback on simulated events and we find that it does a superb job. The same code will also be used to generate the acceptance correction required by the inevitable biases in r, z and E_e. As the chamber design is still incomplete, no code exists for finding tracks, rejecting background and solving other real-life experimental problems.

No code yet exists for the muon loss monitor. Several fairly simple studies have been performed and a few means for extracting muon signals from the calorimeters have been suggested but there is no convincing evidence that we will be able to monitor the muon population at the required level of 1 part in 10000 per lifetime. There is some code for the electric dipole moment analysis but it has yet to be incorporated into the standard analysis package.

The g-2 simulation still needs some work. Like all the analysis code, it does not conform to the standards listed above, although in addition to the standard Ntuple, it does produce data banks resemble the expected form of the MTDC and WFD banks. However, it must be modified to generate real g-2 data banks so that real and simulated data can be analyzed the same way.

There are a number of utility and production routines which need to be written before any of the the analysis code described above can be used. One obvious group consists of

the routines which turn the raw data banks into electron time and energies. As this is the most critical part of the analysis, it will most likely have to be reworked many times. We also need routines for monitoring the basic health of the experiment. On line monitoring will do part of the job, but during commissioning we will undoubtedly want to dump a data tape and form a standard Ntuple (a PAW-readable direct access data file) and a large number of histograms to have a closer look.

19.8. Databases

The database requirements of g-2 are not extensive. As far as the offline is concerned, there are several general types of information that should be stored in a data base.

1 Static information: Basically the size and location of various things. This sort of information changes rarely, if ever. For example, the constants which describe our geometry should be stored in the database and should be read in by the simulation program as the defaults.

2 Calibration information: consists of data which is time dependent, although the frequency with which it is updated may vary. Presumably there will be a set of calibration constants for the detectors which will be written to the database every few runs. Raw data from the 300 fixed NMR probes, which can be read out on the order of seconds probably don't belong in the calibration database and should be written to tape. Summary data should go in the database, however. Data from the plunging probes and trolley, which come far less often, should definitely be in the database in some form.

In keeping with our general policy of using CERN software wherever possible we have decided to choose, on a tentative basis, HEPDB, a general High Energy Physics Database package, as our database manager. Although not yet widely tested, it is based on a database package designed by L3, whose requirements in terms of access time, flexibility and efficiency far exceed those of g-2. Like PAW, CMZ and other CERN packages HEPDB is based on the Zebra memory management system and will run on all the required platforms. HEPDB records can easily be transferred from machines with different binary represenations through the use of FZ sequential exchange mode files.

The more pressing issue is finding out what are the database needs of the various subsystems and how they should be implemented. We expect to gather this information by querying the relevant team leaders this spring and then to specify the structure of each subdatabase as part of an offline workshop planned for the summer of 1994.

19.9. Code Management and Distribution

Code management is concerned with the storage of code at a central repository, restricting access to the code for corrections and updates, keeping track of version numbers,maintaining code histories and releasing consistent code packages. Code distribution, on the other hand, is concerned with making sure that all member institutions have identical versions of the code, apart from possible machine dependencies. Code distribution should be far simpler than in the typical collider experiment. No one, for example, is familiar with every CDF production routine, but several of us on g-2 will probably know virtually every line of our own offline code.

CMZ is the logical choice as the code manager. It runs on all the necessary platforms and can perform all the necessary tasks. Some people object to CMZ, as it is a descendant of PATCHY and uses some PATCHY terminology. Nonetheless, it is easy to use, unlike PATCHY. The casual user need only learn a half dozen commands and online HELP is those who need it. Moreover, it includes many useful features such as a formatting tool for indenting loops, a utility which hunts for undefined variables and even a make facility for updating libraries. It also has direct interfaces to the C and Fortran compilers, the linker and various editors. It has been used extensively by HEP collaborations around the world, including our own collaborators at the Budker institute in Novisibirsk as well as H1 at DESY.

There is an appendix in the CMZ manual which explains how H1 has used CMZ as a code manager. We intend to use the H1 example as a guide for maintaining the G2GEANT simulation over the next few months and to tailor the framework they established to suit our own needs. This should involve little extra work, as the simulation is already maintained via CMZ. However, until recently, we have not had to face the problems created when multiple users try to work on one body of code. Our experience with the simulation should provide a good test of CMZ as a code development environment and help us work out the sorts of issues which will arise when we try to manage a much larger software package.

19.10. Hardware Requirements

The hardware requirements for the g-2 analysis are fairly simple, if demanding. As far as processing data tapes goes, the CPU requirements should not be great. Our online group has estimated that it will take on the order of 20 μsec to process a given pulse on a 68040 (25 MHz) CPU. This may be an optimistic estimate but even if it is off by an order of magnitude the time required to process 30 billion events is still only 6 hundred thousand seconds, or about 8 days. On a fast RISC processor this figure would be reduced by an order of magnitude. We might do well to wait until 1996 to purchase the processing power we'll require for the 1997 data.

Data production will probably be I/O bound. In that case, the time required to process all the data will be comparable to the time required to write it. Naturally, we can speed up the analysis by buying more exabyte drives and enlisting idle DAQ drives during down times. Extra drives will also be required to make copies of the 800 odd data tapes.

In addition to the production hardware, which would likely consist of a few big disks, a few fast processors and as many exabyte drives as we can muster, it is important that a disk and tape drive always be available for diagnostic analysis. Online monitoring should tell us a great deal about the basic health of the system but we will undoubtedly want immediate access to full data samples, particularly during commissioning.

Simulation remains a matter of some concern. In most high energy physics experiments, it is possible to simulate as many events (or more) as one has in the final data sample. In a minimum bias experiment like g-2, this is simply impossible. On a top of the line alpha, we estimate that it would take our full simulation (run with minimal detail) on the order of 100 years to generate 30 billion events. And yet, if there for unknown systematic effects which change ω_a by roughly 1ppm we may need to generate data sets of this size. One can search for effects analytically or exaggerate them and try to extrapolate from results drawn from smaller data sets, but when these more clever alternatives fail, we must turn to our fast Monte Carlo. If we demand that the fast Monte Carlo produce a data set in one day of CPU time, that's an approximate rate of 350 KHz or 1000 clock cycles/event on the fastest Alpha, a very demanding specification. We will do our utmost to make sure that this sort of supercomputing is not necessary.

19.11. Appendix: A more detailed summary of the simulation

19.11.1. Introduction

G2GEANT is Geant based Monte Carlo of g-2 storage ring. Elsewhere, we have outlined its functionality. Here, we give a little more detail.

19.11.2. Geometry

When the ring is fully simulated, the vacuum tank geometry is specified by BNL drawing D19-M-3443. This drawing is now fairly old, but remains adequate for our purposes. The other elements, the calorimeters, wire chambers, FSDs, Lightguides,PSDs, electrodes, etc., are described in terms of GEANT volumes and are then set in the storage ring. Here is the status of the more important elements:

1 Electrodes: The position and geometry of the electrodes are up-to-date as of 3/94. The support pieces are largely in place,

2 Collimators: The position and geometry of the collimators is up to date as of 3/94. There are 3 sets in each of the electrode sectors which are not just downstream of the inflector,

3 Yoke: Not modeled

4 Pole tips: Modeled crudely

5 Inflector: Not modeled

6 Calorimeter: Updated in 10/93 to reflect new Illinois design

7 SSD and FSD: Ditto

8 Lightguides: Reflect 10/93 design. FSD guides are reasonable approximations of true design. No SSD lightguides

9 PSD: No current design available. Model reflects status in 1991.

10 Bellows sections: Not modeled

11 Wire Chambers: A detailed straw tube design from P. Debevec was introduced in 2/94.

Design parameters are adjustable in most cases. Detailed geometries (like the calorimeter) can be replaced by approximations

19.11.3. Input

S. Mane has provided the detector group with the initial and final (typically at 22.5 microseconds) coordinates of large groups of stored muons. In either case, G2GEANT tracks the muons until their point of decay, using a parametrization of the muons' betatron motion. The decay electron is then handed over to GEANT itself for tracking and shower simulation. It is also possible to input muons or pions (also provided by S. Mane) which are useful for studies of the flash, the muon loss monitor or some of the muon phase space monitoring devices.

19.12. Magnetic field

The magnetic field is described in a giant 2 dimensional matrix, with indices corresponding to r and z, which contains the value of B_z at 1661 lattice points, 151 in r by 11 in z. It was obtained from a Poisson simulation of the magnet and will be updated with actual measurements when they become available. A pseudo-electric field option is also available. Although GEANT supports only magnetic field tracking, the electric field of the quadrupoles can be reasonably mimicked by an equivalent electric field, since the force on the muons and decay electrons is largely perpindicular to their motion.

19.13. Output

G2GEANT output is of two types, HBOOK and g-2. HBOOK output includes a standard Ntuple which is collected by G2GEANT and user defined histograms and Ntuples. g-2 style output consists of data banks which bear a strong resemblance to the raw data banks from the MTDC and waveform digitizer.

19.14. Appendix: A brief survey of the offline code

19.14.1. Traceback with GEANE

One of the issues left unaddressed in our first studies of the electron traceback was how to do the traceback in a non-uniform field. Because the traceback routine we used was fairly unsophisticated, we always kept the magnetic field uniform in our studies. Naively, one might expect that since one can use GEANT to track positrons forward in time, one should be able to use GEANT to trace them back. Once again, naive expectations are correct. A group at CERN has put together a package called GEANE which (with some slight modifications) will not only do the traceback, but calculate the errors involved as well. We have written a short program which employs the package and performs the traceback in a general non-uniform field.

The basic physics and geometry of GEANE comes from GEANT. For our purposes, the principal difference in operation is that because the particles travel backward in time, their charges and momenta must be reversed, and instead of losing energy through ionization and other physical processes, they gain energy. Furthermore, because we are also interested in the random errors introduced by, for example, multiple scattering, an error matrix is associated with each track, and is propagated with the track as it curves in the magnetic field and passes from one medium to the next.

The traceback is done in two steps. In the first, the positron is traced backwards through the three wire chambers. GEANE is given the position of the hits in the chambers and a trial momentum provided by the simple traceback, where the field is assumed constant. It then calculates a χ^2 for the trajectory and calculates a new starting momentum based on the track residuals. This process is repeated (3 iterations is generally sufficient) until the results converge. At that point, the track is propagated outward until its radial component of motion vanishes.

19.14.2. FASROF - The CERN III fast rotation code

19.14.3. Introduction

The fast rotation analysis, which seeks to measure the distribution of muon momenta by examining the beam debunching early in the spill, is based directly on copies of the original CERN III Fortran 66 code and includes two separate packages: BOBAN and REVFR. BOBAN looks at the pattern of hits before overlap and calculates the mean momentum of the bunch and the injection time. REVFR looks at the spreading of the bunch over time and calculates the equilibrium orbit distribution or, equivalently, the muon momentum distribution. Both have been rewritten in Fortran-77 for the g-2 experiment but are substantially unchanged. For complete details please consult Peter Hattersley's (and others') original notes on the two programs.

FASROF accepts as input HBOOK histograms of electron arrival times. These histograms can be made from the standard G2GEANT ntuple with a standard kuip macro. The output of both packages is very simple. REVFR prints out the radial distribution at each of its 5 iterations and then plots the last one. It also prints out the average field and the mean and rms of the radial distribution. BOBAN prints out its best guess as to the injection time and rotation frequency and plots the arrival time of the bunch and its width vs. time.

A mentioned earlier, Y. Orlov has written a program which attempts to measure the muon phase space distribution using Fourier analysis. It will soon be integrated in the offline package.

19.14.4. G2MIN - A g-2 interface to MINUIT

It will be some time before we will be spending a lot of time fitting g-2 decay spectra. However, for the purposes of evaluating the effect of pileup and other easily modeled distortions of the canonical spectrum, it's handy to have a program which will do such fits. Naturally, g2min does no minimization itself. Rather, it is an interface to Minuit (the CERN minimization package, also used by CERN III) which can be modified to suit individual needs.

The code performs a six parameter fit. Five are the traditional N, τ, ω, A and ϕ. The sixth is an overlap parameter, call it α, which modifies the spectrum as follows. Instead of the traditional form:

$$N_0(t) = Ne^{\frac{-t}{\tau}}(1 + A\cos(\omega t + \phi)) \tag{19.14.1}$$

we have

$$N(t) = \frac{N_0(t)}{1 + \alpha N_0(t)} \tag{19.14.2}$$

Fitting to other functional forms is easily done.

G2MIN's input is a formatted data file with g-2 spectrum data. The format is 10(1x,I11) but can be adjusted. Running the code requires the following steps. **READ** the data. Set the starting parameters with **PARAM**. Use **COMP** to eyeball the result. MINUIT's **STEP** sizes and BOUNDs can then be set. **LIST** each to see if they need adjustment. The time interval over which to do the fit can be set with **INTER(VAL)**. All numbers are single precision but are translated into double precision for MINUIT. To do the fit, use **CHISQ** which turns control over to MINUIT and type MINI. When MINUIT is done, it will return control to g2min and print out the final fit values and errors.

The control knobs are as follows

1 READ_DATA: Read in a formatted data file which contains the g-2 spectrum. The bin width, which determines the time, should be set first.
2 COMPARE: Plot the fitted spectrum on the workstation screen
3 INTERVAL: set the period in microseconds over which to do the fit
4 LIST_DATA: print the first microsecond of data.
5 PARAMETERS: Set initial parameters of fit
6 LIST_PARAM: Print out initial parameters of fit
7 STEP_SIZE: Set initial step size for Minuit search through parameter space
8 LIST_STEP: List initial step sizes
9 BOUNDS: Set bounds on parameters
10 LIST_B: List parameter bounds
11 CHISQ: Do the fit
12 EXIT: Exit the program

5 ns is the default bin width. Other defaults are reasonable and need not be changed, with the exception of N which depends on the number of events. Bounds and step sizes are automatically scaled when guesses are changed but can be reset with BOUNDS and STEP. CHISQ turns control over to MINUIT. Simply type MINI at the prompt and MINUIT will search out the minimum, spewing out possibly useful information as it goes. If it finds a minimum, it returns control to the user menu, and g2min prints out the location of the minimum and the statistical errors on each parameter.

19.14.5. Other programs

One other piece of code now integrated with the simulation is E. Hazen's simulation of data flow in the MTDC. The rate of data flow is critical to the MTDC design for its front end buffers are small and must be flushed often early in the spill if data is not to be lost. Eric's code runs on the MTDC data buffers produced by G2GEANT.

Chapter 20.
Work Breakdown and Coordination

Revised March 1994

The leadership responsibility to level 4 of the work breakdown is shown below. The work breakdown was done by the ten technical teams.

We are approaching a different phase in the experiment. We have almost all the pieces of the storage ring magnet at BNL, and we have begun assembly of the magnet. It is important to have coordinators with well defined responsibilities to coordinate the assembly and finally, the operation of the ring.

The complete management structure, including team leaders and coordinators is discussed in Chapter 24.

The leadership responsibility for Installation and Commissioning the Hardware (see Chapter 21) has been approved by the Parameters Committee. The Parameters Committee has requested that L. Roberts be responsible for the work breakdown for commissioning with beam.

Chapter 21.
Installation and Testing the Hardware

Revised March 1994

A workshop was held on March 10, 1994 on the work breakdown and schedule for installation and commissioning the hardware. A first pass schedule was done. Briefly, this schedule is as follows:

Commissioning the Storage Ring Magnet	November, 1994 - January, 1995
Shimming the Magnetic Field	January, 1995 - August, 1995
Installation of vacuum chambers, etc.	August,1995 - January, 1996
Commissioning with the beam begins	January, 1996

The detailed work breakdown presented at the workshop with schedule and leadership responsibility is shown in Appendix I. The calendar time is shown at level 3. The detailed time estimates are shown at lower levels. The detailed estimates may not add up to the calendar time, because some activities are in parallel, etc.

1.10	Installation & Testing	W. Morse
1.10.1	Commissioning Storage Ring Magnet - 11 weeks	W. Morse
1.10.1.1	Cool down - 2 wks	L. Jia
1.10.1.1.1	Cryo system evacuation - 1 week	
1.10.1.1.2	Cryo system set-up - 0.5 day	
1.10.1.1.3	Start refrigerator - 2 days	
1.10.1.1.4	Magnet system cool-down - 3 days	
1.10.1.1.2	Power to half nominal current - 2 weeks	G. Bunce
1.10.1.1.3	Magnetic measurements at half current -2 weeks	K. Woodle
1.10.1.1.4	Extract the energy with the quench protection circuit - 1 day	G. Bunce
1.10.1.1.5	Analyse the coil instrumentation data and compare with the quench analysis.	G. Bunce
1.10.1.1.6	Power to half current and repeat magnetic measurements - 1 week	K. Woodle
1.10.1.1.7	Study methods to "degauss" magnet to correct magnetic effects due to quench-back - 2 weeks	K. Woodle

1.10.1.1.8	Make decision on quench protection based on results of tests.	W. Morse
1.10.1.1.9	Power to full current - 1 day	G. Bunce
1.10.1.1.10	Make magnetic measurements and re-evaluate decision - 1 week	K. Woodle
1.10.2	Shim Magnetic Field - 27 weeks	K. Woodle
1.10.2.1	Install & Test Power Supply	J. Geller
1.10.2.1.1	Quench Protection	
1.10.2.1.2	NMR Feedback	
1.10.2.1.3	Transductor	
1.10.2.1.4	Reversing Switch	
1.10.2.1.5	Controls	
1.10.2.2	Install & Test Shim Trolley	I. Polk
1.10.2.2.1	Capacitec	S. Dhawan
1.10.2.2.2	Trolley NMR	R. Prigl
1.10.2.2.2.1	low-field NMR	
1.10.2.2.2.2	full-field NMR	
1.10.2.2.3	Drive	I. Polk
1.10.2.2.4	Azimuth Readout	J. Cullen
1.10.2.2.5	Computer Control	K. Woodle
1.10.2.3	Install & Test Shimming Fixed NMR	R. Prigl
1.10.2.3.1	low-field NMR	
1.10.2.3.2	full-field NMR	
1.10.2.4	Install & Test Radial Field Meas.	G. Danby
1.10.2.5	Install & Test Yoke Tilt Sensors	G. Danby
1.10.2.6	Yoke Corrections	I. Polk
1.10.2.7	Install Inflector Field Measurement	W. Meng
1.10.2.8	Map Field	R. Prigl
1.10.2.9	Map Radial Fiel	G. Danby
1.10.2.10	Survey Gap	S. Dhawan
1.10.2.11	Wedge Corrections	Z. Armoza
1.10.2.12	Rose Shim Corrections	Z. Armoza
1.10.2.13	Install & Test Pole-face windings	S. Dhawan
1.10.2.14	Pole-face Winding Corrections	S. Dhawan
1.10.3	Installation - 17 wks	W. Morse
1.10.3.1	Beam Vacuum Chamber	L. Snydstrup

1.10.3.1.1	Vacuum Chamber Sectors - 11 wks	L. Snydstrup
1.10.3.1.1.1	Clean/Bakeout - 440 hrs	D. Hseuh
1.10.3.1.1.2	Vacuum Test - 360 hrs	D. Hseuh
1.10.3.1.2	Bellow Adapters - 4 wks	L. Snydstrup
1.10.3.1.2.1	Clean Parts - 24 hrs	"
1.10.3.1.2.2	Assemble Rails/Scrapers - 104 hrs	"
1.10.3.1.2.3	Vacuum Test - 48 hrs.	D. Hseuh
1.10.3.1.3	Standard Support Frames - 8 wks	L. Snydstrup
1.10.3.1.3.1	Clean/Assemble/Align Frame - 110 hrs	"
1.10.3.1.3.2	Clean/Polish Quad Elec/Leads - 224 hrs	"
1.10.3.1.3.3	Assy/Align Quad Elec/Insul/Leads - 224 hrs	"
1.10.3.1.4	Special Support Frames (5) - 4 wks	L. Snydstrup
1.10.3.1.4.1	Clean/Assy/Align Trolley Gar Frame - 24 hrs	"
1.10.3.1.4.2	Clean/Assy Trolley Drive Frame - 24 hrs	"
1.10.3.1.4.3	Clean/Assy Inflector Frame - 64 hrs	"
1.10.3.1.4.4	Clean/Assy Fiber Monitor/PU Elec Frame - 72 hrs	"
1.10.3.1.5	Assemble/Align Vac Chbr Sectors/Sup Frm - 8 wks	L. Snydstrup
1.10.3.1.5.1	Assy/Align - 216 hrs "	
1.10.3.1.5.2	Vacuum Test - 384 hrs	D. Hseuh
1.10.3.1.5.3	Electrical Test (Quads)	Y. Semertizidis
1.10.3.1.6	Vacuum Ring Assy - 17 wks	L.Snydstrup
1.10.3.1.6.1	Install/Align Inflector Chbr in Magnet - 240 hrs	C. Pai
1.10.3.1.6.2	Test/Shim Inflector	W. Meng
1.10.3.1.6.3	Assemble/Align Vac Chbrs/Belllows in Ring (include NMR fixed probes) -960 hrs	L. Snydstrup
1.10.3.1.6.4	Install NMR Plunge Probe, Fiber Monitor, Calibrate Position - 160 hrs	L. Snydstrup
1.10.3.1.6.5	Test/Checkout NMR Plunge Probe	S. Dhawan
1.10.3.1.6.6	Test/Checkout Fiber Monitor	Y. Mizumachi
1.10.3.1.6.7	Test/Checkout Quad Electrodes	Y. Semertizidis
1.10.3.1.6.8	Install/Test/Checkout Trolley System	R. Prigl
1.10.3.2	Beam Vacuum System - 2 months	D. Hseuh
1.10.3.2.1	Gate Valves, Pumps, Gauges - 12 man-days	D. Hseuh
1.10.3.2.2	Utilities (Air, N2 Vent.) - 4 man-days	D. Hseuh
1.10.3.2.3	Instrumentation and Cabling - 15 man-days	J. Geller
1.10.3.2.4	Vacuum PLC and CPU - 10 man-days	J. Geller

1.10.3.3	Quad High Voltage System - 3 weeks	Y. Semertzidis
1.10.3.3.1	Install Ac Power to 4 Rack stations	3 days 6-95
1.10.3.3.2	Install 4 high voltage racks	4 " -
1.10.3.3.3	Install 8 high voltage conduits	4 " -
1.10.3.3.4	Install Dielectric gas system	2 " -
1.10.3.3.5	Install Quad pulsing controls	1 " -
1.10.3.3.6	Install High voltage Protection system	3 " -
1.10.3.3.7	Connect to Slow Controls	1 " -
1.10.3.3.8	Connect to Vacuum Inhibit Line	1 " -
1.10.3.3.9	High Voltage Test	1 " -
1.10.3.4	Detectors - 4 months	J. Miller
1.10.3.4.1	Install 1 or two complete stations w/electronics calibration May,1995	D. Hertzog
1.10.3.4.2	Install all detectors 1 mo Sept. 1-Oct 1, 1995	D. Hertzog
1.10.3.4.3	Install all electronics 1 mo Oct 1-Nov 1, 1995	R. Carey
1.10.3.4.4	Install cables 1 week Sept 1995	D. Hertzog
1.10.3.4.5	Wire in, shake down, calibrate electronics 2 months Oct-Dec, 1995	R. Carey
1.10.3.5	DAQ & Control - 13 months	P. Cushman
1.10.3.5.1	Purchase Host Computer 8/94	Timmermans
1.10.3.5.2	Occupy Control Room 9/94	Timmermans
1.10.3.5.3	Cold Test(Slow Control integration on Host)10-11/94	Stillman/Lopati
1.10.3.5.4	Install test beam VME crate4-5/95	Hertzog/Timmerma
1.10.3.5.4.1	supply Temporary host	
1.10.3.5.4.2	hook up CPU and ethernet	
1.10.3.5.4.3	Install and test WFD, MTDC	
1.10.3.5.4.4	Install and connect CAMAC	
1.10.3.5.5	Install Flight Simulator and Host interface 6/95	Hertzog
1.10.3.5.6	Install event-builder VME crate 5/95	Timmermans
1.10.3.5.6.1	Connect ethernet to host and test	
1.10.3.5.6.2	Install and connect fast CAMAC	
1.10.3.5.6.3	Set up Tape Drive and diff'l SCSI	
1.10.3.5.7	Install 2 VME stations in Ring 6/95	Carey/Worstell
1.10.3.5.7.1	Connect MXI interconnect to central crate	

1.10.3.5.7.2	Test WFD, MTDC readout to tape and host monitoring	
1.10.3.5.8	Flight Simulator Run on 2 stations 7/95	Hertzog
1.10.3.5.9	Install and test 4 more VME stations as calorimeters	Carey/Worstell
become ready.	7/95-10/95	
1.10.3.5.10	Transfer testbeam crate to Cont Rm as spare.10/95	Timmermans
1.10.3.5.11	Full Flight Simulator Run 11/95-12/95	Hertzog
1.10.3.5.12	Data taking 1/96–¿	Everyone
1.10.3.6	Magnetic Field Control	S. Dhawan
1.10.3.6.1	DCC	TBA
1.10.3.6.1.1	Installation of 72 coils - 2 hrs ea = 140 hrs	
1.10.3.6.1.2	Cabling from DCC to control rack	
	1 hr ea = 72 hrs	
1.10.3.6.1.3	Installation of DCC Power Supply Rack	
	and control system - 3 days	
1.10.3.6.2	Surface Coils	TBA
1.10.3.6.2.1	Installation of 72 coils - 2 hrs each = 144 hrs	
1.10.3.6.2.2	Cabling from coils to control rack	
	300 cables @ 1/2 hr each = 150 hours	
1.10.3.6.2.3	Installation of DCC Power Supply	
	Rack and Control systems = 5 days	
1.10.3.6.3	NMR	TBA
1.10.3.6.3.1	Control Electrons and VME = 5 days	
1.10.3.6.3.2	Fix probes 300 @ 1/6 hours = 50 hours	
1.10.3.6.3.3	Plunging Probes 10 @ 4 = 40 hours	
1.10.3.6.3.4	Calibraton Probe = 10 hours	
1.10.3.6.3.5	Cabling = 5 days	
1.10.3.7	Inflector	W. Meng
1.10.3.7.1	Cryostat installation	C. Pai
1.10.3.7.2	Power Sypply installation	J. Sandberg
1.10.3.7.3	Leads and He Transfer Line	L. Jia
1.10.3.7.4	Instrumentation & Control	A. Stillman
1.10.3.8	Beam Monitors - Oct. 94-Dec.95	L. Roberts
1.10.4	Testing - 4 weeks	W. Morse

1.10.4.1	Beam Vacuum - 4 weeks	D. Hseuh
1.10.4.1.1	Vacuum Testing, Conditioning - 10 man-days	D. Hseuh
1.10.4.1.2	Electrical - 10 man-days	J. Geller
1.10.4.1.3	PLC & Interlock - 10 man-days	J. Geller
1.10.4.2	Quads - 2 wks	Y. Semertzidis
1.10.4.2.1	Connect Quads to High Voltage system	4 days
1.10.4.2.2	High Voltage Commissioning, Magnet Off	2 “
1.10.4.2.3	High Voltage Commissioning, Magnet On	2 “
1.10.4.2.4	Run Quads in Beam Tuning Mode	1 “
1.10.4.2.5	Run Quads in Data Taking Mode	1 “
1.10.4.2.6	Test Slow Control and Run Controls	1 “
1.10.4.2.7	Test other interactive systems	1 “
1.10.4.3	Detectors	J. Miller
1.10.4.3.1	Detector calibration Spring and summer 1995 at a test beam	
1.10.4.3.2	Test 1 or 2 complete stations w/flight sim, calibration syst. in ring May 1995-Oct 1995	
1.10.4.3.3	Test all detectors and electronics Oct-Dec 1995.	
1.10.4.4	Magnetic Field Control - 5 weeks	S. Dhawan
1.10.4.4.1	DCC Tests = 1 week	
1.10.4.4.2	Surface Coil Tests = 1 week	
1.10.4.4.3	NMR Testing = 3 weeks	
1.10.4.5	Inflector	W. Meng
1.10.4.5.1	Cryostat Vacuum Test	C. Pai
1.10.4.5.2	Power Supply Test	J. Sandberg
1.10.4.5.3	Cryogenic Supply	L. Jia
1.10.4.5.4	Instrument Control	A. Stillman
1.10.4.6	Beam Monitors - no schedule	L. Roberts

Chapter 22.
Storage Ring Commissioning with Beam

Revised April 1994

22.1. Introduction

The muon $(g-2)$ storage ring is a unique storage ring which differs from conventional storage rings in several important aspects. There is no RF power, or cooling, so it is essentially a static device. The magnetic field value is fixed by the equilibrium radius and the magic momentum to be $\sim 1.45\ T$. The n value of 0.135 for the ring was chosen both to avoid resonances, and because it could be achieved with reasonable high voltages ($\pm 30\ kV$) and modest coverage of the storage region ($\sim$ 33%) with electrostatic quadrupoles. The quadrupole and vacuum system can be brought into operation before the beam is available, as can the superconducting inflector.

Furthermore, because of the finite muon lifetime (64.4 μs at the magic value of γ), and a cyclotron period of 149 ns, one has a maximum of approximately 4000 turns following injection. This means that the usual equilibrium of stable orbits is never reached and there will be particle losses during the entire storage time. These muon losses will be monitored during the storage time, and they have been studied with the tracking code.

The only parameters which can be "tuned" to optimize injection (besides the steering of the incident beam) are the inflector angle, and, in the case of pion injection, the incident beam momentum.

The only other parameter which can be changed is the high voltage on the electrostatic quadrupoles, as discussed in Chapter 5. Initially the quads will be powered asymmetrically, so that the beam is displaced sideways and vertically. After 100 turns, the lower voltage plates are brought up to full voltage over 50 turns, so that they are powered symmetrically, with a quadrupole field centered on the storage aperture. The scraping voltage can be varied, as can the final voltage which will change the average field index of the weak focussing ring.

Muon injection introduces an additional complication, since the fast kicker must be fired such that the full kick is there when the bunch enters, and then gone 149ns later. The beam momentum will be set at the "magic momentum", but there will need to be some optimization of the full aperture kicker, when it is brought on-line.

22.2. The Primary Proton Beam and Secondary π/μ Beam

The primary proton beam will be brought to a new target station as described in Chapter 6. The usual beam diagnostics for such a beam will be in place, so that both targeting and losses can be monitored by the AGS Main Control. Responsibility for the primary proton beam will reside with the AGS operators, and in the initial tuning the experimenters, especially H. Brown, will be involved. We are fortunate to have several collaboration members who have extensive experience in both proton and secondary beam tuning at the AGS. Bunce, Miller, Morse and Roberts have all had such responsibility, and H. Brown has been responsible for many of the AGS beams over the years.

22.2.1. The Fast Kicker to the V-line

The AGS contains twelve proton bunches which are equally spaced with a peak to peak separation of 217 ns, although it is likely that this will be changed to eight bunches. When fully operational, the fast kicker will be able to extract from one to 12 (or 8) bunches per AGS cycle, with a separation of 40 ms between extractions. With full Booster operation each bunch will contain up to 5×10^{12} protons and the bunch width is less than 10 ns full width one tenth maximum.

The fast proton kicker to the U/V lines is currently scheduled to be installed in the AGS in the shutdown after the 1994 running. It will have to be commissioned at the turn-on in January 1995. Since we will not run until January 1996, this system should be installed and fully operational before we need it.

22.2.2. V1 Line and the π/μ Beam

The beamline and beam monitoring is fully described in Chapter 6.

The V1 line setup is straightforward, since except for the fast extraction feature, it is similar to existing beam lines. C. Pearson has suggested a beam- stop just before the last dipole in the secondary line to the $(g-2)$ ring, which would permit commissioning and tune-up of the primary proton line and the muon/pion line while work is still going on in the $(g-2)$ hall.

The commissioning of the beam line will take several weeks for the necessary fault studies, tuning, etc. Pion injection will be used during the first running period and the rough procedure will be:

a. Set up all magnets to dead reckoned values, say for p=1.005p_μ.
b. Adjust D3,4 and Q3-6 to get an acromatic (dispersion free) beam centered in Q10,Q12.

c. Adjust steering magnets progressively down V1 Line to align beam on SWIC's and QUAD magnetic centers (i.e., no quad steering).
d. Adjust D5,6 and Q21-25 for an achromatic beam into Q26-29.
e. Adjust steering magnets to align beam on SWIC's and QUAD magnetic centers before entry into ring backleg.
f. Adjust final steering and inflector field to get beam to enter ring and make a turn.

22.3. The Storage Ring

The storage ring will be operated at first with the quadrupole high voltage turned off. This makes it an extremely high quality spectrometer magnet, coupled to a beamline. The only adjustments which can be made are the beam momentum, and the inflector angle. The scintillating fiber monitors will provide information on the beam at 180^0 and 270^0.

22.3.1. Using the Storage Ring as Spectrometer

One can use the $(g-2)$ storage ring dipole magnetic field as an analyzing magnet/spectrometer system when the electrostatic quadrupoles are turned off. This will permit us to determine a number of properties of the beam, which will help us tune up the ring.

With the electrostatic quadrupoles turned off, $\beta_x = X_p = R_0 = 7.112m$, where β_x is the betatron function and X_p is the dispersion function. One can observe the centroid position of the beam using a scintillating fiber profile monitor placed at 180 degrees around the ring from the inflector exit. The transform to there is the negative Unit Matrix. For a single particle in matrix notation we write

$$\begin{pmatrix} X_f - R_0\frac{dp}{p} \\ X'_f \end{pmatrix} = \begin{pmatrix} -1 & 0 \\ 0 & -1 \end{pmatrix} \begin{pmatrix} X_i - R_0\frac{dp}{p} \\ X'_i \end{pmatrix}$$

One will observe an average central value (denoted by <>) given by

$$< X_f > -R_0 < \frac{dp}{p} >= -\left(< X_i > -R_0 < \frac{dp}{p} > \right)$$

independent of X'_i, and

$$< \frac{dp}{p} >= 0.5 \left(\frac{< X_f > + < X_i >}{R_0} \right)$$

where $< X_i >$ is the mean centroid at the inflector exit and $< X_f >$ is the mean centroid at 180^0. Some fiddling needs to be done to feel assured that beam is centered in the

inflector exit aperture; then, $< X_i >= 76mm$. (The ring field should be adjusted to put the $< X_f >$ near the center for good measurement.) Then,

$$< P >= P_0 \left(1 + < \frac{dp}{p} >\right) \qquad P_0 = eB_0R_0$$

In this way we can calibrate the momentum defining dipoles D1,D2 and then select a desired $< P >$ with some confidence. If the X centroids above are determined to about 5 mm, then the accuracy of the measurement will be about $\sqrt{2} \times 5/7112 = .0010$. ($R_0$ will be known to better than 1 mm and B_0 known very well.)

22.3.2. Measurement of Mean Angle of the Beam Exiting the Inflector

If we also have a scintillating fiber detector placed well away from the 180^o point, we can measure the mean angle of the beam exiting the inflector. Suppose we have a monitor at 270^o. The transformation (with quads off) is:

$$\begin{pmatrix} X_f - R_0\frac{dp}{p} \\ X'_f \end{pmatrix} = \begin{pmatrix} 0 & -R_0 \\ 1/R_0 & 0 \end{pmatrix} \begin{pmatrix} X_i - R_0\frac{dp}{p} \\ X'_i \end{pmatrix}$$

so

$$< X_f > -R_0 < \frac{dp}{p} >= -R_0 < X'_i >$$

and

$$< X'_i >= -\frac{< X_f >}{R_0} + < \frac{dp}{p} >$$

Thus, having first measured $< \frac{dp}{p} >$, we can measure the mean angle at the inflector exit and set it as desired. The accuracy of measurement will be about 1 $mrad$.

In above procedure, the scattering and interactions caused by the passage of particles through the quadrupole electrodes may cause an offset in the observed beam centroid $< X_f >$, so we'll have to be cautious about the results.

22.3.3. Scraping and Loss Studies

Once the beam is injected into the storage ring, we will turn on the quadrupoles to their setpoint voltages and study the unscraped beam. Since the fiber monitors are so thin, they are useful for measuring the beam during several turns, and will be a useful diagnostic tool during the turn on.

The CERN ring [1] had muon losses of 1.0% per lifetime without scraping the beam. Our calculations show that we can do considerably better than CERN, as discussed in Chapter 6.

We will measure the lost muons, as discussed in Chapter 16, so that on-line we will be able to tell the effectiveness of the scraping.

22.3.4. Detector and Electronics Set-up

Once the beam is set up, the performance of the electron calorimeters can be optimized. With pion injection the response of the detectors/electronics to the pion flash must be studied. This will be essential, since the muon-decay-electron detectors will provide an essential monitor of the performance of the injection into the storage ring, and will play a key role in the setting-up of muon injection in the following year.

The decay-electron traceback system will provide information on the distribution of muons in the storage ring at all times. Whereas the information from this system may not be as useful as the destructive monitors during the initial set up, they will be an important tool in the continuous monitoring of the performance of the storage ring.

The pickup electrodes will be installed in the ring as well. This device will provide information on the muon distribution in a non-destructive way.

Once the system is optimized with pion injection, the CERN experiment can be repeated, and systematic studies can be performed. We will then have a number of months to correct any problems and to prepare for muon injection into the storage ring.

A full WBS section is under preparation on the commissioning of the experiment and will be included in the final version of this edition.

22.4. References

1. J. Bailey et al. Nucl. Phys. B150, 1 (1979).

Chapter 23.
Safety for $(g-2)$

Revised June 1994

23.1. Summary of Hazards

23.2. Description of $(g-2)$ Structures

23.3. Services and Utilities for $(g-2)$

23.4. Description of $(g-2)$ Experimental Area Equipment

23.5. AGS Organization and Administration

23.6. AGS Department Organization and Administration of Safety

23.7. Operations Procedures

23.8. $(g-2)$ Design Criteria

23.9. Identification of Hazards

23.10. Consequences of Hazards and Probability of Occurrence

23.11. References

Chapter 24.
Personnel and Responsibility

Revised February 1994

The organization of the collaboration is now rather complex, with the work divided among 10 teams. A number of coordinators oversee areas where the team responsibilities either overlap, or directly affect one another. The team structure and coordinators are listed below.

While the overall leadership comes from the Co-Spokesman, all major decisions are approved by the Parameters Committee, which consists of the Co-Spokesmen V. Hughes and L. Roberts, the Resident Spokesman W. Morse, the Project Manager G. Bunce, H.N. Brown (BNL), P. Cushman (Minnesota) (current chairman), D. Hertzog (Illinois), J. Miller (Boston), G. zu Putlitz (Heidelberg), and Y. Mizumachi (KEK).

The Parameters Committee has the authority to approve designs, key technical issues, and budgets, and is responsible for ensuring that the experimental goals are achieved. All conceptual and final designs proposed by the technical teams are submitted to the Parameters Committee for approval.

Most matters are referred to the Parameters Committee from the teams. Any change in scope from the approved design report must come before the Parameters Committee for approval. Issues can be brought to the attention of the Committee by the Spokesmen, or indeed any other concerned individual. The meetings of the Parameters Committee are open to any interested member of the collaboration, and the meetings are scheduled in conjunction with collaboration meetings, in as much as is possible, to encourage participation by the individual members of the collaboration.

The Parameters Committee also handles all matters regarding publications, conference submissions, invited talks, etc. where the work of the collaboration is presented to the external physics community.

24.1. Collaboration Management and Responsibilities

The Co-Spokesmen are Vernon W. Hughes and B. Lee Roberts. They are responsible for the overall experiment and for collaboration matters. These include, but are not limited to, making sure that adequate resources and manpower are available for carrying out the project, making sure that all teams are making adequate progress to meet the schedule for 1996 running, for calling and scheduling collaboration meetings, keeping the design report up to date, etc.

The Resident Spokesman is W. Morse. He is responsible for the overall construction and day to day management of the construction project. He has the authority to allocate the BNL capital funds specifically earmarked for the project, whether they are spent at BNL or elsewhere.

The Project Manager is Gerry Bunce. He is responsible for coordinating the project construction with the Accelerator department personnel, and working with the resident spokesman to manage the budget and schedule of the construction project.

24.2. Fraction of Collaborators' Time Committed to E821

The fraction of time each collaborator has committed to the experiment is listed below. The present time is April 1994. Future means 1995. Engineers and technicians are not listed. Individuals who serve in an advisory capacity to the collaboration are listed with a $*$ rather than a time fraction. It is understood that for university faculty members, the fraction listed is fraction of research time. Those listed as * are in an Advisory Capacity only.

Institution	**Experimenter**	**Present**$^{10/94}$	**Future**
Boston	R. Carey	1.0	1.0
	E. Hazen	0.3	0.3
	F. Krienen	0.5	0.5
	J.P. Miller	0.5	0.7
	J. Ouyang	0.8	0.8
	B.L. Roberts	1.0	1.0
	L.R. Sulak	0.1	0.1
	W. Worstell	0.5	0.5
	G. Varner	0.3	0.3
BNL	H.N. Brown	0.5	0.5
	G. Bunce	0.5	0.5
	G.T. Danby	0.25	0.25
	D. Hseuh	0.5	0.5
	J.W. Jackson	0.25	0.25
	R. Larsen	1.0	1.0
	Y.Y. Lee	0.5	0.5
	W. Meng	0.5	0.5
	W.M. Morse	1.0	1.0
	A. Prodell	*	*
	Y. Semertzidis	.1	1.0
	R. Shutt	*	*
	A. Stillman	0.5	0.5
	K. Woodle	0.5	0.5
Cornell	T. Kinoshita	0.1	0.1
	Y. Orlov	0.1	0.1
Fairfield	D. Winn	0.5	0.5

Illinios	P.T. Debevec	0.67	0.9
	D.W. Hertzog	0.5	0.5
LANL	W.P. Lysenko	*	*
Minnesota	P. Cushman	0.7	0.7
	C. Timmermans	1.0	1.0
Yale	S.K. Dhawan	0.5	0.5
	F.J.M. Farley	0.25	0.25
	X. Fei	0.75	0.75
	V.W. Hughes	0.2	0.5
	R. Prigl	1.0	1.0

Non-U.S. Collaborators

Institution	**Experimenter**	**Present**	**Future**
Heidelberg	K. Jungmann	0.25	0.25
	G. zu Putlitz	0.25	0.25
MPI-Heidelberg	U. Haeberlen	0.25	0.25
KEK	K. Endo	0.15	0.15
	H. Hirabayashi	0.1	0.1
	S. Ichii	0.1	0.1
	S. Kurokawa	–	–
	Y. Mizumachi	0.2	0.2
	T. Sato	0.1	0.?
	A. Yamamoto	0.2	0.2
Riken	L. Ishida	0.1	0.?
Tokyo	M. Iwasaki	0.1	0.5
	K. Nagamine	0.15	0.15
Novosibirsk	L.M. Barkov	–	–
	B.I. Kazin	0.2	0.2
	D.N. Grigorev	–	0.2
	E.A. Kuraev	–	–
	Ya.M. Shatunov	0.1	0.1
	E. Solodov	0.2	0.2

Institution	**Present Students**	**+6 Months**
Boston	0	+2
Illinois	2	2
Minnesota	3	3
Yale	1	1

Institution	**Student**	**Present**	**Future**

Boston		1.0	thesis
Illinois	B. Bunker	1.0	thesis
	W. Deninger	1.0	thesis
	K. McCormick	1.0	
Minnesota	D. Miller	1.0	thesis
	J. Kindem	1	thesis
	S. Giron	1	
Yale	S. Redin	1	1

24.3. Team Structure

The various tasks necessary to complete the construction, commissioning, data collection, and analysis have been assigned to working groups which have been given the title of teams by the Resident Spokesman. Below we list the teams, their responsibilities and the individuals responsible for the leadership of the teams.

1. Detector Team: Responsible for electron detectors and first level electronics design and construction. Ultimately responsible for measuring ω_a with systematic errors less than $0.1ppm$. Team Leader: J. Miller, Deputy: D. Hertzog
2. Beam Dynamics Team: Responsible for calculations and simulations of beam behavior from injection to decay. Ultimately responsible for beam stability and monitoring. Team Leader: L. Roberts.
3. Magnetic Field Shimming Team: Responsible for Magnet Shimming Plan. Ultimately responsible for shimming the field seen by the muons to a uniformity of $1ppm$ with iron and current shims. Team Leader: K. Woodle.
4. Field Measurement and Control Team: Responsible for the Magnetic Field Measurement Systems design and construction. Ultimately responsible for knowledge of the field to $0.1ppm$. Team Leader: V. Hughes, Deputy: X. Fei.
5. Storage Ring Team: Responsible for engineering and construction of beam line, storage ring magnet, and vacuum chamber. Project Manager: G. Bunce, Deputy: J. Cullen.
6. DAQ and Controls Team: Responsible for data acquisition system (hardware and software) and coordination of controls efforts. Team Leader: P. Cushman, Deputy: A. Stillman.
7. Vacuum Systems Team: Responsible for attainment of $10^{-7}Torr$ vacuum. This includes specification, purchase, and testing of vacuum pumps, specification of vacuum controls, control of materials and procedures in vacuum chamber. Team Leader: D. Hseuh.
8. Electrostatic Quadrupole Team: Responsible for design, testing, and performance of electrostatic quadrupoles with field index $n = 0.135$. Team Leader: Y. Semertzidis, Deputy: G. Bennett.

9. Muon Kicker Team: Responsible for the design and construction of the muon full aperture kicker. Team Leader: Y.Y. Lee.

10. Inflector Team: Responsible for the design and construction of the inflector magnet. This includes the testing program and interfacing with the magnetic field shimming team on reduction of the fringe field of the inflector. Team Leader: W. Meng.

24.4. Coordinators

A number of coordinators have been appointed to oversee critical parts of the construction, and to make sure that issues which stretch across team boundaries are dealt with appropriately. These coordinators and their job descriptions are listed below.

1. Magnetic Susceptibility Sheriff - K. Woodle

   Approves and logs the use of materials and electrical currents in or near the storage ring to assure that the magnetic field shimming tolerances are not exceeded.

2. Vacuum Policeman - D. Hseuh

   Approves and logs the use of materials in the beam tube vacuum chamber to assure that the vacuum tolerances are not exceeded.

3. Clock Coordinator - S. Dhawan

   Assures that NMR and muon clock frequencies are known to better than $30 ppb$.

4. Storage Ring Coil Test Coordinator - G. Bunce

   Approves and schedules storage ring coil tests and logs results.

5. BNL Inflector Coil Test Coordinator - W. Meng

   Approves and schedules inflector coil tests at BNL and logs results.

6. KEK Inflector Coil Test Coordinator - A. Yamamoto

   Approves and schedules inflector coil tests in Japan and logs results.

7. Survey Coordinator - W. Morse

   Compiles survey requirements and positional tolerances and logs survey results.

8. Space in the Ring Coordinator - G. Bunce

   a) Deputies - J. Powers and R. Larsen

   Allocates space in the experimental hall.

9. Groundskeeper - A. Stillman.

   Responsibilities of the Groundskeeper are to write rules for distribution of electrical power to ring systems and for connection of the shielding leads for instrumentation.

A secondary responsibility is to write rules for the cabling runs and the contents of cable trays. The cabling rules are to ensure conformance of wiring with the National Electric Code. There will be no enforcement of these rules other than by compliance of the various teams.

10. Vacuum Interface Coordinator - W. Morse

    Coordinates the integration of the vacuum chamber, NMR trolley, fixed and plunging NMR probes, electrostatic quadrupoles, muon kicker, and beam monitoring instrumentation designs.

Chapter 25.
Budget and Schedule

Revised March 1994

25.1. Funding Profile and Non-DOE Contributions

The past funding (FY88-FY94) for E821 is shown in the table below in $\$k$:

Year	FY88	FY89	FY90	FY91	FY92	FY93	FY94
Funding	56	926	1900	1750	2825	1600	1971

The funding we have been told to use for planning purposes for FY95-96 is given in the next table in $\$k$:

Year	FY95	FY96	Total
Funding	2500	2000	15528

In addition to the DOE support, there are major non-DOE contributions to E821 totalling about $\$2100k$.

KEK contributed the much of the superconducting coil conceptual design and the superconductor for the four 14 m diameter superconducting coils and the low carbon steel for the pole pieces of the storage ring. They also assumed full responsibility for the engineering-design and construction of the superconducting inflector, and they have assumed responsibility for the scintillating fiber beam monitors which will go inside of the storage ring, as well as just upstream of the inflector.

The University of Heidelberg is contributing the NMR system for field measurement and control. In addition to the NMR probes and electronics, they have constructed the NMR trolley to be used in the shimming of the field. Furthermore they have assumed full responsibility for the NMR trolley which travels inside of the vacuum chamber and maps the magnetic field.

The Budker Institute of Nuclear Physics at Novosibirsk is contributing the beamline trim magnets.

The National Science Foundation is supporting the participation of the Boston University Intermediate Energy Group (Miller and Roberts) and the University of Illinois group. The NSF is funding the calorimeter construction, a large portion of the front end electronics, and the muon decay electron traceback chamber system.

25.2. Schedule

The detailed integrated schedule was published in the Semester Report for April 93 - September 93. [1] Briefly, the major construction milestones are:

Milestone	Date	Status
Coils and Cryostats	Sept-93	Done
Yoke Iron	Jun-93	Done
Magnet Assembled	Nov-94	Started
Cryogenics Complete	Nov-94	Started
Storage Ring Commissioned	Jan-95	Future
Iron Shimming Complete	Aug-95	Future
Installation Complete	Jan-96	Future
Beamline	Jan-96	Started

The experiment will be carried out in phases. After the fast extraction line, the production target station and secondary beamlines are commissioned, there will be a period of time when the storage ring itself will be brought on line. After some weeks of beam-dynamics studies, during which the detectors, electronics and data acquisition system can be tested, the dedicated running can begin. It will take some time to bring the 24 detector stations on-line.

We expect to take one bunch from the AGS per AGS cycle, during all of this shakedown period. After the initial commissioning is finished, we can expect to receive 3 out of the 12 (or 2 out of 8 if the machine is running with 8) to take data. [2]

In the first year of running we expect to commission the experiment and to repeat and improve upon the CERN experiment, *viz.* we will use pion injection. If time permits,

and we get a dedicated several week run, we could achieve around an order of magnitude improvement on the CERN result. We have been told to count on a dedicated month run each year, but it is unclear whether this is true for 1996. [2]

We would expect to bring on the muon kicker in 1997. Because we have been told to plan for \$2.5 M in FY95, rather than \$3.0, it is not certain that the kicker can be ready for the 1997 run. We will do everything in our power to keep it on schedule, but with this loss of funding this year, it will be a challenge.

After the kicker is brought on, we will have to understand the beam dynamics of the ring/kicker system. Once this is understood, we will collect data and improve on our previous result at least down to an error of ± 0.4 *ppm* if the systematic errors are as expected. In the dedicated run of 1998 we will spend substantial time understanding the systematic errors, as well as collecting statistics, and we will achieve, or surpass, the goal of ± 0.3 *ppm* in the statistical error.

25.3. References

1. W. Morse, *E821 Semester Report (April - September 1993)*, *Muon (g-2) Note # 181*, December 1993.

2. M. Schwartz, private communication to the *(g-2)* management when asked for guidance on beam and running time.

Contents